INNOVATIVE MEASUREMENT METHODOLOGY IN THE STUDY OF WEATHERING OF AUTOMOTIVE COATINGS

ELIZABETH LAKIN

Doctor of Philosophy

ASTON UNIVERSITY

March 2010

ASTON UNIVERSITY

MEASUREMENT METHODOLOGY IN THE STUDY OF WEATHERING OF AUTOMOTIVE COATINGS

ELIZABETH LAKIN
DOCTOR OF PHILOSOPHY

SUMMARY

An initial aim of this project was to evaluate the conventional techniques used in the analysis of newly prepared environmentally friendly water-borne automotive coatings and compare them with solvent-borne coatings having comparable formulations. The investigation was carried out on microtomed layers as well as on complete automotive multi-layer paint systems. Methods used included the very traditional methods of gloss and hardness and the commonly used photo-oxidation index (from FTIR spectral analysis). All methods enabled the durability to weathering of the automotive coatings to be initially investigated and information to be gathered about the modes of photodegradation of the automotive coatings. However, a primary aim of this work was to develop methods for analysing the early stages of chemical and property changes in both the solvent-borne and water-borne coating systems that take place during outdoor natural weathering exposures and under accelerated artificial exposures. This was achieved by using thermal analysis, namely dynamic mechanical analysis (DMA), in both tension mode on the microtomed films (on all depths of the coating systems from the uppermost clear-coat right down to the electro-coat) and bending mode of the full (unmicrotomed) systems, as well as MALDI-Tof analysis on the movement of the stabilisers in the full systems. From the DMA analysis, the changes in glass transition temperature and relative cross-link density were determined after weathering and these were related to changes in the chemistries of the binder systems of the coatings after weathering, together with the aid of the results from the other methods of analysis.

Concentration profiles of the UV-stabilisers (UVA and HALS) in the coating systems were analysed as a consequence of migration in the coating systems in separate microtomed layers of the paint samples (depth profiling) after weathering and diffusion co-efficients and solubility parameters were determined for the UV stabilisers in the coating systems.

The methods developed were used to determine the various physical and chemical changes that take place during weathering of the different (water-borne and solvent-borne) systems (photoxidation) and the performance of the various newly developed water-borne paint formulations with that of the corresponding solvent-borne formulations prepared under similar conditions. It was seen for all tests that the solvent-borne formulations showed less changes after weathering (both natural and accelerated) than the corresponding water-borne formulations due to the lower level of cross-links in the binders of the water-borne systems. Additionally, it was found that the silver systems examined were more durable than the blue systems due to the reflecting power of the aluminium and the lower temperature of the silver coatings. The effect of the absence/presence of the UVA in the coating systems was also investigated after weathering, and the importance of the presence of the UVA was seen in all tests.

Keywords: Natural weathering, artificial accelerated weathering, solvent-borne, water-borne, clear-coat, base-coat, primer, electro-coat, photoxidation, FTIR, UV-Vis, migration, DMA.

ACKNOWLEDGEMENTS

I would like to thank my supervisor, Dr. Sahar Al-Malaika for all her help and support, Dr. Husam Sheena and all the rest of the Polymer Processing and Performance Unit.

This research work forms one part of a large European project (MANIAC) with a consortium of partners including; two different European car producer (Volvo, Daimler Chrysler), automotive paint manufacturers (PPG), additive suppliers and manufacturers (BYK-Chemie, Clariant), an accelerated weathering device manufacturer (Atlas MTT), an automotive paint application specialist (FhG-IPA) and a national testing institute (SP, Sweden). In particular, I would like to acknowledge the assistance of PPG in producing the full automotive coating panels, SP for planar microtoming and HPLC analysis and Clariant for GC analysis.

List of Contents

List of Tables

Chapter 1

Chapter 2

Chapter 3

Chapter 4

Chapter 5

List of Figures

Chapter 1

Chapter 2

Chapter 3

Chapter 4

Chapter 5

List of Schemes

Chapter 1

Chapter 2

Chapter 3

Chapter 4

Chapter 5

ABBREVIATIONS

ATR	Attenuated total reflectance
BC	Base-coat layer of the automotive coating system
CC	Clear-coat layer of the automotive coating system
CAM	Artificial accelerated weathering regime, SAE J1960
D	Diffusion coefficient
DRA	Diffuse reflectance accessory
E'	Storage (elastic) modulus, a measure of the stiffness/rigidity of the sample
E''	Loss modulus, reflects the energy absorbing (damping) properties of the sample
E'min	Minimum of the E' curve, a measure of the relative cross-link density
E'amb	Value of E' at ambient temperature
EC	Electro-coat layer of the automotive coating system
FTIR	Fourier transform infra-red spectroscopy
HALS	Hindered amine light stabiliser
HPLC	High performance liquid chromatography
MALDI-Tof	Matrix assisted laser desorption ionisation-time of flight
MS	Mass spectroscopy
OM	Optical microscopy
PAS	Photo-acoustic spectroscopy
ΔPI	Photo-oxidation index
P	Primer layer of the automotive coating system
S	Solubility coefficient
SB	Solvent-borne
SPART	Artificial accelerated weathering regime, SAE J1960, modified with periodic acid rain cycles
tan δ	Ratio of the loss modulus to the storage modulus (tan δ = E'/E'')
Tg	Glass transition temperature
UVA	Ultra violet absorber
UV-Vis	Ultra violet-visible
WB	Water-borne

CHAPTER 1:

INTRODUCTION

CHAPTER 1: INTRODUCTION

1.1 General Introduction

Automotive coatings, which are highly complex multilayer polymer systems, play an important role in enhancing both the aesthetics and durability of automotive vehicles. The coating is the first line of defence to the vehicle protecting it against many damaging environments such as radiation, pollution and rain, see **Figure 1.1**. The effect of sunlight radiation is most damaging to automotive coating systems causing problems with loss of gloss, discolouration and in extreme cases blistering on the surface of the coating. Automotive coatings need to be robust and are expected to have a service life of at least five to ten years even under very harsh conditions, including extremes of temperature, pollution, acid rain, anti-freeze, fuel spills on the paintwork, and long periods of exposure to rain and sunlight.

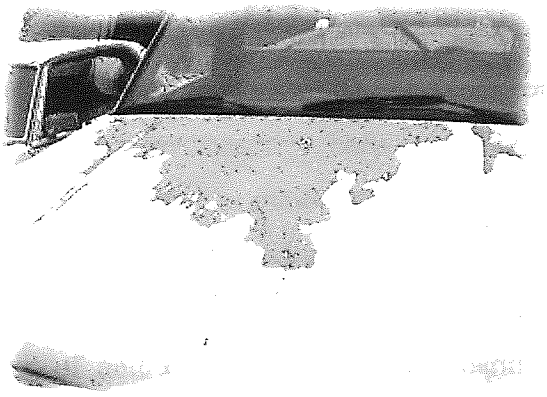

Figure 1.1 An example of failure of automotive coating due to environmental effects

Due to the fast-changing, and competitive nature, of vehicle markets, new coating systems are continuously being developed. Traditionally, coatings have been based on solvent-borne (SB) technology. However, new, more environmentally-friendly water-borne (WB) coating technology has been developed recently and the key driving forces for this development are based on the need to reduce continuous emissions, lower energy consumption, reduce costs and reduce the length of the application process without loosing performance and durability of the coating system. However, the service life performance, migration tendency of additives or the degradation mechanisms of the new future-orientated WB-coating systems are not well understood, hence the

weathering and long-term service performance properties of these systems need further investigation. However, it is not possible to wait for very long times typically required under normal service conditions to evaluate the exposure data for new coating systems, thus accelerated aging techniques have to be used.

It is important, therefore, to have a better understanding of the migration tendency of additives between the different layers of coatings, as well as their photoxidative degradation mechanisms, particularly the very early stages of chemical changes which occur prior to visually observed discolouration of WB-coating systems. These characteristics can then be compared with those of the conventional SB-coatings which are currently in use by most car manufacturers in Europe, the USA and Japan. Also there is a need to develop a robust accelerated ageing tests and analysis methodology to reduce the time-to-market for new coating systems. The methods developed must be applicable to both solvent-borne and water-borne systems containing different polymer systems and different stabilisation packages along with a number of other additives.

Common methods used to examine the weathering of coatings involve visual examination of the surface of the coatings before and after weathering; optical microscopy **[1]**, gloss **[2, 3]** and hardness measurements **[1, 4]**. Other methods involve the use of FTIR (Fourier transform infrared spectroscopy) to calculate the extent of photoxidation in the coating systems **[5-10]**, UV-Vis (ultra-violet visible) analysis to track the movement/loss of additives present in the coating system, using either transmission or reflection measurements **[6, 11-15]**. More recently, thermal analysis has also been used, particularly DMA (dynamic mechanical analysis), more recently employing different ways of mounting the coating samples **[16-19]**. The loss of additives from coatings through migration is also an important issue as coatings would lose protection from weathering and other environmental factors **[20-24]**.

The research work reported here firstly focuses on the more traditional methods of investigating the weathering of coatings through the use of microscopy, gloss, hardness and photoxidation measurements (from FTIR), and subsequently employs more innovative methodology including the use of thermal analysis by DMA, the movement of additives through the coatings, by UV-Vis spectroscopy under both transmission and reflection and the migration characteristics of the additives in the coatings, by

examining diffusion and solubility parameters of the stabilisers using two different methods.

1.2 Typical Composition of Automotive Coatings

The conventional solvent-borne automotive coatings consist of complex multilayer systems represented schematically in **Figure 1.2, [5].** A typical system consists generally of a clear-coat (CC approximately 50 μm thick, section 1.2.4), a base-coat (BC, 20 μm thick, section 1.2.3), a primer (25-30 μm thick, section 1.2.2) and an electrocoat (25 μm thick, section 1.2.1) on a steel substrate.

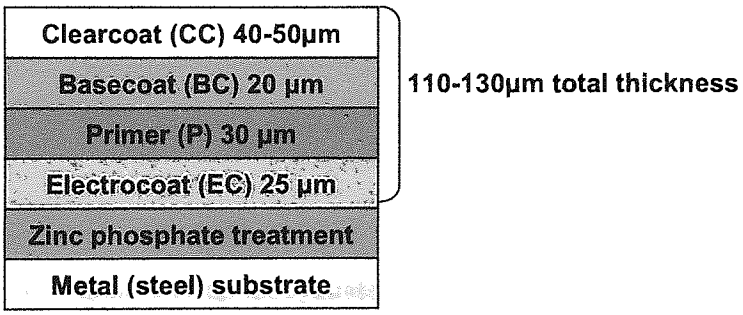

Figure 1.2 Typical composition of solvent-borne automotive coating system, with metal substrate **[5].**

1.2.1 Electrocoat

The layer closest to the substrate (normally steel), the **electrocoat** (EC), is normally responsible for corrosion protection and chip resistance as well as ensuring a uniform thickness of the coating system that is applied to all areas of the substrate, with the aim of avoiding imperfections such as thin spots, ripples or sagging which can occur when the main coating layers are applied **[5].**

1.2.2 Primer

A **primer** is typically applied on top of the EC layer in order to cover the steel roughness and seal any pores, hence ensuring a uniform surface for the upper layers of the coating and to improve adhesion. Commercially available primers include **acrylic-based powder primers**, polyester based SB or powder primers. An example of an acrylic powder primer is a methacrylic resin and a 1,12 dodecanedioc acid (DDDA)

cross-linker. The resin consists of a polymethymethacrylate (PMMA) backbone attached to a glycidyl acrylic polymer, **Scheme 1.1, [25];**

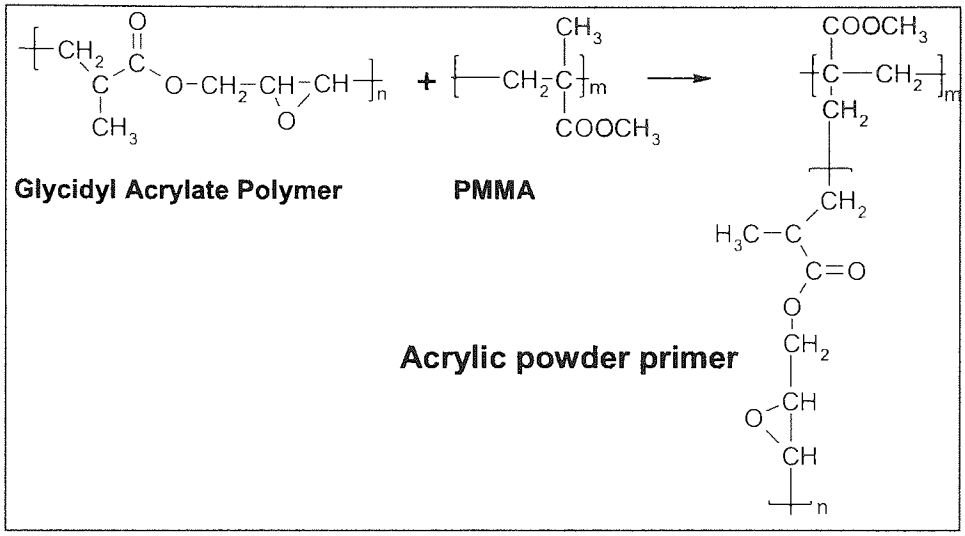

Scheme 1.1 PMMA backbone attached to glycidyl acrylic polymer, components of an **acrylic powder primer [25].**

Polyester resin primers can also have a hydroxyl functionality and the cross-linker used is generally an isocyanate **[25], (see Scheme 1.2)**. Polyesters are reaction products of multifunctional polyols with multifunctional acids or anhydrides. The ratio of polyol/acid or acid anhydride determines the type of reactive end-group.

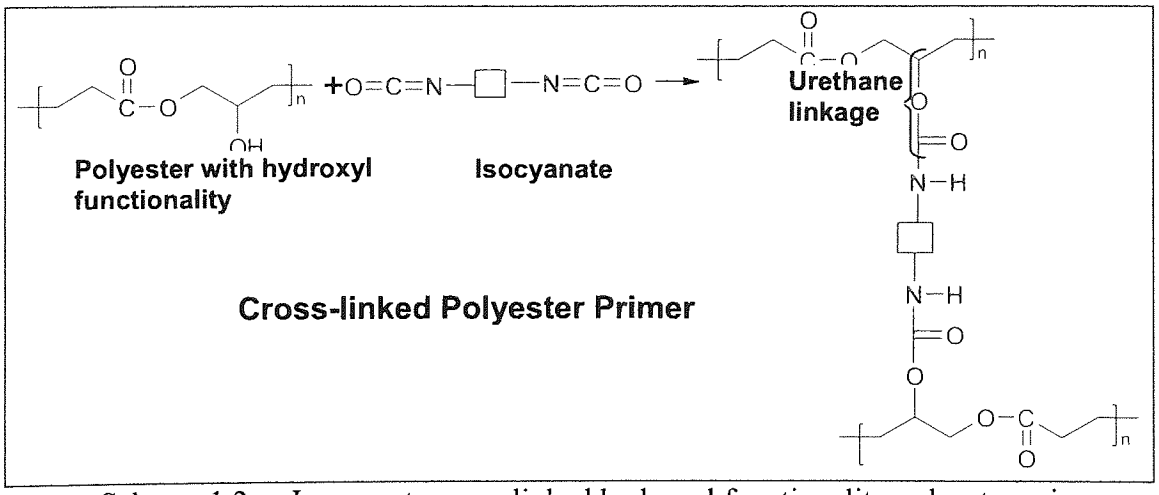

Scheme 1.2 Isocyanate cross-linked hydroxyl functionality polyester primer.

Primers based on powder coatings are typically based on polyols and are cross-linked with isocyanates to form polyurethanes, **[26]. Polyester solvent-borne primers** can also be used (they consist of a polyester resin cross-linked with methyl formaldehyde),

typical solvents utilized include butanol and xylene. Water-borne primers based on **polyurethanes cross-linked with melamines** are also in use (**Scheme 1.3**). Aqueous PU primers can offer a range of mechanical properties **[27].** The properties of polyurethane dispersions can be modified by varying the composition of the building blocks (for example polyols and polyisocyanates), or the chain extension chemistry.

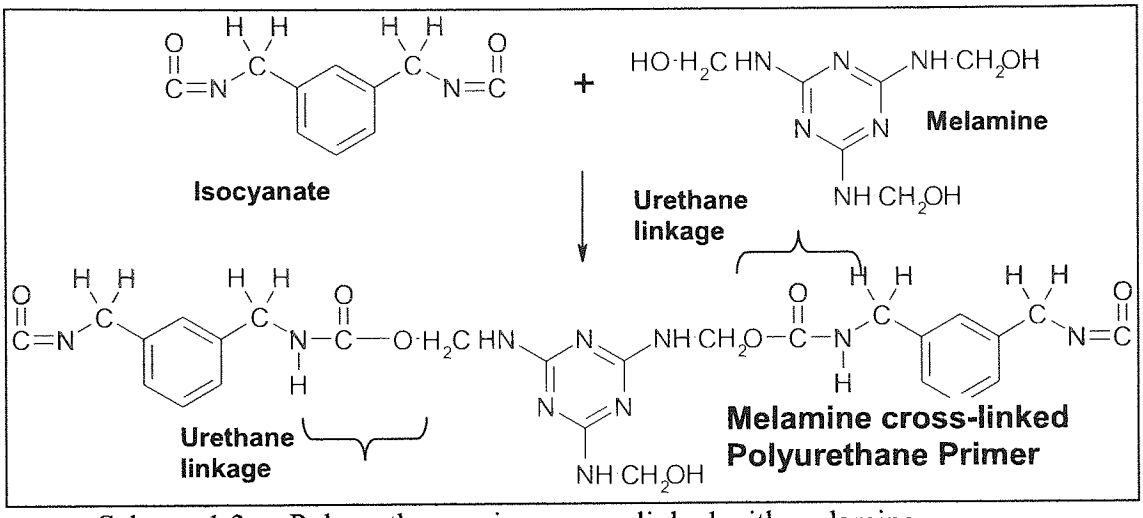

Scheme 1.3 Polyurethane primer cross-linked with melamine

1.2.3 Basecoat

The **Basecoat (BC)** layer is mainly responsible for the colour and partly for the mechanical performance and humidity resistance of the total paint system. Several different chemistries are used in these systems, each formulation typically contains several components (resins, cross-linkers) and a selection of additives. Resins used include acrylics, polyesters, alkyds, aminos, epoxies and polyurethanes, all of which cross-link by a number of different ways. The BC system can be based on SB-BC or WB-BC technologies – though most are now water-borne. The following is a discussion of the various components of basecoats. The differences between SB and WB coatings are discussed more in section 1.2.4, Clearcoats.

Acrylic resins are often used in BC, both SB and WB, they are formed through the polymerization of acrylic and methacrylic acids or their corresponding esters (**Scheme 1.4**), **[28].** Thermoset acrylic resins form a cross-linked structure through a chemical reaction either with itself or with other types of resins. However, for use as thermoset

material, the acrylic resin needs to be functionalized with reactive groups such as carboxyl, amino or epoxy to allow for cross-linking.

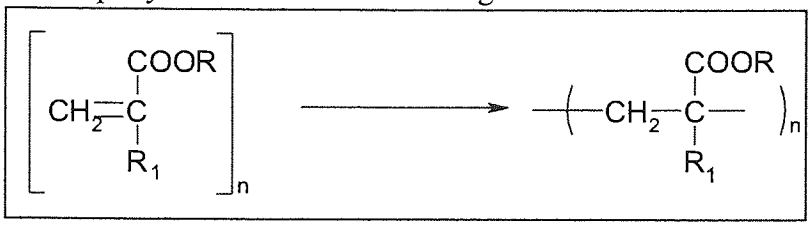

R = H,	$R_1 = H$	Poly(acrylate)
R = H,	$R_1 = CH_3$	Poly(methacrylate)
$R = CH_3$,	$R_1 = CH_3$	Poly(methyl methacrylate)

Scheme 1.4 Types of **Acrylic Resins [28]**

Polyester resins are also commonly used and are formed from the reaction of alcohols with dibasic or tribasic acids or anhydrides (**Scheme 1.5**).

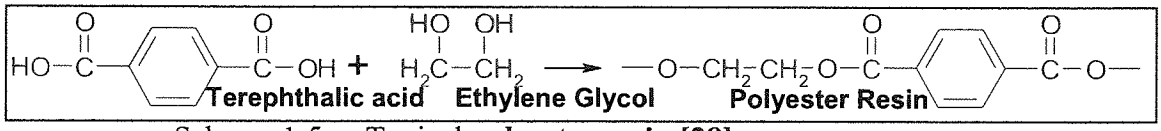

Scheme 1.5 Typical **polyester resin [28]**

Alkyd resins are polyester resins obtained through a reaction between fatty acids, polyols and a dibasic acid or anhydride (**Scheme 1.6**). They differ from other polyester resins because they contain unsaturated fatty acid functionality.

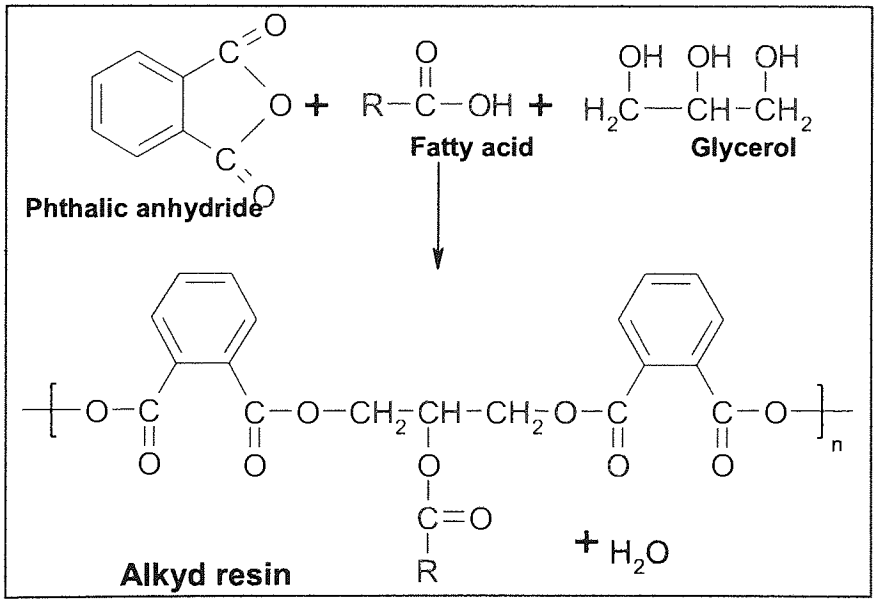

Scheme 1.6 Typical alkyd resin **[28].**

Amino resins may also form part of coatings systems, they are produced through a condensation reaction between formaldehyde and either urea or (more commonly) melamine (**Scheme 1.7**);

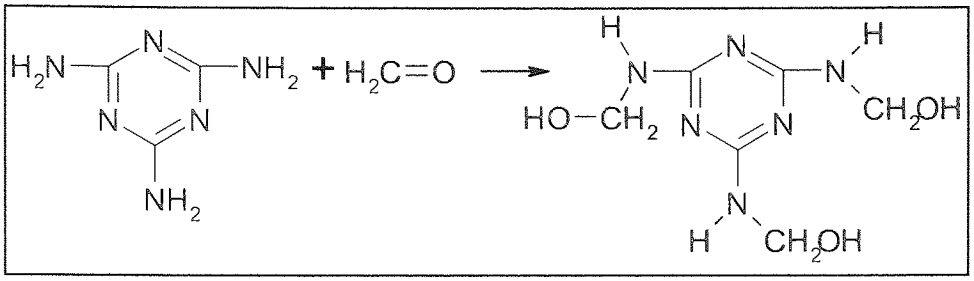

Scheme 1.7 Formation of **Methylolated-melamine** resin **[28].**

Small amounts of epoxies may be present in the coating formulation, however the occurrence of yellowing often limits their use. Epoxy resins are formed from a condensation reaction between diphenylol propane derivatives (usually bisphenol A) and epichlorohydrin (**Scheme 1.8**) **[28].** Polyamides can be used as curing agents.

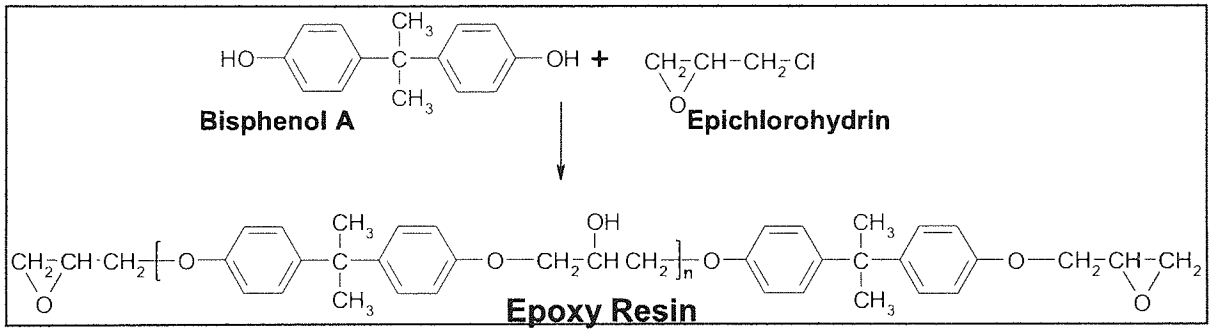

Scheme 1.8 Formation of an **epoxy resin [28].**

Polyurethanes are also used in basecoats, formed from the reaction of an isocyanate with compound containing an active hydrogen (also found in primers). The active hydrogen can be from a hydroxyl group, a carbonyl group or an amine.

However, coatings rarely contain one type of resin, they are usually extensively cross-linked structures. Isocyanates are the most commonly used cross-linkers, the first polyisocyanate commercialized for a SB coating was the reaction product of toluene diisocyanate and trimethanolpropane (TMP) **[29],** but yellowing occurs with all aromatic polyisocyanates. This problem led to the development of more light stable polyisocyanates made from aliphatic isocynates, hexamethylene diisocyanate (HDI), isophorone diisocyante (IPDI) and their adducts (**Scheme 1.9**);

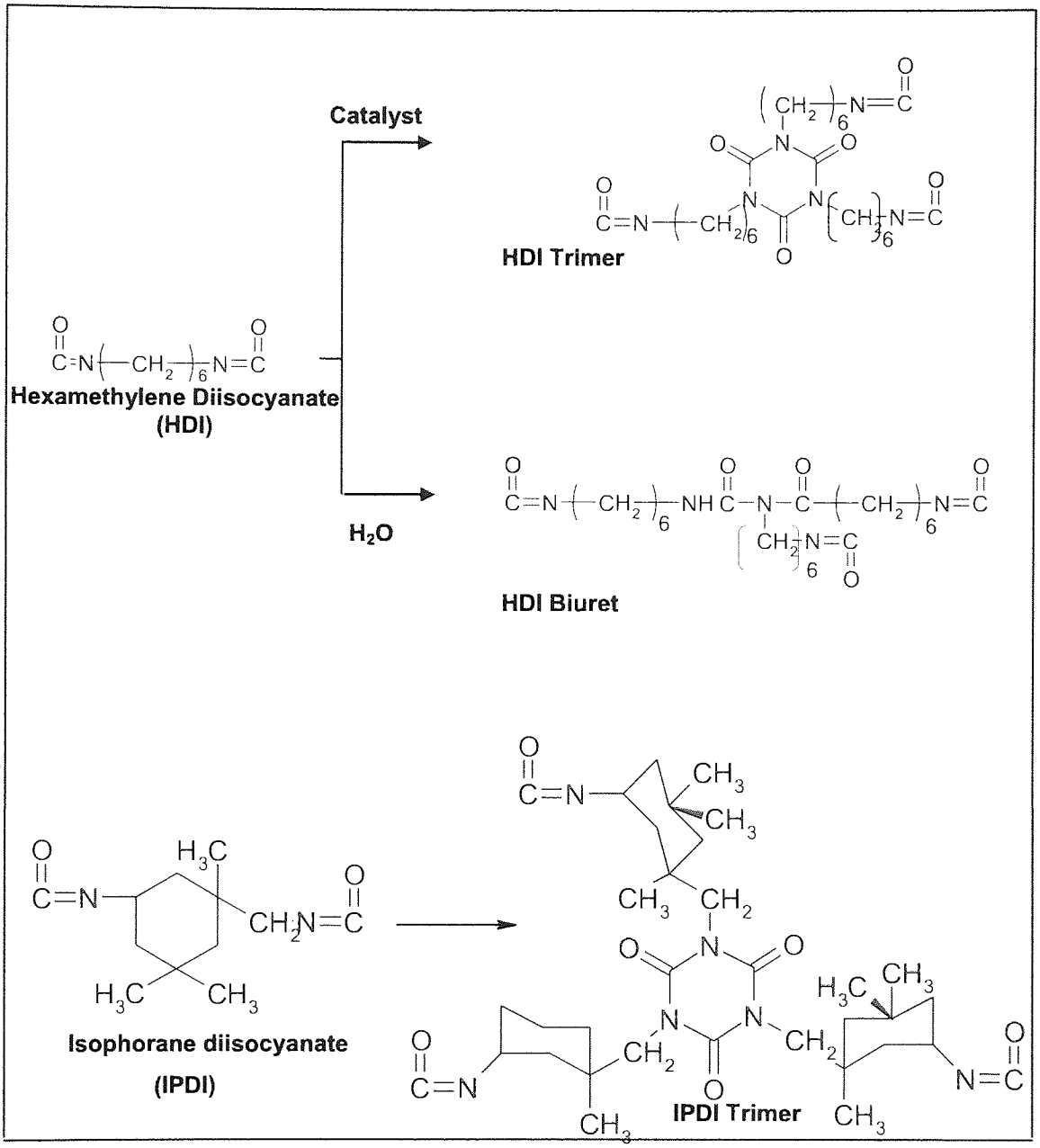

Scheme 1.9 Polyisocyanate Structures **[29]**

Thus, usually isocyanates are used as cross-linkers for other types of resins in coating systems. A major method of applying a water-based **two pack** isocyanate cross-linking (curing) binder is using a hydroxyl functional binder, with an isocyanate functional crosslinker **[30].** The wanted reaction results in a urethane linkage (**Scheme 1.10**).

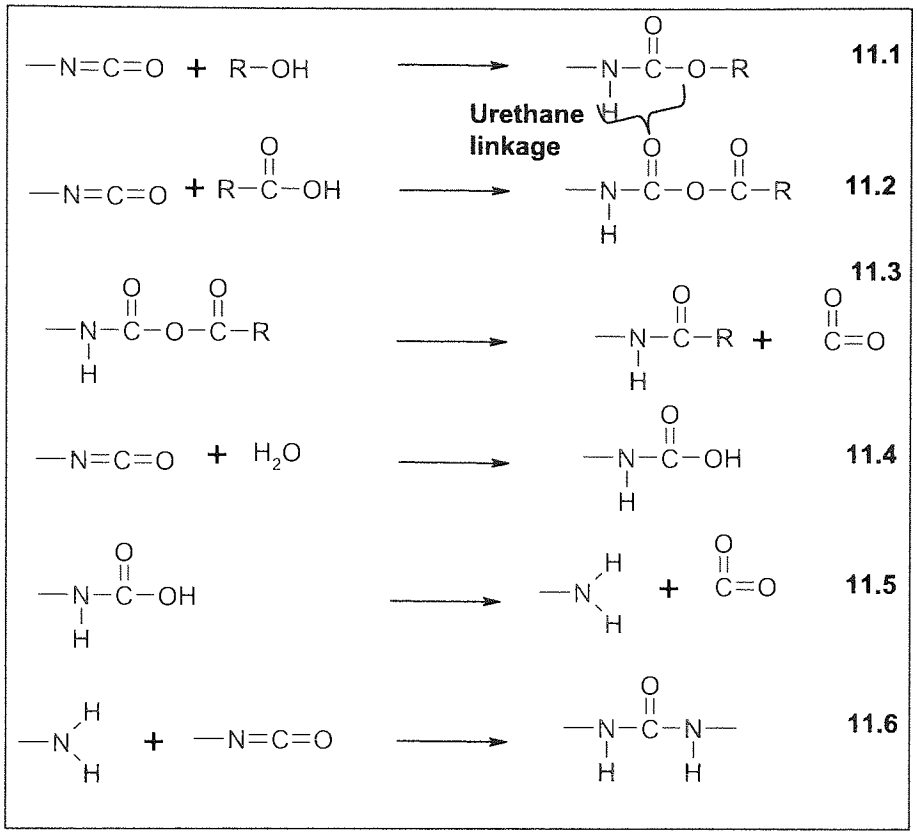

Scheme 1.10 Possible curing reaction occurring in a water-based two-pack isocyanate coating system **[30].**

Polyurethane coatings can also be used in **one-pack** coatings, the same chemicals are used as in two-pack systems except for three modifications;

(1), The polyisocyanate group is blocked,

(2), all the chemicals are blended into one container,

(3), and the coating must be heat cured (as opposed to radiation cured) **[29].**

Blocked isocyanates use a chemical group to protect the isocyanate from reacting with itself, the group blocks the isocyanate by reacting with the NCO functional groups. Common blocking agents are phenols and alcohols, however materials such as methyl ethyl ketoxine (MEKO), triazoles, imidazoles and amines can be used. When heat is applied, the blocked isocyanate breaks apart, regenerating the isocyanate functional group. The coating can then be cured by the reaction of the freed NCO groups with OH groups on the polyol. **Scheme 1.11** shows the unblocking/curing of blocked isocyanates **[29, 31]. Scheme 1.12 [31]** shows a more specific route to produce an anionic blocked-isocyanate product. DMPA (dimethylolpropionic acid) was reacted with excess

isocyanate to form an NCO-terminated group with pendent COOH groups. The NCO groups were blocked with MEKO (methyl ethyl ketoxine). The polyisocyante was then neutralized with TEA (triethylamine) **[31].**

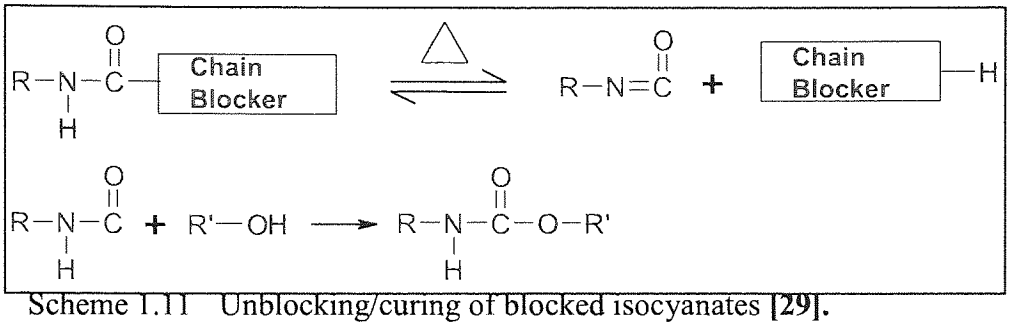

Scheme 1.11 Unblocking/curing of blocked isocyanates **[29].**

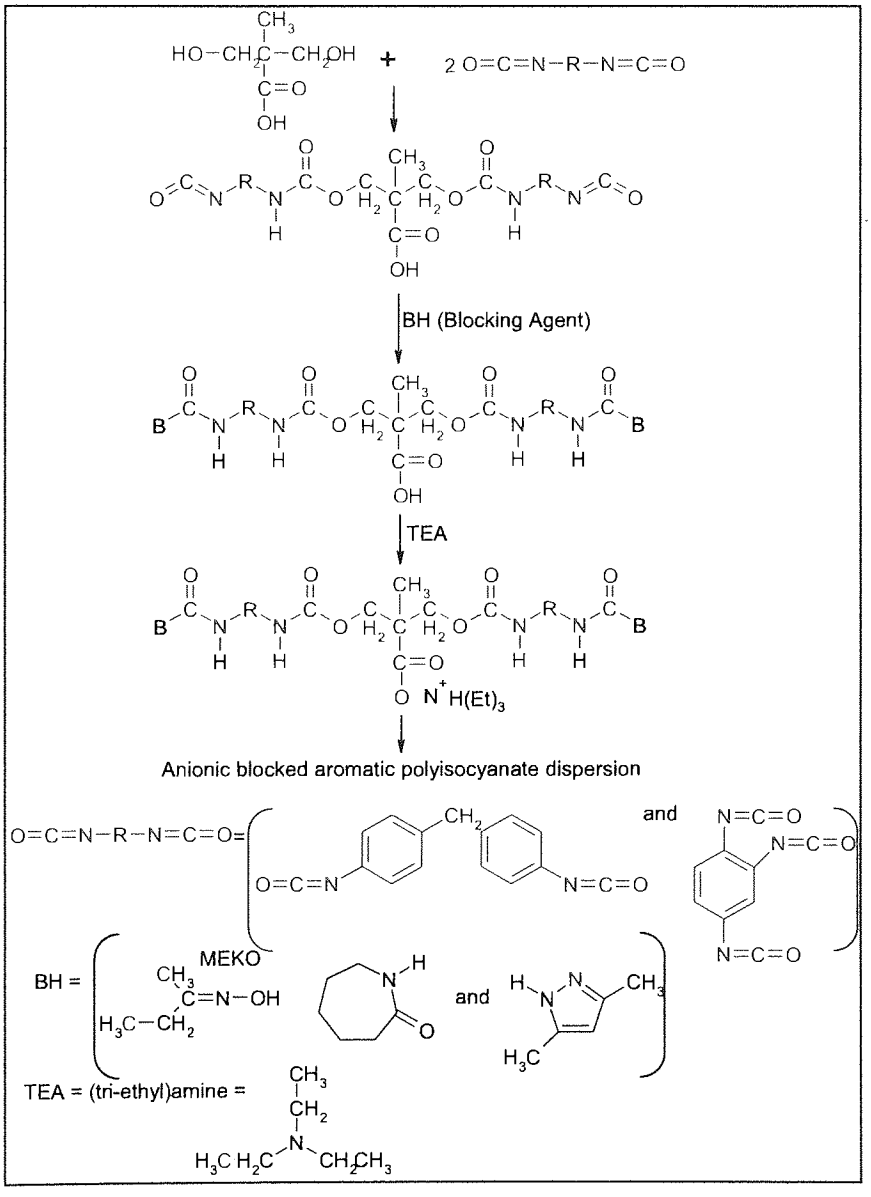

Scheme 1.12 Synthesis of anionically modified blocked-isocyanates **[31].**

Commonly cross-linked acrylics are used in coatings, the hydroxyl functional acrylic resins can be cured with blocked isocyanates, acid functionalized acrylics with epoxy functionalized curing agents, and glycidyl acrylic resins with polyfunctional acids or acidic resins. Both aromatic and aliphatic polyisocyanates can be used as the cross-linking agent for hydroxyl functionalized acrylic resins. The process can be accelerated by the use of a catalyst such as tertiary amines.

Acrylate polymers can also be cross-linked with melamine to form melamine/acrylate binders **[9], Scheme 1.13** shows an acrylate-polyol copolymer and a methyoxylated melamine cross-linker, upon heating in the presence of toluene sulphonic acid catalyst, it undergoes a transetherification reaction to form the tridimensional polymer network, in this case a thermoset melamine acrylate network.

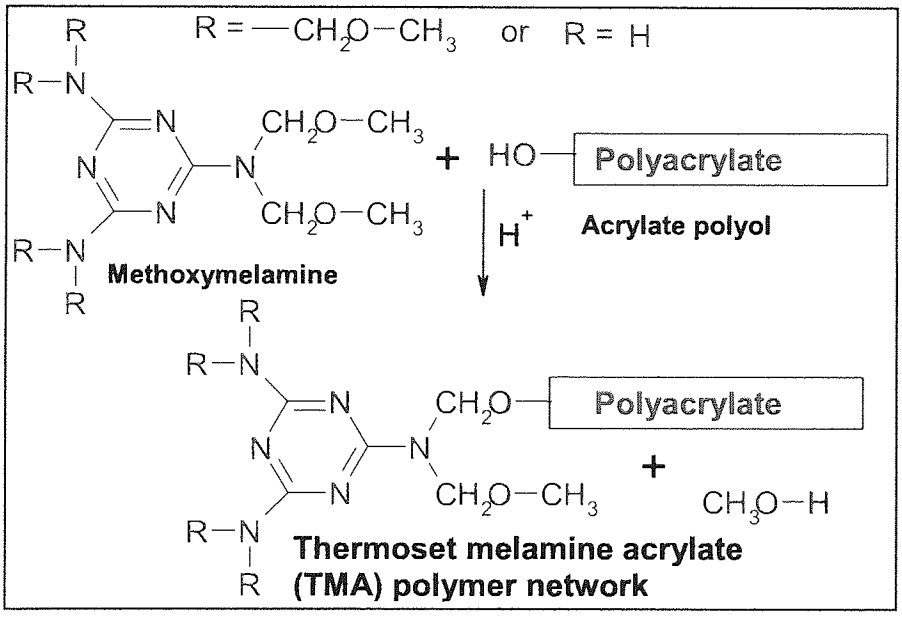

Scheme 1.13 Reaction between acrylate-polyol copolymer and a methyoxylated melamine cross-linker, to form the tridimensional polymer network.

Cross-linked alkyd resins may also be utilized; the alkyd resins are modified by the incorporation of groups such as urethane, polyamide or phenol formaldehyde. An example is the use of toluene diisocyanate to replace the dibasic acid to form a modified urethane alkyd.

Cross-linked polyurethanes are commonly a major ingredient in full coating networks, **Scheme 1.14** shows an example of a 4,4'-bis(isocyanato-cyclo-hexyl) methane based polyurethane **[32]** that can be used in a basecoat.

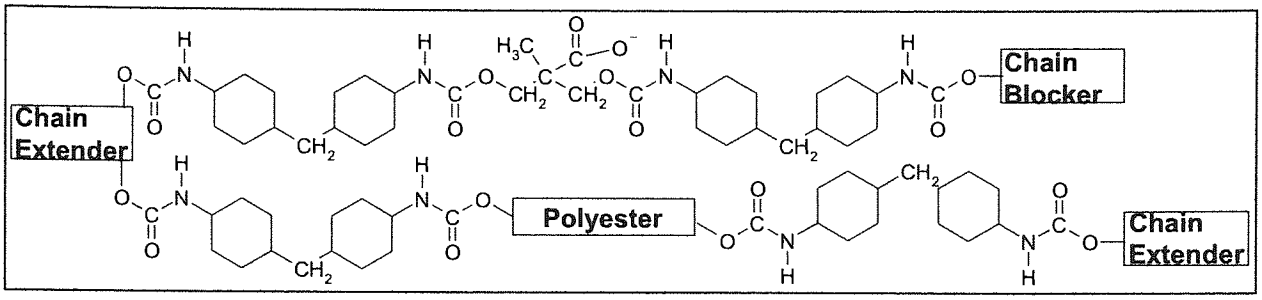

Scheme 1.14 Water-borne polyurethane base-coat **[32].**

Polyurethanes based on meta tetramethyl xylene diisocyante (**Scheme 1.15**) however, have a lower viscosity, which can allow a higher pigment concentration **[32].**

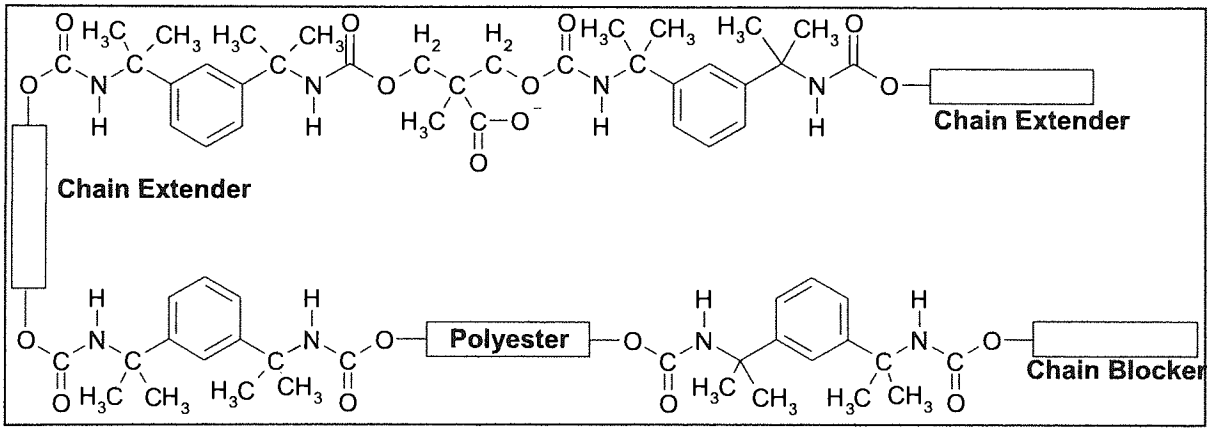

Scheme 1.15 Water-borne polyurethane base-coat **[32].**

As has been mentioned previously, the BC provides the colour to the coating system, the final colour on the finished product can be metallic or non-metallic. In the case of metallic paint, there are two different systems, two coat and one coat. In the one-coat system, the main colour coat is composed of a clear binder pigmented with sparkling aluminium powder, together with a light stable colouring pigment. In the two coat system, the first coat is a base-coat with the aluminium powder and the transparent colouring pigment. The second coat is a thick clear-coat that often contains light stabilizers. A thermo-setting acrylic binder is often used in the pigmented layer. It has been stated that pigmented coatings can last up to four times longer than clear-coats made with the same polymer backbone **[33].** Pigments and dyes have some differences in their characteristics. A pigment consists of polymer insoluble finely divided particles,

being white, coloured or aluminium flakes. Examples of commonly used white pigments include titanium dioxide and zinc oxide. Colour pigments selectively absorb some of the wavelengths of visible light. On the other hand, dyes are soluble in the polymer backbone and can develop brighter and clearer colour than pigments. Basecoats may contain stabilisers to protect against damage from sunlight, but the clearcoat is more stabilised, (stabilisation will be discussed in section 1.2.4).

1.2.4 Clearcoat

The **clear-coat (CC)** layer is the top layer of the multilayered automotive coating system and this can be either solvent-borne or water-borne. The CC is the key layer in the coating system for appearance, performance and durability. The CC is again made up of resins and binders (cross-linkers). The CC normally contains an additive package including UV-stabilisers (typically UV absorbers and hindered amine light stabilisers), defoamers and levelling agents (for example silicon derivatives). The systems can be based on a 2K-system, i.e. supplied in two containers, or 1K system, i.e. supplied in one container. CCs can also be SB or WB (**Figure 1.3**)

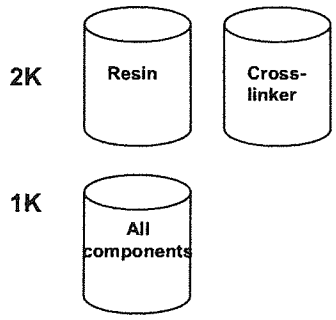

Figure 1.3 2K and 1K Clearcoats

A WB-CC system utilizes water as the main volatile liquid component. They typically contain small amounts of solvent to provide adequate flow, film formation, wetting and drying behaviour. A SB-CC coating system has an organic solvent as the main solvent carrier, this is a major disadvantage due to the amounts of solvents used in production, environmental discharge of the organic solvents is undesirable and expensive upon recycling. The advantages of WB coatings are that they exhibit low viscosities, a low volatile organic content, reduced flammability, less colour and are easily applied using conventional equipment **[28].** However WB-CCs can be expensive with high capital

costs and high storage costs due to the need for ambient temperature storage conditions in order to accommodate the freezing point of water, their tendency to trap air (foam) during high speed applications can also cause problems. Another drawback is the necessity for pre-treatment of many substrates due to the high surface tension of water, microbiological degradation, high conductivity and the effect of atmospheric humidity and temperature on the associated evaporation rates **[28].**

A common feature between the different types of WB coatings is the basic structure and reactivity associated with the polymeric binders and resins used in the formulations. Resins used in conventional SB coatings are usually modified by increasing their hydrophilic nature before being incorporated into a WB coating formulation **[28].** Typical resin chemistries include acrylics, alkyds, polyesters, epoxies and polyurethanes, common cross-linkers include melamines, and glycidyl compounds. There are two broad classes of water-dispersible resins (resins that when dispersed in water form aggregates of resin in water that are swollen with water and sometimes with solvent and water), those in which the aqueous dispersion is stabilized by anionic groups on the resin from the neutralization of an acid group on the resin with a low molecular weight amine and those which are stabilized with cationic groups from neutralization of an amine group on the resin with a low molecular weight carboxylic acid **[34].** The resins are all thermoset resins – they all have functional groups, hydroxyl, amine, carboxylic acid which can react with a cross-linker.

Water-reducible acrylic resins are prepared from a combination of acrylic and methacrylic esters, sometimes styrene, a hydroxyl-functional (meth)acrylic and meth(acrylic) acid (see scheme 1.4). The non-functional monomers control the glass transition temperature (Tg) of the coating. The resin is neutralized with an amine and diluted with water, a dispersion is obtained which is stabilized by the salt groups orientated on the surface. The structure and amount of amine used in neutralizing the resin has an important effect on many properties of the system including mechanical stability **[34].** Cationic water-reducible acrylic resins have also been produced for use with an emulsion of a solution of HDI biuret as a cross-linker in 2K coatings **[34].**

A different type of system consists of a blend of two resin types, polyester resins cured by heating with a hardening agent such as trigylcidyl isocyanurate (**Scheme 1.16**), the

reaction that may occur in a hybrid resin system containing only acid functionalized polyester and epoxy resin is also shown.

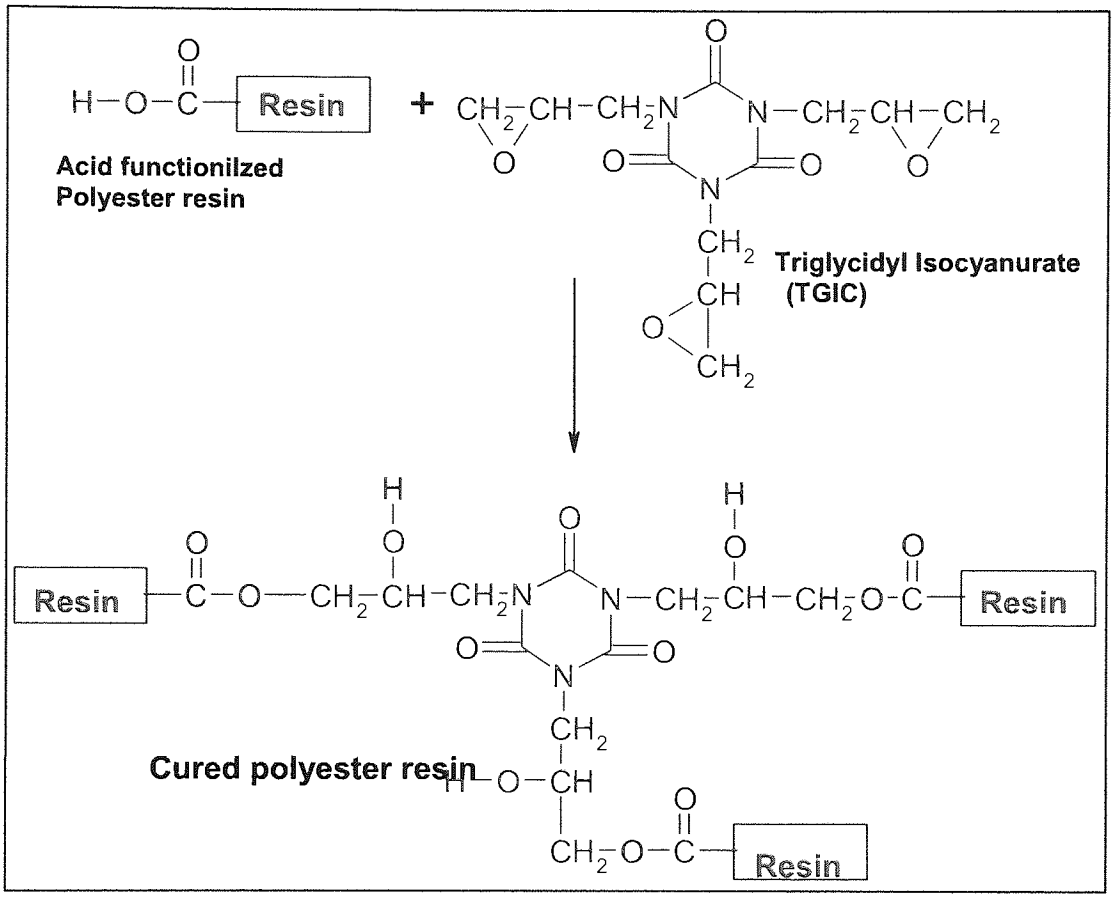

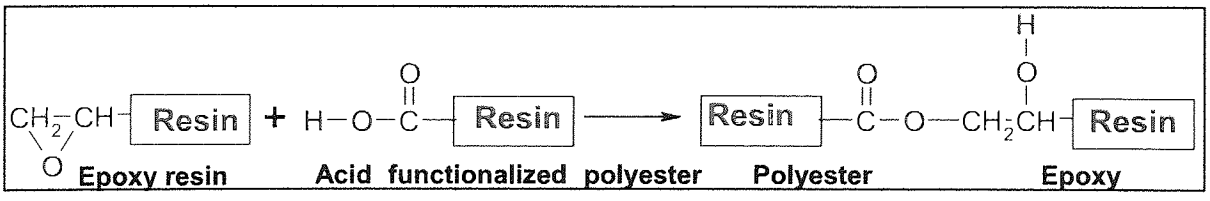

Scheme 1.16 Reaction between an acid functionalized polyester resin and triglycidyl isocyanurate (top) or an epoxy resin (bottom).

Polyurethanes are frequently used in WB-CCs, as compared to their SB equivalent, urethane dispersions can have several advantages; viscosity and flow properties independent of molecular weight, the absence of external emulsifiers, environmental safety, good adhesion and rheology characteristics. However, aqueous urethanes can have lower chemical resistance **[35].** The properties of polyurethane dispersions can be modified by varying the composition of the building blocks, such as polyols and polyisocyanates or the chain extension chemistry. One approach to produce WB

polyurethane coatings is the development of two-component WB coatings. Polyurethane dispersions are produced with a water-stabilizing group built into the polymer, most of those used in 2K coatings have reactive functional groups (often hydroxyl groups). Most polyurethane dispersions are made with aliphatic isocyanates, as colour retention and exterior durability are superior to aromatic derivatives, but also aromatic isocyanates are generally more reactive with water, the HDI isocyantes and IPDI have been most widely used **[34].**

Cross-linkers are also needed in WB systems; however another feature in which WB and SB systems differ is the miscibility of the crosslinker and the binder. In SB coatings, the cross-linker is soluble in the continuous phase that also dissolves the polymer, in WB coatings, the cross-linker has to be emulsified well enough in the formulation not to cause any stability problems or defects in the final film **[30].** Acrylic resins can again be cross-linked, a reaction between an acid functionalized acrylic polymer and an epoxy resin is shown in **Scheme 1.17,** which forms ester linkages or cross-links **[28].**

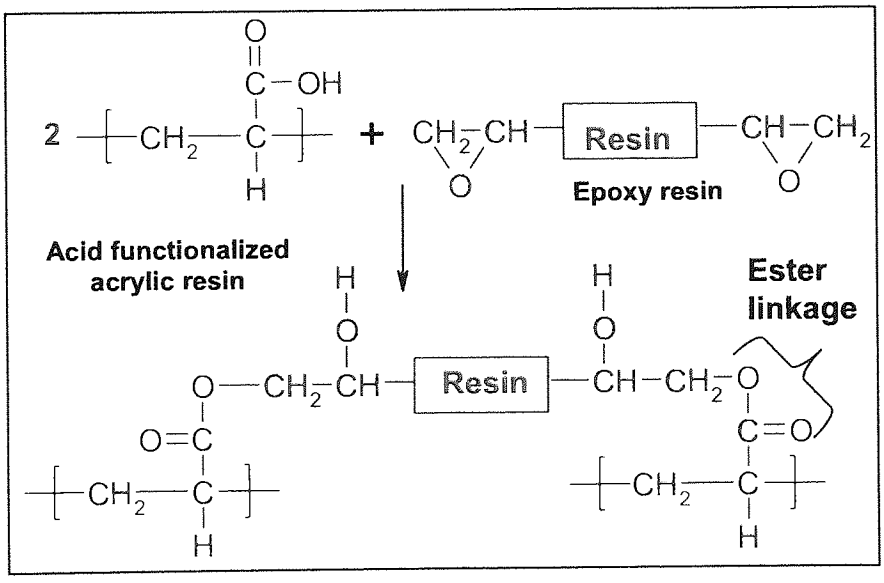

Scheme 1.17 Reaction between an acid functionalized acrylic polymer and an epoxy resin to form ester linkages or cross-links **[28].**

Acrylic polymers can also be cross-linked with isocyanates to form aliphatic polyisocyanate cross-links, **Scheme 1.18 [36].**

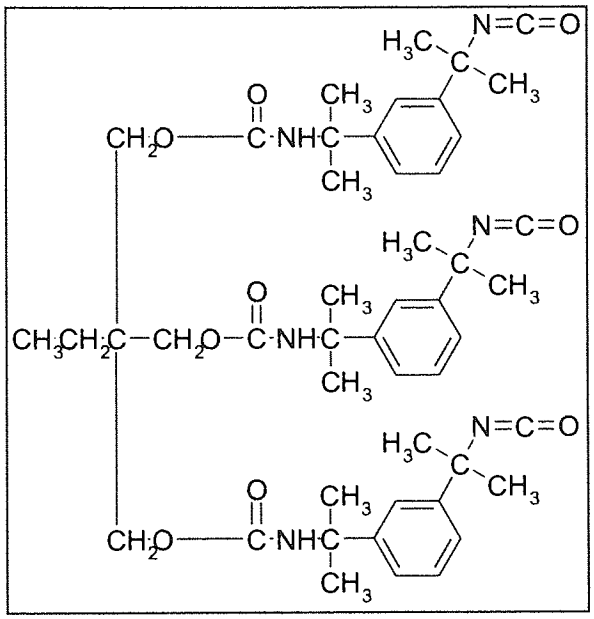

Scheme 1.18 Aliphatic polyisocyanate cross-linker **[36].**

Polyol/isocyanate systems again offer high performance coatings in terms of appearance, gloss, durability, hardness and scratch resistance, however the use of many unmodified isocyanates in many 2K systems is limited because they can be difficult to mix into a system, increasing the possibility of phase separation before reaching the substrate. Problems also exist with foam sensitivity depending upon the application window, layer thickness and reactivity. These problems can be overcome if curing at higher temperatures is possible **[37].**

Most unmodified isocyanates can only be used in proportioning spray guns that allow mixing immediately because their pot lives are so short **[34].** Thus isocyanates can be modified in a number of different ways; hydrophilically, nonionically, though the use of emulsions, and through blocking agents **(Schemes 1.11, 1.12).** The coatings can be hydrophilically modified with ethylene or propylene oxide to make them water dispersible. However, this approach requires a high degree of control over mixing **[36],** and the films are susceptible to water. A different approach is to use a water reducible polyol to disperse an unmodified polyisocyanate. However, the primary and secondary isocyanate groups react with the water in the system requiring the use of an excess of an isocyanate. The excess isocyanate then reacts with water to generate carbon dioxide that may then cause pinholes in the coating. The use of a tertiary cross-linker may help to solve these problems **(see Scheme 1.13).**

For several reasons, water-based binders for use in 2K isocyanate curing coatings has proved problematic. A major factor is the ability of the cross-linker to react with water, generating all kinds of side products (**Scheme 1.10, 10.4), [34, 38],** thus causing the loss of cross-link capacity. The carbon dioxide released as a result of the side reactions can also affect film appearance, and also cause films to be porous, decreasing the chemical resistance of the film **[30].** Polyurethanes can also be cross-linked during or after film formation, possible cross-linkers include aziridines, carbodiimides and water dispersible isocyanates. **Scheme 1.19** shows some possible cross-linking reactions that can take place with these materials **[39].** The aziridine, and carbodiimide react with the carboxylic acid on the backbone of the urethane. The isocyanate and methoxysilane silane can react with hydroxyl groups on a urethane if they are present, or will react with water to form higher molecular weight condensation products.

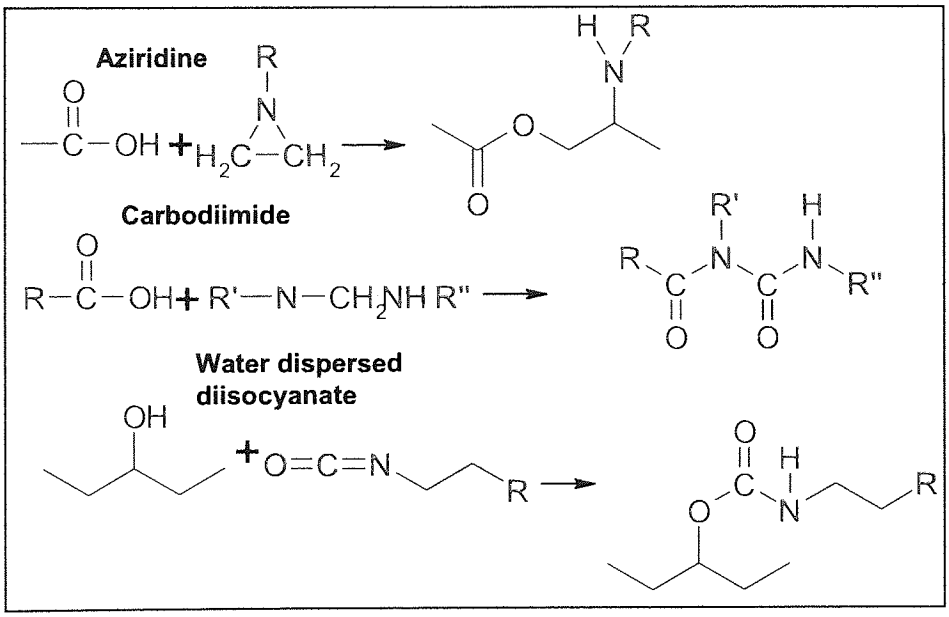

Scheme 1.19 Cross-linkers for urethanes **[39]**

Amine-functional systems are another possibility for WB CCs, and can be based on different binder components. Important factors are the amounts of amine groups, type of resin backbone, and stability of the emulsions (both chemically and physically). Amine-functional resins can be based on polyacrylates, the amines can be incorporated into isocyanate- functional polymers, however the emulsions are not very stable **[37].** Amine-functional emulsions can also be based on polyurethanes, prepared by the application of blocked amine-functional building blocks. However, these emulsions can

also be unstable **[37]**. Once again CCs usually contain a mixture of resins; **Scheme 1.20** shows a typical acrylic-melamine clearcoat **[10]**.

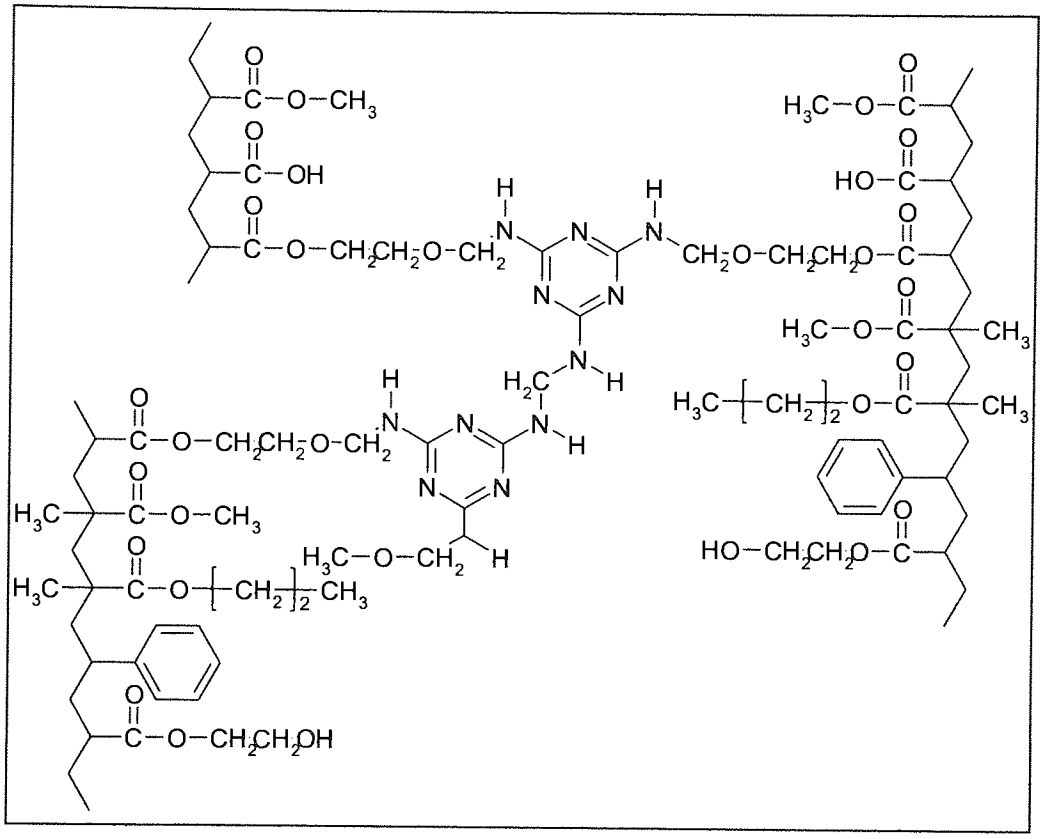

Scheme 1.20 Typical acrylic-melamine clearcoat **[10]**.

1.2.5 Stabilisation of Clearcoats

As a consequence of the long service life required and variation in service conditions of the coatings (particularly with respect to photoxidative conditions), it is necessary to add stabilisers to the coating (typically added to the clearcoat layer) formulations. Common classes of additives used include ultra-violet absorbers (UVA) and hindered amine light stabilisers (HALS). The UVA absorb the UV light (without undergoing decomposition) more readily than the polymer and in most cases they may be able to interact and deactivate free radicals formed in the substrate, this reduces the energy level of the harmful radiations that can otherwise cause damage to the coating. The absorbance (A) of a typical UVA may be regarded as a measure of its screening effect, which follows the Beer-Lambert Law **[40]**. Many pigments that are capable of absorbing strongly in the UV region can provide good protection – but are limited when transparent or translucent materials are required. As an example, carbon black provides

good absorption in the UV range (as well as providing abrasion resistance) **[41]**, but as it is black it cannot be used in the CC.

Types of UVA include benzophenones and hydroxylphenylbenzotriazoles, in both cases the transfer of UV energy to less damaging quanta is achieved due to the UVA arranging to a quinoid structure, which reverts to its original structure by giving up the acquired energy in the form of heat as shown below in **Scheme 1.21 [42].**

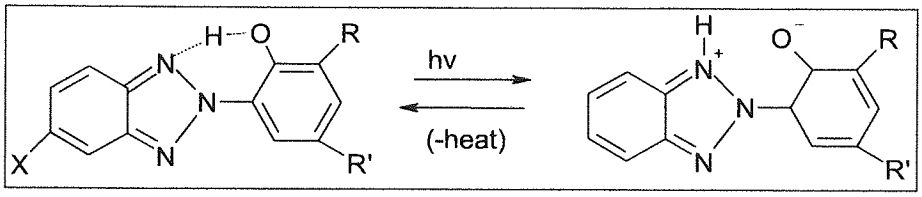

X = H or Cl, R = H or alkyl, R' = alkyl.

Scheme 1.21 Mode of action of UV Absorbers, hydroxylphenylbenzotriazoles **[42].**

UVAs are typically only added to the CC layer in the coating system, the lower layers are mostly well protected due to the filtering effect of the full depth of the base-coat, other additives may be present in the lower layers of the system. Physical factors can influence the choice of UVA, some UVAs can migrate from the clear-coat to the base-coat, lowering the light-screening power at the surface. Some migration problems can be reduced by using UVA with higher molecular weight and/or forming covalent bonds with components of the binder **[40].** The migration of photostabilisers is strongly affected by their solubility in the individual layers of the coating.

The lightfastness of a coating can be increased by the addition of hindered amine light stabilisers (HALS), see **Scheme 1.22** for a generic example.

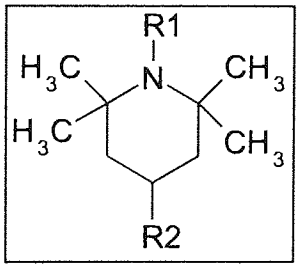

Scheme 1.22 Generic structure of a typical hindered amine light stabiliser.

HALS act through their oxidation products as free-radical traps to break the photo-oxidative chain reaction **[43]**, see **Scheme 1.23**. However, HALS can reduce the gloss of a coating **[40]** and can also migrate from the clear-coat to the pigmented base-coat and even to the primer, eventually leaving layers which may be unprotected. If only a HALS stabiliser was used, very high concentrations would be needed to prevent degradation of the polymer. Consequently HALS are normally used in conjunction with UVA stabilizers to achieve efficient stabilization of the polymers in the coating systems at low concentrations. These stabilisers can also be polymer-bound, or polymeric in nature which are beneficial whenever thin films have to retain durability over an extended service period **[40]**. However, the photochemical mechanism in polymer-bound UVA is more complex than in monomeric UVA studied under comparable conditions.

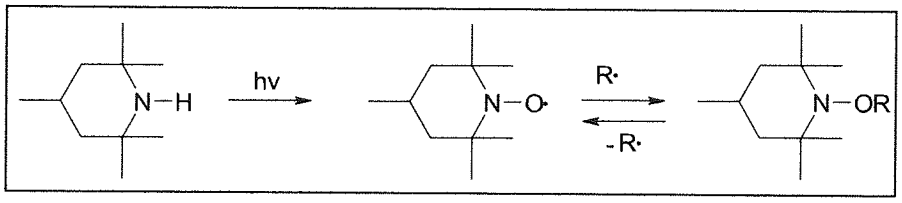

Scheme 1.23 Action of a typical HALS

1.3 Typical Curing Regimes of Automotive Coatings

Both thermoset SB and WB coatings need heat to allow the cross-linking reactions to take place between the same and/or different resins in the coating formulation, however the two types of systems do show differences in their type/level of cure. Conventional SB coatings are allowed to cure fully between the application of each layer of the coating system, for example after the basecoat has been applied, the whole system is cured at the appropriate temperature (up to 130^{0}C), before the clearcoat is sprayed. This is known as a **wet-on-dry** application process and allows the application of slightly thicker films as a full cure should be achieved right to the centre of each layer. Experimental examples include the laboratory preparation of SB clearcoats containing acrylate copolymers cross-linked with melamine being cured in a forced air oven at 120^{0}C for 30 minutes **[44]** and another acrylic/melamine clearcoat and a two-pack polyurethane, cross-linked with isocyanate, being cured for 30 minutes at 130^{0}C for the acrylate and 80^{0}C, respectively **[9]**.

The cure associated with coatings containing WB resins is often not considered to be a form of cross-linking and WB coatings are not usually as highly cross-linked as their SB counterparts. Typically the cure associated with these coatings reflects the creation of conditions under which the WB resins become insoluble and water resistant **[28].** For example, a copolymer of acrylic acid and methyl acrylate is made soluble in water by reacting the acid groups with sodium hydroxide to form polar sodium acrylate functionalities. Reversal of this neutralization process (removal of the neutralizing species) causes the polymer to form an insoluble coating. The most commonly used method of removing a neutralizing agent is through volatilization induced by the addition of heat. The cross-linking of resins in a WB paint can be achieved either through conventional cross-linking reactions (such as those used in SB systems), or through the use of novel reactions employing the use of functional groups that allow water compatibility **[28].** Often WB resins are applied in a slightly different way, instead on the 'wet-on-dry' of conventional SB coatings, they are often sprayed **'wet-on-wet'** that is, instead of the system being allowed a complete cure between the application of the different layers, the system is only given a partial cure (through a shorter time period and/or temperature). As a consequence of this, the layer thicknesses for the inner layers (such as BC, P) are often less, so that they do not need the same level of cure. However, SB coatings can also be sprayed 'wet-on-wet', an experimental example is a SB acrylic/melamine BC and a SB acrylic CC, applied wet-on-wet and cured fully only after the application of both layers at 140-145^{0}C for 20-25 minutes **[1].**

1.4 Typical Weathering Regimes for Automotive Coatings

Weathering techniques are used to assess the performance of the sample in the end use environment, and can either be indoors in artificial accelerated weathering cabinets or outdoors under natural weathering conditions. The following discussion describes and compares the two types of weathering. Traditional weathering techniques involve the exposure of experimental test materials along with materials of known weathering performance (reference materials), or merely measuring the property changes of a test material on exposure. However, more recent weathering techniques are now much more sophisticated. The fundamental parameters normally considered in selection of a weathering test used for polymers are; radiation, radiation intensity, sample

temperature, moisture (humidity, condensation, dew or rain) [**45**] and the effects of pollutants (for example acid rain).

Outdoor weathering is often carried out in the harshest environments that the end product (the coating) will face. The high humidity, temperature, rainfall and light dose make **Miami** a much more harsh environment when compared to the rest of the USA **[46],** other sites include desert sites in **Arizona** and acid rain at **Jacksonville**, Florida. Tests in Miami are typically carried out at a latitude of 25^0 52' N, and 80^0 27, W longitude and an elevation of 3m. The average high temperature in Summer months is 34^0C and 26^0C in Winter, with an average relative humidity of 78%, a total rainfall of 1685 mm, total UV radiation (295-385 nm) 280 MJ/m^2, and a total radiant energy (295-3000nm) of 6588 MJ/m^2. This compares to Arizona desert conditions, at a latitude of 80^0 27' N, and 112^0 8, W longitude and an elevation of 610m. The average high temperature in the summer is 39^0C and 20^0C in winter, with an average relative humidity of 37%, a total rainfall of 255 mm, total UV radiation (295-385 nm) 333.5 MJ/m^2, and a total radiant energy (295-3000nm) of 8004 MJ/m^2. Conditions used in the environmentally polluted region of Jacksonville, Florida include a latitude of 30^0 29' N, a longitude of 81^0 42' W at an elevation of 8m, an average ambient temperature of 20^0, an average relative humidity of 76%, a total rain fall of 1303mm and total radiant energy of 5800 MJ/m^2 **[47].**

With outdoor natural weathering, the test environment can also be changed by altering the method of specimen mounting. A variety of methods exist for the mounting of outdoor weathering samples; **open backed exposures** allow for the majority of specimen to be exposed to air circulation of ambient air, **backed exposures** are aimed to simulate end-use environment by insulating the back sides of specimens to increase sample temperature, and **black-box** exposures are aimed to simulate the heat sink characteristics of automotive bodies and increase sample temperature, the samples are mounted on a black painted, metal box, the panels on exposure cover the open top of the box and reach temperatures comparable to those of hoods and roofs of automobiles parked in direct sunlight **[47].** Selection of the most appropriate exposure angle is an issue in designing an outdoor weathering test. There are many angles to choose from, ranging from 0^0 (horizontal) to 90^0C (vertical) facing South, North or any other direction **[48].** Test racks normally face upwards towards the sun in order to achieve the

maximum solar effect. Frequently more algal growth and other fungal growth is found on test racks which do not face the sun **[48]**. There are some angles which are traditionally used, such as 5^0 facing south for many automotive coatings. When selecting the angle, the end use of the product must be kept in mind. The test method used may specify the angle to be used, for example SAE J 1976 **[49]** requires a 5^0 angle. The length of the test can often be a function of the goal of the experiment and the test parameter being measured. The test may be timed by a fixed calendar exposure, a fixed dose of radiation, or the amount of degradation measured. As weather is incapable of repeating itself, then any outdoor exposure test is unique, so starting times are often staggered either randomly or statistically. It has also been shown that for other types of polymers (stabilized polyethylene films), the rate of degradation depends upon on the climate factors to which the polymer was exposed **[45]**. Faster degradation was observed in Southern France over that seen in Miami, possibly due to the spectral distribution of solar radiation, especially that just above the short wavelength cut-off of sunlight reaching the earth at 300nm, which could be important **[45]**.

Artificial accelerated weathering techniques are used to reduce the testing times of coatings. Laboratory weatherometers accelerate sunlight degradation in a controlled environment with the advantage that more consistent results can be generated in comparison to outdoor exposure methods. Several different types of commercial equipment are available. Two main factors are considered in the selection of a light source;

1. The spectrum should at least have a cut off at a similar wavelength to the end-use environment to reduce unnatural degradation, it is advantageous if the full sunlight spectrum is included.

2. The intensity of the irradiance level should be controlled and maintained at the set point. If the Miami average optimum daylight is used as a baseline reference for sunlight, a setting of 0.35 Wm^2 can be used to simulate sunlight intensity. However for automotive coating tests, the international standard SAE J 1960 **[50]** is often applied, with a higher irradiance level used of 0.55 W/m^2. Also a more severe xenon filter is used with a combination of quartz inner and borosilicate outer filters. This produces a spectrum that includes some wavelengths that are shorter than those found in sunlight

(which are consequently more damaging), this increases the acceleration rate, thus degradation of the coating. However, there is then the risk that a different degradation mechanism may occur in the polymer that would not occur in the end-use environment.

Other factors can be accounted for in accelerated indoor testing; the relative humidity may be controlled and spray cycles can be utilized to simulate rainfall and condensation. Air may also contain pollutants which may also effect degradation reactions and may be included in weathering devices. An example of multiple pollutants on automotive coatings is the phenomena of 'environmental etch damage', this is microscopic blisters, material erosion, clear-coat cracking and non-removable water spots that are the result of a combination of acidic atmospheric pollution and UV light **[48]**.

Experimental examples of artificial accelerated weathering include panels of automotive clearcoats exposed to three different accelerated weathering programs (**Table 1.1**) **[2]**, which were all variations of SAE J1960 [50]. Samples were removed from the test after exposure to UV light doses (295-385 nm) of 56, 112, 168 and 224 MJ/m^2. Some panels were sprayed with an acidic solution (pH 3.2), other panels were placed in a chamber with a high content of sulphur dioxide gas. The acidic solution was a mixture of sulphuric acid, nitric acid and hydrochloric acid – the aim of this was to simulate acid rain. These weathering cycles were carried out in an Atlas Weather-ometer **[10]**.

Condition	Test Programme		
	CAM 1	CAM 2	CAM 3
Light source	Xenon arc, filtered through borosilicate inner and outer filter	Xenon arc, filtered through borosilicate inner and outer filter	Xenon arc, filtered through borosilicate inner and outer filter
Irradiance level	0.35 W/m^2 at 340 nm	0.5 W/m^2 at 340 nm	0.35 W/m^2 at 340 nm
Test Cycle	40 minutes light only 20 minutes light plus front spray 60 minutes light only 60 minutes dark plus back spray	40 minutes light only 20 minutes light plus front spray 60 minutes light only 60 minutes dark plus back spray	40 minutes light only 20 minutes light plus front spray 60 minutes light only 60 minutes dark plus back spray
Black standard temperature	70 ± 3°C light/38 ± 3°C dark	70 ± 3°C light/38 ± 3°C dark	80 ± 3°C light/38 ± 3°C dark
Relative humidity	50 ± 5% light/95 ± 5% dark	50 ± 5% light/95 ± 5% dark	50 ± 5% light/95 ± 5% dark

Table 1.1 Experimental artificial accelerated weathering cycles **[2]**.

Artificial accelerated weathering can also be carried out in a Q-UV machine (Q-panel company). These are equipped with fluorescent lamps, designed to shine at different wavelengths of UV light, for example UVA-340 lamps only emit UV radiation above 300 nm (with a maximum at 340 nm), like terrestrial sunlight. However, if some coatings contain HALS and UVA stabilizers, they may not be affected by the wavelengths used. This type of weathering is said to reproduce satisfactorily natural weathering conditions, with an acceleration factor depending on the particular polymer tested **[9]**. Experiments can also be carried out with the harsher QUV-B-313 weathering conditions, these tests can also be run in wet and dry cycles. A second example of the use of Q-UV weathering is on acrylic-melamine clearcoats **[10]**. An FS-40 bulb was used, which has a spectral energy distribution with a high-energy UV component (which is not present in natural sunlight). Again a cycle of 8 hours irradiation at 70^0C, followed by four hours of water condensation at 50^0C in the dark was used.

Recently, a new artificial accelerated weathering test was developed, to overcome the disadvantages of outdoor weathering tests, and understanding the synergisms of acid precipitates and solar UV radiation – known as the acid dew and fog test (ADF) **[51]**. The test involves the simulation of acid atmospheric precipitation; emphasis was given to dew and fog as they are generally more acidic than rain, and it was known that acid rain penetrates and interacts with the clear-coat **[51]**. The test was carried out in a commercial fluorescent UV lamp weathering device. Spectral radiation was not below the normal solar cut-off of 295 nm, the lamps reached and output of 45 W/m^2.

As the aim of artificial weathering tests is to replicate the effects of sunlight of samples, it is advantageous to be able to compare the two types of weathering, to extrapolate the results from artificial weathering to that of natural weathering. However, a major drawback is that outdoor weathering is very variable, materials exposed to a constantly changing environment. Due to the variability in weather, specimen replication can be a problem, so often several specimens are used, to try to reduce the variability in results **[48]**. However, it has been found that temperature and UV dose data for the years 1989-2002 show that variability of Florida weathering exposures should be within 15% of the 95% confidence limit for one year exposures. Exposures for shorter duration have greater variation and exposures over two years have little variation **[46]**, thus often two

years of exposure time is often used to compare results. In comparing artificial accelerated weathering (in particular SAE J1960) to Florida exposure, anecdotal evidence equates 2500 kJ/m^2 at 340nm to produce the weathering effects seen in two and sometimes even three years of Miami weathering **[52]**. The spectral power distribution of the SAE J1960 test method does not match actual Miami sunlight. The test has UV energy at wavelengths significantly lower than the 300 nm cut-off of terrestrial sunlight (possibly even down to 275 nm), the low wavelength UV may have sufficient energy to cause much more damage to the polymeric coatings than sunlight. Thus, SAE J1960 may have the potential to change the photochemistry of degradation of the coating systems. While this may result in faster degradation of the same type in the coating (hence the two-three year Miami 'equivalent'), it can also cause failures not seen in outdoor exposures as well as different kinds of changes than will happen in outdoor exposure. Thus it can be difficult to compare SAE J1960 to outdoor weathering. Thus, to be representative, the laboratory conditions must produce degradation mechanisms as similar as possible to the degradation occurring in the natural environment while accelerating the ageing process **[53]**.

1.5 Techniques for the analysis of automotive coatings before and after weathering

Traditionally, the industry has relied on appearance-based (such as gloss) measurements to monitor finish condition and durability of automotive coatings. The primary limitation in using appearance-based (physical) measurements is the time required for significant (i.e. measurable and reproducible) changes to take place. Additionally, while easily measured, these physical measurements provide little information on the extended weatherability of the clearcoat/basecoat coating systems which often retain excellent appearance until catastrophic failure occurs by cracking of the clearcoat, chipping, or delamination. However, changes in chemical composition/distribution, physical properties and mechanical properties can often be monitored well before appearance-based events can be detected, reducing development time, and can provide more fundamental information about the processes taking place during weathering.

A variety of measurement technologies have been used for both surface and depth-profiled analysis before and after weathering (natural or artificial accelerated); surface methods include optical microscopy, gloss and hardness, depth-profiled methods

(looking at the changes at different depths in the coating) include FTIR (transmission and ATR), UV-Vis analysis of the additives in the clearcoat (transmission and diffusion reflectance) and dynamic mechanical analysis. However, it would be very useful to be able to link the weathering induced chemical composition changes with physical property changes in the coatings.

1.5.1 Gloss measurements

The most important traditional method of detecting changes in automotive coatings is the use of gloss measurements. To the consumer, the gloss is related to how shiny and reflective the vehicle is. However, while gloss is easily measured, the method provides little information on the extended weatherability of the paint systems which normality maintains excellent appearance until failure of the coating occurs **[54].** Gloss is usually measured at 20^0 angle **[3, 18]** on the surface of the vehicle and is rated on a scale of 0-100, with 100 being the best. Often, after carrying out a weathering experiment particularly outdoor, before the gloss is measured the paints can be washed of surface dirt with flowing water containing a trace amount of soap, then patted dry with paper towels **[3],** or air dried **[55].** Gloss measurements can be made in the middle top, centre and bottom of the panel and the three readings can be averaged, or standard deviations can be calculated from four replicate results **[53].** Acceptable readings range from 80 or above on vertical areas and 85 or above on horizontal areas **[5].** Gloss readings are often reported as a percentage of the original gloss obtained in comparing unweathered and weathered samples **[1, 2].**

The level of gloss on a sample can change (usually fall) with both natural and accelerated artificial weathering. The loss of gloss results from loss of organic material from the surface **[2, 53].** The short organic moieties that result from degradation processes (scission reactions) are readily eliminated from the polymer matrix during the water spray stages in artificial accelerated weathering **[53].** This increases the surface roughness, in turn giving rise to more light diffusion at the surface of the clearcoat, and hence diminishing gloss **[1, 18].**

1.5.2 Optical Microscopy

A traditional area of studying degradation in automotive coatings is the use of optical microscopy (OM) and visual observation, looking at micrographs before and after weathering has taken place. Often illumination is used to look in detail at defects in samples, back lighting, or dark-field mode can be used to help differentiate defects in samples **[56]**. However, this method is qualitative, the samples need some sort of ranking with visual observation, Spearman correlations can be used **[51]**. Alternatively, for a densely damaged sample (particularly for scratch damage), a pixel count method (where each scratch appears as a light streak and the damage assessed by the number of pixels at each count of brightness, a histogram can then be formed, (scaled to average human perception), scaled from 0 at the poorest extreme to 100 for a perfect sample can be used to quantify and rate the damage in the samples **[57]**.

1.5.3 Hardness measurements

Hardness is an unusual physical property in that it is the result of a defined measurement procedure and not a material property susceptible to precise definitions in terms of the fundamental units of mass, length, and time **[58]**. Usually, hardness is measured in terms of the size of an impression made on a specimen by an indenter of a specified shape when a specified force is applied for a specified time, the indent being measured after the force has been removed. There are three main methods for expressing the relationship between hardness and the size of the impression; Brinell, Rockwell and Vickers. Each of the methods is divided into a range of scales, defined by a combination of applied load and indenter morphology. With the recent introduction of instrumented indentation hardness, it is possible to measure the indent under the applied force **[58]**. With the test procedure for micro-indentation hardness all parameters can be determined; for example hardness at maximum force, creep at minimum and maximum force, elastic and permanent deformation energy, the dissipated plastic indentation modulus, the residual indentation depth and the calculated hardness for permanent deformation **[59]**.

Despite the simplicity, hardness measurements have not often been used as a characterization tool in the ageing of paints **[53].** With weathering cycles, a low increase in the hardness of samples exposed to salt spray and wet condensation tests has been ascribed to physical ageing and/or migration of paint components. In contrast, the increase in hardness of cycle exposed samples likely results from chemical changes of the binder **[53].**

1.5.4 Microtoming

A microtome is often used to produce sections used for depth profiling techniques. The depth resolution of any subsequent analytical techniques carried out on the slices is thus limited by the thickness of the microtomed sections. Practical handling dictates the use of cutting sections of a minimum thickness of approximately 6μm when cutting at room temperature. Sections any thinner than this tend to shred under handling. Ageing (caused by weathering) also tends to mechanically weaken the coatings further, increasing handling difficulty **[6, 10].** Although cutting thinner sections may result in loss of mechanical integrity, the material can still be harvested and subject to solvent extraction. Cryo-microtomy is another possibility that may permit the cutting of sections than are significantly thinner than 6μm [6, 10].

1.5.5 FTIR, ATR and PAS Infra-red Analysis

FTIR is very commonly used in the analysis of coatings, both in transmission and attenuated total reflectance modes (ATR). The weathering resistance of a given polymer can be readily evaluated from the chemical changes that occur with weathering. FTIR is a sensitive and reliable technique which permits to quantify these changes at an early stage of the photodegradation process – often before physical and optical changes can be observed **[60].**

A depth profile is obtained by sequential analysis of the microtomed sections **[5].** However, there are practical limits in the thickness of the sample being analysed. Typically in order to prevent spectral distortions, sample thicknesses under 5-7μm are used.

With ATR, differences in surface/near-surface composition as a function of depth can be obtained using different ATR internal reflection elements (IRE's), which provide a method to vary the IR beam penetration depth. ATR measurements can be made with very little sample preparation. Often diamond is used as the IRE (as it is very hard), under sufficient contact pressure the sample opposite the diamond will deform to provide uniform surface contact, optimizing the quality of the resultant ATR spectrum **[6].** Most applications of ATR in coating systems are of a qualitative nature or semi-quantitative based on comparison to reference materials. ATR depth-profiling can be carried out directly from microtomed sections. However the quality of the contact between the IRE and sample is a major contributor to the quality of the spectrum.

ATR and transmittance spectra cannot be compared directly, because factors affecting the former modify the spectrum aspect, so that relative intensities are not in the same ratio as in the transmittance spectrum. The first factor is the dependence of the depth of penetration (dp) on the wavelength. As a result, going to the right side of the spectrum (high wavelengths, low wavenumbers), ATR bands are of increasing intensity with respect to bands on the left side. Software makes it possible to apply an 'ATR correction' that consists of multiplying the absorbance at a certain wavelength value by a coefficient **[60].** Hence, the spectrum intensity is increasingly reduced going from low to high wavelengths. The other source of discrepancy between ATR and transmittance spectrum is imperfect contact between the ATR crystal and the sample which brings about a further reduction in the ATR absorbance values. This parameter is also wavelength dependent; bands at high wavelength are more attenuated than bands at short wavelengths. The ATR correction allows a contact term to be introduced into the correction equation **[9].** The only way to verify if the correction of an ATR spectrum has led to the corresponding transmittance spectrum of a film sample having the same effective thickness is to take two reference bands and calculate their absorbance ratio for the two methods. After having transformed the relative intensities of the bands in the ATR spectra into those of a transmittance spectrum, they can be normalized with respect to spectra associated to samples used to build up a calibration curve [**9].**

To carry out transmission experiments, the paint film can be mounted over a window on an aluminium holder for direct transmission measurements **[61].** Alternatively, the coating can be sprayed onto silicon, the silicon discs used were notched to allow them

to be positioned reproducibly in the FTIR spectrometer by using a sample holder with a corresponding pin. An uncoated silicon disk was used as the FTIR background **[7]**; otherwise, films can be clamped inside sodium-chloride plates, used in conventional sample holder **[12]**. For ATR experiments, no further sample preparation is needed, however, it was found that the infrared response increased about 10% by waiting ten minutes after tightening the clamp to allow the paint surface to settle into making better contact with the IRE **[3]**, but this may depend on the physical nature (hardness) of each sample.

There are different approaches to investigating the effect of weathering on the FTIR spectra of automotive coatings, they include; tracking erosion of the coating **[8]**, tracking the changes in specific functional groups in the coating **[1, 2, 3, 9, 31, 61, 62, 63, 64]**, and tracking generalised photoxidation of the coating **[5, 7, 8, 10, 57]**.

The occurrence of erosion of the coatings that undergo weathering is important to ensure that the coating lasts for the required amount of time. The rate at which coatings lose film thickness can be assessed by measuring the decrease in –CH region absorbance area as a function of exposure. Film-loss rate can change rapidly during the early stages of exposure, then slows to a lower rate that is sustained for the duration of exposure **[8]**. One way to compare film-loss rates between coatings is to calculate the amount of film eroded at a given exposure time. FTIR can also be used to detect the formation of specific functional groups, such as carbonyl containing photooxidation products e.g. aldehydes, ketones and carboxylic acids **[44]**. However, different types of clearcoat families (such as acrylic/melamine with acrylic/urethane) cannot be compared using this method due to the occurrence of different absorbances in the FTIR spectrum.

It is now assumed that the long term weathering performance is determined primarily by the systems ability to resist photodegradation **[12]**. To be able to do this, a generic photooxidation parameter of the clearcoats is investigated, the photooxidation index (PI). The PI can be used to compare the photooxidation resistance of coatings from different chemical families **[8]**. For example, carbonyl formation rates are easily used to compare the photooxidation resistance of acrylic/melamine clearcoats with one another, and crosslink-scission rates are easily used to compare the photooxidation resistance of acrylic/urethane clearcoats with one another, but carbonyl formation and carbonyl

scission rates are not easily used to compare the photoxxidation resistance of acrylic/melamine clearcoats with acrylic/urethane clearcoats. Furthermore, neither carbonyl formation nor crosslink-scission rates are easily measured in epoxy/acid clearcoats.

Photo-acoustic spectroscopy (PAS) FTIR has been said to be a good indicator of the actual performance of automotive coatings, PAS can be used to monitor chemical changes associated with photoxidation and hydrolysis **[5]**, the method allows deeper sampling of the clearcoats without the need for having it isolated (such as by microtoming). PAS directly measures the absorbance spectrum without requiring a direct radiation reflection or transmission measurement **[5, 8]**. When modulated mid-IR radiation is absorbed by the sample, the material heats and cools in response to the modulated IR energy impinging on it. The heating and cooling is converted to a pressure wave, which interacts with the coupling gas (usually He). Thermal expansion and contraction of the gas is then detected by an acoustic detector and transduced into the photoacoustic signal. Contributions to the signal come from each region of the sample in which IR radiation is absorbed.

1.5.6 UV-Vis Analysis

UV-vis (UV-visible) can be used to track the movement/ changes in concentration of any UVA (and possible HALS) present in the coating, either for the microtomed slices or for free films. UVA analysis can be carried out using transmission or diffuse reflectance measurements. The technique monitored all UV-Vis absorbing species encountered in the beam path, including UVAs, HALs and possible degradation products.

A simple measurement of a thin film containing a UVA can turn out to be a good method for analysing the UVA in a coating **[64]**. The mostly particle free clearcoat layers give the highest quality spectra relative to the other particle containing system layers. Scattering of the incident radiation can be quite substantial, even for those relatively thin sections. Therefore, most UV-Vis transmission mode analyses that have been reported are on clearcoats or particle-free binders of other layers. Alternatively,

the clearcoat samples can be cured on quartz slides **[8]**. When studying a UVA concentration across the whole thickness of the clearcoat, it must be noted that the thickness of the clearcoat and the concentration of the additive may be a limiting factor that may cause the UV signal to saturate **[11]**. Typically, UVAs are used at a concentration of 3% (by weight), as the thickness of the clearcoat can be up to 50μm, which could give a clearcoat absorption of around six, which was not useful due to instrumental limitation **[11]**, thus a way around was needed; the reference beam can be attenuated to measure greater absorbances, using filters **[11]**.

In transmission measurements, the usual assumption is that the optical properties of the material under examination follow the requirements of the Beer-Lambert Law; the material is non scattering or 'optically clear' **[65]**. However for some materials: i) the light may be scattered out of the optical path and therefore be undetected, ii) although the light may not be lost, multiple scattering may occur, which will greatly increase the pathlength of the light. Thus, when a scattering sample is used, the measured values may be attenuance (absorption plus scattering) and results will differ significantly from those of absorption alone. These differences may be observed as either an increase in apparent absorption or a shift in the absorption peaks **[65]**. The incorporation of an **integrating sphere** into a UV-Vis spectrophotometer increases the accuracy of absorption or transmission measurements as any scattered light is reflected back into the light path and therefore not lost. Reflection consists of two components: specular and diffuse. Specular reflection is the mirror-like reflection off a sample surface, diffuse reflection occurs when the surface reflects light in many different directions, giving the surface a matt finish. The basic principles of an integrating sphere are shown in **Figure 1.4 [15]**.

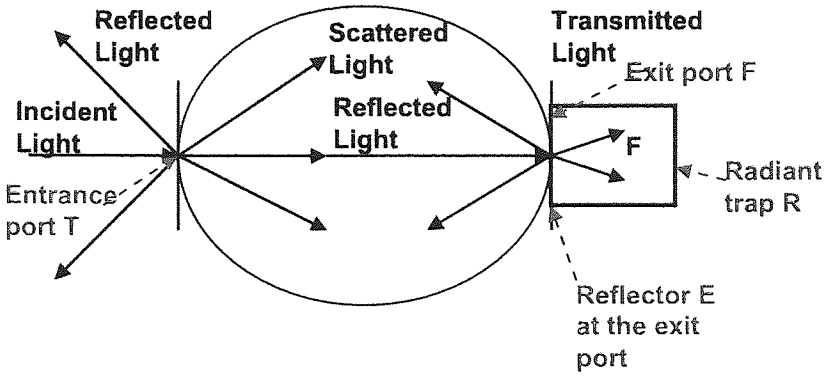

Figure 1.4 Basic Principles of an Integrating Sphere, the sample is placed at entrance port **T** to obtain a transmission spectrum, a reflector may be placed at the exit port **E**. When a reflectance spectrum is obtained, the sample is placed at the exit port together **F** with the radiant trap **R.**

Typically, a sample is first placed at the **entrance port** of the sphere; in principle all radiation passing the sample is collected by the sphere. The majority of light scattering originates from regular transmittance. To obtain the reflectance spectra the sample is placed behind the exit port, at the **reflectance port**. A radiation trap is often placed behind the sample, which has black internal surfaces that absorb all the radiation entering the trap, in this way, only radiation reflected by the sample is collected by the sphere. The spectra from samples at the **entrance** and **exit ports** are then added, in the resultant spectrum, all the effects of scattering and reflection will have been removed. This spectrum may then be transformed into an absorption spectrum, where the baseline should be very close to zero, with a good signal-to-noise ratio **[15].**

1.5.7 HPLC Analysis

Chromatography-based techniques such as high performance liquid chromatography (HPLC) have also been found to be useful in determining depth profiles of species that had been first extracted from microtomed slices **[5, 66].** This technique had been used in the study of UVAs and HALS in clearcoats **[5].** A solvent appropriate to the material of interest is used to extract each section **[6, 10].** The chromatographic signals obtained for a given sample are then normalized to the weight of material extracted **[5].**

1.5.8 DMA Analysis

DMA permits the characterization of the viscoelastic properties of coatings, of both free (microtomed) layers, and the whole coating system with the substrate – although different methods may be used. In a typical DMA measurement in tension when the force, (F), is exerted on the sample, the sample elongates through a small displacement, (x). If the force is applied in the form of a sinewave, the resulting deformation exhibited by the sample (i.e. the strain) will also take the form of a sinewave. Energy dissipation in the coating, due to molecular motions, causes the sample strain to be out of phase with the applied force (**Figure 1.5**).

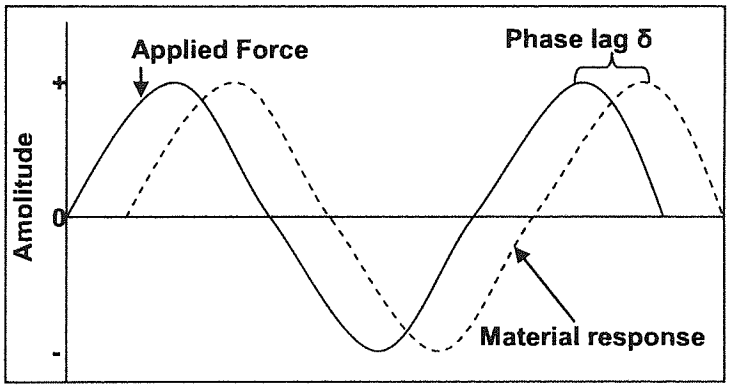

Figure 1.5 Phase lag in DMA tension analysis

Due to the viscoelastic nature of polymers, the point of maximum strain does not occur at the same instant as the maximum applied force. The **phase lag**, defined as the phase angle (δ) is then measured in conjunction with the sample geometry (length and cross-sectional area) to determine the quantitative mechanical properties of the sample. The phase lag results from the time required for molecular rearrangements and is associated with relaxation phenomena **[67].** The parameters measured by the DMA include **[68];**

E' Storage (elastic) modulus, a measure of the stiffness or rigidity of the sample

E'' Loss modulus, which reflects the energy absorbing properties of the sample. The absorption of mechanical energy is related to the movements of specific molecular segments (i.e. main chain, side groups or small groups).

tan δ Ratio of the loss modulus to the storage modulus (tan δ = E''/E) and is a useful index of material viscoelasticity since it is the ratio of the viscous and elastic

components. The damping is a measure of the internal friction of the material and indicates the amount of energy loss in the material as dissipated heat **[16].**

From the relation between force (stress) and deformation (strain), the storage modulus E' and the loss modulus E'' can be calculated. If the applied amplitude of force and deformation are in the range of the theory of linear visco-elastic behaviour, then E' and E'' are independent of the applied forces and deformations **[17].** Modulus data in the form of the storage modulus E' is equivalent to that collected from traditional mechanical tests and gives a measurement of the strength and stiffness of the material **[16].** The coatings networks can be crosslinked weakly or strongly, they can form flexible or rigid chains or a combination of both in different chain segments. Most of the networks consist of an amorphous structure.

The measurement of dynamic material properties of a coating is complex **[19],** since samples generally need to be applied to a support. Accurate analysis requires the use of supports that do not significantly influence the results **[69].** The coatings are strongly adhered to the metal substrate meaning that they are difficult to remove for the purpose of conducting standard tensile tests **[19].** Testing the coating in situ (bending) avoids the problems of preparing free-standing films and retains the structure (composition profile, morphology and internal stresses) associated with the coating and curing operation. Typical experimental parameters for a coating film (in tension) include, heating from -90 to 150 ^{0}C at 5^{0}C per minute, at a frequency of 1 Hz **[56].** Alternatively, bending tests can be used to test the whole system, including the substrate. Typically, samples 60mm*10mm are cut from the painted steel panels and mounted in the 3-point bending fixture of the DMA. A static load of 2N is applied to the sample whilst a dynamically oscillating deflection (maximum 40μm amplitude) is applied during a temperature ramp. The frequency of oscillation typically used is 1 Hz, under a temperature regime of 39-130^{0}C at 3^{0}C per minute **[19].**

Determination of Tg of the coating involves measurement of the temperature at which a property undergoes a significant change when the material converts from a glassy to a rubbery state. The Tg is associated with the initiation of the micro-Brownian motion of the molecular chains, it is affected by a number of chemical and molecular structures;

the flexibility of the molecular chain, the bulkiness of the side groups **[67].** As a general rule, the values for Tg obtained by means of different techniques are not generally comparable **[64].** The methods for determination of Tg from DMA measurement have been debated. Methods used include the peak or onset of the tan δ curve, the onset of E' drop, or the onset of the peak of the E'' curve. Values obtained from these methods can differ up to 25^0C from each other on the same run, so it is important to state which method has been used **[16]** (**Figure 1.6**). It is also important to state how the Tg has been determined, by defining the heating rate, applied stresses, frequency and any purge gases. The Tg is frequently determined as the temperature at the maximum of the tan δ peak **[7, 19, 68, 70].** The magnitude of the tan δ reflects the mobility of the chain segments between crosslinks in the glass transition region. The broadness of the tan δ reflects the homogeneity of the network **[56].** All cured resins have broad tan δ curves which is characteristic of a non-homogeneous highly crosslinked network **[70].**

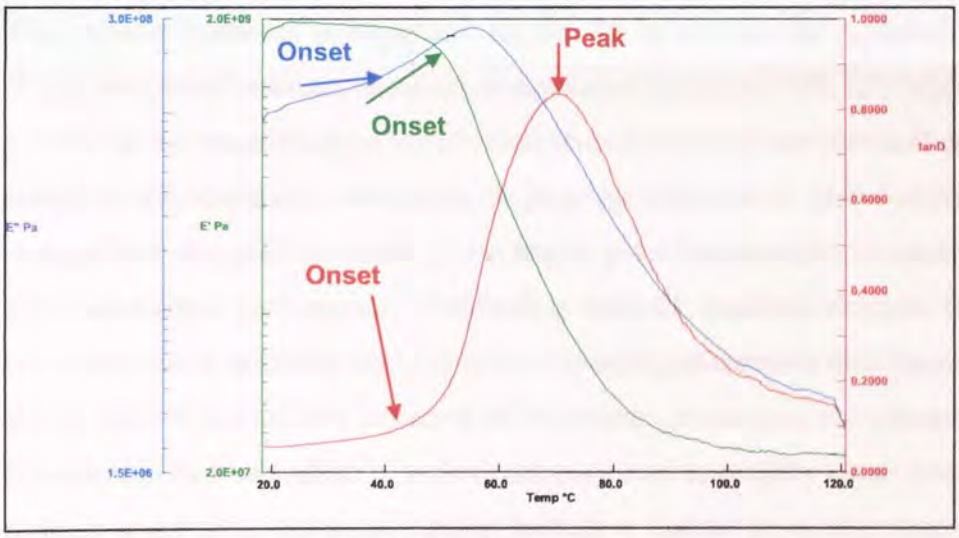

Figure 1.6 Sample DMA chart, showing the determination of Tg

DMA also provides a direct method for determining the crosslink density of crosslinked coatings by measuring the modulus at a temperature well above the Tg, **[7, 68].** Crosslink density (ν_ε)can be calculated using the following equation (1.1);

$$\nu_e = E'/3RT \qquad (1.1)$$

E' = minimum in the storage modulus (E' curve)

R = gas constant

T = temperature at which this minimum in storage modulus was reached **[71].**

A coating with higher E' value at a particular temperature shows higher mechanical strength than a corresponding film with lower E' value. E'' quantifies the energy that is converted to heat during deformation of the material. The coating network consists of completely incorporated chains and free chain ends (ties), resulting from incompletely performed chemical reactions. There is a relationship between the molecular weight between two crosslinking points (M_x) and the tensile storage modulus (E') see equation (1.2);

$$E' = \frac{3nRT}{M_x} \qquad (1.2)$$

Where E' is the storage modulus, n is the density, M_x the molecular weight between two crosslinking points, R is the gas constant and T is the absolute temperature **[17].**

In order to characterize the coating behaviour after differing weathering treatments, the polymer degradation processes can be discussed in terms of E'min values versus Tg. The polymer hardness is dependent on the Tg as well as the crosslink density **[68].** Weathering tests based on chemical composition (such as FTIR, UV-Vis) change rates provide no information about the physical repercussions of the chemical changes. Thus, these tests can make no comment on the physical tolerance of clearcoats to the chemical composition changes they undergo, leading to possible erroneous conclusions regarding their weathering performance. Weathering induced chemical changes that effect the crosslink density are more likely to effect physical performance than those that occur on side groups. There are two extremes of behaviour; at one end, the changes in chemical composition that take place in a clearcoat may lead to roughly equal rates of crosslink formation and crosslink/chain scission, leading to limited physical property changes, on the other hand, a different clearcoat may undergo a slower overall rate of photooxidation, but the specific photooxidation chemistry may give rise to crosslink formation, with dramatic physical property consequences. It has been shown previously that modulus measurements in the rubbery plateau region can yield quantitative values for the crosslink density **[44].** The net effect of weathering on coatings can either be an increase or decrease in crosslink density, depending upon the formulation of the coating and the weathering conditions. For acrylic/melamine coatings (with HALS), it has been said **[44]** that the crosslink density tends to decreases as weathering progresses. In acrylic/urethane coatings, the addition of HALS slows down the rate of crosslink

density decrease. However these results were for only for 500 hours of artificial weathering [44].

1.5.9 MALDI-Tof MS Analysis

MALDI-Tof MS (matrix-assisted laser desorption/ionisation time-of-flight mass spectrometry) experiments have been used to identify the molecular weight distribution of chemical species. In a conventional MALDI experiment, the analyte, the polymer is first dissolved in a solvent (the type of solvent depends upon the analyte), often a material is added that absorbs ultraviolet light (commonly an organic acid **[72]**). After mixing, the sample is placed in a airtight chamber, on the tip of the sample probe, under vacuum, thus the solvent evaporates and the result is a layer of the UV absorbing material with a small amount of the polymer under investigation in it. The polymer has been dispersed in a matrix of the UV absorbing compound.

A laser is then fired at the sample (usually a UV laser in the 330-360 nm range **[73])**, as the sample contains UV absorbing material, all of the energy from the laser is absorbed and some of it is passed to the polymer molecules. The matrix material also reacts with the polymer so the polymers become charged ions, as the polymers have absorbed a great deal of energy, they evaporate. In the chamber that contains the polymer there are two electrodes; a positive cathode and a negative anode, depending upon the type of matrix material the polymers may be cations or anions. The polymer has been vaporized between the two electrodes, the acceleration is used to shoot the polymer molecules down to the detector at the far end of the chamber, as the polymer molecules have different masses, the heavier polymer molecules take a lot longer to reach the detector as force equals mass times acceleration. Thus, the polymer molecules hit the detector in order by mass, as they hit the detector, the detector registers a peak, and the size of the peak is proportional to the number of molecules that hit at one time, thus the result is a molecular weight distribution. The advantage of MALDI is that it gives an absolute measurement of mass (the polymer is not compared to anything) **[72, 73]**.

1.6 Migration of additives through automotive coating systems

The migration of an additive through a polymer results in its loss which will lead to adverse consequences. Migration depends on the rate of diffusion of the additive and its solubility. Diffusion is the movement of an additive through the polymer, driven by a concentration gradient. Solubility is usually defined as the maximum amount of the additive that is soluble in the polymer at a particular temperature. This section gives an overview of the different methods in which diffusion and solubility measurements of additives in polymers have been made. For an additive to be effective it needs to be in the retained in the polymer, so it is desirable that its diffusion rate is minimal and solubility is high **[21, 22, and 74].**

1.6.1 Solubility Measurements

Solubility is the most important factor in the effectiveness of stabilisation. If too much of the additive has precipitated out of the polymer, and thus is not soluble in the polymer then consequently, the effectiveness of the additive will be reduced **[75].** The solubility of the additive is determined by the free energy change associated with the transfer of the additive from its equilibrium state as a pure material into the polymer matrix. Measurements of solubility require true (saturation) equilibrium to be established between the additive and the polymer.

Different methods are available to determine the solubility of additives in polymers. In the first methods, the solubility of the additive is measured in a series of solvents of similar chemical structure to that of the polymer, thus the solute-solvent interaction parameter is evaluated. A different method is the equilibrium method, and consists of dissolving the maximum quantity of solute in the amorphous phase of the polymer; the equipment used is similar to that used in the stack method for diffusion measurements (section 1.6.2). The polymer sample is placed between two sources with high additive concentration, and the assembly is left for several weeks at a given temperature until constant concentration in the sample is obtained and determined **[75].**

Temperature effects can become very important when the amount of additive in a polymer is close to the solubility limit at the temperature of use. At elevated

temperatures the solubility of such an additive is increased. A van't Hoff equation also exists with solubility measurements, thus the heat of solution can be found (equation 1.3).

$$S = S_0 \exp(-\Delta H_S / RT) \tag{1.3}$$

Where,

S_0 = pre-exponential factor

ΔH_S = enthalpy or heat of solution.

The solubility of the additive in the polymer is determined by the fact that the molar free energy of fusion, ΔF_t, of the additive is exactly compensated by the partial molar free energy of mixing, $\overline{\Delta F}_m$, of the molten additive with the polymer. The free energy of fusion is shown in equation (1.4) **[20]**,

$$-\Delta F_t = \Delta H_t (1 - T/T_m) \tag{1.4}$$

Where,

ΔH_t = heat of fusion per mole

T_m = Melting temperature.

From solution theory, the partial molar free energy of mixing is given by equation (1.5) **[20]**,

$$\overline{\Delta F_m} = RT\left[In\phi_1 + (1 - V_1/V_2)\phi_2 + \chi_1\phi_2^{\,2}\right] \tag{1.5}$$

Where,

φ_1 and φ_2 = volume fractions

V_1 and V_2 = molar volumes of the additive and polymer, respectively

χ_1 = polymer-additive interaction parameter.

By equating the sum of (1.4) and (1.5) to zero and setting $\varphi_1 \approx 1$, equation (1.6) is obtained **[20]**;

$$-\ln\phi_1 = \frac{\Delta H_t}{R}\left(\frac{1}{T} - \frac{1}{T_m}\right) + \left(1 - \frac{V_1}{V_2}\right) + \chi_1 \tag{1.6}$$

The polymer-additive interaction parameter (χ_1) is a measure of the specific interaction between the polymer and the additive. The only term in equation (1.6) that depends on the size of the polymer molecule is the term V_1/V_2. A log plot of the solubility against the reciprocal of molar volume of the solvent is expected to be linear.

1.6.2 Diffusion Measurements

Diffusion processes play an important role with respect to processes of evaporation and leaching of stabilisers from polymers. The rate of loss of additives from polymers is controlled by the rate of their diffusion in the polymer **[21].** Diffusion is a macroscopic manifestation of a random walk or Brownian motion of individual migrant molecules within the polymer, which obey Fick's laws of diffusion **[76].** The theory of diffusion is an isotropic medium is based on the hypothesis that the transfer rate of a diffusing compound through a unit area is proportional to the concentration gradient measured at right angles to the layer section (Fick's first law) **[22].** Fick's first law can only be directly applied to steady state diffusion, that is where concentration is not varying with time **[77]** (equation 1.7).

Fick's first law (1.7), for steady-state diffusion is shown in equation1.7; **[22, 76, 77, 78, 79]**

$$F = D\frac{\delta C}{\delta x} \qquad (1.7)$$

Where,

F = transfer rate per unit area of the polymer

C = concentration of a diffusing compound

x = spatial co-ordinate measures at the right angles

D = diffusion coefficient of migrant in the polymer

D can be dependent both on the concentration and on the spatial co-ordinates x, y, z. If the diffusion occurs only in one direction, i.e. a concentration gradient exists only along the x-axis, the rate of concentration change (i.e. non-steady state) at a certain diffusion time will be given by Fick's second law **[22, 80, 81]** (equation 1.8).

$$\frac{\delta C}{\delta t} = D_P \frac{\delta^2 C}{\delta x^2} \qquad (1.8)$$

Where,

C = concentration of a diffusion compound

x = space co-ordinate measured at right angles

t = elapsed time.

To calculate the diffusion coefficient D, Fick's second law is solved by applying the appropriate boundary conditions (BCs) for the type of experiment; there are several different experimental methods for simulating the migration process. In traditional gravimetric techniques, the sample geometry is adjusted so that analytical solutions to the time-dependent diffusion equation can be obtained, and experiments can be completed in a reasonable time. The time required for a small molecule undergoing Fickian diffusion to move a distance, x, is approximately given by x^2/D, where D is the diffusion coefficient. For large organic molecules (such as some additives), small D values are found and a short diffusion path length is desirable, this can usually be achieved with thin polymer films **[20, 82].**

Simultaneous measurements of solubility and diffusion coefficients of a given additive in a polymer can be achieved by analysing the concentration profile that exists when the additive has diffused through a stack of polymer films, with the assumption that the diffusant's path across the stack is small and that these enter exclusively through the plane faces of the film stack. Thus the boundary conditions that are applied to Fick's second law are **[79] (Figure 1.7)**;

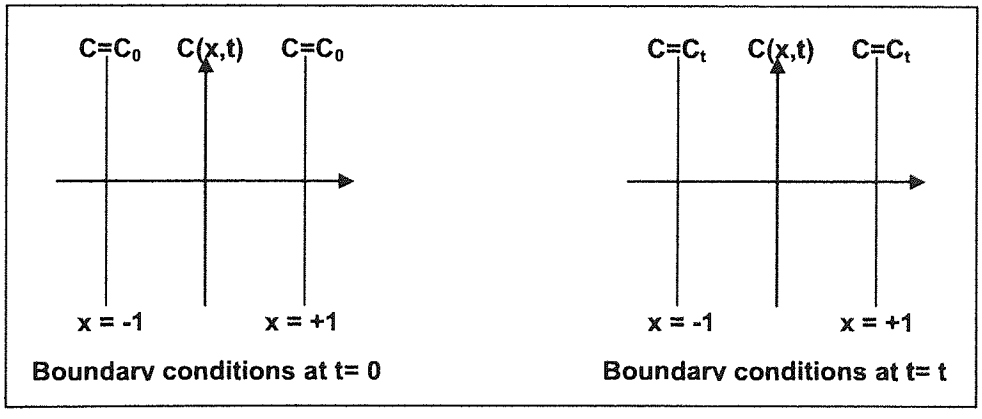

C_0 = surface concentration of the additive, considered to be constant.
C(x,t) = concentration of the diffusant at x distance from the centre of the polymer (of thickness l), at time t.

Figure 1.7 Boundary Conditions for the calculation of the Diffusion Coefficients.

The mathematical solution of Fick's second law is achieved by applying these boundary conditions to form equation 1.9;

$$C = \frac{1}{2} C_0 \left[erf \frac{h-x}{2\sqrt{Dt}} + erf \frac{h+x}{2\sqrt{Dt}} \right] \tag{1.9}$$

Where erf is the mathematical error function as described in equation 1.10;

$$erfx = \frac{2}{\sqrt{\pi}} \int_0^x e^{-t^2} dt \tag{1.10}$$

Where,

t = diffusion time

D = diffusion coefficient at a given temperature

x = space co-ordinate measured at right angles **[22].**

In the diffusion process, there is the polymer bounded by two parallel surfaces additive containing surfaces, which are very large in area compared to the distance between the surfaces. The concentration of additive within the solid interior is initially zero, while the concentration at the surface is maintained essentially at the equilibrium solubility because of the large excess of additive. The solution of Fick's diffusion equation under the boundary conditions (with the diffusion coefficient D independent of concentration) is **[20, 79]** given in (equation 1.11);

$$\boxed{\frac{C_{(x,t)}}{C_0} = 1 - \frac{4}{\pi} C_0 \sum_{n=0}^{\infty} \frac{(-1)^n}{2n+1} \exp\left(\frac{-(2n+1)^2 \pi^2 K}{4l} \right) \cos \frac{(2n+1)\pi x}{2l}} \tag{1.11}$$

Where,

C_0 = the equilibrium solubility of the additive in the polymer

C(x,t) = concentration of the diffusant at x distance from the centre of the solid (of thickness l) at time t.

2l = total thickness of the stack of thin discs

= x is the position co-ordinate with the origin at the centre of the stack

K is given by equation 1.12;

$$K = Dt / l^2 \tag{1.12}$$

A semilog plot of C(x,t) against x/l is calculated for a number of values for K and is shown in Figure 2.22 (chapter 2).

The concentration of additive determined experimentally is plotted on similar scales against x/l, where x is taken to be the co-ordinate of the centre of each film. The first and last thin films are not analysed because of the possibility of physical contamination of their outer surfaces by additive. From the amount of vertical shift, the solubility can then be found, while from the value of K of the best matching curve the value of K can be calculated **[20].**

Alternatively, Fick's second law can be integrated to yield equation 1.13, which gives the mass uptake of the film, M_t;

$$\frac{M_t}{M_0} = 1 - \sum_{n=0}^{\infty} \frac{8}{(2n+1)^2 \pi^2} \exp\left(\frac{-D(2n+1)^2 \pi^2 t}{l^2}\right) \qquad (1.13)$$

Where,

M_t = mass uptake at time, t.

M_0 = mass uptake at equilibrium

t = diffusion time

D = diffusion coefficient at a given temperature

l = film thickness.

At short times the equation reduces to equation 1.14, which enables the measurement of D from mass uptake experiments **[23, 77],** using a gravimetric measurement,

$$\frac{M_t}{M_0} = \frac{4}{l}\left(\frac{D}{\pi}\right)^{1/2} \qquad (1.14)$$

FTIR ATR can be used in diffusion studies; the technique is based upon contact between the infrared transparent crystal (the IRE) and a surrounding medium of lower refractive index. When the IR radiation is totally reflected at the interface between the two a standing evanescent wave is established and the radiation acts as if it penetrates a small distance into the surrounding medium. When a material, which selectively absorbs IR radiation, is in close contact with the reflecting surface the radiation loses energy during each reflection in contact with the sample at the wavelength where the material absorbs. The resultant attenuated radiation is measured and an IR spectrum of the material plotted. The depth of penetration, d_p depends upon the wavelength of the radiation, λ, the refractive index of the more optically dense ATR crystal, η_c, the refractive index of the less optically dense surrounding medium, η_s, and the angle of the beam at the surface of the waveguide, θ, according to equation 1.15, **[83].**

$$d_p = \frac{\lambda}{2\pi\eta_c(\sin^2\theta - (\eta_s/\eta_c)^2)^{1/2}} \tag{1.15}$$

A technique has been developed to analyse the behaviour of a single diffusing additive in the polymer, based upon a combination of Fick's second law and the evanescent field intensity function, one-dimensional Fickian diffusion with a constant surface concentration **[83]**. Thus, the calculations again begin with an integrated version of Fick's second law for a mass uptake experiment (1.13) **[84]**.

For most experiments, only the first term (of equation 1.13) is of interest, thus the equation simplifies to equation (1.16):

$$\frac{M_t}{M_0} = 1 - \sum_{n=0}^{\infty} \frac{8}{\pi^2} \exp\left(\frac{-D\pi^2 t}{4l^2}\right) \tag{1.16}$$

Where,

M_t = mass uptake at time, t.

M_0 = mass uptake at equilibrium

t = diffusion time

D = diffusion coefficient at a given temperature

l = film thickness.

This is solved for time t as (equation 1.17);

$$In\left(1 - \frac{M_t}{M_0}\right) = In\left(\frac{8}{\pi^2}\right) - \frac{D\pi^2 t}{4l^2} \tag{1.17}$$

This equation can be converted into absorbance values to give **[84]** (1.18);

$$\frac{A_t}{A_0} = 1 - \frac{8\gamma}{\pi[1-\exp(-2\gamma l)]} \sum_{n=0}^{\infty} \left[\frac{\exp(g)[f\exp(-2\gamma l) + (-1)^n(2\gamma)}{(2n+1)(4\gamma^2 + f^2)}\right] \tag{1.18}$$

Where g and f are (1.19, 1.20);

$$g = \frac{-D(2n+1)^2\pi^2 t}{4l^2} \qquad f = \frac{(2n+1)\pi}{2l} \tag{1.19, 1.20}$$

A_t = mass uptake at time, t.

A_0 = mass uptake at equilibrium

γ $= 1/d_p$ (explanation of d_p see 1.15)

The equation can be reduced to the first term only (equation 1.21);

$$\frac{A_t}{A_\infty} = 1 - \frac{8\gamma}{\pi[1-\exp(-2\gamma l)]}\left[\frac{\exp\left[\frac{-D\pi^2 t}{4l^2}\right]\left(\frac{\pi}{2l}\exp(-2\gamma l)+(2\gamma)\right)}{4\gamma^2+\frac{\pi^2}{4l^2}}\right] \quad (1.21)$$

If L is large enough (equation 1.22);

$$4\gamma^2 >>> \frac{\pi^2}{4L^2} \quad (1.22)$$

$$1 >>> \exp(-2\gamma l)$$

Which is further simplified to (equation 1.23);

$$\ln\left(1-\frac{A_t}{A_\infty}\right) = In\left(\frac{4}{\pi}\right) - \frac{D\pi^2 t}{4l^2} \quad (1.23)$$

Thus **absorbance** is plotted versus **time** to give a curve, $\ln(1-A_t/A_\infty)$ versus time to give a straight line – which allows the calculation of **D** if the thickness l is known. Alternately, D is found by **direct fitting** of the experimental to the theoretical curve **[23, 83, and 84].**

FTIR-ATR spectroscopy has been shown to be highly effective and sensitive in the study of diffusion. Some the distinct advantages include:

1. The *in-situ* nature of the measurement of concentrations with time,
2. The shorter experimental times over more conventional gravimetric techniques,
3. The small penetration depths (~ 0.1-2 μm) that permit a more surface-sensitive analysis (this depends on the IRE).

However, the testing configuration has proven to be extremely sensitive to film quality, any defects in the film will result in inaccurate diffusion coefficients **[84].**

Several factors influence the diffusion of additives in polymers; they include the influence of the polymer and the physical state of the polymer. The 'hole' theory of diffusion has been put forward, there is a number of pre-existing holes in the polymer, that allow diffusion of small molecules. However, the diffusion decreases when the polymer contains polar groups, the decreases in flexibility is in agreement with the

increase in Tg, this is due to the fact that polymer with Tg lower than room temperature have a lower permeability for organic vapours compared with those with Tg higher than room temperature **[80].** Unsaturation in the backbone of polymers also contributes to the increase in the coefficient of diffusion, due to internal mobility or flexibility. The diffusion of larger molecules through polymers is more affected by the physical state of the polymer. Another factor which affects diffusion is the presence of cross-links in the polymer, diffusion tends to be slower in more cross-linked polymer **[85].**

Diffusion experiments are usually performed over a range of temperatures, and the data presented in Arrhenius co-ordinates. Over a small range of temperatures used, diffusion follows the Arrhenius law (equation 1.24);

$$D = D_0 \exp(-\frac{E_D}{RT}) \qquad (1.24)$$

Where;

E_D = activation energy

D_0 = pre-exponential factor

The diffusion coefficient is related to the temperature and an Arrenhius-type equation is valid for these systems, the diffusion coefficient is also dependent on the Tg, but a discontinuity can be observed at this transition temperature, the diffusion coefficient is also dependent on the polymer morphology (i.e crystallinity, orientation), the diffusion processes are dependent on the melting temperature of the additive penetrant and a discontinuity can be observed at this transition temperature, lastly the diffusion coefficient is dependent on the molecular mass of the stabiliser **[22].**

The Arrhenius equation can be simplified to equation 1.25

$$LogD = LogD_0 - E_d / 2.303RT \qquad (1.25)$$

Thus log D is plotted versus 1/T. This is useful as diffusion rates of additives in polymers at room temperature are too low to measure in a reasonable amount of time **[82].** However, the plots are not linear, there is a deviation from linearity as the temperature increases. A discontinuity of the Arrhenius plot may occur above the melting point of the stabiliser. The diffusant behaves as a rigid sphere below the

melting point of the additive and is less flexible. The activation energy depends upon the polymer and is proportional to the molar volume of the diffusant. The pre-exponential factor is usually predicted to depend upon the square of the molecular diameter of the additive. Over the break in the two regions the difference of a few degrees in test temperature may show greatly different diffusion rates of additives. Apart from temperature effects, physio-chemical and structural characteristics of the polymer substrate, e.g. Tg, morphology, crystallinity, orientation **[79]**.

1.7 Research Aims and Objectives

This research work forms one part of a large European project with a consortium of eight partners including two different European car producers, automotive paint manufacturers and additive suppliers and manufacturers, an accelerated weathering device manufacturer, an automotive paint application specialist and a national testing institute. The overall aim of the project was to develop a mechanism-based methodology for accelerated weathering and analytical tests that will enable a rapid and reliable prediction of quality, durability and long-term performance of automotive coatings. This is important as the development of robust and fast methodology would inevitably reduce markedly the time-to-market and speed up the development for new and more novel environmentally friendly automotive paint systems, for example water-based systems. For the project a total of ten different automotive formulations were produced comprising four 2K solvent-borne coatings and six 1K water-borne coatings, a combination of blue and silver systems that were used by other partners.

The objectives of this part of the project were;

1. To evaluate conventional techniques used in the analysis of newly prepared environmentally friendly water-borne (WB) automotive coatings as well as the traditional solvent-borne (SB) systems, as prepared with comparable formulations. This investigation was carried out on microtomed layers as well as on complete automotive multi-layer paint systems.

2. To develop methods and to establish procedures for analysing the early stages of chemical and property changes in both the water-borne and solvent-borne

automotive coating systems that take place upon outdoor natural weathering exposures and under accelerated artificial exposures using different ageing regimes.

3. To analyse concentration profiles of the UV-stabilisers (UVA and HALS) in the coating systems as a consequence of migration in the coating systems analysed in separate microtomed layers of the paint samples (depth profiling) and to determine both diffusion coefficients and solubility parameters of the UV stabilisers.

4. To compare and correlate the various methods of analysis used to determine the various physical and chemical changes that take place during weathering of the different (water-borne and solvent-borne) systems (photoxidation).

5. To compare the performance of various newly developed water-borne paint formulations with that of the corresponding conventional solvent-borne paint formulations prepared under similar conditions.

CHAPTER 2:

EXPERIMENTAL AND ANALYTICAL TECHNIQUES

CHAPTER 2: EXPERIMENTAL AND ANALYTICAL TECHNIQUES

2.1 Materials, details of automotive panels

The automotive panels used consisted of full multilayer coating systems. **Table 2.1** illustrates the composition of the different coating systems used in this work. The panels were based on solvent-borne (SB) and water-borne (WB), systems and were prepared for the experiments conducted throughout the project by PPG Industries (Germany, one of the project partners).

Layer Composition of various automotive coatings							
System Code Number	**EC on aluminium substrate**	**Primer (WB-P)**	**Base 1**	**Base 2**	**Clearcoat (CC) Type**	**CC- UVA (level)**	**CC- HALS (level)**
3	Yes	WB-Anthracite	No	Blue	SB	Cyasorb 1164 (level 1)	Sanduvor 3055 (level 1)
4	Yes	WB-Anthracite	No	Blue	SB	KB 353 (level 1)	Sanduvor 3055 (level 1)
6c	Yes	No	Anthracite	Blue	WB	Cyasorb 1164 (level 1)	Sanduvor 3055 (level 1)
7	Yes	No	Anthracite	Blue	WB	Cyasorb 1164 (level 3)	Sanduvor 3055 (level 1)
8	Yes	No	Anthracite	Blue	WB	No	Sanduvor 3055 (level 1)
9	Yes	No	Anthracite	Blue	WB	KB 353 (level 1)	Sanduvor 3055 (level 1)
10	Yes	No	Light Grey	Silver	WB	Cyasorb 1164 (level 1)	Sanduvor 3055 (level 1)

Table 2.1 Description of the coatings systems used in the experimental work, for structures of stabilisers see table 2.2.

2.2 Automotive Panels Composition

Figure 2.1 illustrates the major differences between the coating systems. All the systems were composed of an aluminium substrate, over which an electrocoat (EC) was applied (approximately 10-22μm thickness). The electrocoat is responsible for corrosion protection, chip resistance and covers steel roughness. The electrocoat was based on **epoxy-acrylate** resins and did not contain any ultra-violet (UV) stabilisers.

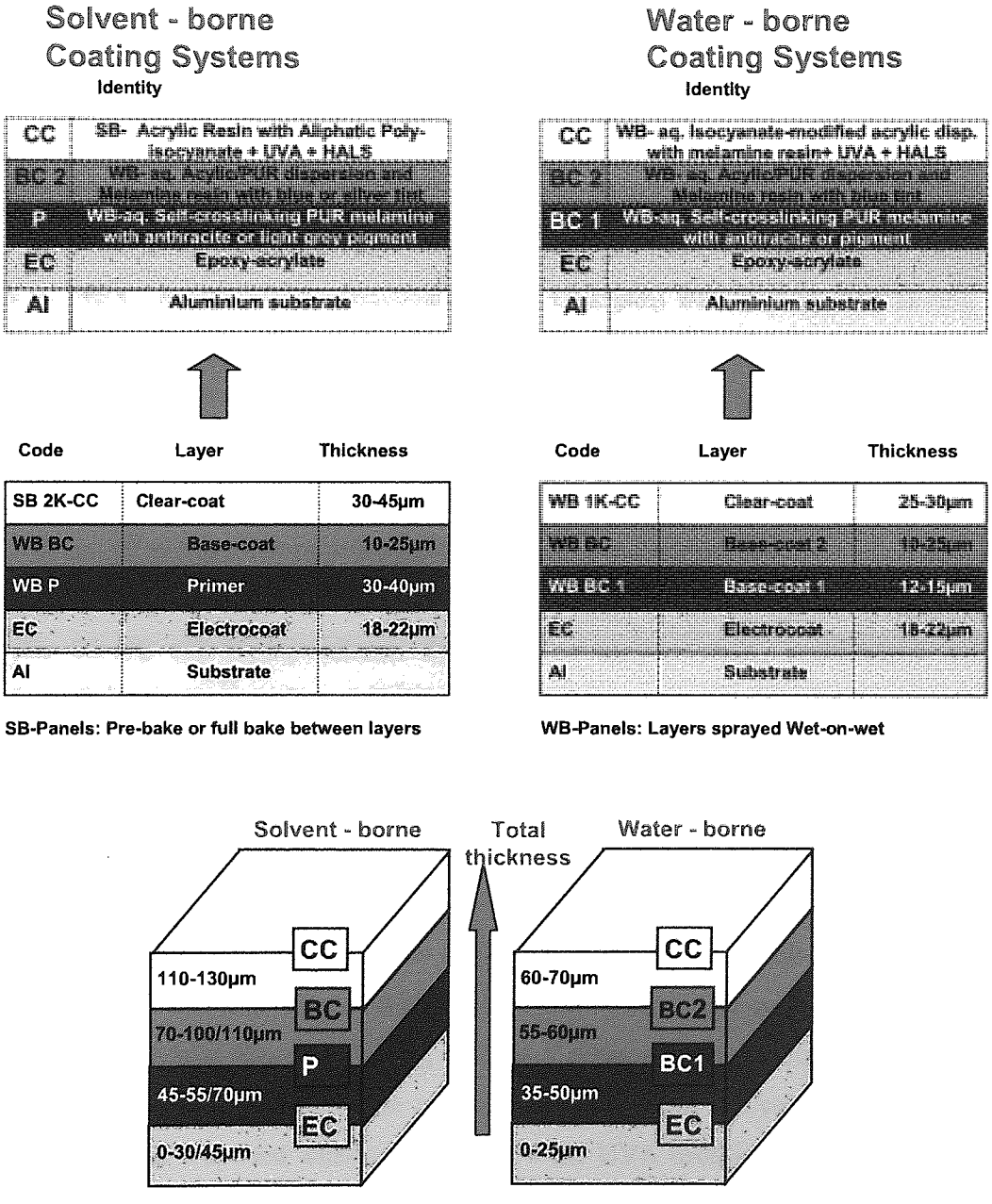

Figure 2.1 Schematic representations of the coatings systems used in the experimental work, showing the differences between solvent-borne and water-borne clearcoats, and the nominal thicknesses of the different layers in the systems

Systems 3 and 4 were the reference solvent-borne multilayer paint systems. Their preparation and composition is described below. Firstly, after applying the electrocoat, an anthracite water-borne surfacer primer (P) (covers roughness in the metal substrate and contributes to mechanical performance) was applied by spraying. The chemical composition of the primer was based on self-crosslinking and melamine cross-linking polyurethane resins (PUR) with anthracite pigment, **Scheme 2.1**. The primer was cured fully by a five minute flash-off at room temperature to allow any volatile solvents to evaporate, followed by pre-baking for 10 minutes at 70^0C, and finally baking for twenty minutes at 140^0C. A water-borne basecoat (BC-2, 12-15μm) was then applied having a chemical composition based on a **WB aqueous acrylic/PU – dispersion and melamine resin** with blue pigment or silver tint, see **Scheme 2.2**. Therefore this layer is responsible for the colour of the coating panel and partly for the mechanical performance and the humidity resistance of the total coating system. This BC-2 layer was only partially cured by 5 minute flash-off at room temperature followed by a 10 minute prebake at 80^0C. The last layer in the coating system was based on a 2K solvent-borne (SB) (two-pack) clearcoat (CC). The SB-CC (30-50μm, **Scheme 2.3**) was an **acrylic resin, crosslinked with aliphatic polyisocyanate** and containing UV stabilizers, responsible for appearance, performance and durability of the coating system. The CC was baked fully; five minutes flash-off at room temperature, followed by a full-bake at 140^0C for 20 minutes. The only difference between systems 3 and 4 was in the ultra-violet (UV) stabilisation package. Both systems contained a standard level 1 of a hindered amine light stabiliser (HALS), Sanduvor 3055, with concentration calculated to be around 0.8 w/w%, (see **Table 2.2** for further details of structures and properties of the HALS). Both systems also contained a standard level 1 of an ultra-violet absorber (UVA), used at a concentration of around 1.4 w/w%. However the UVA was different in the two systems; in system 3 Cyasorb 1164 (a non cross-linkable UVA) was used whereas in system 4 the UVA used had a structure that is overall similar to that of Cyasorb 1164 except for a slight modification to make it capable of crosslinking, KB3531, see Table 2.2 for structures.

Systems 6c, 7, 8 and 9 were WB coating formulations. They did not contain a water-borne primer above the EC layer, but instead had a water-borne basecoat (BC 1). Again this layer

covers any substrate roughness and contributes to the mechanical performance and needs to be compatible with the water-borne layers above. This BC 1 layer (10-15μm) had a chemical composition based on **WB aqueous self-crosslinking PU-melamine dispersion** with anthracite or grey pigment, see **Scheme 2.4**. After the layer was applied, the coating was only partially baked by a 3 minute flash-off at room temperature before the next layer was applied above. This is known as **wet-on-wet application** (whereas for the SB systems 3 and 4 the coating was cured fully between the application of the different layers and this is known as **wet-on-dry** application). A second water-borne basecoat layer (BC 2, a thickness of 12-15μm) was applied which is responsible for the overall colour of the coating panel and partly for the mechanical performance and humidity resistance of the total system. The BC 2 composition was similarly based on a **water-borne acrylic/PU melamine resin** containing blue tint for all water-borne systems except system 10 which contained a silver pigment (BC 2 had a similar chemical composition to BC 1, see **Scheme 2.4**). Once again this was not cured fully after application but was partially cured by a 5 minute flash-off at room temperature, followed by a 10 minute prebake at 80^0C. The last layer in the water-borne system was the clearcoat, which was based on a one-pack (IK) water-borne clearcoat (WB-CC), consisting of a water-borne aqueous isocyanate-modified acrylic dispersion with melamine resin (scheme 2.5) containing both UVA and HALS. All of the clearcoats contained HALS (Sanduvor 3055) at 0.8 w/w %,, along with different concentrations of the UVA (Cyasorb 1164), see table 2.2, 6c and 10 both contained level 1 (1.4 w/w%) of Cyasorb 1164, system 7 contained a higher level 3 (3.8 w.w%) of Cyasorb 1164 and system 9 contained a level 1 (1.4 w/w%) of the cross-linkable UVA, KB 3531.

Stabiliser Code and Supplier	Structure	IUPAC Name	Physical Properties and State
Sanduvor 3055 (Clariant) **(HALS)**	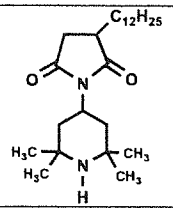	Dodecyl-1-(2,2,6,6-tetramethyl-4-piperidyl)pyrrolidine-2,5-dione, (CAS no. 79720-19-7).	• Yellow viscous liquid • MW = 407 • Mpt = -15^{0}C • Bpt = 212^{0}C • Purity = 91%
Cyasorb 1164 (Cytec) **(UVA)**	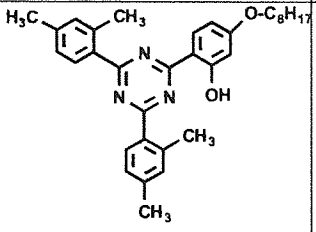	2-[4,6-Bis(2,4-dimethylphenyl)-1,3,5-triazin-2-yl]-5-(octoxy)phenol, (CAS no. 2725-22-6).	• Yellow powder • MW = 510 • Mpt = 88–91^{0}C • Purity = 96%(min)
KB 3531 (Clariant) **(X-UVA)**	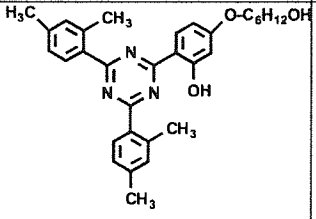	2-[4,6-Bis(2,4-dimethylphenyl)-1,3,5-triazin-2-yl]-5-(hexanoloxy)phenol.	• Yellow powder • MW = 498 • Mpt = 114–118^{0}C • Purity = +99%

Table 2.2 Structure and Properties of the stabilisers used in the different automotive clearcoats.

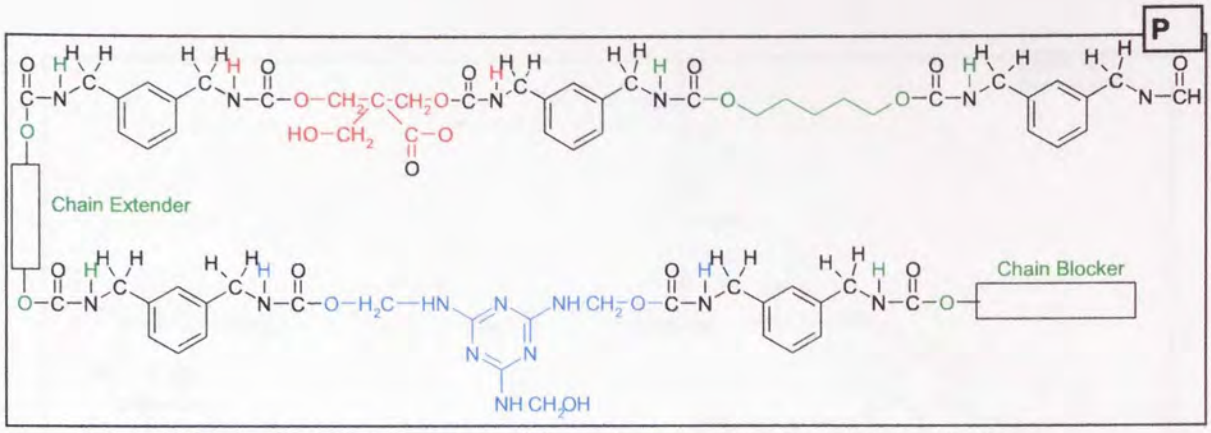

Scheme 2.1 A typical structure of the **primer** used in the reference (solvent-borne) systems

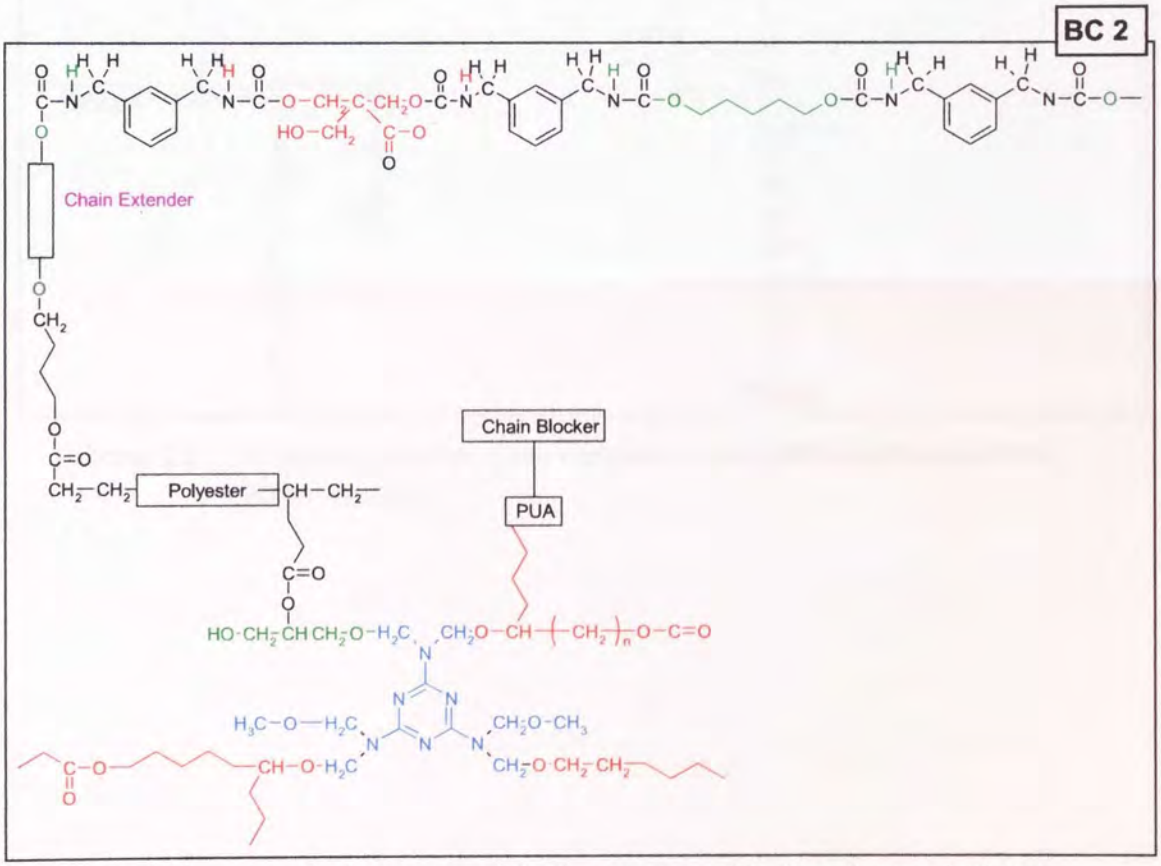

Scheme 2.2 A typical structure of the **basecoat** used in the reference (solvent-borne) systems

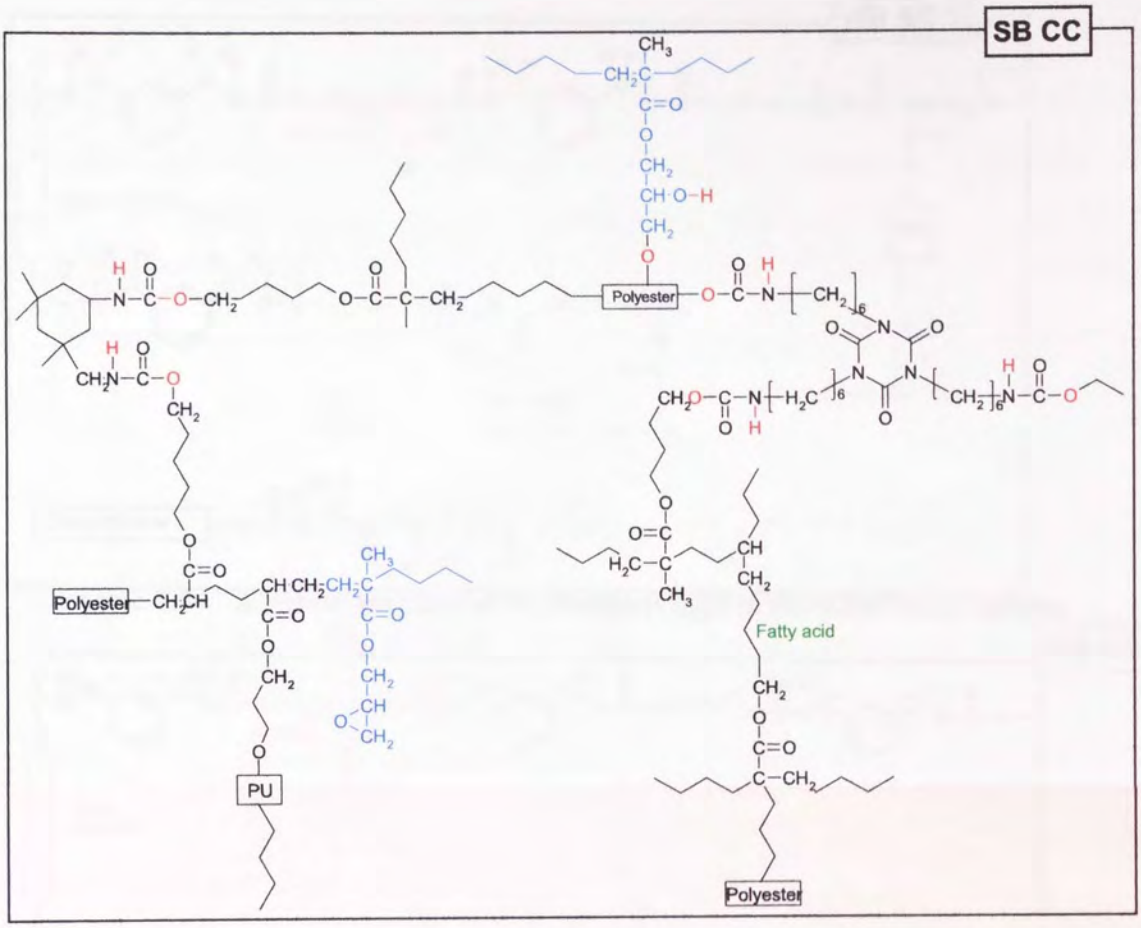

Scheme 2.3 A typical structure of the **clearcoat** used in the reference (solvent-borne) systems

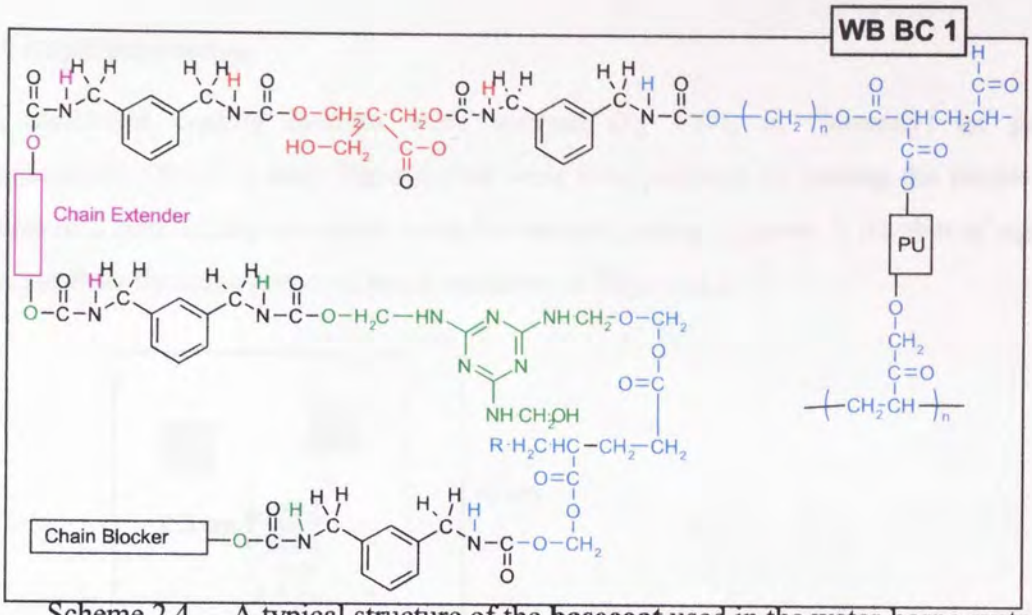

Scheme 2.4 A typical structure of the **basecoat** used in the water-borne systems

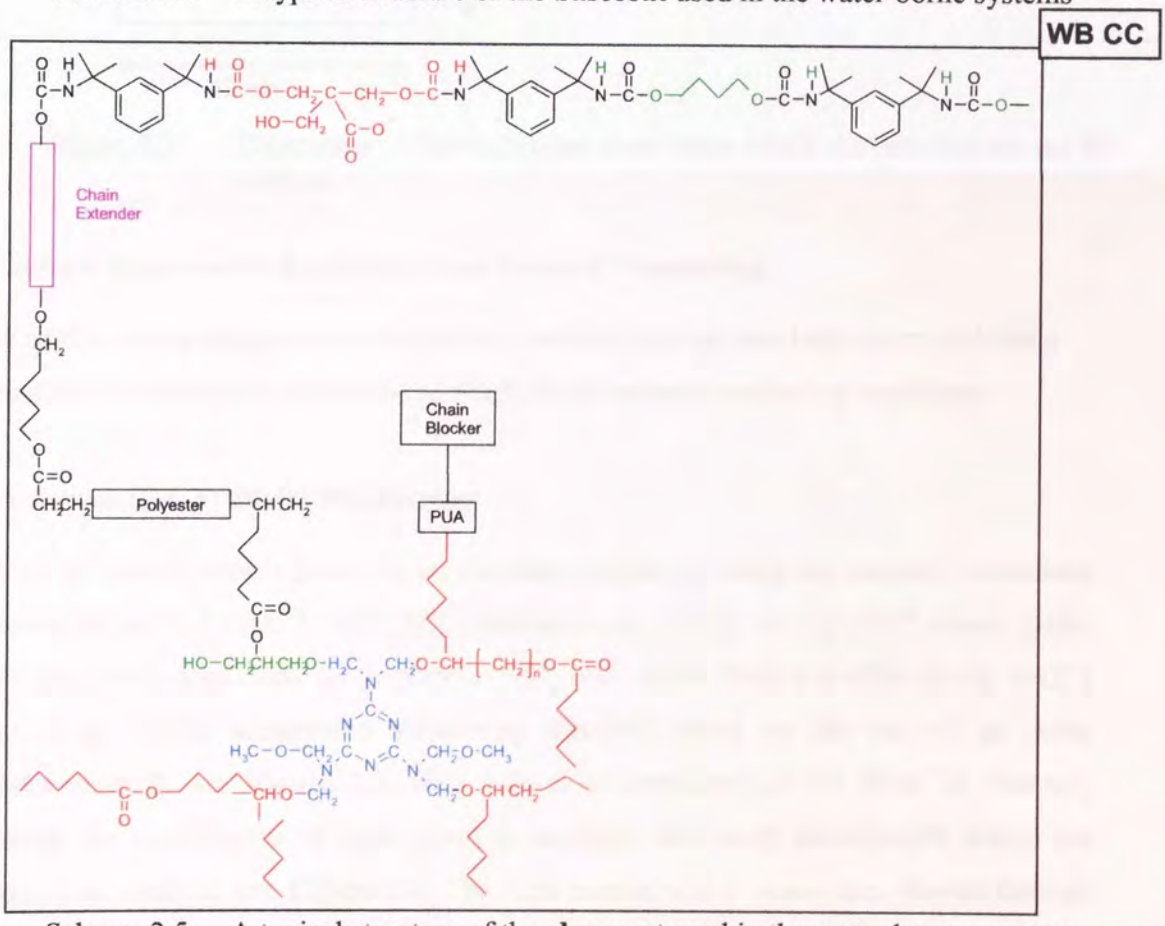

Scheme 2.5 A typical structure of the **clearcoat** used in the water-borne systems

2.3 Sample production

The multilayer coating systems were sprayed (by PPG, in Germany) on panels approximately $10cm^2$ in size. The samples were then prepared by cutting the panels into squares of $2.5cm^2$ taking care not to twist the samples, using a jigsaw. A number of squares were cut from the same prepared panel as shown in **Figure 2.2**.

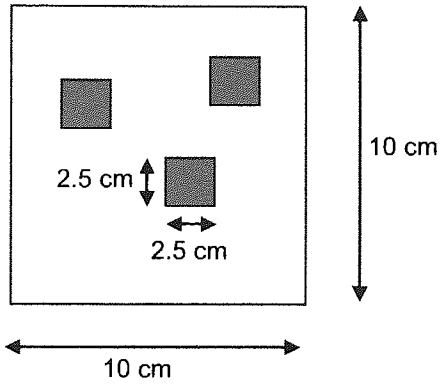

Figure 2.2 Illustration of the multilayer panel from which the sections are cut for analysis.

2.4 Sample Exposure to Accelerated and Natural Weathering

Each of the coating samples was divided into two sets, one set was kept unexposed and a second set was subjected to accelerated artificial and natural weathering conditions.

2.4.1 Accelerated Artificial Weathering

One set of panels were exposed to accelerated weathering using the standard conditions described in ASTM SAE J 1960 **[50]** (referred to as 'CAM' or 'SPART' where acidic water was used) conditions for periods of 333, 666, 1000, 2000 and 4000 hours. SAE J 1960 is an ASTM accelerated weathering standard based on the use of an Atlas Weatherometer®, see **Figure 2.3**, with a level of irradiance of 0.5 W/m^2 at 340 nm, covering the wavelengths of light found in sunlight, and some wavelengths which are shorter than sunlight, see **Figure 2.4**. The light source was a xenon arc, filtered through borosilicate inner and outer filters with test cycles described in **Table 2.3.**

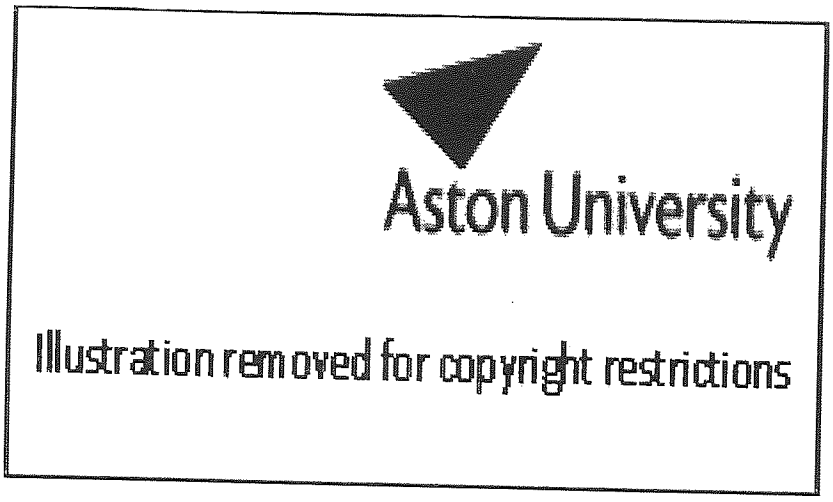

Figure 2.3 Photograph of automotive panels exposed to artificial accelerated weathering.

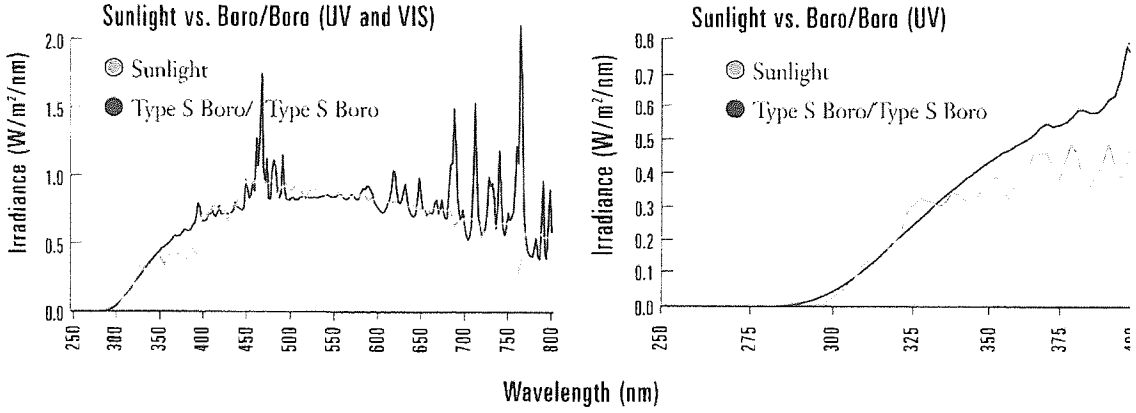

Figure 2.4 Spectral Power Distribution of High Borate / Borosilicate Type S Filters Compared to Sunlight.

CAM Conditions	**SPART** Conditions
Irradiance level of 0.5 W/m^2 at 340 nm Light source xenon arc, filtered through borosilicate inner and outer filters Test cycle • 40 minutes light • 20 minutes light with a front water spray • 60 minutes light • 60 minutes dark with a back water spray Black standard temperature and relative humidity • 70^{0}C and 75% for light periods • 38^{0}C and 95% for dark periods.	Irradiance level of 0.5 W/m^2 at 340 nm Light source xenon arc, filtered through borosilicate inner and outer filters Test cycle • 40 minutes light • 20 minutes light with a front water spray • 60 minutes light • 60 minutes dark with a back water spray **The water in every 14th 20 minute cycle was replaced with acidic water with a pH of 3.2)** Black standard temperature and relative humidity • 70^{0}C and 75% for light periods • 38^{0}C and 95% for dark periods.

Table 2.3 Details of CAM and SPART accelerated weathering regimes.

2.4.2 Natural Weathering

A third set of each of the coating systems was also exposed (by Atlas, a project partner) to natural weathering, see **Figure 2.5**. Two sites were chosen; **Miami** in Florida was chosen as it is a harsh, sub-tropical environment and **Jacksonville** in Florida was chosen as the area has high levels of acid rain and other environmental pollutants. The local Miami environment provides increased weathering variables above most end-use environments; higher solar radiant exposure, increased temperature and greater moisture **[47].** The samples were placed at an angle of 5^{0}C, according to the standards (ASTM 67), the angle of 5^0 exposes the sample to the maximum possible sky-dome. In subtropical Miami, approximately 50% of the UV radiation is the diffuse component of solar radiation (not from the direct beam of the sun). As the surface exposure angle of the sample was increased, the sample received less of this diffuse component (this effects radiant exposure levels most at greatest solar elevations. An angle of 5^0 can maximize critical weathering variables near the summer solstice in the Miami area. The angle also allows the run-off at

rain-fall and condensation liquid and allows residue that has accumulated on the surface of the specimen to be washed off. The samples were exposed at a latitude of 25^0 52' north and a longitude of 80^0 52' west, at an elevation of 3 metres, the average temperature was around 23^0C, the average relative humidity 78%, total rainfall of 1685mm and a total radiant exposure of 5588 MJ/m^2 **[47]**, the conditions are summarized in table 2.4. In Jacksonville, samples were exposed at a latitude of 30^0 29' north and a longitude of 81^0 42' west, at an elevation of 8 metres, the average temperature was around 20^0C, the average relative humidity 76%, total rainfall of 1303mm and a total radiant exposure of 5800 MJ/m^2 **[47]**. The samples were exposed for periods of 6, 12 and 18 months, according to the standards, from February 2001 to March 2003.

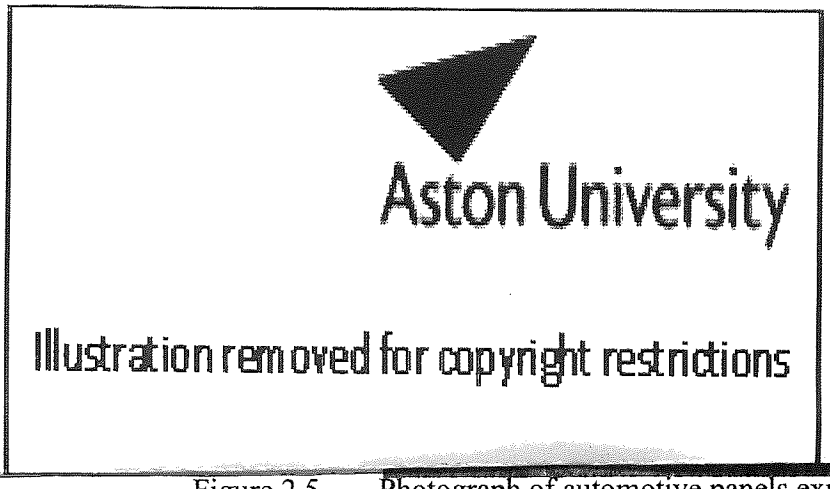

Figure 2.5 Photograph of automotive panels exposed to natural artificial weathering.

Condition	Miami Exposure	Jacksonville Exposure
Latitude:	25° 52' North	30° 29' North
Longitude:	80° 52' West	81° 42' West
Elevation:	3 metres	8 metres
Average Temp:	23 °C	20 °C
Avg. Relative Humidity:	78 %	76 %
Total Rain:	1685 mm	1303 mm
Total Radiant Exposure:	5,588 MJ/m^2	5,800 MJ/m^2
Specimen angle	5^0	5^0

Table 2.4 Details of outdoor Miami and Jacksonville exposures.

2.5 Microtoming

Depth profiling analysis was carried out on different layers of the coating systems before and after exposure to weathering, the coating systems were sliced up (microtomed) into very thin slices of 5μm thickness (**Figure 2.6**).

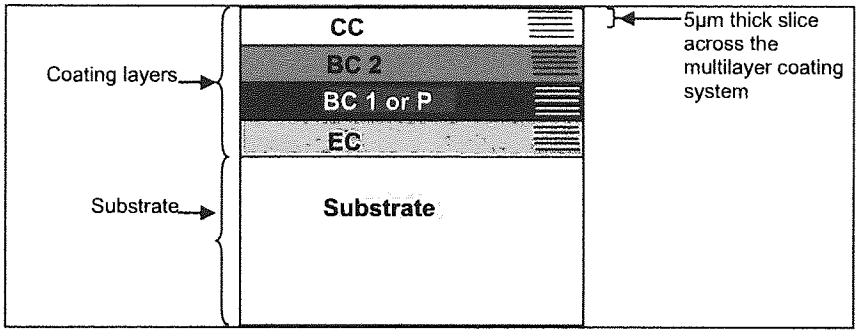

Figure 2.6 Details of microtoming 5μm slices of the coating system.

Two different microtomes were used in this work, a rotary microtome (in the PPP unit), where the sample was clamped vertically and the knife blade moved up and down, and a planar microtome (at one of the project partners in Sweden), where the sample was clamped horizontally and the knife blade moved backwards and forwards. The rotary microtome was a Leica RM 2165 fitted with a stereo microscope. The sample having sides of 2.5cm square was mounted onto a very flat (machined) square of Perspex whose sides were slightly larger than that of the coating system using a minimum amount of cyano-acrylic glue. The sample was then clamped vertically in the microtome with the front face of the sample facing forwards. The sample was adjusted so that the front of the sample was as flat as possible using the orientating head, with the aid of the stereo-microscope. The blade was mounted at 5^0 to avoid jarring the sample when cutting. The motor was then set to begin cutting continuously and consecutive slices of the coating system were cut, and were gently transferred to glass microscope slides for storage using tweezers, gently unrolling with a wooden orange stick if they began to curl, see **Figure. 2.7.**

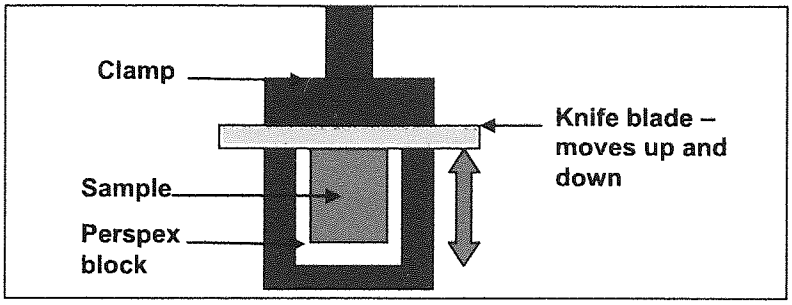

Figure 2.7 Rotary microtome

Conversely on a planar microtome (also by Leica), the sample (which can be slightly larger, 4cm x 6cm) was mounted onto a very flat piece of Perspex using very flat, strong double-sided tape. The block was then clamped in the bottom of the microtome, the blade angle was set at 5^0, and cutting resumed – no orientating of the sample occurred to ensure that the surface of the sample was as flat as possible, the sample was aligned without the aid of the stereomicroscope. Cutting then began and slices of the coating collected, see **Figure 2.8 [86].**

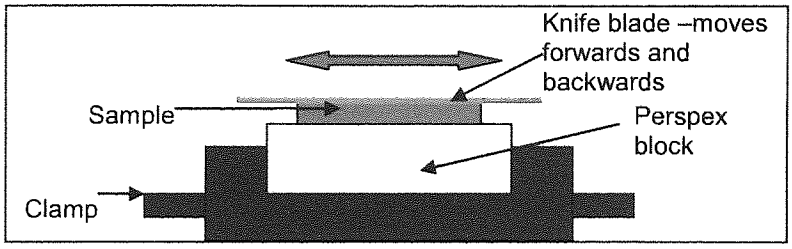

Aston University

Illustration removed for copyright restrictions

Figure 2.8 Planar microtoming **[86].**

The main differences between the types of microtome used in this work are summarized in **Table 2.5.**

Rotary Microtome	Planar Microtome
Smaller samples (2.5 x 2.5 cm)	Larger samples (4 x 6 cm)
Can cut thinner slices (down to 0.5μm)	Cuts thicker slices (down to 5μm)
Orientated head with stereomicroscope	No orientated head or stereomicroscope
Sample mounted on Perspex with glue.	Sample mounted on Perspex with strong double-sided tape.

Table 2.5 Comparison of the rotary and planar microtomes used in this work.

2.6 Analysis of Automotive Coatings

The systems were analyzed before and after weathering exposure, methods involving both the full systems and the microtomed slices, an overview of the methods used is shown in Figure 2.9. Methods include optical microscopy, gloss, hardness, FTIR analysis, UV-Vis analysis and thermal analysis (DMA) of both the microtomed slices and the full systems.

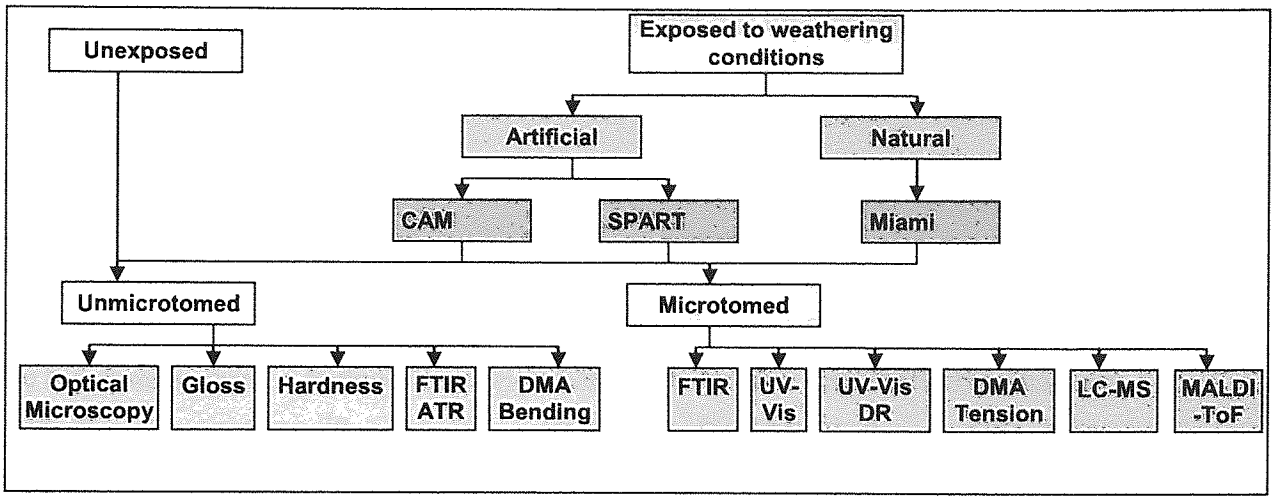

Figure 2.9 Flow diagram of analytical methods used to investigate weathering induced changes in automotive coatings.

2.6.1 Optical Microscopy

Optical micrographs were taken for the full multilayer coating systems in reflectance mode for different CAM and SPART exposures. Different magnifications (500, 100 and 25 times) were used, and the resulting micrographs examined for defects on the surfaces on the coating.

2.6.2 Gloss Measurements

Measurements of gloss were carried out using a Sheen glossmeter at 45^0 to determine if any changes had occurred during exposure to different types of weathering conditions, several representative measurements were carried out, so the average and standard deviation could be determined.

2.6.3 Hardness

Hardness of the full systems was measured using a Fischerscope with a Vickers diamond tipped indenter, to monitor any changes in hardness with weathering. The hardness was measured by two methods; by placing the required force to achieve indentations of 0.5, 1, 1.5μm and measuring the hardness of the coating, or by placing a load of $100mN/m^2$ on the

coating and measuring the hardness (hardness measurements were conducted by one of the project partners in Germany).

2.6.4 FTIR Analysis

FTIR analysis was carried out on both full systems and on microtomed slices on both unexposed and weathered samples. Attenuated total reflectance (ATR) was carried out on the full systems using a Perkin-Elmer Spectrum 1, fitted with a single reflection diamond-ATR Top-plate system with a sapphire anvil (Golden Gate Mk II, Specac, UK), **Figure 2.10**. Samples were applied at maximum pressure for higher sensitivity and reproducibility of recorded spectra (32 scans were used). Transmission FTIR was carrried out on the microtomed samples; the slices were clamped between sodium-chloride plates to keep them flat. The spectra were again produced using a Perkin-Elmer Spectrum 1, using 32 scans also for both background and the sample.

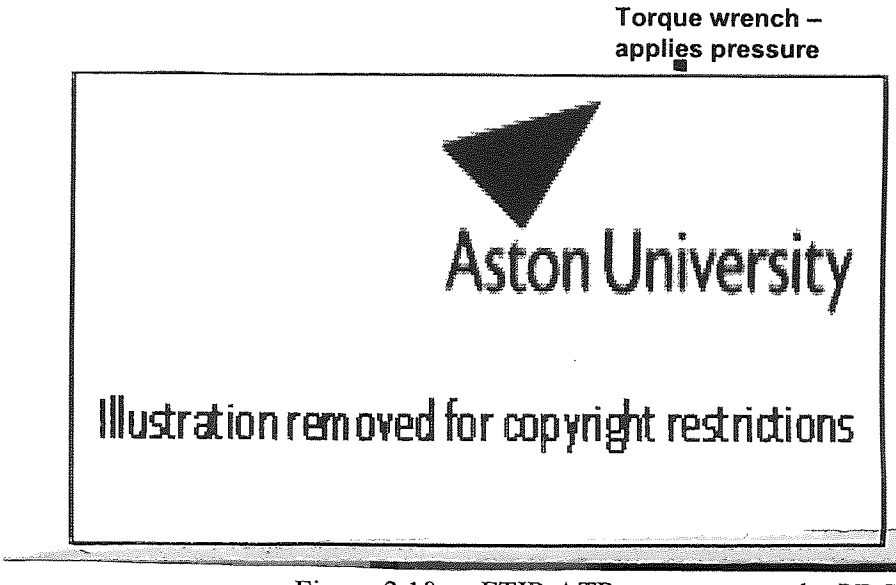

Figure 2.10 FTIR ATR accessory on the PE Spectrum one.

To determine the extent of photoxidation during accelerated ageing, a photoxidation index (PI) was defined. This is described as the normalised spectral data (for the OH/NH/COOH region, 3600-2200 cm^{-1}) with respect to an oxidation-insensitive region or a reference band

(taken as the absorption region of the C-H bond, 3115–2720 cm^{-1}) of the infrared spectrum of the clearcoat layer to maintain true comparisons between weathered and non-weathered paint samples (thus the PI was defined as equation 2.1 (**Figure 2.11**);

$$\mathbf{PI = Absorption\ area_{[OH/NH/COOH,\ 3600\text{-}2200cm^{-1}]} / Absorption\ area_{[CH,\ 3115\text{-}2720cm^{-1}]}} \quad (2.1)$$

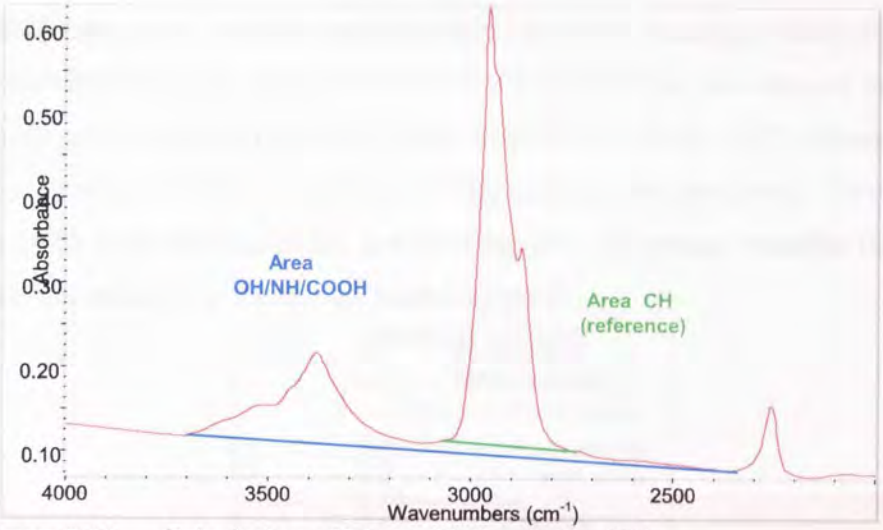

Figure 2.11 Calculation of Photoxidation Index (PI)

In order to compare different systems, the PIs were compared using a delta change PI (ΔPI, equation 2.2). The value for the unexposed sample was averaged for that type of clearcoat, taken across the depth of the clearcoat.

$$\mathbf{\Delta PI = PI_{(exposed)} - PI_{(unexposed)}} \quad (2.2)$$

Also in order to compare the systems and types of exposure, the experimental results were fitted to an exponential curve using a curve fit. The results were plotted against depth for the different exposures, and against time for the clearcoat (at 17.5μm intervals), to examine the changes with exposure.

2.6.5 Thermal Analysis

Thermal analysis was carried out on the full systems (unmicrotomed) and on the microtomed slices, both before and after artificial and natural weathering, using dynamical mechanical analysis (DMA), on a Perkin Elmer Pyris Diamond DMA. Tension analysis

was carried out on the microtomed samples. The slices had to be trimmed using a scalpel to a width of 10mm so that they could fit the clamp (taking care not to cause any nicks in the edges, as these are weak points, causing fractures to begin and the sample to fail prematurely). The length of the samples had to be at least 3cm to ensure that it was held firmly at both the top and bottom of the clamp, any excess could be trimmed after loading. The slice was loaded on the machine (**Figure 2.12**), clamping first by the top screws, then the bottom to ensure that the slice was not twisted or was at an angle, which would distort the force distribution on the slice and influence the results. The slice was run in sinusoidal tension mode, with a heating rate of 20^0C/min from 20^0C to up to 140^0C (depending on the layer), at a strain of 0.5%, a frequency of 1Hz, under a nitrogen purge. Throughout the cycle, the DMA took readings of the loss modulus (E'), the storage modulus (E'') and the ratio of the loss modulus to the storage modulus (tan δ).

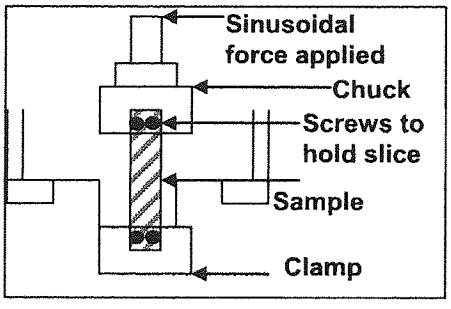

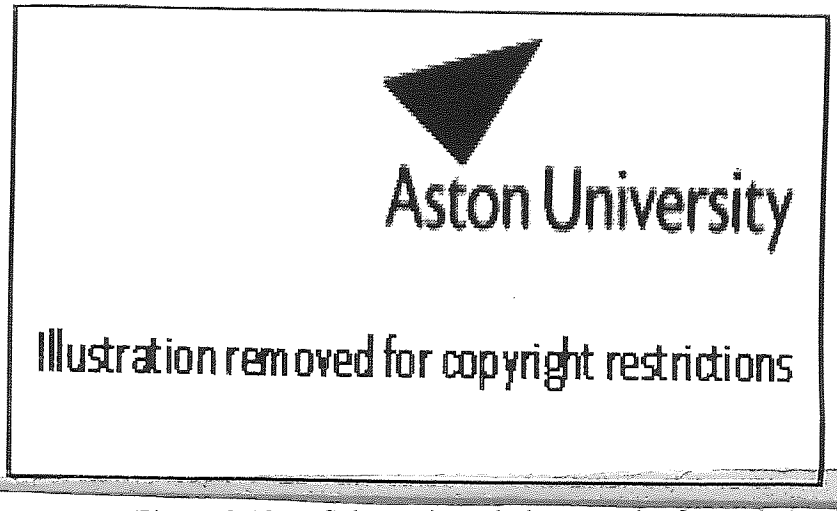

Figure 2.12 Schematic and photograph of sample loaded in tension on the DMA.

The glass transition temperature of the sample (Tg) was taken as the maximum temperature of the tan δ curve, the E'_{min} (minimum of the loss modulus curve, at the maximum temperature) was taken as a reference for the cross-link density of the coating so the different systems could be compared (**Figure 2.13**). In order to compare different systems, the Tg or E'_{min} values were compared using a delta change Tg or E'_{min} (ΔTg or $\Delta E'_{min}$, equation 2.3), to determine if any changes had occurred after weathering. The value for the unexposed was averaged for that type of clearcoat, across the depth of the clearcoat.

$$\Delta Tg \text{ (or } E'min) = Tg \text{ (or } E'min)_{(exposed)} - Tg \text{ (or } E'min)_{(\text{ unexposed})}. \qquad (2.3)$$

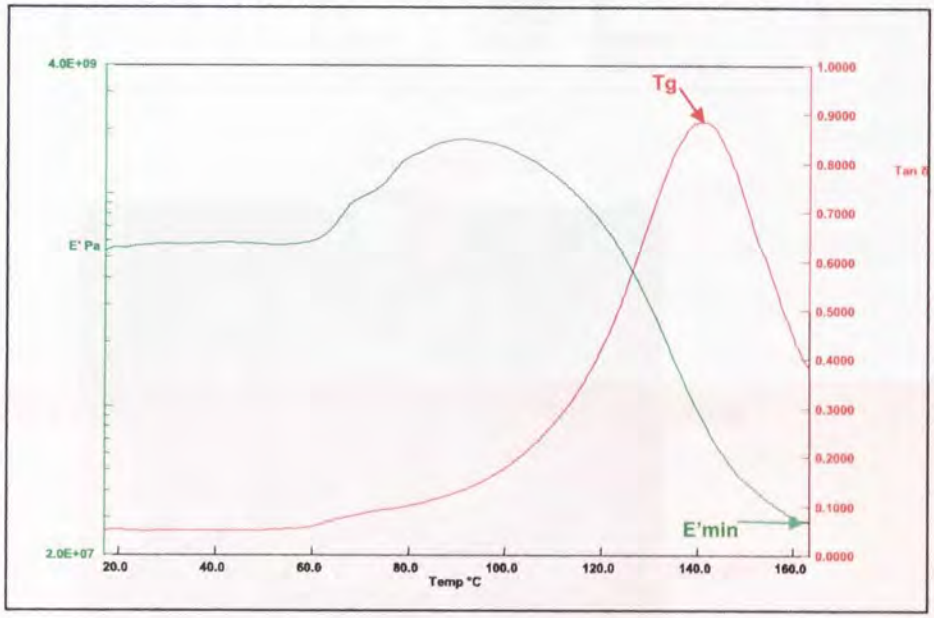

Figure 2.13 Sample DMA chart, showing the determination of Tg and E'min.

Bending analysis was performed on the full (unmicrotomed) systems to determine changes during exposure. The tests were carried out using a single cantilever bending (**Figure 2.14**). Single cantilever performs viscoelasticity measurements of only one side of the sample using a bend attachment. With sample loading, care had to be taken to ensure that the sample was not touching another part of the bend clamp or the bend base. The sample length was defined as 10mm, the width cut to 10mm, and the thickness measured as 1.4mm. The sample was run under the same conditions as for tension tests, and the thermogram was analysed in the same way.

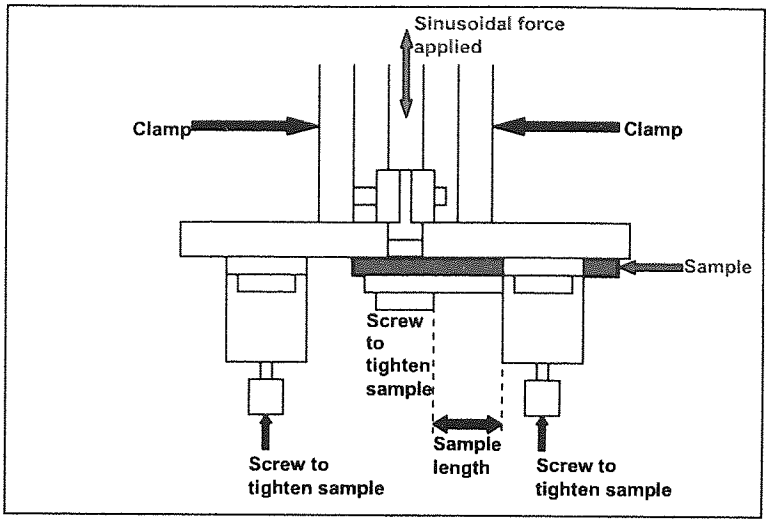

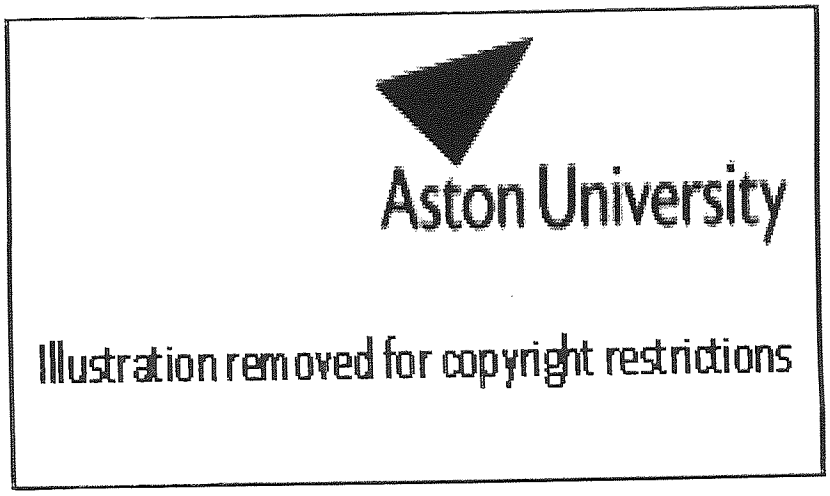

Figure 2.14 Schematic and photograph of sample loaded in bending mode on the DMA.

2.6.6 UV-Vis Analysis of the microtomed samples

Ultraviolet-visible (UV-Vis) spectrometry was used to monitor the changes in the concentration of UVA during accelerated weathering of clearcoats in multilayer paint systems. The analysis was carried out on a Varian Cary 5000i UV-Vis Spectrometer. The analysis could only be carried out on the clearcoat layer of the paint system as these were the

most particle free layers and would give spectra with the lowest amount of scattering. Two different types of analysis were carried out, transmission analysis and diffuse reflectance measurements using an external diffuse reflectance accessory (DRA) with the Cary spectrometer. Both types of measurements were taken under the same conditions, scanning was run from 200-800nm at a scan speed of 100nm/minute.

For transmission experiments, the slices were clamped between quartz plates to keep the slices flat and immobile, quartz has no absorption in the wavelength range investigated. Absorbance data were converted into concentration values using molar extinction coefficient value for the characteristic Cyasorb 1164 absorption band maximum (at 342 nm) and assuming the validity of Beer Lambert law of light absorption ($\mathbf{A = \varepsilon.c.l}$, where **A** is absorbance units, ε is the molar extinction coefficient; $\varepsilon = \mathbf{22{,}400\ litre\ mol^{-1}cm^{-1}}$ for Cyasorb 1164 measured at 342 nm in an ethanolic solution, **c** is molar concentration in $mol.l^{-1}$ and **l** is the path length of the sample in cm), with a correction made for scattering, for a sample spectrum see **Figure 2.15**. As in previous methods, in order to compare different systems, the concentration values were compared using a delta change UVA concentration, equation 2.4. The value for the unexposed sample was averaged for that type of clearcoat, across the depth of the clearcoat.

$$\mathbf{\Delta UVA\ concentration = UVA\ concentration_{(exposed)} - UVA\ concentration_{(\ unexposed)}} \quad (2.4)$$

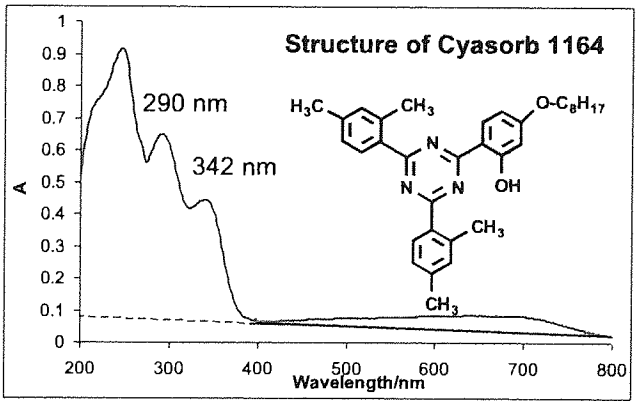

Figure 2.15 Typical UV-VIS spectra of automotive clearcoat containg UVA, Cyasorb 1164.

Diffuse reflectance measurements were carried out using an external 15cm diameter DRA (**Figure 2.16**). Diffuse reflectance occurs when the surface reflects light in many different directions, giving the surface a matt finish, (**Figure 2.17**), which contrasts with conventional transmission measurements, commonly used in UV-Vis analysis (**Figure 2.18**), in these, the sample is placed between the incident beam and the detector, the incident beam hits the sample, any transmitted radiation passes through the sample and out into the detector.

The DRA is a 15cm integrating sphere accessory that replaces the sample compartment in the spectrometer. The sphere is a hollow optical device, coated internally with a white diffusing material (Teflon) and fitted with the same detector configuration as the host spectrometer. With the DRA, as well as collecting the transmitted radiation (by placing the sample in front of the DRA), the diffuse component was also collected (by placing the sample behind the DRA). The diffuse reflected radiation thus passed into the DRA, to the detector connected to the DRA, with the specular plug attached to include this component of the reflected light. As the slices of the coating were very small, a small spot kit was also used to focus on a particular part of the coating.

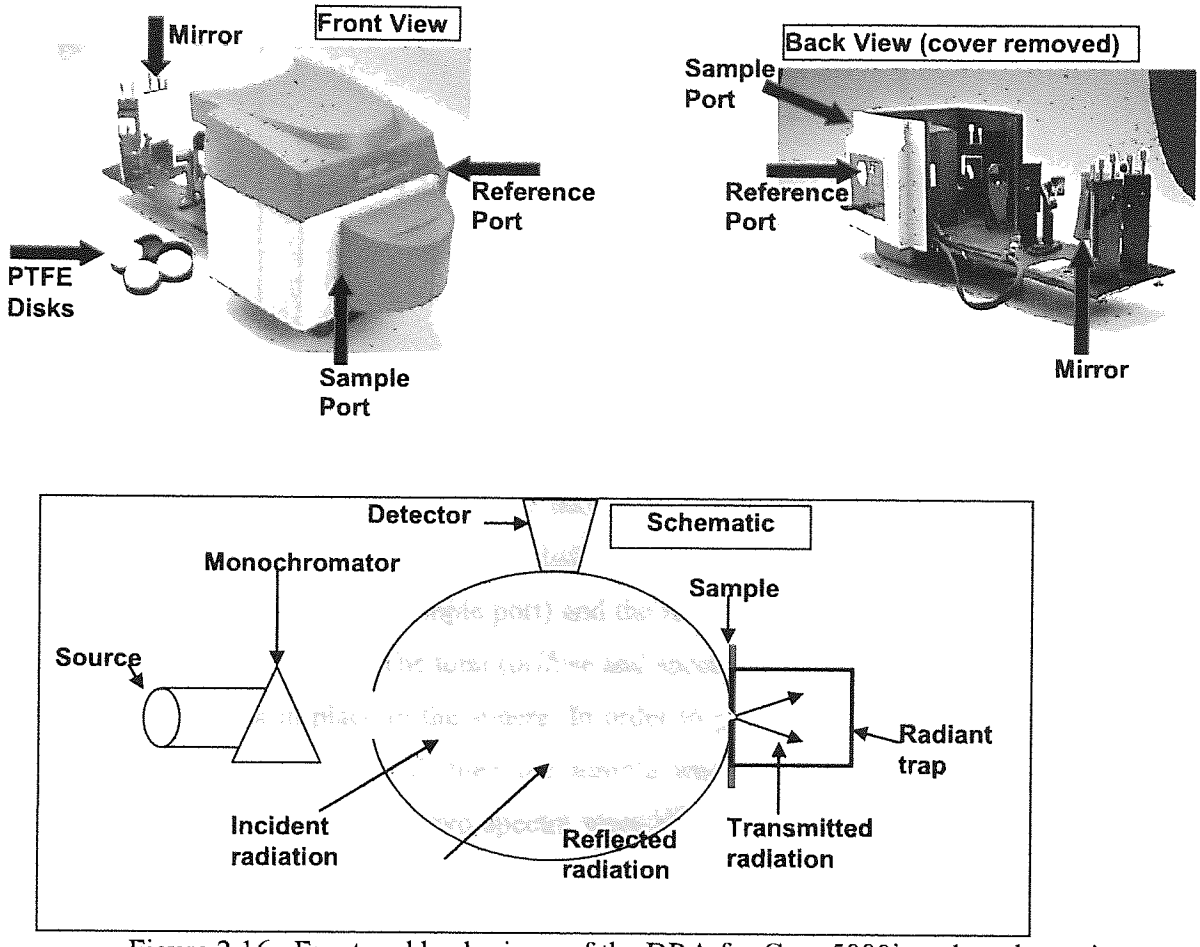

Figure 2.16 Front and back views of the DRA for Cary 5000i, and a schematic view

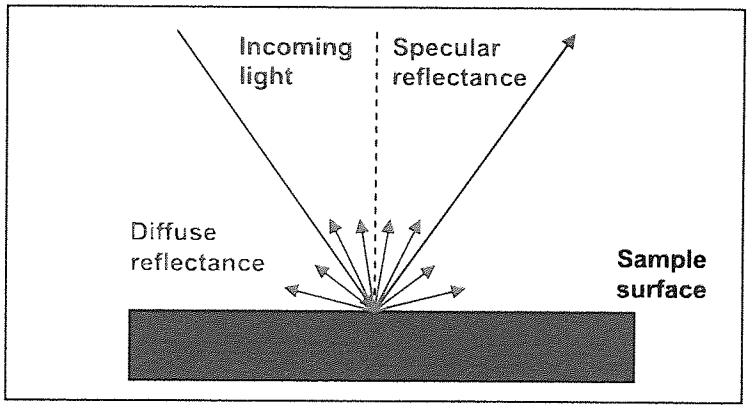

Figure 2.17 Schematic representation of diffuse reflectance

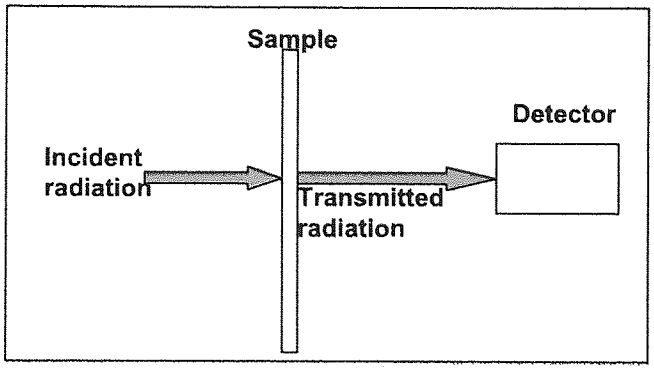

Figure 2.18 Schematic representation of transmission UV-Vis measurements

Firstly, reflectance measurements were taken for the slice under examination, a baseline was recorded with the PTFE reference disk covering the reflectance port. The sample was then clamped over the port (sample port) and the reflection off the sample collected by the detector within the sphere. The total (diffuse and specular) reflectance was measured as the specular plug was in place in the sphere. In order to produce transmission measurements, the beam was first refocused, then the sample was placed before the sphere and the transmission measured. Thus, two spectra were collected for each sample (**Figure 2.19**). These were then added to form a composite spectrum, whose units were lastly converted into absolute absorption units (**Figure 2.19**), thus the Beer-Lambert Law could again be used as previously to calculate the concentration of UVA in the coating.

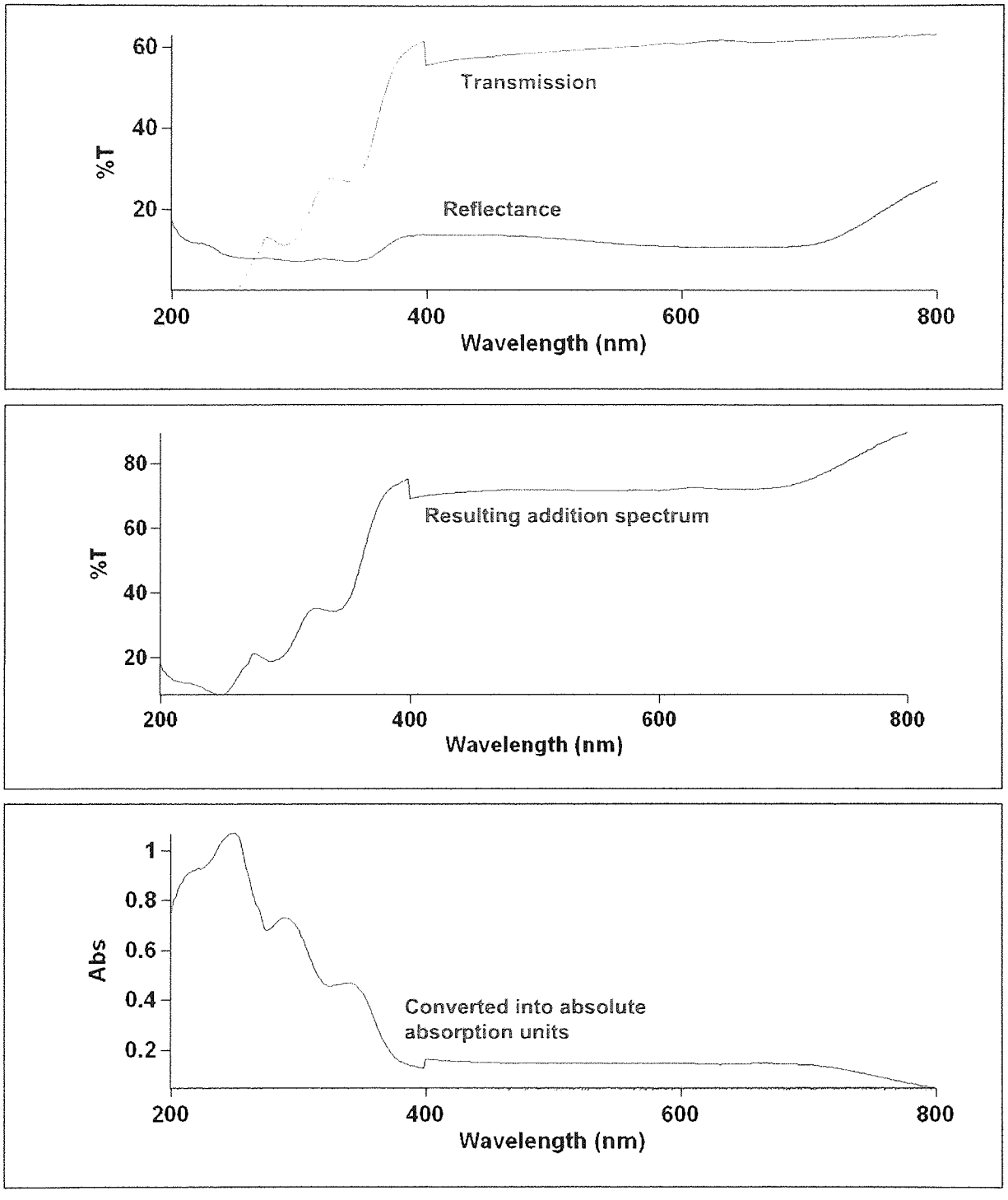

Figure 2.19 Typical diffuse reflectance UV-VIS spectra of automotive clearcoat containing UVA, Cyasorb 1164, showing the original transmission reflectance spectra, the resulting addition spectra, and the addition spectra converted into absolute absorption units.

2.6.7 Solvent Extraction – GC and MS Analysis

To determine the content of the additive (both the UVA and the HALS) from the microtomed slices (from all of the layers), the additives were first extracted by ultrasonic treatment using a solvent such as toluene. The extract solutions were then analyzed by gas-chromatography (GC, using a 12m column), or, the extract solutions were analyzed using MS (mass spectrometry), these analyses were carried out by project partners.

2.6.8 MALDI-ToF MS

MALDI-ToF MS was used to monitor surface changes in the coating systems following weathering, the clearcoat acted as a homogeneous sample in the laser desorption/ablation experiments. A conventional MALDI-ToF experiment involves the use of a matrix that absorbs the laser light with subsequent transfer of a small fraction of this energy to the analyte molecule to effect the formation of a gas-phase plume of ions (made up of matrix and analyte molecules, clusters of matrix molecules, and cations with different alkali metals, mainly sodium and potassium), with minimum source fragmentation. However, the MALDI-ToF MS experiments here were non-conventional as they involved a role reversal; the matrix (the cured clearcoat) was almost transparent to the laser light, whereas the analyte (the stabilizer) absorbed the laser light, depending on its absorbancy.

Neat samples of the stabilizers (UVA and HALS) were hand-spotted on the target, air-dried and subjected to MALDI-ToF MS (Bruker Omniflex) experiments (3 ns N_2 laser pulses, 200 μJ at 337 nm, reflectron mode, negative polarization, 20 kV) to investigate the pattern of absorption. Complete multilayer systems were also examined before and after artificial accelerated weathering, repetitive multiple laser pulses were delivered sequentially with spectral monitoring of the same spot (200 laser pulses, full power for each). The aim was that the total laser power delivered would cause significant levels of ablation to the surface of the coating system, gradually revealing the underlying layers.

2.7 Diffusion and Solubility Measurements

In order to understand the movement of the UVA additive in the clearcoat layer, the diffusion and solubility characteristics were investigated.

2.7.1 Production of Materials for Migration Experiments

For solubility and stack diffusion experiments, films of the water-borne additive free clearcoat were produced, by either spin-coating or draw-down coating of the raw material (supplied by PPG, Germany), onto sheets of a Teflon impregnated material. The material was then cured using a method closely resembling the industrial process (5 minute flash-off at room temperature, then placed in a cold oven with temperature ramped up to 140^0C over a 20 minute period, and lastly the temperature was held at 140^0C for a further 20 minutes). The coatings were then gently peeled off from the Teflon sheets, ready for use. The final thickness of the films was measured and found to be 30-100μm. For both solubility and stack diffusion experiments, reservoir plaques containing the additive were also produced by compression moulding (using a Daniels press) of polyethylene at 200^0C 20% w/w Cyasorb 1164 at 200^0C under 25 kg/m^2 pressure for 30 seconds to give a final thickness of approximately 2mm.

For determination of diffusion characteristics using FTIR-ATR, reservoir plaques containing the additive (Cyasorb 1164) were compression moulded by the same method described above. Additive-free plaques containing the polymer under analysis were also produced (again by compression moulding, these were thicker than the films used in stack analysis (up to 2mm).

2.7.2 Solubility Experiments

The solubility cell is shown in **Figure 2.20**; 3 additive free films (of a similar thickness, measured individually) were sandwiched between the saturated reservoir plaques containing a high (saturated) concentration of the UVA. Usually several film stacks were placed in a cell, to examine the repeatability of the experiments, the stacks were separated by aluminium foil to ensure that no cross-contamination could occur. Pressure was applied

symmetrically to the cell by screws. This was to ensure the removal of air bubbles and to achieve intimate contact between layers of the film and the plaque. These variations are in the order of the experimental error of the measurements. The solubility cells were then placed in a vacuum oven at a specified temperature, 30, 45 or 60^{0}C (to minimize degradation from exposure to the atmosphere), until the concentration of the additive was identical in all three (originally additive free) films, thus the maximum solubility had been reached. The concentration of the additive in the films was measured using transmission UV-Vis analysis in a similar manner to the automotive slices (section 2.6.6, Figure 2.15), again assuming the validity of the Beer-Lambert Law. Thus the results yielded a single average value of the maximum concentration of the additive in the film at the specified temperature, which was then plotted as a van't Hoff plot (Log of Solubility vs 1/T), through the gradient the heat of solution was determined.

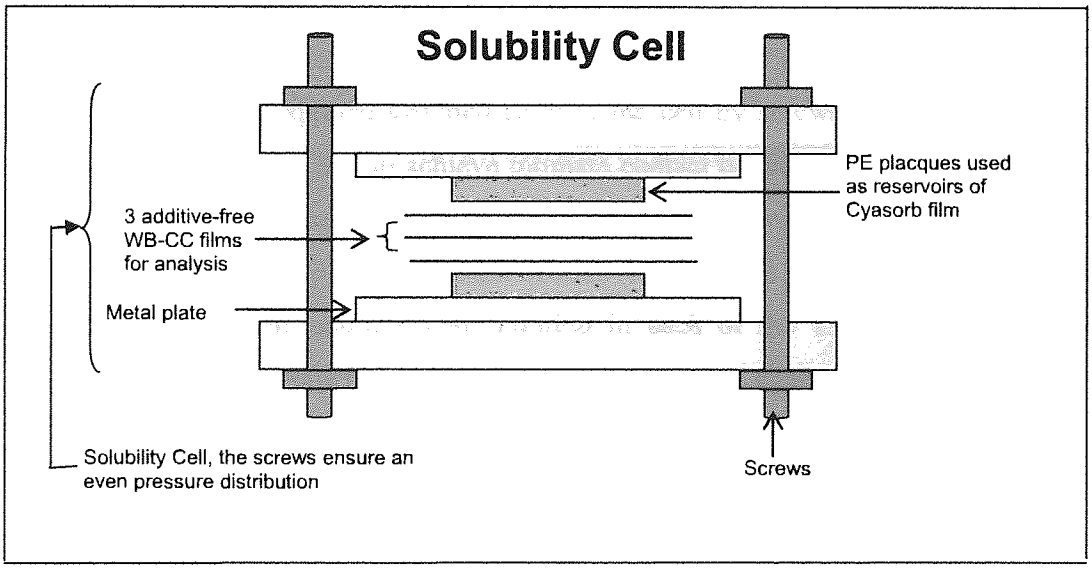

Figure 2.20 Solubility Experimental set-up

2.7.3 Diffusion Experiments

The diffusion characteristic for Cyasorb 1164 UVA in the clearcoat, was first determined using the stack (or Roe) method (section 2.7.3.1). The experimental results were examined using two methods, and the diffusion coefficient was calculated using either the traditional

method of comparison to the theoretical curves or by the graphical method of calculation of the gradient of the results, these methods were known as **'fitting'** or **'gradient'** respectively. The diffusion characteristic was also examined using FTIR-ATR spectroscopy (section 2.7.3.1). Again, the diffusion coefficient was calculated using either the method of comparison to calculated theoretical curves or by the graphical method of calculation of the gradient of the results, these methods were again known as **'fitting'** or **'gradient'** respectively.

2.7.3.1 Stack Diffusion Experiments

The diffusion cell constructed is shown in **Figure 2.21;** 13 additive free films (of a similar thickness, individually measured) were sandwiched between the saturated plaques. Usually several film stacks were placed in a cell, to examine the repeatability of the experiments, the stacks were separated by aluminium foil to ensure that no cross-contamination could occur. Pressure was applied symmetrically to the cell by screws. This was to ensure the removal of air bubbles and to achieve intimate contact between layers of the film and the plaque. The diffusion cells were then placed in a vacuum oven at a specified temperature (30, 45 or 60^0C) for a specified amount of time (to minimize degradation from exposure to the atmosphere). The additive concentration in each of the 13 films of the stack was determined at appropriate intervals using UV-Vis analysis, again assuming that the additive concentration followed the Beer-Lambert Law.

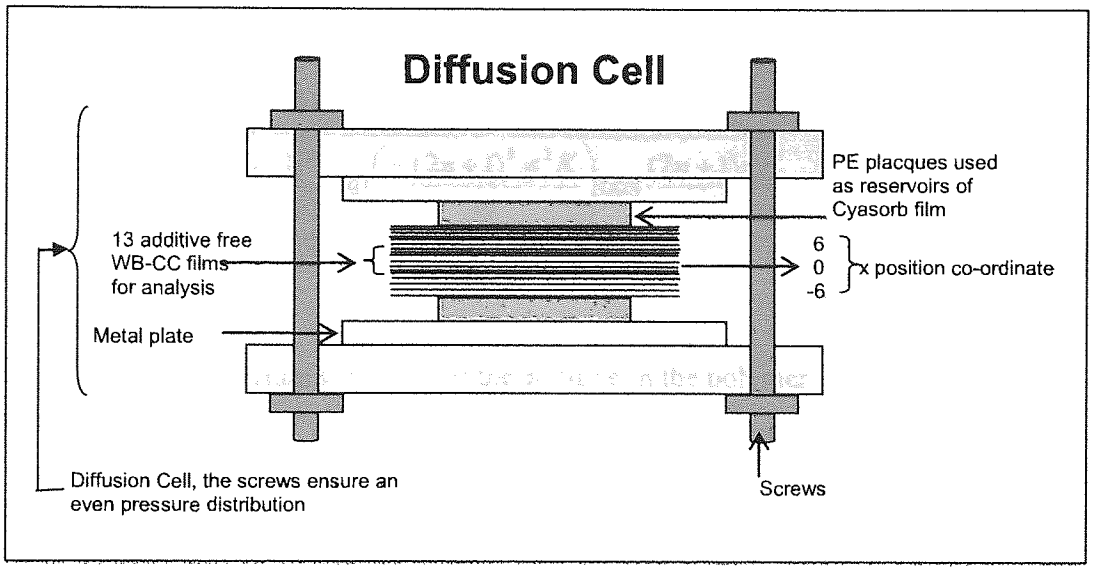

Figure 2.21 Diffusion Cell set-up

Thus the raw results measured were the concentrations of the additive at the different positions in the stack at the different temperatures. Additive concentration vs. film position profiles were constructed for a specified length of time at the temperature of measurement. The diffusion coefficient was calculated using either the traditional method of comparison to the theoretical curves **[20]** or by the graphical method of calculation of the gradient of the results.

To recap, the theory behind migration studies begins with equation (2.5), Fick's second law,

$$\frac{\delta C}{\delta t} = D_P \frac{\delta^2 C}{\delta x^2} \qquad (2.5)$$

Where,

F = rate of transport per unit area of the polymer

C = concentration of a diffusion compound (g/l)

x = space co-ordinate measured at right angles

t = elapsed time (s).

If a stack of polymer films are placed in infinite contact with the diffusant (the additive), above and below the stack of polymer films, then equation (2.6) is another applicable solution to equation (2.5);

$$\frac{C_{(x,t)}}{C_0} = 1 - \frac{4}{\pi} C_0 \sum_{n=0}^{\infty} \frac{(-1)^n}{2n+1} \exp\left(\frac{-(2n+1)^2 \pi^2 K}{4l}\right) \cos\frac{(2n+1)\pi x}{2l} \qquad (2.6)$$

Where,

C_0 = the equilibrium solubility of the additive in the polymer

C(x,t) = concentration of the diffusant at x distance from the centre of the solid (of thickness l) at time t.

2l = total thickness of the stack of thin additive free discs

= x is the position co-ordinate with the origin at the centre of the stack

K is given by equation 2.7;

$$K = Dt/l^2 \qquad (2.7)$$

The total thickness of the stack of the 13 polymer films is 2l, with the outside faces located at +l and –l (top and bottom) with respect to x=0 at the centre of the film, C(x,t) is the concentration of the additive in the polymer film with respect to the position of the film in the stack and the length of time that the polymer films have been in contact with the additive. Co is the maximum concentration of the additive which can be dissolved in the polymer (the maximum solubility). Edge effects of the surface of the polymer are not taken into account in this model, it is assumed that the additive can pass through the layers of polymer that are in intimate contact with each other. For the **fitting method**, theoretical values of C(x,t)/Co are plotted against x/l for several values of Dt/l^2 (also between 0 and 1) are calculated by substituting values of x/l between 0 and 1 into equation (2.6), for n=0 and n=1, using an Excel Spreadsheet. Experimental values of C(x,t)/Co against x/l were then plotted on the theoretical curve (**Figure 2.22**), and the closest value of K obtained. Then by substituting the value of K into equation **(2.7),** D was calculated.

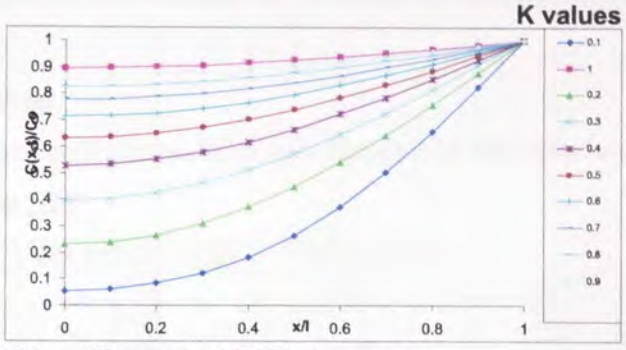

Figure 2.22 Theoretical Diffusion curve

In the **gradient** method, if one assumes that in equation 2.6 n=0, then equation 2.8 is obtained;

$$\boxed{C(x,t)/Co = 1 - 4/\pi \exp(-D\pi^2 t/4l^2)\cos(\pi x/2l)} \qquad (2.8)$$

By plotting the experimental values of C(x,t)/Co vs.cos(π x/2l), a straight line is found (for n=0 to apply, the line must be linear). The gradient of the straight line can be used to determine the diffusion coefficient, as the gradient is equal to $1\text{-}4/\pi \exp(-D\pi^2t/4l^2)$, thus D can be found by solving equation (2.9). This method is referred to as the 'gradient' method, or the 'gradient fitted' data where the experimental data has been fitted to a curve.

$$\boxed{Gradient = 1 - 4/\pi \exp(-D\pi^2 t/4l^2)}$$

Gradient = $1\text{-}4/\pi \exp(-D\pi^2t/4l^2)$

Gradient + 1 = $-4/\pi \exp(-D\pi^2t/4l^2)$

$\exp(-D\pi^2t/4l^2)$ = $-4/(\text{Gradient} + 1) * 1/\pi$

$$\boxed{D = e^{\left(\frac{4}{Gradient+1}\cdot\frac{1}{\pi}\right)}\left(\frac{4l^2}{\pi^2 t}\right)} \qquad (2.9)$$

Worked Examples of Calculations of Diffusion Coefficients from the stack method

1. 'Fitting' Method

Using sample data, collected at 30^{0}C (see Figure 2.19 for experimental set-up), **Table 2.6**, plotted in **Figure 2.23**;

C(x,t) (w/w %)	**C(x,t)/Co** (w/w %)	Film Number	x	**x/l**
2.8	**1.12**	2	0.000044	**0.33**
2.1	**0.84**	3	0.000066	**0.5**
1.7	**0.68**	6	0.000132	**1**
1.8	**0.72**	7	0.000154	**1.2**
2.3	**0.92**	9	0.000198	**1.5**
2.4	**0.96**	10	0.00022	**1.7**
2.8	**1.12**	11	0.000242	**1.8**
2.9	**1.16**	12	0.000264	**2**

Table 2.6 Experimental Diffusion Data at 30^{0}C

C(x,t) = Experimentally measured concentration of Cyasorb in the polymer film, %w/w

Co = maximum solubility of the additive in the polymer at the specified temperature = 2.5w/w % at 30^{0}C.

Film Number = Position of the film in the stack, 1 at the top.

x = cumulative thickness of the film
= 2l * film thickness (with film number 1 at the top and 13 at the bottom of the stack).

l = ½ the total thickness of the stack of polymer films
= 0.000132m.

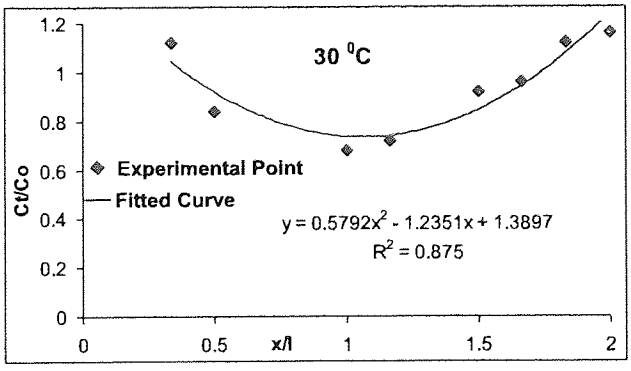

Figure 2.23 Experimental sample stack diffusion data at 30^{0}C

The experimental points were fitted to a quadratic curve, the experimental data was plotted on the theoretical curves in **Figure 2.24**;

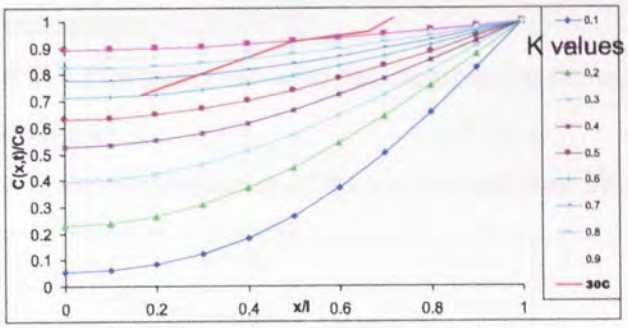

Figure 2.24 Experimental sample stack diffusion data at 30^0C, fitted to the theoretical curve

Closest fit, K = 0.7, Using equation (2.7), D can be found;

$$D = (K * l^{2)}/t \quad (2.7)$$

Where;

l = ½ the total thickness of the stack of polymer films
= 0.000132m.

l^2 = $1.75 * 10^{-8}$

t = 66 days on test
= 5702400 seconds

D = $2.14 * 10^{-15}$ m^2/s

D = $2.14 * 10^{-11}$ cm^2/s

2. 'Gradient' Method

Using actual experimental data

Plot of C(x,t)/Co vs.cos(π x/2l), is used, **Table 2.7, Figure 2.25**

x/l	C(x,t)/Co	x	π x/2l	cos(π x/2l
0.17	**0.72**	0.000022	0.261	**0.965**
0.5	**0.92**	0.000066	0.785	**0.707**
0.67	**0.96**	0.000088	1.04	**0.5**
0.83	**1.12**	0.00011	1.30	**0.258**
1	**1.16**	0.000132	1.57	**6.125 E-17**

Table 2.7 Gradient diffusion method at 30^0C

Co = maximum solubility of the additive in the polymer at the specified temperature = 2.5w/w %
= 2l * film thickness (with film number 1 at the top and 13 and the bottom).

l = ½ the total thickness of the stack of polymer films = 0.000132m.

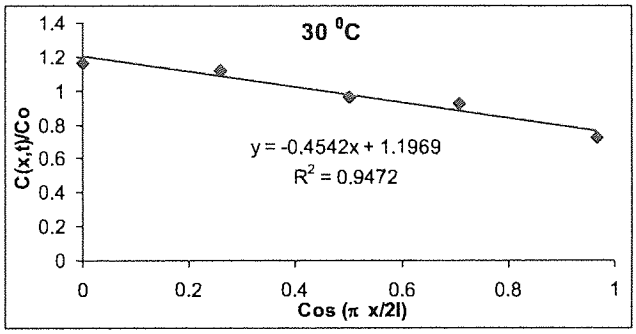

Figure 2.25 Gradient method for calculation of diffusion coefficient using the actual experimental data.

Slope of chart = -0.4542

l = 0.000132 (from previous)

$4l^2$ = $6.97 * 10^{-8}$

t = 66 days on test
= 5702400 seconds

$$Gradient = 1 - 4/\pi \exp(-D\pi^2 t/4l^2)$$

-0.4542 = $1-4/\pi \exp(-D\pi^2t/4l^2)$

-1.4542 = $-4/\pi \exp(-D\pi^2t/4l^2)$

1.8515 = $\exp(-D\pi^2t/4l^2)$

6.3697 = $D\pi^2t/4l^2$

0.000000444 = $D\pi^2$

D = $7.9 * 10^{-15} m^2/s$

D = $7.9 * 10^{-11} cm^2/s$

2.7.3.2 FTIR ATR Method of Determining the Diffusion Coefficient

A far faster method of obtaining the diffusion coefficient (each experiment lasting around 12 hours, as opposed to several months for the stack method), involves the use of FTIR-ATR. A Perkin Elmer Spectrum was again used for these experiments, with a zinc-selenide horizontal ATR (HATR) accessory (Specac) with an external heater (Specac), with time-base software (Perkin-Elmer). PE Plaque additive reservoirs and slightly PE thicker polymer films were used for these experiments, the plaques again produced by compression molding, (note the polymer films in this case were not WB-CC but polyethylene produced by compression molding).

The apparatus was constructed as shown in **Figures 2.26, 2.27;** the cell was a modified commercially available HATR unit. A steel cover was produced that contained a pressurizable chamber, the chamber was pressure sealed against the top surface of the ATR accessory by a rubber seal gasket. The polymer film was held in place between the seal gasket and the top surface of the ATR crystal when the top plate was bolted down. The nitrogen gas in the sealed chamber above the ATR was used to achieve good uniform contact between the polymer film and the ATR crystal. The ATR crystal was not produced with an airtight seal, thus the bottom surface of the polymer film was at atmospheric pressure, which created a pressure differential across the polymer film. This kept the polymer in contact with the ATR crystal throughout the diffusion process. Nitrogen was used as the contact gas as it is IR inactive. Accurate temperature control of the polymer was achieved using an attached heater.

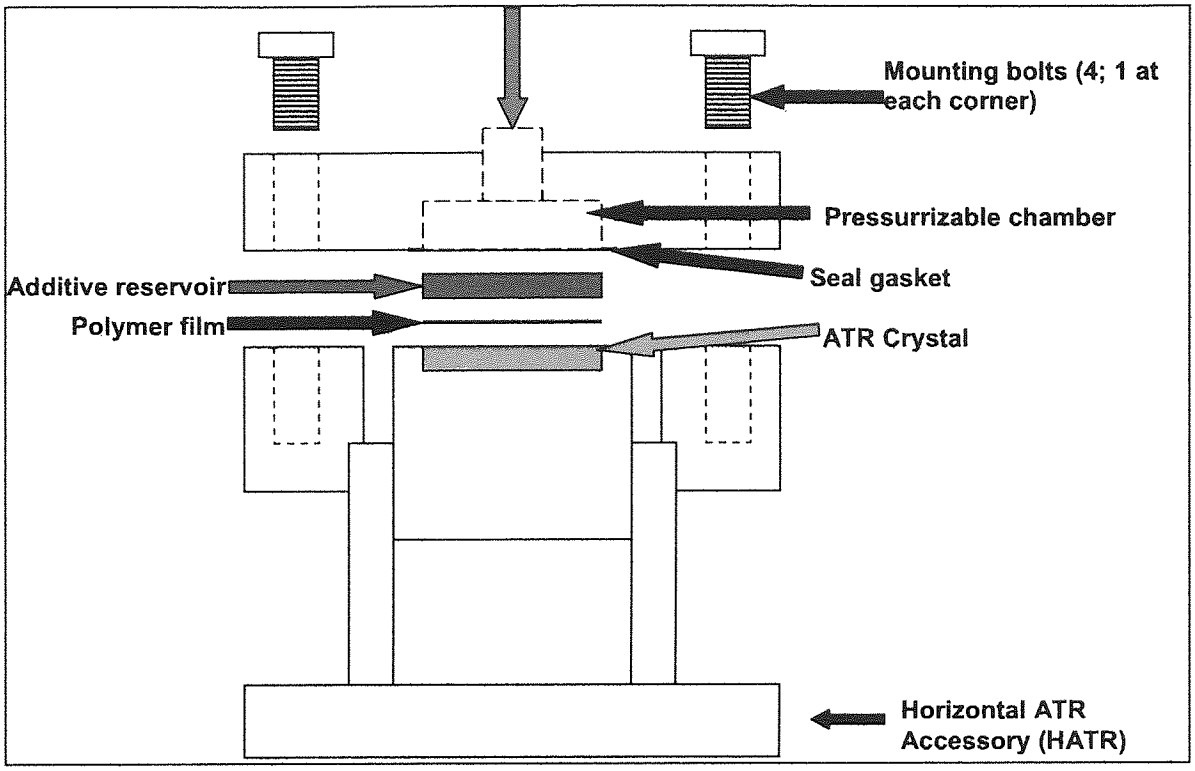

Figure 2.26 End view of the modified ATR accessory used for diffusion measurements, the FTIR beam path passes through the paper.

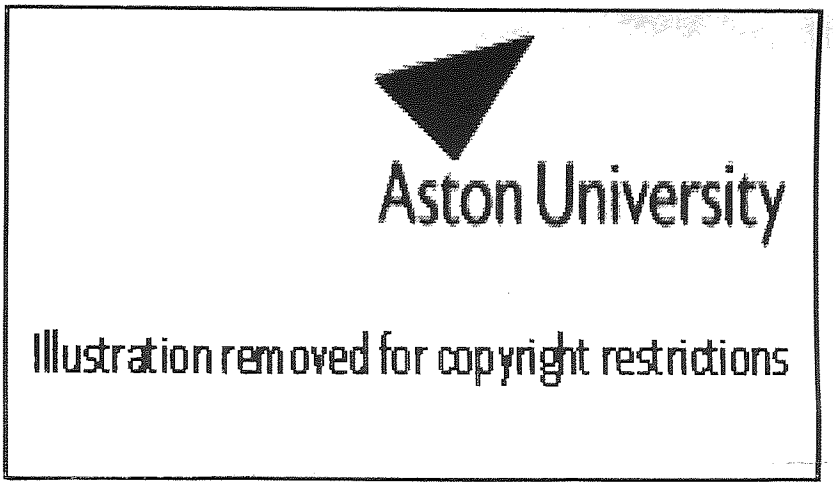

Figure 2.27 Modified ATR accessory used for diffusion measurements, on the PE Spectrum One.

Experimentally, a background spectrum was first taken without the polymer film in place. Afterwards, the polymer film was gently placed on the ATR crystal, then heated to 80^0C, allowed to cool to allow the polymer film to relax. The apparatus was then constructed with the polymer film and reservoir in place, the top was then screwed down, and the nitrogen pressure applied. The apparatus was heated up to the desired temperature, and IR spectra recorded at regular intervals (every 10-15 minutes), each experiment lasted 12-16 hours. Thus, the raw results obtained were IR spectra at the different times. The absorbance's at the specific wavelength were converted into concentration of the additive at that time interval using the Beer-Lambert Law and the appropriate extinction coefficient, thus had results of the concentration of the additive at different time periods.

In order to calculate the diffusion coefficients, the experimental data also had to be compared to theoretical diffusion data, the theoretical curve was based on equations 2.10, 2.11, 2.12 the equation was again built up using an Excel spreadsheet. The experimental values were then plotted in a similar way to the theoretical curve.

$$\frac{A_t}{A_\infty} = 1 - \frac{8\gamma}{\pi[1-\exp(-2\gamma L)]} \sum_{n=0}^{\infty} \left[\frac{\exp(g)[f\exp(-2\gamma L) + (-1)^n (2\gamma)]}{(2n+1)(4\gamma^2 + f^2)} \right] \tag{2.10}$$

Where;

$$g = \frac{-D(2n+1)^2 \pi^2 t^2}{4L^2} \tag{2.11}$$

$$f = \frac{(2n+1)\pi}{2L} \tag{2.12}$$

A_t = Absorbance at time, t.

A_0 = Absorbance at equilibrium

γ = $1/d_p$ (d_p is the depth of penetration of the ATR crystal, 0.5μm)

If L is large enough (equation 2,13);

$$4\gamma^2 >>> \frac{\pi^2}{4L^2} \tag{2.13}$$

$$1 >>> \exp(-2\gamma l)$$

The diffusion coefficient, D was then calculated using equation (2.14)

$$In\left(1-\frac{A_t}{A_\infty}\right)=In\left(\frac{4}{\pi}\right)-\frac{D\pi^2 t}{4l^2} \qquad (2.14)$$

A_t = Absorbance at time, t.

A_0 = Absorbance at equilibrium

Worked Example of Calculating Diffusion Coefficients using FTIR ATR

The absorbance of the appropriate peak was measured at the different elapsed time (in seconds), the absorbance was normalized with respect to a reference peak to account for any thickness differences in the films, A_{eq} was the equilibrium absorbance, raw results are shown in **Table 2.8 and Figure 2.28.**

Time	A_t	A_t/A_{ref}	A_t/A_{eq}	$1-A_t/A_{eq}$	$\ln(1-A_t/A_{eq})$
0	0	0	0	1	0
1200	0.0144	0.032034	0.0506	0.9494	-0.05192
2400	0.0902	0.200658	0.316951	0.683049	-0.38119
3600	0.135	0.30032	0.474372	0.525628	-0.64316
4800	0.165	0.367058	0.579788	0.420212	-0.86699
6000	0.182	0.404876	0.639523	0.360477	-1.02033
7200	0.199	0.442694	0.699259	0.300741	-1.20151
8400	0.207	0.460491	0.72737	0.27263	-1.29964
9600	0.218	0.484962	0.766022	0.233978	-1.45253
10800	0.223	0.496085	0.783592	0.216408	-1.53059
12000	0.231	0.513881	0.811703	0.188297	-1.66973
13200	0.233	0.518331	0.81873	0.18127	-1.70777
14400	0.239	0.531678	0.839813	0.160187	-1.83142
15600	0.24	0.533903	0.843327	0.156673	-1.8536
16800	0.246	0.54725	0.864411	0.135589	-1.99812
18000	0.248	0.5517	0.871438	0.128562	-2.05135
19200	0.251	0.558373	0.88198	0.11802	-2.1369
27600	0.268	0.596191	0.941716	0.058284	-2.84242
28800	0.269	0.598416	0.945229	0.054771	-2.9046
30000	0.271	0.602865	0.952257	0.047743	-3.04193
31200	0.274	0.609539	0.962799	0.037201	-3.29141

A_t = Absorbance at time t

A_{ref} = Absorbance of the reference peak

A_{eq} = Equilibrium absorbance = 0.284587

Table 2.8 Raw data for FTIR ATR method for calculation of the diffusion coefficient.

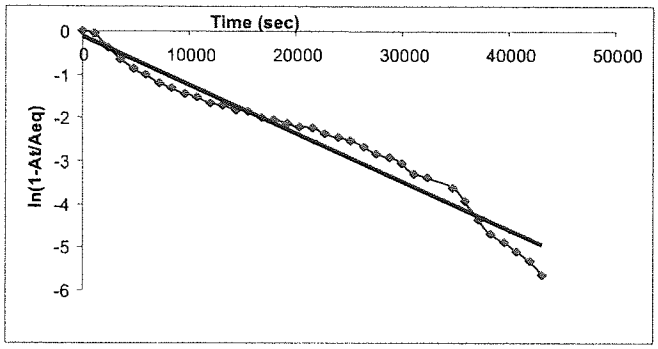

Figure 2.28 Calculation of the diffusion coefficient using FTIR ATR

The slope of the line in Figure 2.28 includes the D term and allows its calculation.

Slope = $D\pi^2 / 4L^2$
L = 0.007 cm
D = 1.98 * 10^{-9} cm^2/sec

This curve was then compared to the theoretical curve, which was obtained from equation 2.10

$$\frac{A_t}{A_\infty} = 1 - \frac{8\gamma}{\pi[1-\exp(-2\gamma L)]} \sum_{n=0}^{\infty} \left[\frac{\exp(g)[f\exp(-2\gamma L) + (-1)^n (2\gamma)}{(2n+1)(4\gamma^2 + f^2)} \right] \tag{2.10}$$

$$g = \frac{-D(2n+1)^2 \pi^2 t^2}{4L^2} \tag{2.11}$$

$$f = \frac{(2n+1)\pi}{2L} \tag{2.12}$$

A_t = absorbance at time, t.

A_0 = absorbance at equilibrium

γ = $1/d_p$ (d_p is the depth of penetration of the ATR crystal)

In order to simulate the theoretical profile of HATR experiment, above equation was put into MS Excel spreadsheet software. The values of A_t/A_{eq} was then plotted against time to get the theoretical curve, **Figure 2.29.**

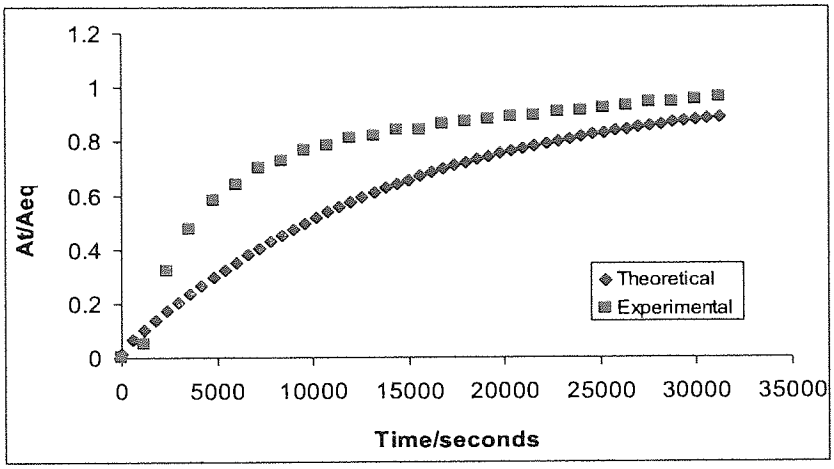

Figure 2.29 Theoretical curve used in the using FTIR ATR diffusion method.

CHAPTER 3:

CONVENTIONAL METHODS FOR ANALYSING THE DEGRADATION OF AUTOMOTIVE COATINGS BEFORE AND AFTER WEATHERING

CHAPTER 3: CONVENTIONAL METHODS FOR ANALYSING THE DEGRADATION OF AUTOMOTIVE COATINGS BEFORE AND AFTER WEATHERING

3.1 Objectives and Methodology

The aim of the work described in this chapter was to employ and compare the effectiveness of different traditional methods typically used to investigate weathering induced changes in various water-borne and solvent-borne automotive coating systems prepared and investigated in this study. Traditional methods discussed in this chapter are based on measurements of physical properties, in particular hardness, gloss and surface appearance by optical microscopy and photography, as well as by Fourier Transform Infra-red Spectroscopy (FTIR). Changes in physical properties of automotive coatings often require a substantial period of natural/artificial weathering exposure before any meaningful change is observed. However a much shorter induction time is often obtained for weathering-induced chemical changes determined by FTIR spectroscopy (transmission and reflectance, e.g. attenuated total reflectance, ATR).

Hardness, gloss, optical microscopy and FTIR-ATR measurements were carried out on full coating systems (not microtomed) before and after artificial accelerated weathering in an Atlas Weatherometer (using CAM and SPART conditions, see section 2.4.1 for details) and natural (in Miami, USA, see section 2.4.2 for details) weathering exposures. On the other hand, FTIR-transmission spectra were conducted on microtomed slices used for depth profiling of both solvent-borne and water-borne coating systems (approximately 5 μm slices). **Table 3.1** and **Scheme 3.1** show the systems examined and gives an overview of the methodology used. Photographs were also taken of the individual microtomed and weathered coating slices (unexposed slices were also used) to determine any weathering-induced erosion that may have taken place. The microtomed slices were numbered with a nominal depth of 5μm each; i.e. slice 1 was 2.5μm and slice 2 was 7.5 μm and so on. The slices of the unexposed samples were then labeled according to the coating layers they belong to, (e.g. a clearcoat), taking particular care with the interfaces between the layers. By counting back from the lower interfaces of the unexposed samples, the extent of erosion in the clearcoat in the exposed samples could be determined. However, it is important to point

out here that the determination of the level of erosion was limited by the thickness of the microtomed slices, in this case 5μm. Pictures were taken on slices of the same samples microtomed using both planar and rotary microtomes to determine any differences in the samples produced by the two microtoming methods.

Table 3.1 Structure and Properties of the stabilisers used in the different automotive clearcoats and a summary of the coating systems presented in this chapter

Layer Composition of various automotive coatings						
System Number (total thickness)		Type of curing regime	HALS level in clearcoat (Sanduvor 3055)	UVA level in clearcoat		Colour of basecoat
				Type	Level	
Solvent-borne	1 (120 μm)	Wet-on-dry	1	1	Standard	Silver
	3 (120 μm)	Wet-on-dry	1	1	Standard	Blue
	4 (120 μm)	Wet-on-dry	1	1	Cross-linkable	Blue
Water-borne	6c (65 μm)	Wet-on-wet	1	1	Standard	Blue
	7 (65 μm)	Wet-on-wet	1	3	Standard	Blue
	8 (65 μm)	Wet-on-wet	1	0	#	Blue
	9 (65 μm)	Wet-on-wet	1	1	Cross-linkable	Blue
	10 (65 μm)	Wet-on-wet	1	1	Standard	Silver

will be referred to as 'unstabilized'.

Stabiliser Code and Supplier	Structure	Physical Properties and State
Sanduvor 3055 (Clariant) **(HALS)**	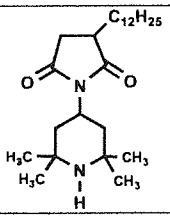	• Yellow viscous liquid • MW = 407 • Mpt = -15^{0}C • Bpt = 212^{0}C • Purity = 91%
Cyasorb 1164 (Cytec) **(UVA)**	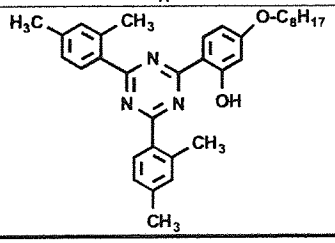	• Yellow powder • MW = 510 • Mpt = 88–91^{0}C • Purity = 96%(min)

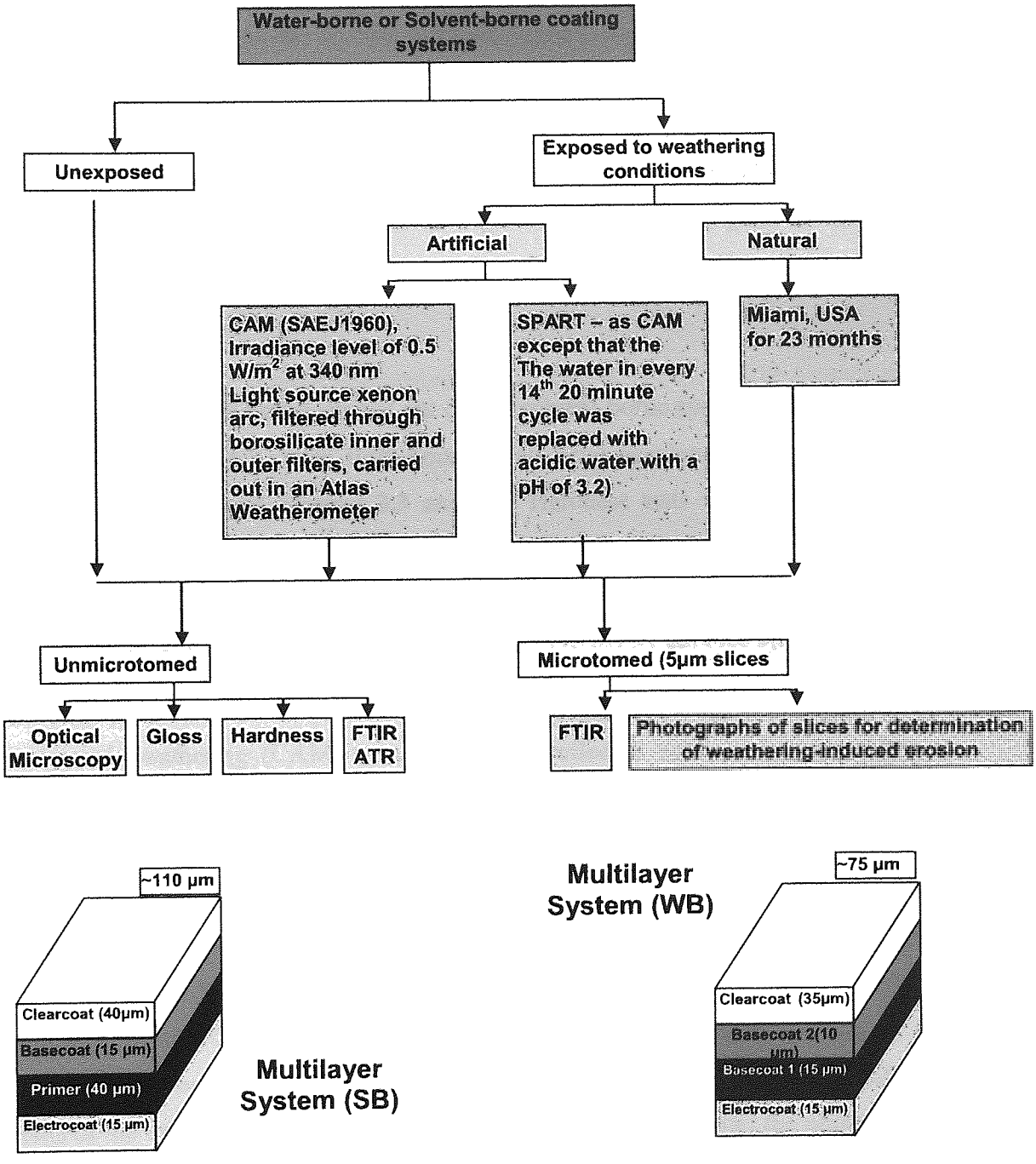

Scheme 3.1 Schematic illustration of traditional analytical methods used to investigate weathering induced changes in automotive coatings.

3.2 Results

3.2.1 Determination of weathering induced degradation of coating systems using physical property measurements

The gloss retention after natural Miami exposure of coating systems 1, 3, 4, 6c, 7, 8, 9 and 10 is shown in **Table 3.2** (results from artificial accelerated weathering are shown in the appendix) and are also displayed in **Figures 3.1** and **3.2**, all gloss measurements were within ± 0.5 gloss units, calculations of confidence limits are shown in appendices A3.2.1 and A3.2.2.

Hardness measurements were carried out on the solvent-borne systems 3 and the water-borne systems 6c and 8, after 1000 hours of artificial accelerated exposure and are shown in **Table 3.3** and **Figures 3.3 and 3.4**. Hardness tests were carried out by a project partner and are given as the average of three results.

3.2.2 Weathering induced changes of coating systems by surface appearance

Optical micrographs for water-borne coating system 6c before and after artificial accelerated weathering (CAM) measured under reflected light, and under different magnifications are shown in **Figure 3.5**. For results of other systems see appendix A3.1.1 to A3.1.6.

Photographs of microtomed slices for coating systems 3, 6c and 8 at different depths before and after exposures under CAM conditions for 4000 hours and SPART conditions for 1000 hours and outdoor Miami exposures for 23 months on rotary and planar microtomes are given in **Figures 3.6 and 3.7. Table 3.4** and **Figure 3.8** give details of the level of erosion in the coating systems determined from the photographed slices. Results for other systems are given in appendix A3.3.

3.2.3 FTIR Spectroscopic analysis for determining the structural changes and the extent of degradation of the coatings during weathering by depth profiling and surface measurements by FTIR

Depth profiling determined from microtomed slices across the depths of coating systems was investigated using FTIR-transmission spectroscopy for the unexposed

solvent-borne and water-borne coating systems 3 and 8 (**Figures 3.9** and **3.10**), to examine the differences in the structures of the various coating layers (**Table 3.5**). Figure 3.9 shows clearly that for the solvent-borne system 3 the major spectral change that takes place within the depth of the coating system is in the C=O peak at 1699 cm^{-1} which is absent in the deeper coating layers (electro-coat and primer). Moving from the electro-coat to the upper layers the absence of the peaks at 1525 (N-H and C-N urethane combination bands) and the C-N peak at 1029 cm^{-1} was noted together with the formation of the C-H peak at 1464 cm^{-1}.

Figure 3.10 shows the spectral differences between the layers of the unstabilized water-borne coating number 8. The C-O ester peak at 1380 cm^{-1} was absent in the deeper electro-coat layers and the C=O peak at 1720 cm^{-1} was much smaller, whereas there was a clear peak at 1525 cm^{-1} in this layer due to combination bands of N-H deformation stretch and C-N stretch in the urethane groups of the electro-coat layers. The differences in the layers chemistry are clear in all the solvent-borne and water-borne systems (see chapter 2, Schemes 2.1-2.5).

In order to determine the effect of weathering exposures, FTIR spectra of unexposed and exposed samples which were microtomed (depth profiled) were examined. To determine the changes due to weathering of the clear-coats, infra-red transmission spectra were measured on the 4^{th} microtomed slice (nominal depth 17.5 μm) of the water-borne and solvent-borne coating systems at different exposures (**Figures 3.11-3.14**). The band intensities were seen to increase in the fingerprint region after weathering. For all the systems examined, the difference in photoxidation index based on changes in the OH region (with respect to changes in a C-H reference band) was used to monitor the extent of degradation during weathering (**Figure 3.15**).

Figure 3.16 compares the FTIR-transmission spectrum and FTIR-ATR spectrum for the unexposed unstablized (no UVA) water-borne system 8, measured (in transmission) at a depth of 5μm (1^{st} microtomed slice) and at the uppermost surface (not microtomed, full system for ATR), to determine if any differences between the two types of infra-red measurements for the purpose of PI (photoxidation index) calculation. It is clear that the differences in the spectra are only in the intensity of the peaks (due to the depth of penetration of the ATR crystal) and not in the position of the peaks.

Photoxidation index (PI) based on changes in the OH region (see section 2.6.4) was used for assessing the extent of degradation that took into account the level of erosion that may have occurred in the coating systems during weathering with the aid of the pictures of the weathered microtomed slices. **Table 3.6** and **Figure 3.17** show the ΔPI changes during accelerated exposures to CAM and SPART conditions measured using FTIR-ATR for the uppermost surface of the different coatings. It is clear that the CAM conditions give rise to higher extent of degradation in all systems compared to that of the SPART conditions (which contained acidified water cycles). It is also clear that the solvent-borne coating (system 3) is more stable than all the different water-borne systems examined here.

Depth profiling across the microtomed layers of the different coating systems (examined by FTIR transmission) is shown in **Figures 3.18-3.25**. Examination of the extent of degradation across the depth of the clear-coat under different weathering exposure regimes shows clearly that it is highest near the uppermost surface layers and decreases more slowly in the deeper layers of the clear-coat of all systems (**Figure 3.18**). Also it is shown that the solvent-borne systems 1 and 3 are more stable than the water-borne samples under all conditions examined, with the unstabilzed water-borne system 8 showing the highest levels of degradation (**Figure 3.19**). Changes in all coating systems examined due to weathering in the deeper layers were not very different (**Figures 3.20-3.24**).

3.3 Discussion

3.3.1 Effect of weathering on physical and optical properties of the coating systems

Optical microscopy is a quick and simple method for visually determining the occurrence of early changes on the surface appearance of coatings upon weathering, without the need for microtoming, however this method was shown to be only qualitative and selective [57]. The results (using system 6c as an example) showed that before weathering there were only very few defects on the surface whereas weathering resulted in the formation of defect regions (**Figure 3.5**) which may have been caused by

a number of factors: erosion of the top section of the clear-coat layer **[10]**, etching of the coating causing the formation of pits, in addition to the possible formation of water-spots on the surface of the coating. Optical microscopy could not be done for the water-borne system 10 as the coating for this system was silver and this would have reflected the light under the microscope, thus no changes would be seen after weathering. This shortcoming of the optical microscopy meant that it was not possible to determine the level or type of degradation that took place during the weathering of coating systems. Thus no conclusions could be made from the results obtained by this test method with respect to which coatings were more resistant to weathering or the nature of the changes that occur upon weathering of the coating systems.

Gloss measurements gave more conclusive results although for this to be representative several areas of each coating system needed to be analysed and an average was therefore taken (results were quoted to ± 0.5 gloss units in a 95% confidence limit (for details, see appendix A3.2.3). The gloss values in all systems dropped with exposure time (see **Figure 3.4**) due to increase in surface roughness caused by both erosion and chemical changes with degradation, and this would results in more light diffusion and hence diminishes the gloss **[1, 2, 53]**.

Outdoor exposures (in Miami), showed clear differences between the solvent-borne (e.g. system 3) and water-borne (e.g. system 8) clearcoats (**Figure 3.1, 3.26**) with the solvent-borne samples having higher gloss retention than their water-borne counterparts. This is most likely because the polymers in the solvent-borne clearcoats are more highly cross-linked and thus more resistant to weathering reactions. **Figure 3.3** confirms that for the unexposed solvent-borne system 3 a higher initial hardness is obtained compared to the water-borne clear-coat systems (6c and 8) which is certainly due to the higher initial level of cross-linking in the solvent-borne clear-coat.

It is important to point out here that within the water-borne coating samples, the silver coating (system number 10) showed the highest gloss retention (**Figure 3.26**). This is almost certainly due to the presence of reflective aluminium particles in the base-coat of this system which reflects the light hence resulting in less damage. It is also worth mentioning that temperature measurements carried out during Miami exposures for the silver coating showed clearly that the silver panels were up to 7°C cooler than the blue

coating panels (**Table 3.7**) which is again due to better reflection of the heat by the silver colour resulting in lower potential for gloss reduction. The remaining water-borne coatings were all blue and the differences in gloss between the samples were too small to be able to discriminate between their performance (**Figure 3.26**) and this clearly is a major drawback of this measurement technique.

The unexpected rise in gloss values under the Miami exposure conditions of the water-borne systems after 18 months (**Figure 3.26**) has been shown to be due to mildew which was seen on all outdoor weathered water-borne samples. This was removed by cleaning and polishing before any gloss measurements were made and has also been previously reported in the literature [**3, 57**]. However, it is interesting to see that this surface growth by mildew seems to protect the underlying coating layers from further weathering damage. Gloss values after 3000 hours of artificial accelerated CAM exposure were compared with values obtained after 23 months of natural Miami exposure (**Figure 3.26**). For a solvent-borne (3) and a water-borne (6c) system the Miami exposure gave less gloss retention compared to CAM exposure conditions whereas in the water-borne system, the Miami weathering resulted in a much greater reduction in gloss. The Miami weathering is believed [**46**] to give closer results to 'real life' as it is outdoors, in the harsh end service conditions of the coating. Overall, therefore, gloss measurements did offer a quick method of discriminating between the two types of clear-coats in terms of changes caused by weathering, but differences could not be seen between the different blue water-borne coatings. The advantage of the test is that it is non-destructive but samples needed to be exposed for a great many hours before any useful results could be obtained and also the mildew which is formed when exposure was done outdoors could cause further complications for the results.

The solvent-borne and water-borne coating systems showed also a major difference in terms of changes in their hardness during exposure. The solvent-borne system 3 gave rise to an increase in hardness, whereas the water-borne coatings decreased in hardness during exposure but again it was difficult to discriminate between the different water-borne clear-coat systems (**Figure 3.4**). During weathering of automotive clear-coats, two types of reactions can take place in the polymers: chain scission which reduces the hardness of the coatings and cross-linking, either within the polymer chains or between different polymer chains, which would result in an increase in the measured hardness.

Thus, it can be argued that the observed increase in hardness in the solvent-borne system 3 with weathering is most likely to be due to an increase in the extent of cross-linking and similarly the decrease in the case of the water-borne systems (6c and 8) suggest a dominance of chain scission reactions during weathering. This is supported by literature results which illustrate the clear competition between these two types of reactions **[53].** The disadvantage of the hardness test is in addition to being a destructive test, would normally require long periods of exposure before any differences in the behavior of the coatings can be observed. However, differences between the weathering responses of the different types of coatings could easily be seen (e.g. between the water-borne and solvent-borne systems) and therefore the hardness tests represented a useful tool.

An understanding of the existence of erosion in coating panels under weathering conditions is important to ensure that the clear-coat lasts for the required period of time. The level at which the different coatings lose film thickness upon weathering was assessed by counting the number of slices of clear-coat after the first base-coat slice (counting upwards) after exposure. It has been reported that film thickness loss rates change rapidly during the early stages of exposure, before slowing down to a level that will be sustained for the duration of the rest of the exposure period **[8, 2].** The lower extent of erosion observed in the solvent-borne coatings (e.g. system 3) is a further indication of its better resistance to weathering compared to the water-borne systems (**Figure 3.8**). The rotary and planar microtomes gave similar levels of erosion, however the slices produced were much larger from the planar microtome and the slices were less likely to be in the form of 'wedges', which happens when the small samples were positioned at a slight angle when mounted on the rotary microtome, thus the resultant slices could contain more than one coating layer when slices were microtomed in regions close to the interfaces between the different coating layers.

3.3.2 Degradation profiles due to weathering across the depth of the coating layers by spectroscopic characterisation

FTIR-ATR analysis was carried out on the surface of unmicrotomed full coating systems, before and after artificial accelerated weathering (CAM and SPART), and the

changes in photoxidation index (Δ PI) were monitored in a similar manner as to that reported in the literature **[5,7, 8, 10, and 57]**. The assumption here is that the long-term weathering performance of coatings is determined mainly by the coatings' ability to resist photodegradation **[12]**. The Δ PI measurements were therefore used to compare the photoxidation resistance of the different coating families **[8]** and is based on the accumulation of -OH, and NH photoxidation products (mainly hydro-peroxides, alcohols, carboxylic acids and amines), thus weathed samples would be expected to give rise to higher Δ PI values. The results were calculated to within ± 0.02 in a 95% confidence interval (appendix A-3.4.1).

Δ PI measurements were carried out using both FTIR-ATR and FTIR-Transmission (section 3.4.5.2), but the two were not directly compared because the relative intensities of the ATR spectra may not be in the same ratio as in the transmission spectra **[60]**, in spite of the fact that **Figure 3.16** did show that in these experiments the differences in the spectra were only in the intensity of the peaks (due to the depth of penetration of the ATR crystal) and not in position of the peaks. Factors that affect the FTIR-ATR spectra include the dependence of the depth of penetration on the wavelength and the imperfect contact between the ATR crystal and the sample which would bring about a reduction in the ATR absorption values. However software is now available that can be used to apply an 'ATR correction' between the two types of spectra [**9**].

Figure 3.17 shows (based on ATR results) that the CAM exposures clearly gave rise to much lower Δ PI in the solvent-borne clear-coats (systems 3 and 4) compared to the water-borne systems. This higher stability of the solvent-borne systems is almost certainly due to the more highly cross-linked clear-coat compared to the water-borne clear-coat systems. The two systems are cross-linked differently; the clear-coat of the solvent-borne systems is based on a 2K-solvent borne acrylic resin cross-linked with aliphatic poly isocyanate with cross-link density (CLD) which is higher than that of the water-borne based systems. The water-borne systems contained a clear-coat based on a 1K-aqueous isocyanate modified acrylic dispersion with melamine resins (acrylic-melamine) having overall a lower CLD, see **Chapter 2, Schemes 2.3 and 2.5**. It has previously been claimed that acrylated polyurethane dispersions can have good exterior durability **[87]**. Only very slight differences were also seen between the solvent-borne coatings, with system 4 being slightly more stable than 3 due to the UVA stabilizers

used here being cross-linkable **Figure 3.17.** Under CAM exposures, the most stable water-borne system was found to be system 7 which had three times the level of UVA compared to e.g. for system 6c. Systems 8 and 6c had reasonably similar results, whereas the least stable system was 9, containing the cross-linkable UVA.

The CAM and SPART exposures were compared and it was shown that CAM exposures resulted in a slightly higher Δ PI (**Figure 3.17**). The only difference between the two types of exposures was that the water in every fourteenth-twenty minute cycle was replaced with acidic water having a pH of 3.2. The effect of the acid on the clearcoat was to etch the surface of the clearcoat, causing pits to form, the water sprays in the cycle washed away the debris formed from the etching, thus revealing new, undamaged clearcoat, causing the observed lower Δ PI. ATR technique which is also a non-destructive method of measuring photoxidative changes in different chemical familes showed also differences between the different types of clearcoats. However, in this method, only the very top layer of the clearcoat could be examined but these uppermost layers may undergo further damage by erosion, and the technique cannot investigate the possibility of weathering-induced erosion in the coatings.

The ΔPI results from the transmission FTIR experiments were calculated to be ± 0.1 in a 95% confidence interval for the unexposed samples, however as the samples were exposed this value became about 0.2 (Appendix section A3.5), due to possible slight variations between weathering conditions. The Δ PI from transmission FTIR of the exposed coatings for all systems increased under all types of weathering exposures, see **Figures 3.18-3.24** due to the formation of various photoxidation products. Furthermore, a higher extent of changes occurred at the surface of the coatings due to both higher levels of exposure to damaging radiation on the surface which results in the occurrence of erosion (see section 3.4.4) (see changes in clear-coats in **Figures 3.20-21 and 3.24-24 C and D).** A major function of the clearcoat is to protect the underlying layers from damage, thus the clearcoat formulations contained UV-stabilising packages, resulting in little changes in the upper layers. The more efficiently stabilized the clearcoat is, the more protection it should give to the lower layers of the coating.

The FTIR results indicated that the solvent-borne and water-borne coatings may have reacted differently to weathering and could therefore have undergone different chemical

changes. The results from the previously discussed hardness tests (**Figure 3.4**) indicated that the solvent-borne coatings underwent more cross-linking after weathering whereas the water-borne coatings underwent more chain-scission. In order to further investigate the differences in the behaviour of the clearcoats of the coating systems, different areas of the FTIR spectra were examined in the water-borne system 8 and the solvent-borne system 3 before and after artificial accelerated (CAM) weathering. **System 8** was chosen for this analysis as this was the unstabilized coating system (with respect to UVA) and thus had shown the most weathering-induced changes. The main carbonyl region (integrated between 1795-1645 cm^{-1} with peaks centering at 1725 and 1698 cm^{-1} for esters and acids respectively) increased with weathering (see **Figure 3.27 for the reference area and 3.28A for results**) indicating the formation of oxidation products. (however the individual carbonyl groups were not determined). Similar changes were reported in the literature [**2, 3, and 10**] for automotive clear-coats after weathering. The alkane deformation peak (C-CH_3 deformation) centering at 1464 cm^{-1}, (integrated between 1481-1417 cm^{-1}) also increased during weathering, possibly due to an increase in the concentration of methyl groups after chain scission reactions (**Figure 3.28B**).

The peak at 1340 cm^{-1} (integrated between 1371-1307 cm^{-1}) was of importance (**Figure 3.28C**) as this peak was only seen in weathered samples. This peak may be indicative of the shearing off of the low molecular weight groups from the triazine ring of the melamine such as amine groups; this type of reaction (**see scheme 3.2**) has been previously reported in the literature [**2**]. The ester (C-O) absorbance at 1153 cm^{-1} (integrated between 1209-1116 cm^{-1}) increased with weathering (**Figure 3.28D**) and this may have resulted from the degradation of the urethane (**see scheme 3.3**). The C-O ether peak at 1080 cm^{-1} (integrated between 1117-1045 cm^{-1}) showed a clear decrease after weathering (**Figure 3.28E**), probably due to ether hydrolysis. The ether stretch has been shown to be very sensitive to photoxidation [**2, 3, and 10**]. This indicates hydrolysis of the cross-linked stucture as well as loss of the residual butoxy groups of the melamine resin (**see scheme 3.4**).

The same analysis was applied to the solvent-borne **System 3** (**Figure 3.29** for the reference area). The main carbonyl region, centred at 1726 and 1694 cm^{-1} (integrated between 1800-1600 cm^{-1}), **Figure 3.30A** did not show a great deal of change in the overall area. This may indicate that under weathering induced changes that either fewer

carbonyl reactions compared to the water-borne system have occurred in the carbonyl region or as many carbonyl products were formed as those that were broken. The peak at 1526 cm^{-1} was thought to be due to an increase in urethane groups (**Figure 3.30B**), indicating that cross-linking was occurring with weathering, this has also been observed in previous work [**9**]. The peaks at 1461 and 1453 cm^{-1} were ascribed to alkane deformation ($C\text{-}CH_3$), showed little change (**Figure 3.30C**). The ester C-O absorbance at 1151 cm^{-1} showed very little change with weathering (**Figure 3.30D, scheme 3.5**). Whereas, the ether (C-O) stretch at 1051 cm^{-1} showed a slight increase after weathering (**Figure 3.30E, Scheme 3.6**), this group absorption is known to be sensitive to photoxidation [**2, 3, 10**].

The transmission-FTIR results have therefore shown some differences in the mode of photoxidation of the solvent-borne System **3** and the water-borne System **8**. The analysis was thus further applied to the water-borne Systems **6c** (blue, stabilized with HALS and UVA) and **10** (silver, stabilized with HALS and UVA) to determine if further differences between these coating systems could be detected. All the clear-coats analysed showed area changes in the main carbonyl area (**Figure 3.31A**). It is clear that very little change occurred in system **3** due to the higher weathering resistance of this solvent-borne system. The water-borne systems on the other hand, showed clear increase in all their carbonyl oxidation products upon weathering with the water-borne system 10 giving the highest resistance level of weathering due to the base-coat being silver (rather than blue) reflecting the damaging incident radiation in addition to being cooler than the blue coating systems. System 8 showed the most increase as it contained no UVA stabilizer. However, as this region contained several different chemical groups, it was not possible to determine the individual group changes in these coatings. Similarly, the solvent-borne system 3 showed very little change in the alkane deformation (at 1460 cm^{-1}) region and ester C-O absorption (at 1153 cm^{-1}) confirming its greater resistance to photoxidation (**Figure 3.31D**). A major difference between the solvent-borne and water-borne systems is the presence of melamine in the clear-coat of the water-borne systems (no melamine is present in the solvent-borne systems) which has resulted in formation of amine groups (absorption at 1340 cm^{-1}) upon weathering due to degradation and chemical breakdown of the triazine ring of the melamine group resulting in the formation of low molecular weight species (**Scheme 3.2** and **Figure 3.31C**).

3.3.3 Overall summary of differences in weathering particularly with respect to the behaviour of solvent-borne and water-borne coatings

It is clear that the solvent-borne coating systems (e.g. system 3) performed better under all weathering conditions examined compared to all the water-borne systems (e.g. system 6c), see for example **Figure 3.22**. The clearcoat of the solvent-borne system (e.g. system 3) consisted of a solvent-borne acrylic resin cross-linked with aliphatic polyisocyanate, while the clearcoat of the water-borne systems (e.g. 6c) contained an aqueous isocyanate-modified acrylic dispersion with melamine resin. It is interesting to note that previous work on UV-cured polyurethane coatings has shown that a water-borne polyurethane can be substantially more resistant to weathering compared to analogous solvent-borne clearcoats [**87**]. However, when an acrylate monomer was introduced into the water-borne polyurethane, the clearcoat was found to be less resistant to weathering, possibly because of the more easily oxidized ether-bond on the acrylate functionality [**87**]. It is interesting to note the photo-oxidation index observed in the solvent-borne systems was very low, i.e. almost no oxidation in the deepest layers of the clear-coat, reflecting the high durability of this system due to the powerful protection by the clear-coat (**Figure 3.20**).

Differences in the extent of photodegradation were also observed in the different coloured coating systems (blue and silver) 6c and 10 for water-borne and 3 and 1 for solvent-borne. **Figure 3.32** shows clearly that the silver systems (solvent-borne 1 and water-borne 10) are most resistant to photodegradation compared to the equivalent blue systems (solvent-borne 3 and water-borne 6c respectively). Firstly, the silver basecoat contained aluminium particles that are able to reflect the radiation, thus reducing the extent of photodegradation. Secondly, the temperature of the exposed blue coating was higher, (32°C, 76°C were the average and maximum temperatures respectively, of the panel at 23 months Miami exposure) than that of the silver coating (30°C, 69°C), helping to accelerate the photoxidative reactions thus and giving rise to the observed higher extent of Δ PI change.

The concentration and the type of the UVA stabiliser used in the clearcoat would be expected to affect the weathering performance of the coating systems. **Figure 3.33** shows clearly that in the water-borne series, system 8 which has no UVA gave the

highest Δ PI, whereas system 7 which had three times the concentration of UVA compared to system 6c gave a slightly lower Δ PI value. Literature work supports the results of this work in that the use of UVA at higher concentrations in automotive coatings results in better resistance to weathering [**2, 57, and 87**]. The UVA in system 9 was of a cross-linkable type but this did not seem to have a significant effect on the Δ PI (**Figure 3.34**), compared to an equivalent level of a standard UVA (non cross-linkable). However, in the solvent-borne series, sample 4 containing the cross-linkable UVA gave lower Δ PI compared to sample 3 with the same level but of a standard UVA suggesting higher stability in the presence of cross-linkable UVA. The reason for this difference cannot be explained at present and further work will be required here.

Exposure up to 1000 hours under CAM and SPART conditions in both water-borne and solvent-borne systems (e.g. 3 and 6c) does not seem to show a great difference in the extent of photoxidation (**Figure 3.35**); This is in line with literature observations, where no FTIR spectral changes were seen in the presence of 'acid rain' [**2**]. The acid in the SPART regime would begin to etch the surface of the coatings, causing erosion and revealing new undamaged coating surfaces with the consequence being little change in the Δ PI with further weathering exposures.

The aim of the outdoor natural weathering in Miami, USA was to compare the effects with conditions used in conventional accelerated J1960 CAM weathering exposure. Miami exposures have been the benchmark for natural weathering testing and industrially accepted throughout the world. Miami has a sub-tropical environment with high levels of UV radiation, humidity and temperature when compared to European climates. However, the main disadvantage of outdoor weathering is that the exposure conditions can be unpredictable. **Figure 3.22** (for systems 3 and 6c) shows that the photodegradation profiles from Miami exposures were in good agreement with those from accelerated weathering. The wavelength range (of filtered xenon light) used in the CAM weathering exposures was similar to that of natural weathering [**47**], thus, the degradative pathways can be expected to be similar [**9**]. Consequently, CAM accelerated weathering exposures can give information about the extent of photodegradation at a much faster time scale compared to outdoor (e.g. Miami) weathering. However, Miami exposures give information about the effects of photodegradation in the actual end-use service environment of the automotive coatings.

Therefore, to design new coating systems it is advisable to use both accelerated weathering and outdoor weathering exposure tests.

The effects of using different microtome systems was examined and **Figure 3.25** shows that the results from both rotary and planar microtomes were reasonably close, the major differences being at the surface of the coatings or at higher exposure times. Section 3.3.2 discusses the differences seen in the samples produced from the different microtomes. Based on the results presented above it is clear that the use of FTIR-Transmission for analyzing microtomed coating slices was most useful for following up the extent of photoxidative changes in the different coating systems. It was possible to differentiate between the different coating systems with different exposure types, and the method allowed the investigation of all the layers, right down to the electro-coat. Even at just 1000 hours of accelerated exposure it was possible to measure the photoxidative changes in the different coating systems. However, the drawback is that this method is destructive and a considerable amount of time and skill are needed in the production of good microtomed slices.

Table 3.2 Percentage Gloss Retention for Natural Weathering (in Miami, USA).

System		Percentage Gloss Retention at Miami Exposure time/months				
		0 (June 2001)	6 (December 2001)	12 (June 2002)	18 (December 2002)	23 (May 2003)
1	Silver,solvent-borne	100	94	95	90	84
3	Blue, solvent-borne	100	-	93	-	85
4	Blue, solvent-borne	100	-	90	-	83
6c	Blue, water-borne	100	80	43	61	63
7	Blue, water-borne	100	79	48	60	55
8	Blue, water-borne (no UVA)	100	85	50	63	67
9	Blue, water-borne	100	86	47	54	54
10	Silver, water-borne	100	98	60	70	79

Table 3.3 Hardness load testing results of systems 3, 6c and 8 before and after 1000 h of artificial accelerated weathering (CAM and SPART) 1000 hours.

System	Exposure details	Load [N/mm²]	Percentage, % Hardness Change
3	Unexposed	162	100
	SPART 1000h	167	3
	CAM 1000h	167	3
6c	Unexposed	121	100
	SPART 1000h	101	-17
	CAM 1000h	107	-12
8	Unexposed	114	100
	SPART 1000h	102	-11
	CAM 1000h	109	-5

Table 3.4 Comparison of the determined level of erosion from photographs of microtomed (rotary and planar) samples **3, 6c, 8 and 10,** unexposed, and after artificial weathering (CAM and SPART) and natural weathering (Miami).

System 3				
	Rotary Microtome		Planar Microtome	
CAM Exposure/h	Primer/electrocoat interface/µm (slice number)	Extent of erosion/ µm	Primer/electrocoat interface/µm (slice number)	Extent of erosion/ µm
0	82.5 (17)	0	82.5 (17)	0
1000	87.5 (18)	0	-	-
2000	82.5 (17)	0	77.5 (16)	5
4000	77.5 (16)	5	77.5 (16)	5
SPART 1000	87.5 (18)	0	-	-
23 months Miami	87.5 (18)	0	92.5 (19)	0

System 6c				
	Rotary Microtome		Planar Microtome	
CAM Exposure/h	Basecoat 1/electrocoat interface/µm (slice number)	Extent of erosion/ µm	Primer/electrocoat interface/µm (slice number)	Extent of erosion/ µm
0	67.5 (14)	0	67.5 (14)	0
1000	67.5 (14)	0	-	-
2000	62.5 (13)	5	62.5 (13)	5
4000	57.5 (12)	10	-	-
SPART 1000	62.5 (13)	5	-	-
23 months Miami	62.5 (13)	5	57.5 (12)	10

System 8		
	Rotary Microtome	
CAM Exposure/h	Basecoat 1/electrocoat interface/µm (slice number)	Extent of erosion/ µm
0	72.5 (15)	0
1000	67.5 (14)	5
2000	62.5 (13)	10
4000	57.5 (12)	15
SPART 1000	62.5 (13)	10
23 months Miami	62.5 (13)	10

System 10				
	Rotary Microtome		Planar Microtome	
CAM Exposure/h	Basecoat 1/electrocoat interface/µm (slice number)	Extent of erosion/ µm	Basecoat 1/electrocoat interface/µm (slice number)	Extent of erosion/ µm
0	67.5 (14)	0	72.5 (15)	0
1000	62.5 (13)	5	-	-
2000	62.5 (13)	5	62.5 (13)	10
4000	57.5 (12)	10	-	-
SPART 1000	62.5 (13)	5	-	-
23 months Miami	62.5 (13)	5	-	-

Rotary icrotome		Planar Microtome	
Level of erosion in **2000** hours of artificial accelerated (CAM) weathering		Level of erosion in **2000** hours of artificial accelerated (CAM) weathering	
System	Extent of erosion/ µm	System	Extent of erosion/ µm
3 SB - blue	0	3	5
6c WB - blue	5	6c	5
8 WB - blue	10	-	-
10 WB - silver	5	10	10

Table 3.5 Main differences between the FTIR spectra of systems **3 and 8**, across the depths of the systems.

System 3 (Solvent-borne Clearcoat)				System 8 (Water-borne clearcoat)			
Peak / cm^{-1}	**Intensity**	**Assignment**	**Layer details**	**Peak / cm^{-1}**	**Intensity**	**Assignment**	**Layer details**
1730	Strong	C=O Ester	Strongest in clearcoat	1727	Strong	C=O Ester	Decrease in electrocoat
1699	Strong	C=O Acid	Clearcoat only				
1600	Medium	N-H Bend	Forms in electrocoat only	1600	Medium	N-H Bend	Forms in electrocoat only
1544	Medium	N-H Triazine - symmetric	Primer only	1552	Medium	N-H Triazine - symmetric	Not in electrocoat
1525	Strong	Combination bands of NH deformation stretch and CN stretch	Forms in electrocoat	1525	Strong	Combination bands of NH deformation stretch and CN stretch	Forms in electrocoat
1464	Medium	$-CH_3$ Antisymmetric deformation	Not in electrocoat	1464	Medium	$-CH_3$ Antisymmetric deformation	Not in electrocoat
1415	Weak	Combination bands of NH deformation stretch and CN stretch	Primer and electrocoat				
1370	Weak	-(CO)- Ester symmetric stretch	Strongest in primer	1380	Medium	-(CO)- Ester symmetric stretch	Decreases from clearcost
1305	Medium	Combination bands of NH deformation stretch and CN stretch	Electrocoat mainly	1349	Weak	N-H amine	Electrocoat mainly
				1241	Strong	C-N Amine	Not in clearcoat, start basecoat 2
				1153	Medium	C-O Stretch ester	Not in electrocoat
				1080	Weak	C-O-C acyclic ether	Strongest in Clearcoat
				1020	Medium	C-N Amine	Clearcoat and EC only
832	Medium	-(C-O)-C Ether symmetric stretch	Increases in electrocoat	832	Medium	C-O- Ether symmetric stretch	Increases in electrocoat
769	Weak	C-H stretch	Decreases after clearcoat				
				702	Medium	C-H stretch	Decreases after clearcoat

Table 3.6 FTIR ATR PI results for systems 3, 4, 6c, 7, 8 and 9 for artificial accelerated weathering (CAM and SPART), where; $\Delta PI_{OH} = \Delta PI_{OH\ t=t} - \Delta PI_{OH\ t=0}$.

FTIR ATR Analysis					
System	Exposure Time/hours	SPART Exposure		CAM Exposure	
		PI	Δ PI	PI	Δ PI
3	0	0.32	0	0.32	0
	333	0.34	0.02	-	-
	666	0.4	0.08	-	-
	1000	0.41	0.09	0.58	0.26
4	0	0.34	0	0.34	0
	333	0.38	0.04	-	-
	666	0.43	0.09	-	-
	1000	0.44	0.1	0.57	0.23
6c	0	0.41	0	0.41	0
	333	0.57	0.16	0.58	0.17
	666	0.59	0.18	0.69	0.28
	1000	0.59	0.18	0.75	0.34
7	0	0.43	0	0.43	0
	333	0.49	0.06	0.56	0.13
	666	0.55	0.12	0.65	0.22
	1000	0.57	0.14	0.71	0.28
8	0	0.39	0	0.39	0
	333	0.54	0.15	0.65	0.26
	666	0.62	0.23	0.68	0.29
	1000	0.57	0.18	0.77	0.38
9	0	0.41	0	0.41	0
	333	0.52	0.11	0.67	0.26
	666	0.56	0.15	0.68	0.27
	1000	0.6	0.19	0.75	0.34

Table 3.7 Temperature differences of panels weathered in Miami, USA

Miami Summer season, 2003	Temperature of blue panel/°C	Temperature of silver panel/°C	Temperature difference between blue and silver panels/°C
Average air temperature	26	26	0
Average panel temperature	32	30	2
Maximum panel temperature	76	69	7

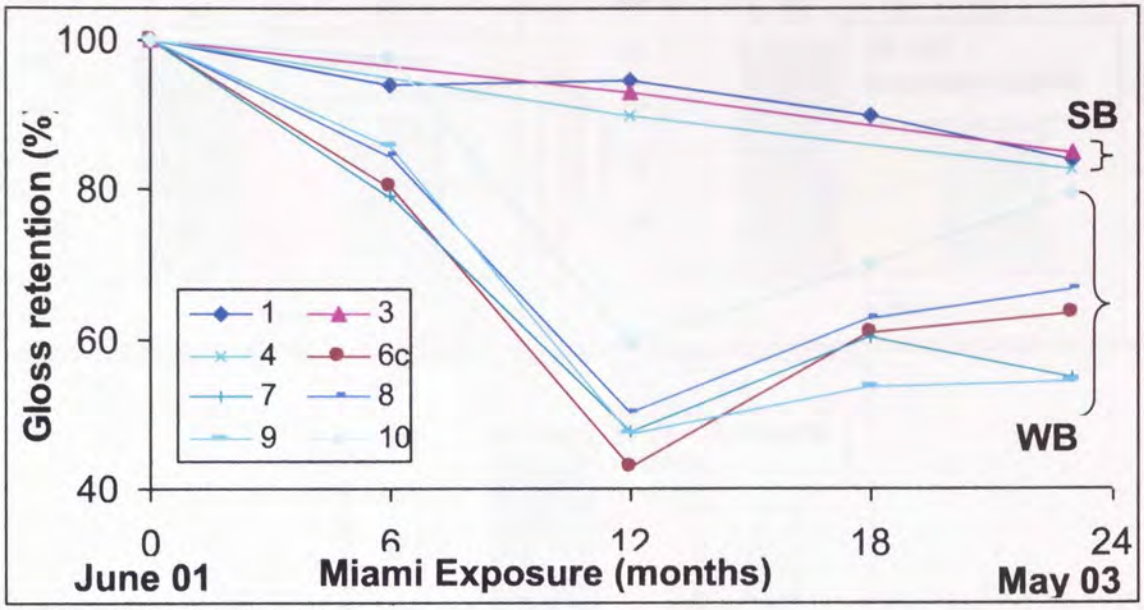

Figure 3.1 Percentage Gloss retention for natural weathering (in Miami, USA).

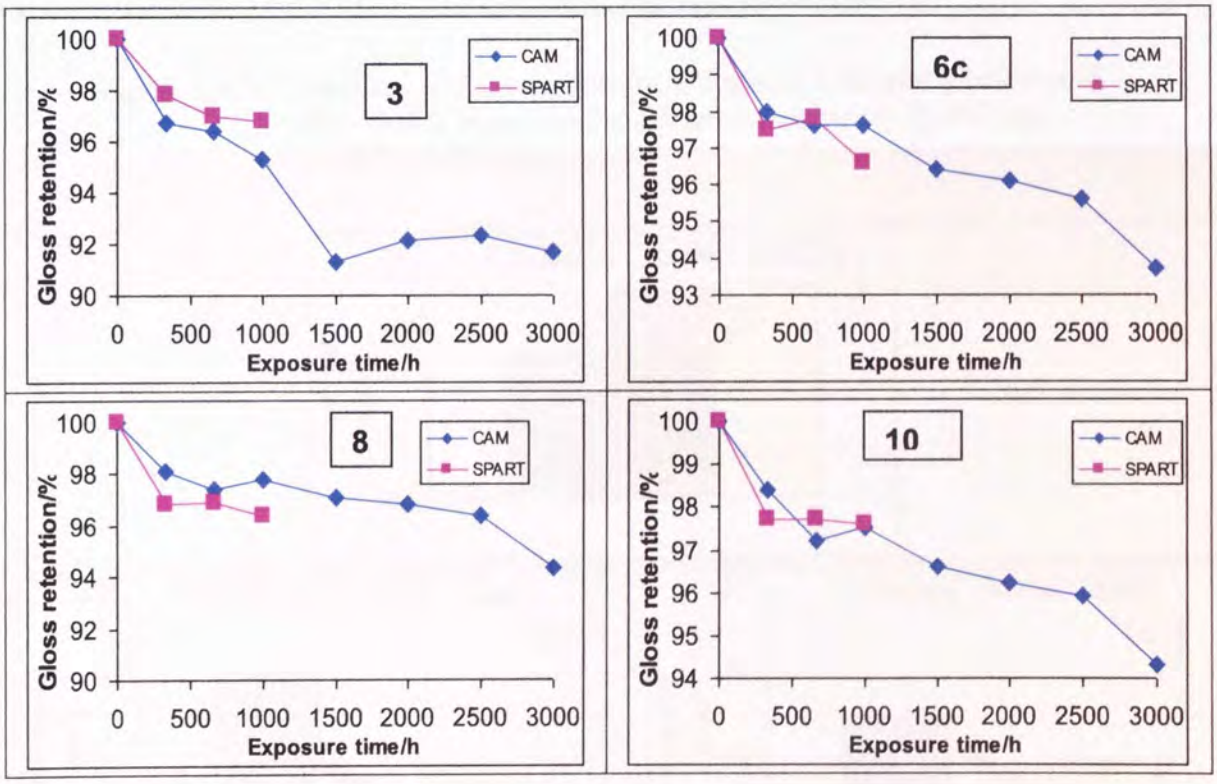

Figure 3.2 Comparison of gloss retention for automotive coatings **systems 3, 6c, 8 and 10** under accelerated artificial exposure (CAM and SPART) conditions in an Atlas Weatherometer.

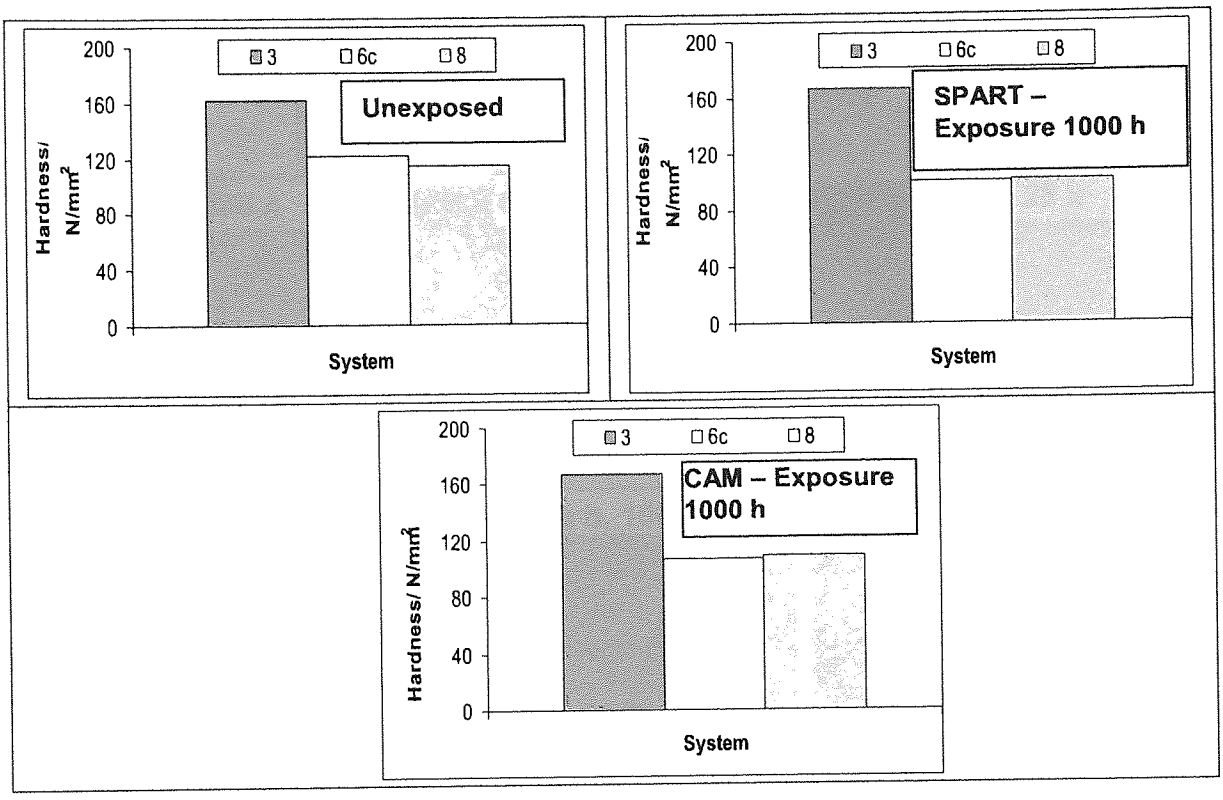

Figure 3.3 Hardness load testing results of **systems 3, 6c and 8** before and after 1000 h of artificial accelerated weathering (CAM and SPART) 1000 hours.

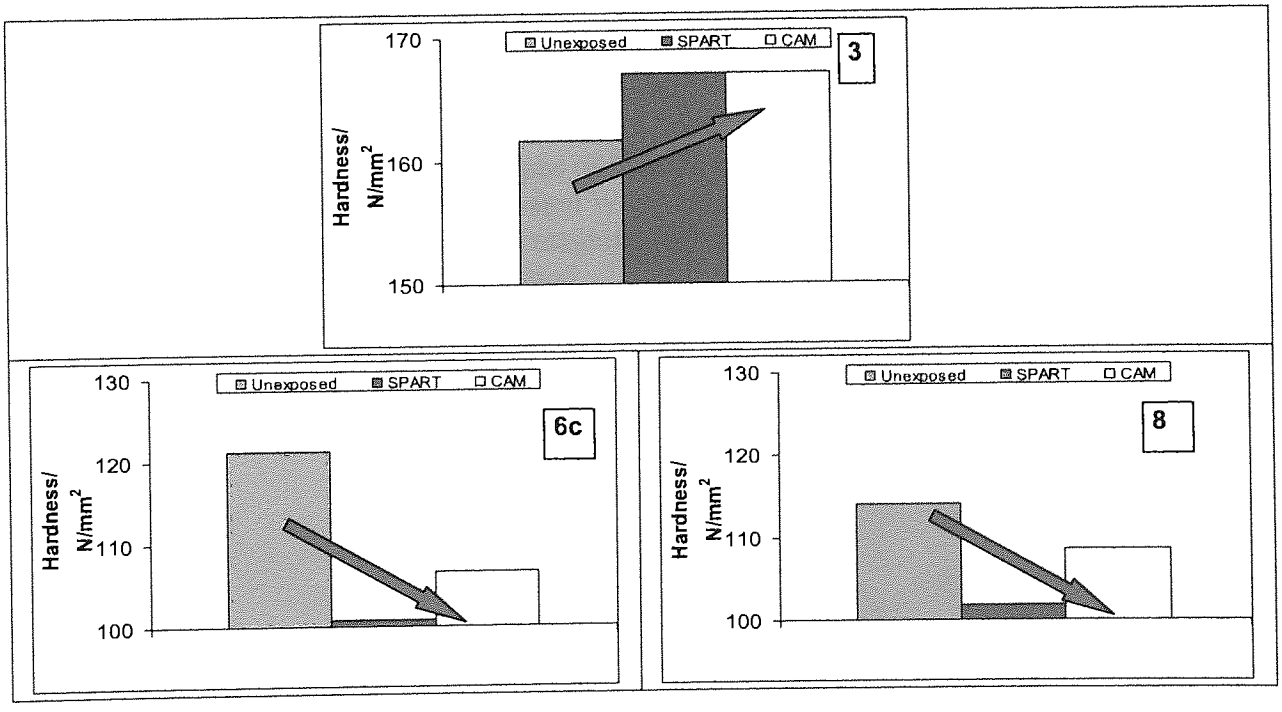

Figure 3.4 Hardness load testing results of systems 3, 6c and 8 before and after 1000 h of artificial accelerated weathering (CAM and SPART) 1000 hours.

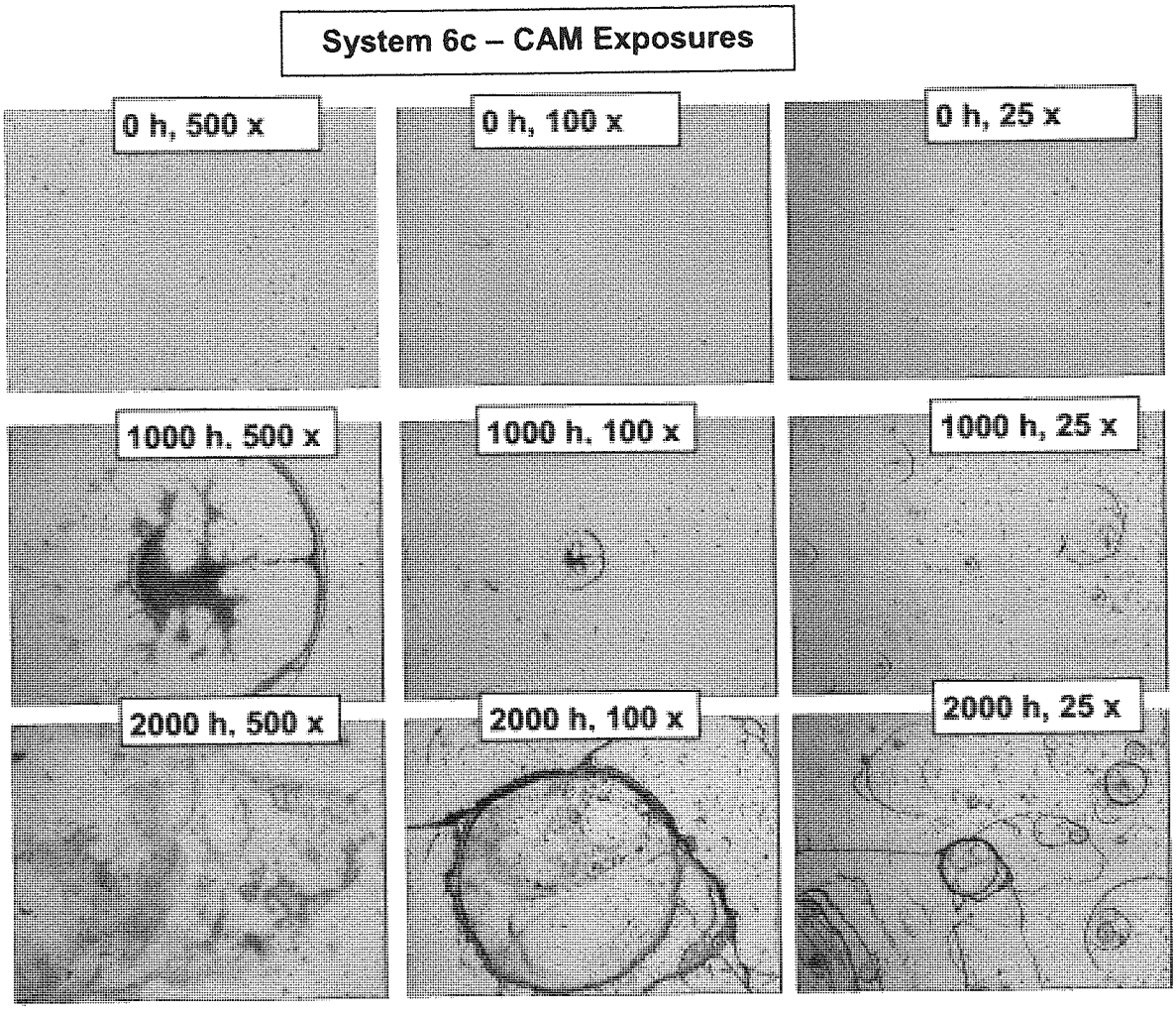

Figure 3.5 Optical micrographs of **System 6c**, unexposed and with Artificial Accelerated Weathering (CAM), after 1000 and 2000 hours using magnifications of 500, 100 and 25 for each exposure period.

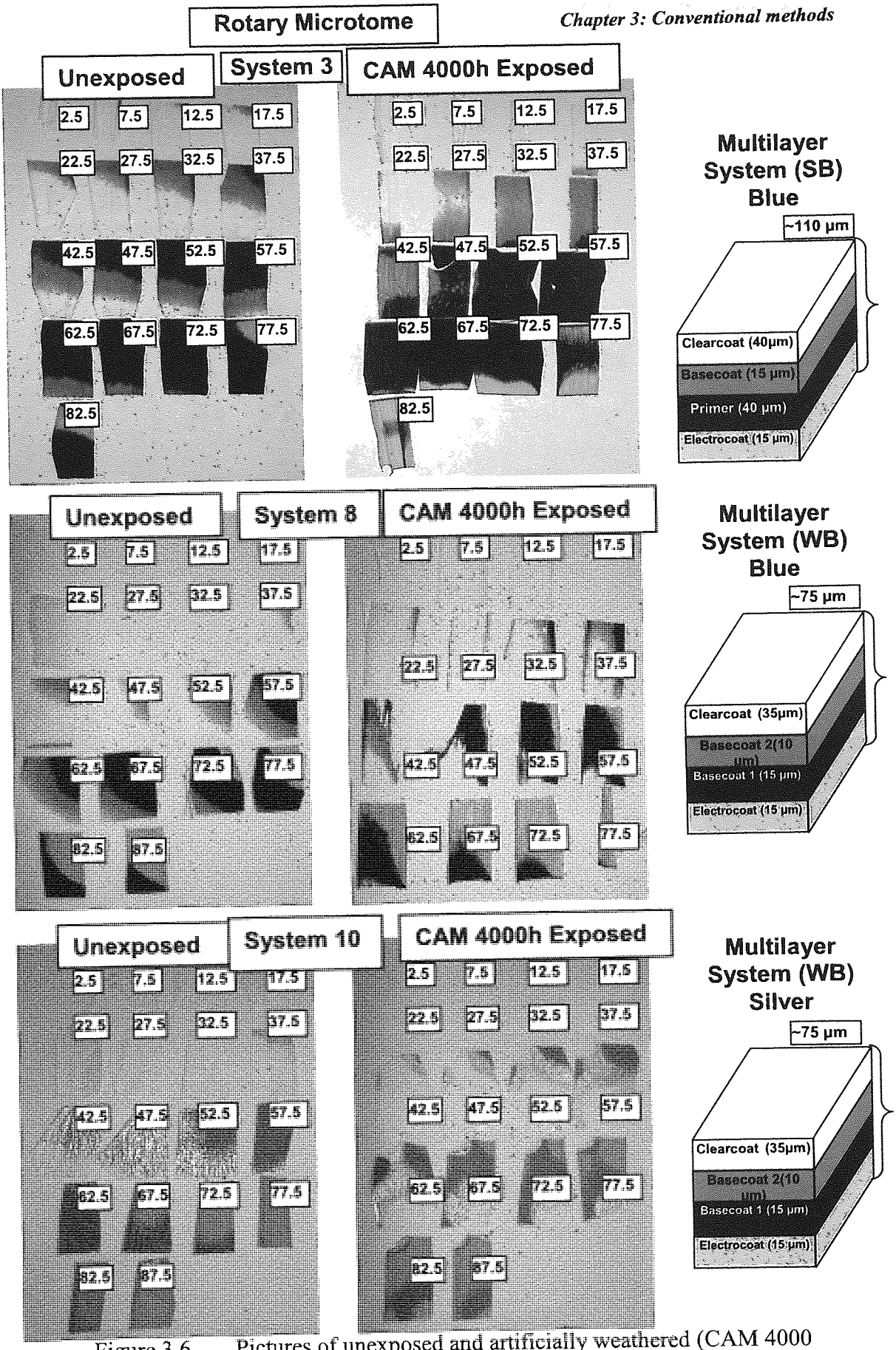

Figure 3.6 Pictures of unexposed and artificially weathered (CAM 4000 hours) microtomed (5µm thick) slices, systems 3 (SB), 8 and 10 (both WB), produced on a rotary microtome. Numbers on slices are the nominal depths in µm.

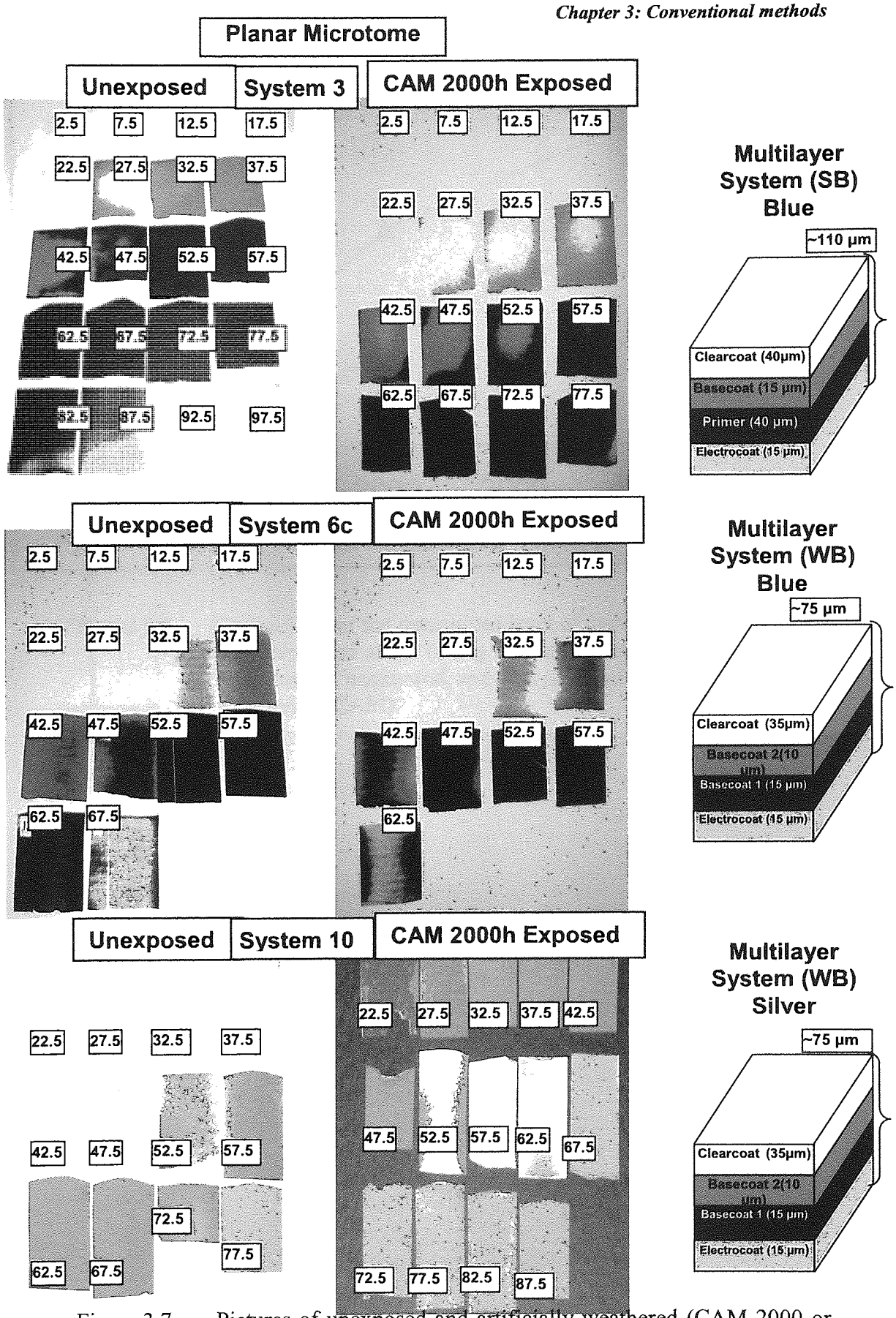

Figure 3.7 Pictures of unexposed and artificially weathered (CAM 2000 or 4000 hours) exposed microtomed (5µm thick) slices of systems 3 (SB), 6c and 10 (both WB), produced on a planar microtome. Numbers on slices are the nominal depths in µm.

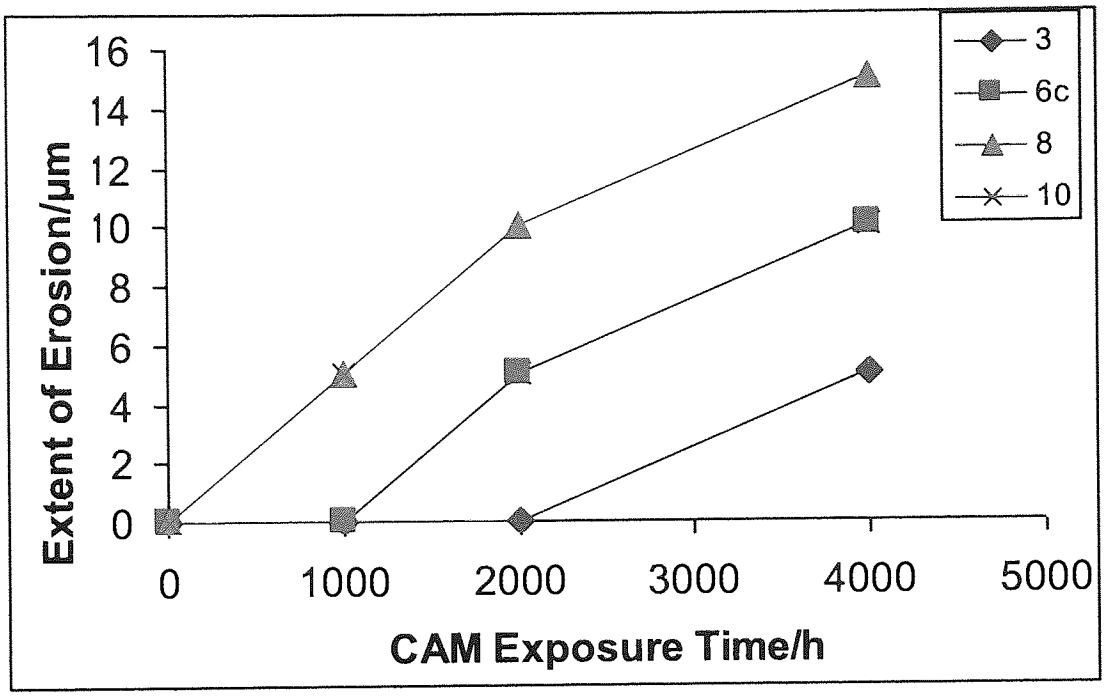

Figure 3.8 Comparison of the determined level of erosion from photographs of microtomed slices (using a rotary microtome) of samples **3, 6c, 8 and 10**, unexposed, and after artificial accelerated weathering (CAM).

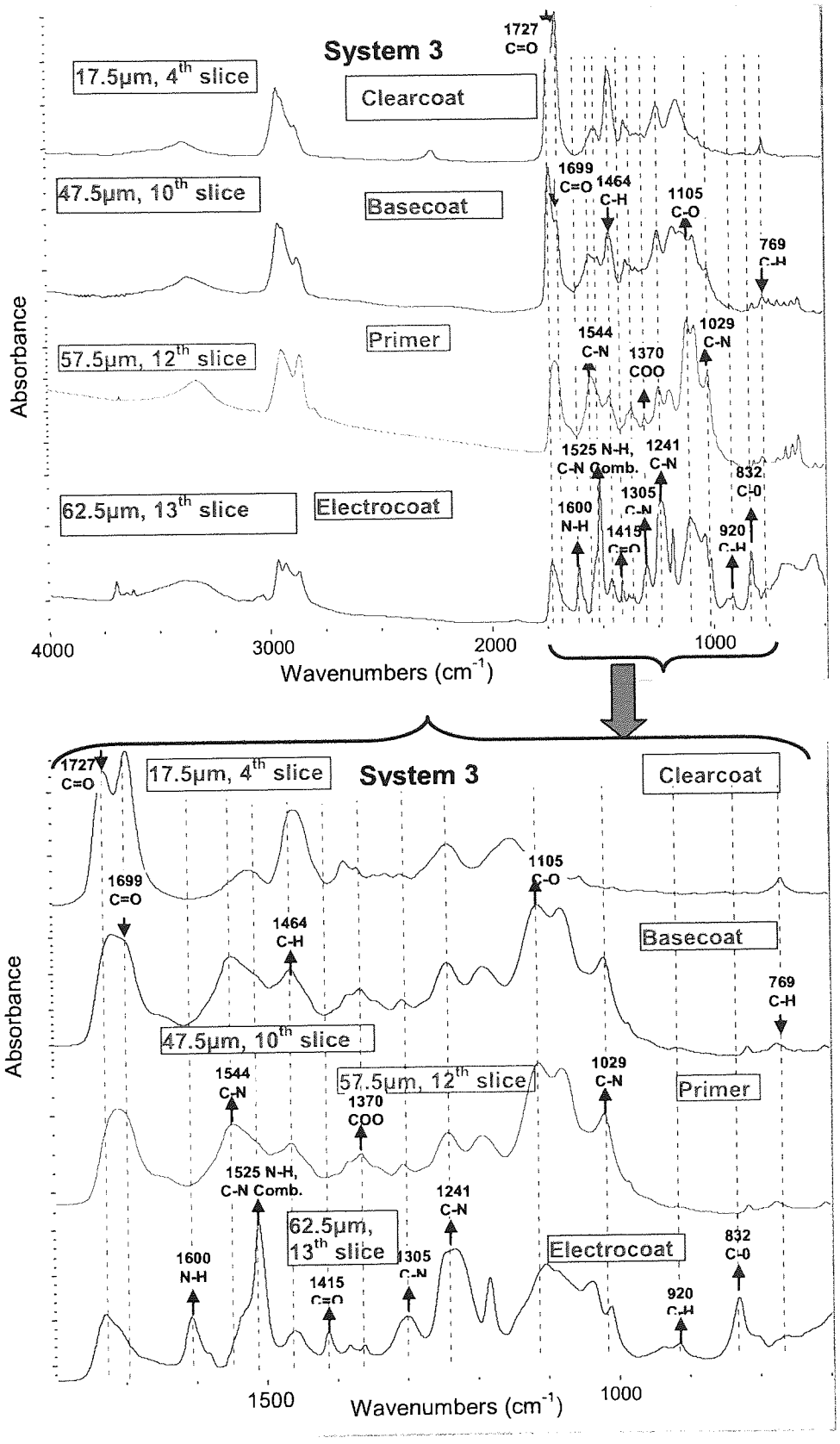

Figure 3.9 FTIR transmission spectra of the microtomed layers of unexposed **system 3**, the depths are the nominal layer depths.

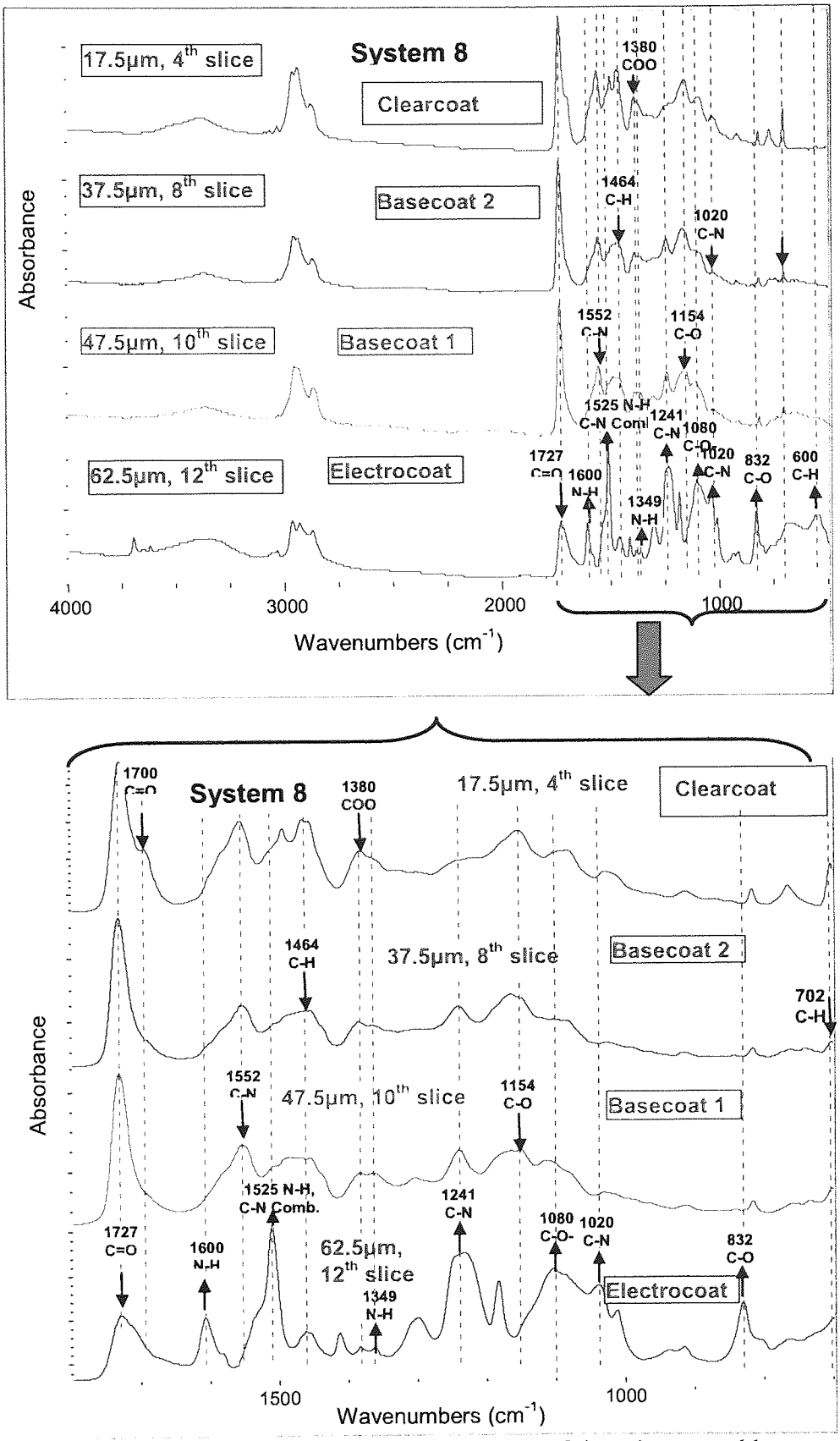

Figure 3.10 FTIR transmission spectra of the microtomed layers of the unexposed **system 8**, the depths are the nominal layer depths.

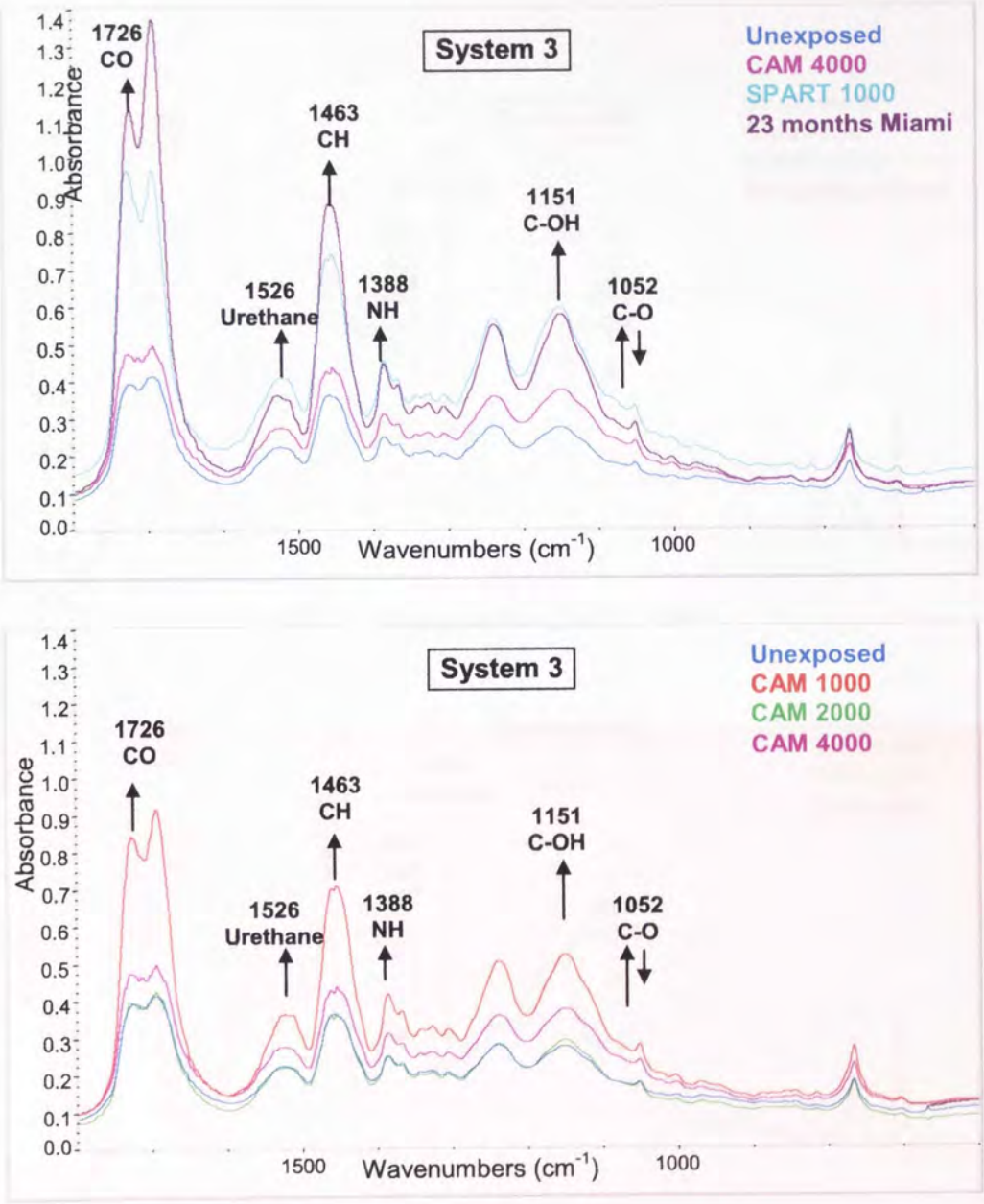

Figure 3.11 FTIR transmission spectra of the 4th microtomed slice (17.5 µm) of the solvent-borne **system 3** unexposed and after artificially accelerated weathering (CAM or SPART) or natural weathering (in Miami).

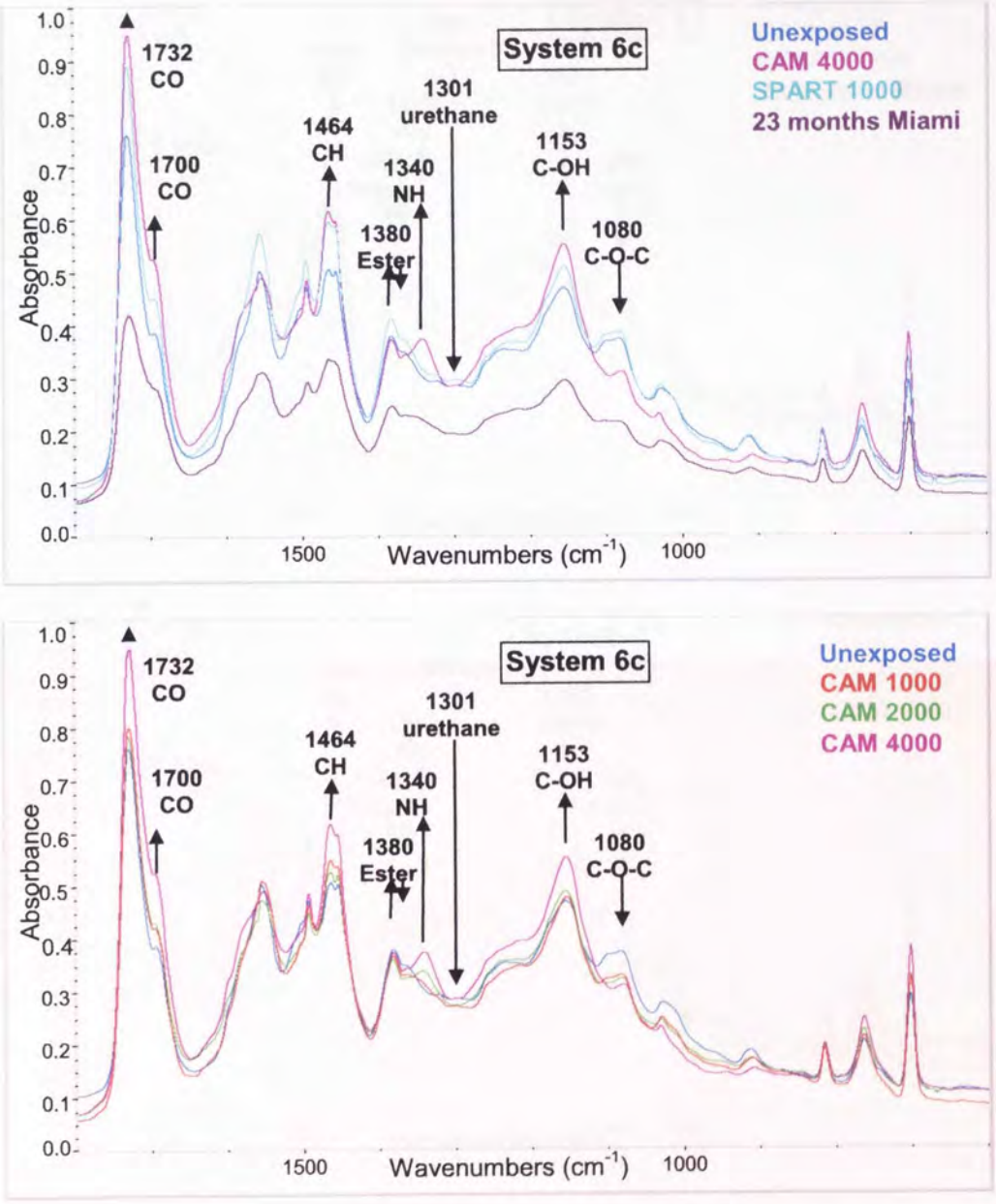

Figure 3.12 FTIR transmission spectra of the 4th microtomed slice (17.5 μm) of the water-borne **system 6c** unexposed and after artificially accelerated weathering (CAM or SPART) or natural weathering (in Miami).

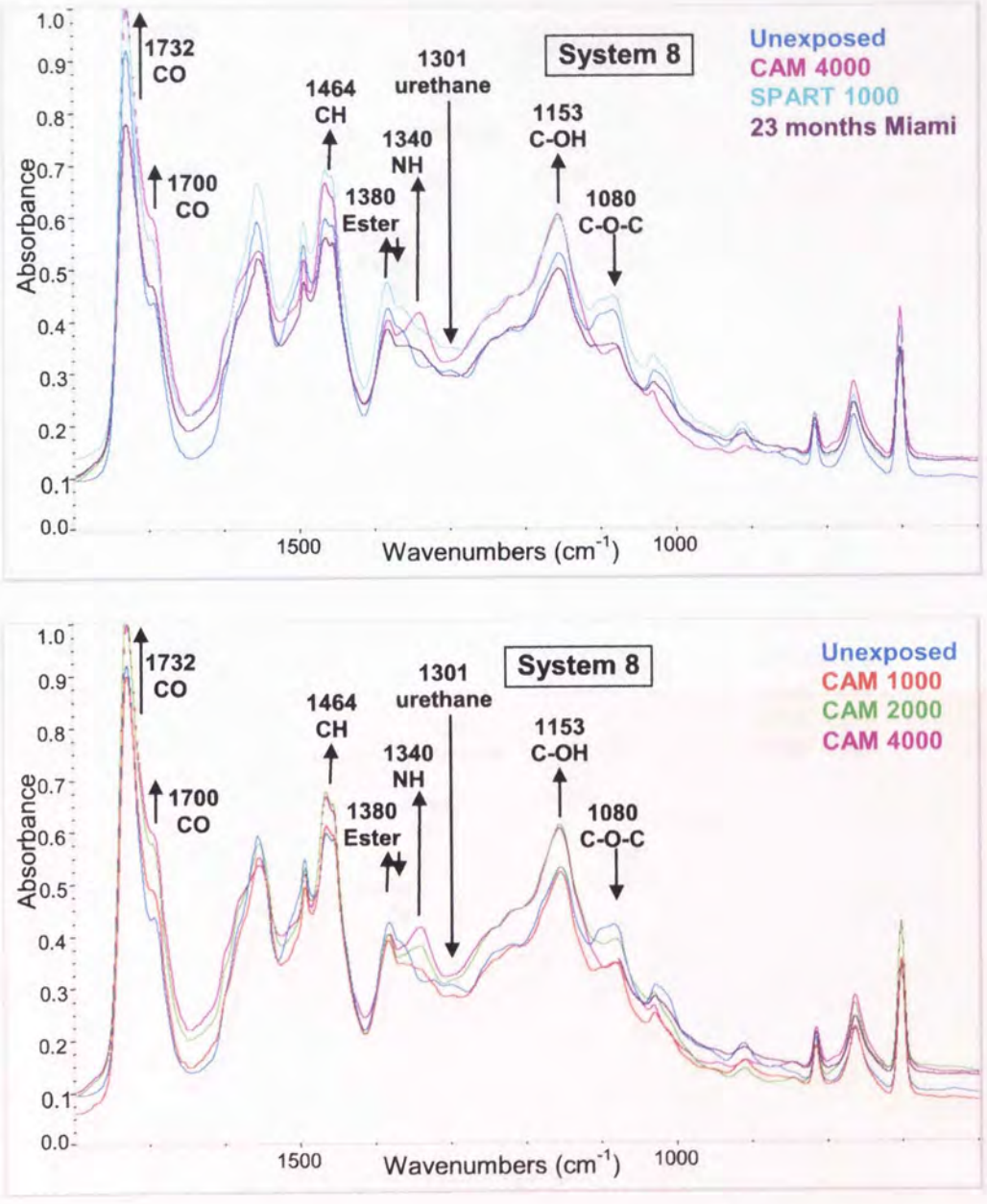

Figure 3.13 FTIR transmission spectra of the 4th microtomed slice (17.5 μm) of the water-borne **system 8** unexposed and after artificially accelerated weathering (CAM or SPART) or natural weathering (in Miami).

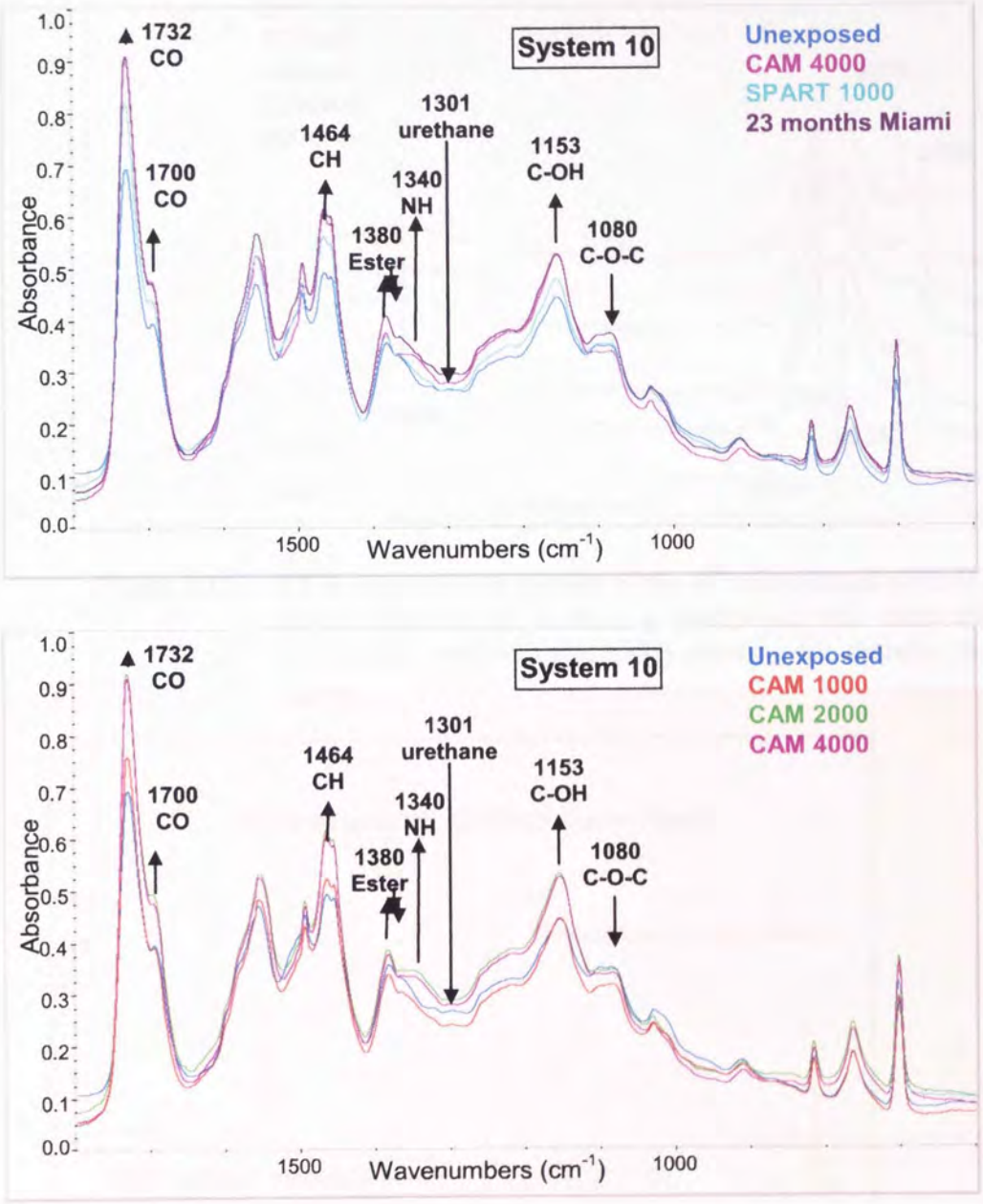

Figure 3.14 FTIR transmission spectra of the 4th microtomed slice (17.5 μm) of the water-borne **system 10** unexposed and after artificially accelerated weathering (CAM or SPART) or natural weathering (in Miami).

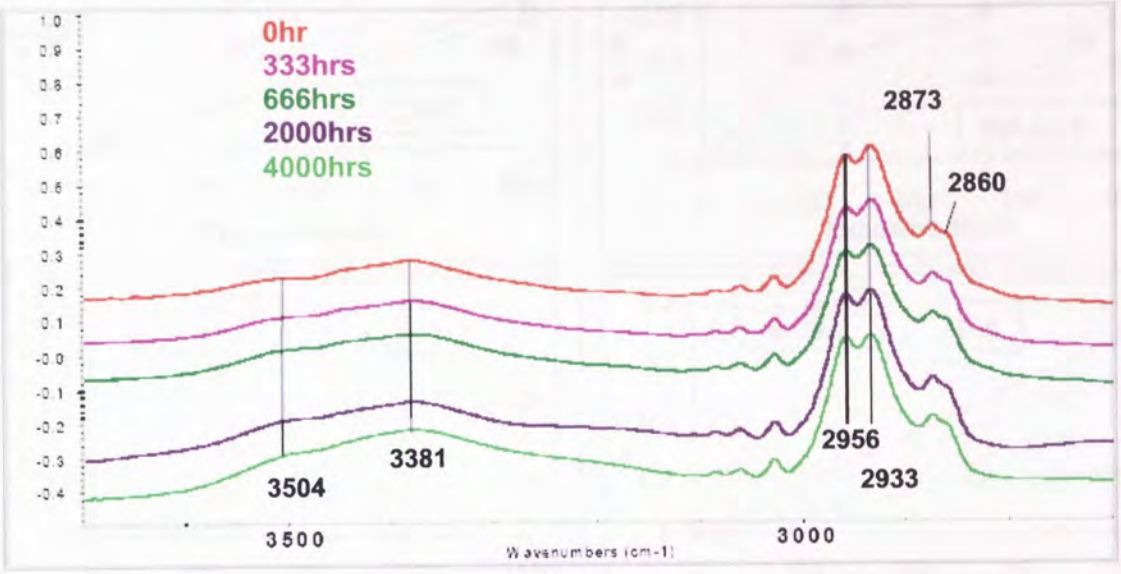

Figure 3.15 FTIR transmission spectra of the 4th microtomed slice (17.5 µm) of the water-borne **system 8** unexposed and after artificially accelerated weathering (CAM) showing the changes in the OH region.

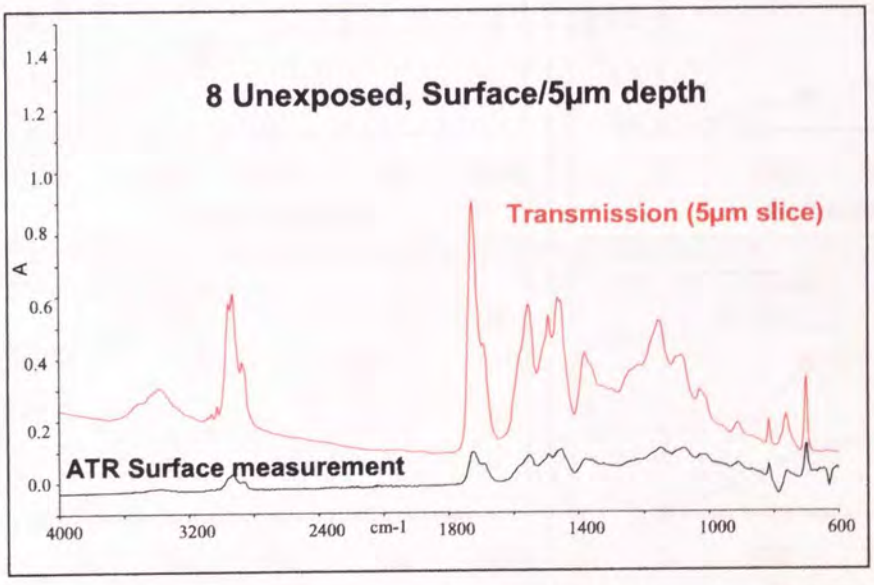

Figure 3.16 FTIR transmission, FTIR ATR spectra of the waterborne **system 8**, unexposed at a nominal depth of 7.5µm (microtomed) and surface measurement (unmicrotomed, full system), respectively.

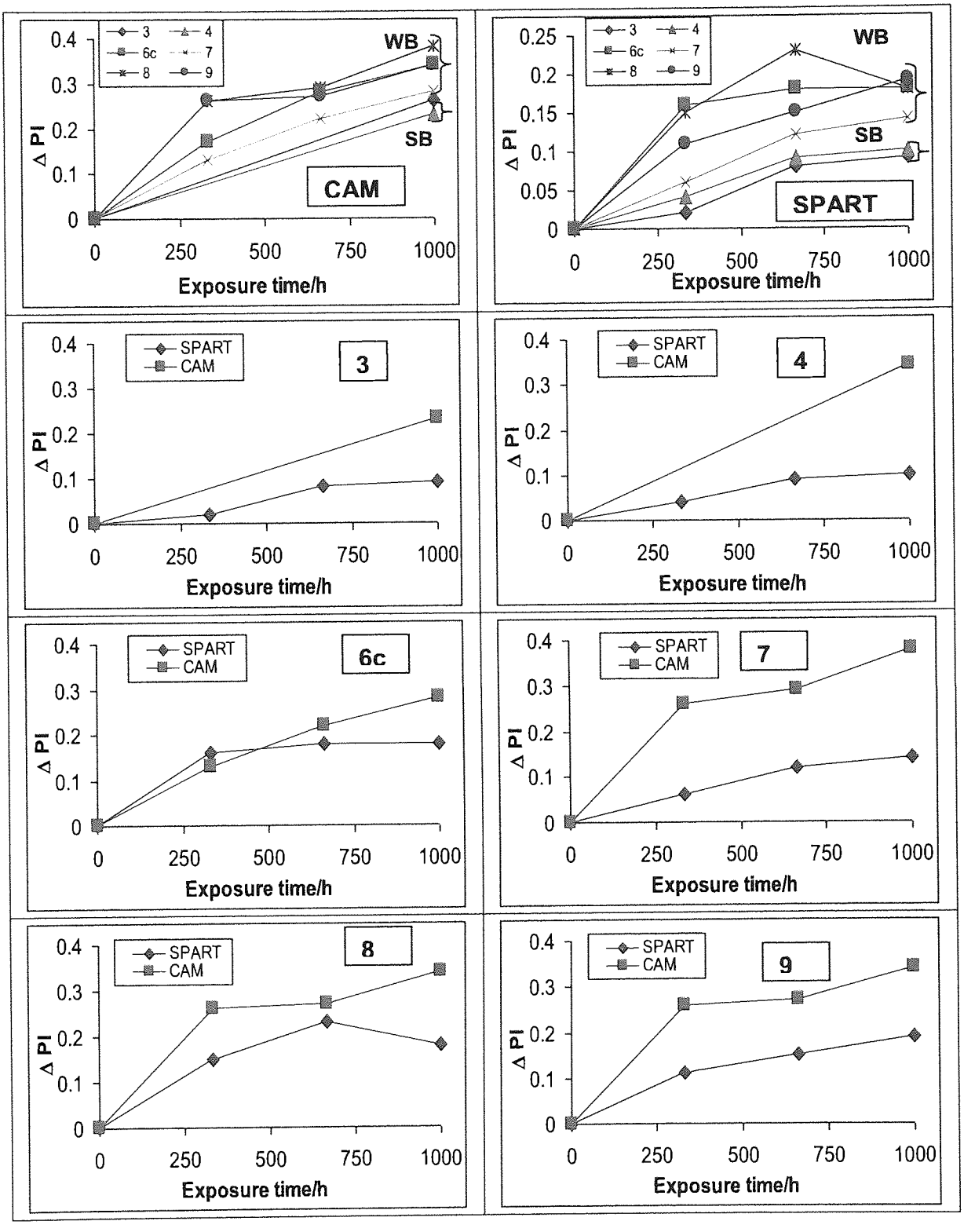

Figure 3.17 FTIR ATR PI results for the uppermost surfaces systems **3, 4, 6c, 7, 8 and 9** unexposed and after artificial accelerated weathering (CAM and SPART), where; $\Delta PI_{OH} = \Delta PI_{OH\ t=t} - \Delta PI_{OH\ t=0}$.

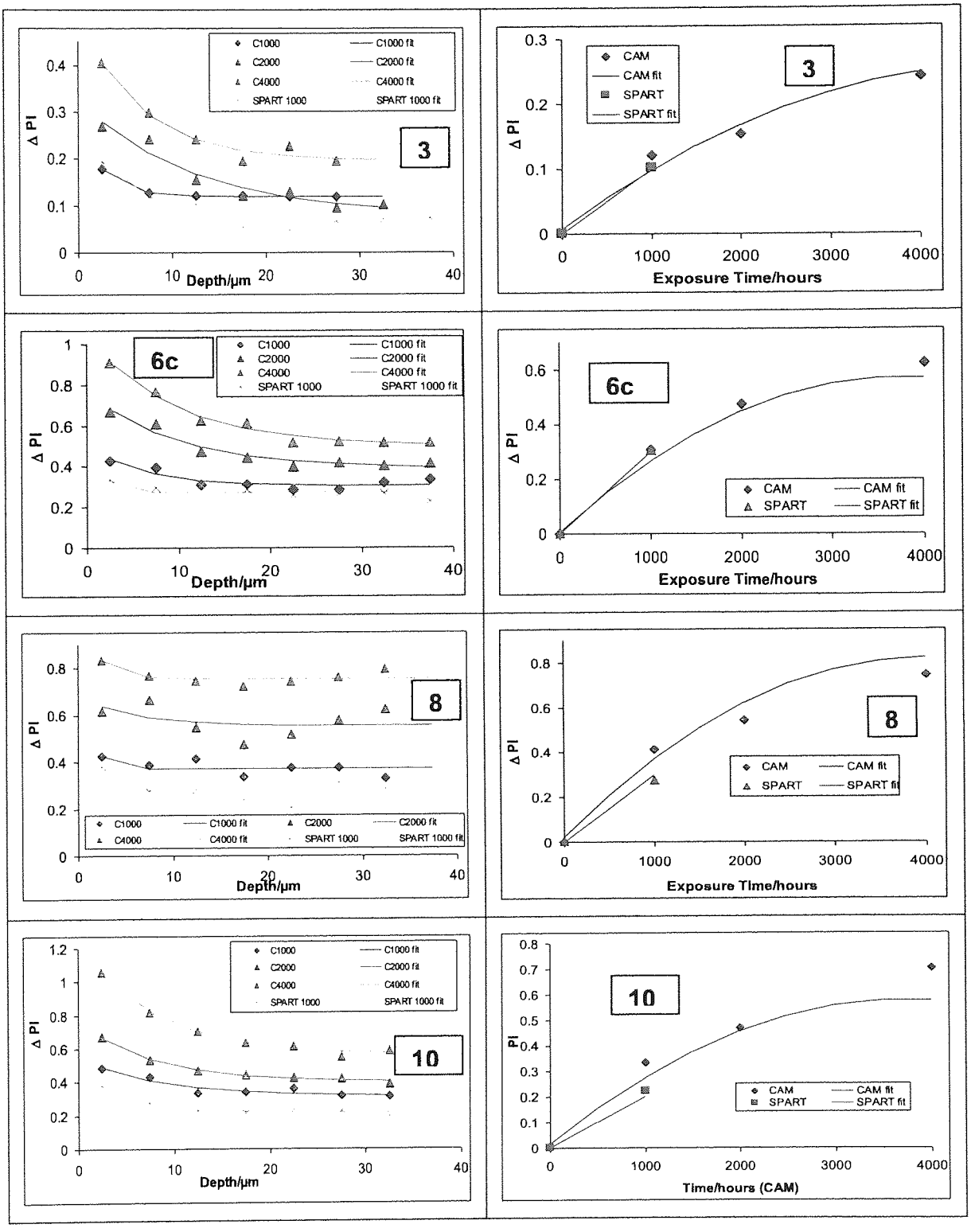

Figure 3.18 Planar microtomed, ΔPI results for **Systems 3, 6c, 8 and 10**, for artificial weathering (CAM and SPART), where;

$\Delta PI_{OH} = \Delta PI_{OH\ t=t} - \Delta PI_{OH\ t=0}$

and, Calc ΔPI_{OH} = data for clearcoat fitted to an exponential equation.

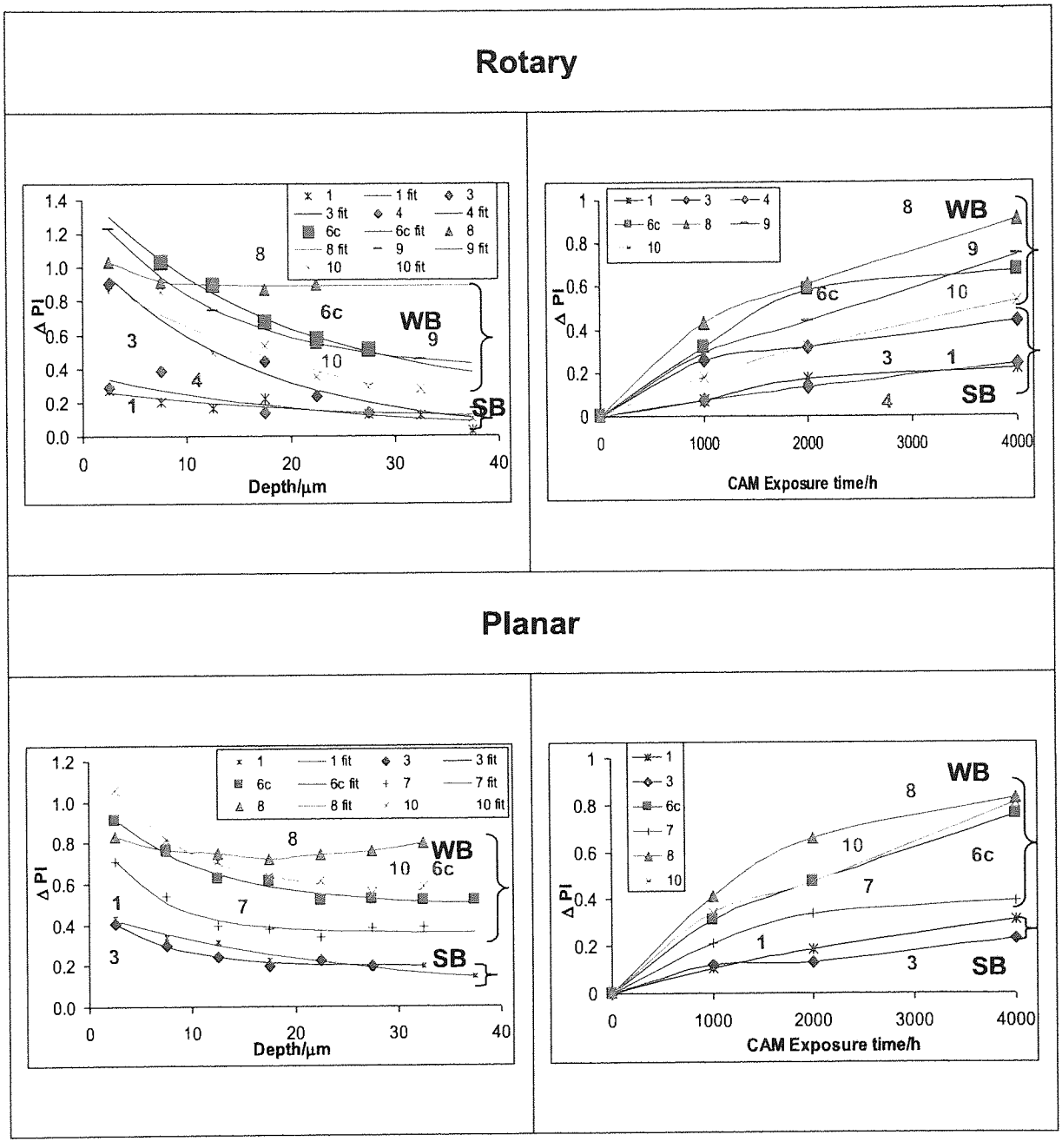

Figure 3.19 Comparison of rotary planar microtomed ΔPI data for accelerated artificial exposure (CAM) for **Systems 1, 3, 4, 6c, 8, 9 and 10,** for chemical changes with exposure time, and chemical changes with depth at CAM 4000 hours exposed.

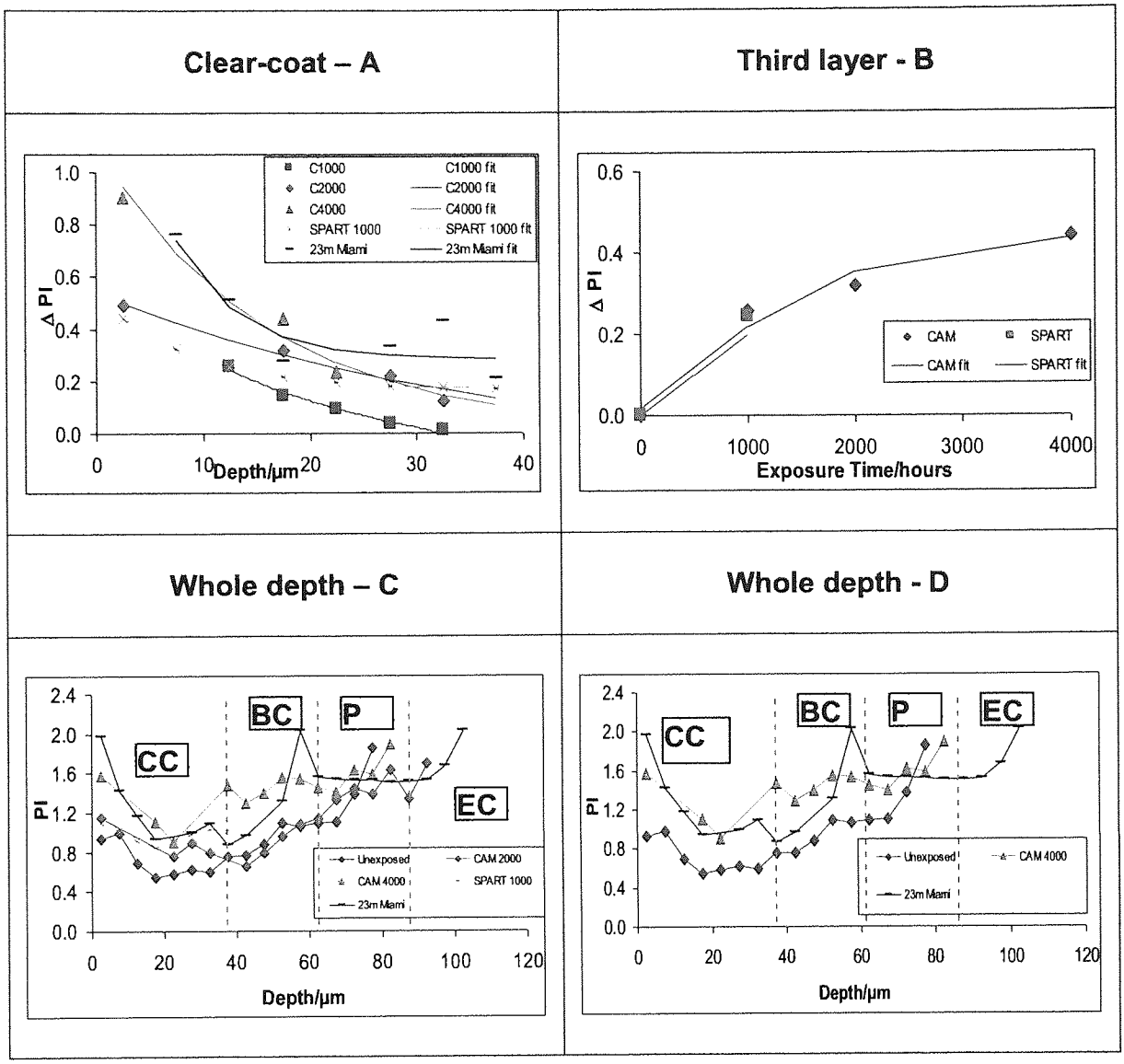

Figure 3.20 Depth profiling showing rotary microtomed PI changes in **System 3** under natural weathering (Miami) and artificial weathering (CAM and SPART), where;

$\Delta PI_{OH} = \Delta PI_{OH\ t=t} - \Delta PI_{OH\ t=0}$.

The points are the experimentaldata and lines are calculated from curve fitting, see section 2.6.4.

A ΔPI_{OH} changes across the depths of the coating with weathering

B ΔPI_{OH} changes with weathering of the 3rd clear-coat slice

C, D PI raw data changes across the depths of the coating with weathering.

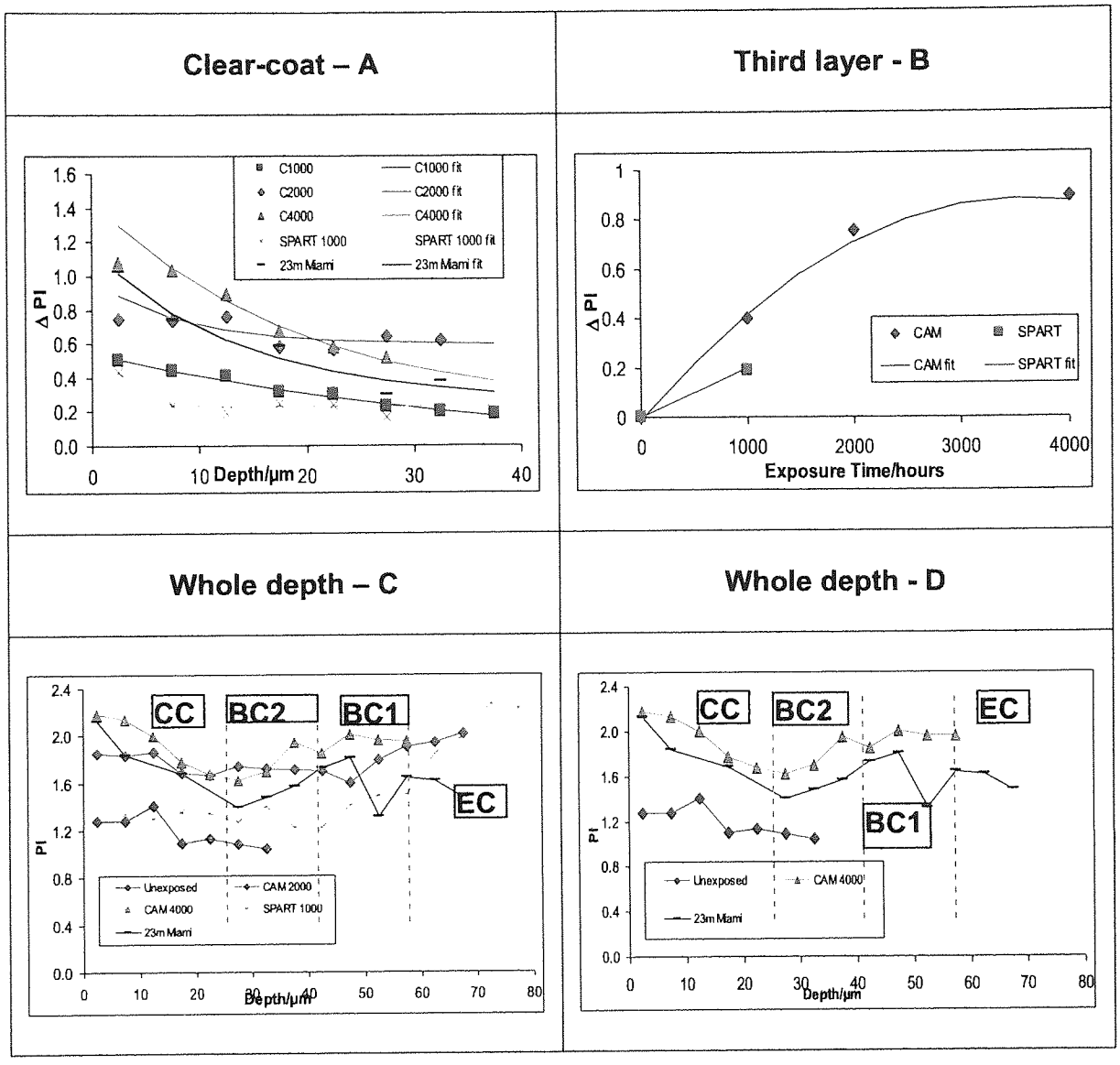

Figure 3.21 Depth profiling showing rotary microtomed PI changes in **System 6c** under natural weathering (Miami) and artificial weathering (CAM and SPART), where;

$\Delta PI_{OH} = \Delta PI_{OH\ t=t} - \Delta PI_{OH\ t=0}$.

The points are the experimentaldata and lines are calculated from curve fitting, see section 2.6.4.

A ΔPI_{OH} changes across the depths of the coating with weathering

B ΔPI_{OH} changes with weathering of the 3rd clear-coat slice

C, D PI raw data changes across the depths of the coating with weathering.

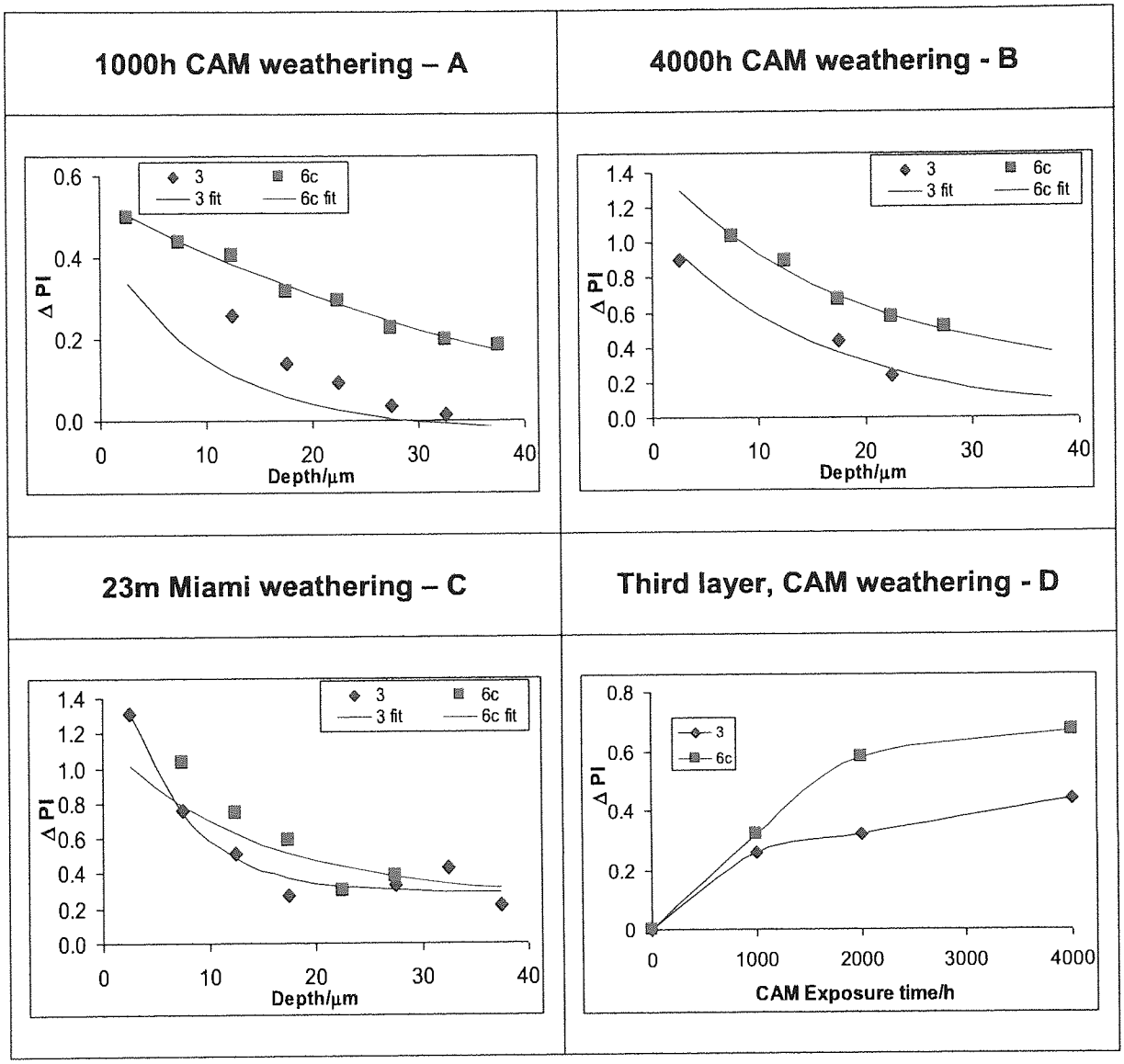

Figure 3.22 Depth profiling showing rotary microtomed PI changes in **Systems 3 and 6c** under natural weathering (Miami) and artificial weathering (CAM and SPART), where;

$\Delta PI_{OH} = \Delta PI_{OH\ t=t} - \Delta PI_{OH\ t=0}$. The points are the experimental data and lines are calculated from curve fitting, see section 2.6.4.

A ΔPI_{OH} changes after 1000 hours of CAM weathering
B ΔPI_{OH} changes after 4000 hours of CAM weathering
C ΔPI_{OH} changes after 23months of natural weathering in Miami
D ΔPI_{OH} changes with weathering of the 3rd clear-coat slice.

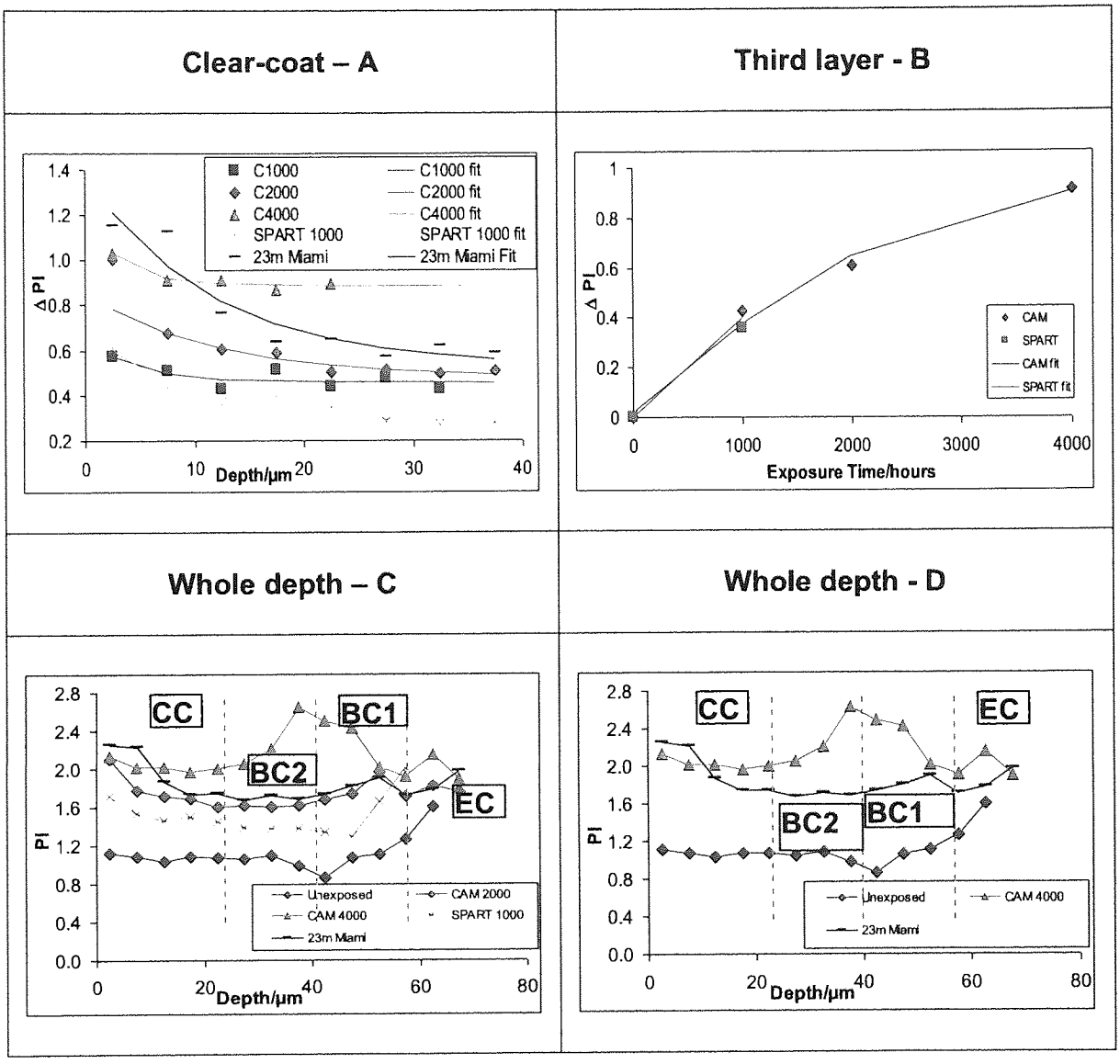

Figure 3.23 Depth profiling showing rotary microtomed PI changes in **System 8** under natural weathering (Miami) and artificial weathering (CAM and SPART), where;

$\Delta PI_{OH} = \Delta PI_{OH\ t=t} - \Delta PI_{OH\ t=0}$. The points are the experimental data and lines are calculated from curve fitting, see section 2.6.4.

A ΔPI_{OH} changes across the depths of the coating with weathering

B ΔPI_{OH} changes with weathering of the 3rd clear-coat slice

C, D PI raw data changes across the depths of the coating with weathering.

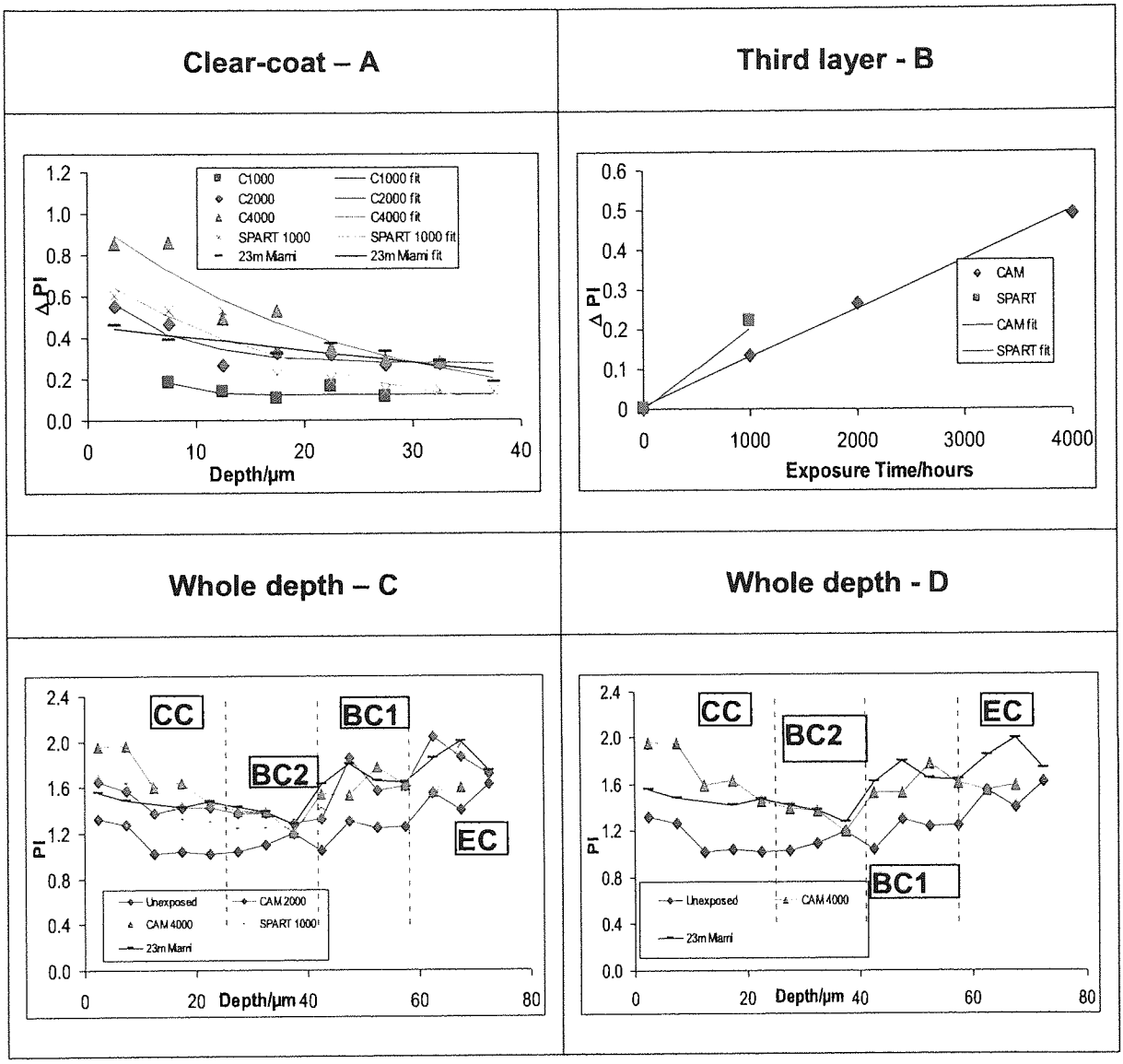

Figure 3.24 Depth profiling showing rotary microtomed PI changes in **System 10** under natural weathering (Miami) and artificial weathering (CAM and SPART), where;

$\Delta PI_{OH} = \Delta PI_{OH\ t=t} - \Delta PI_{OH\ t=0}$. The points are the experimental data and lines are calculated from curve fitting, see section 2.6.4.

A ΔPI_{OH} changes across the depths of the coating with weathering

B ΔPI_{OH} changes with weathering of the 3rd clear-coat slice

C, D PI raw data changes across the depths of the coating with weathering.

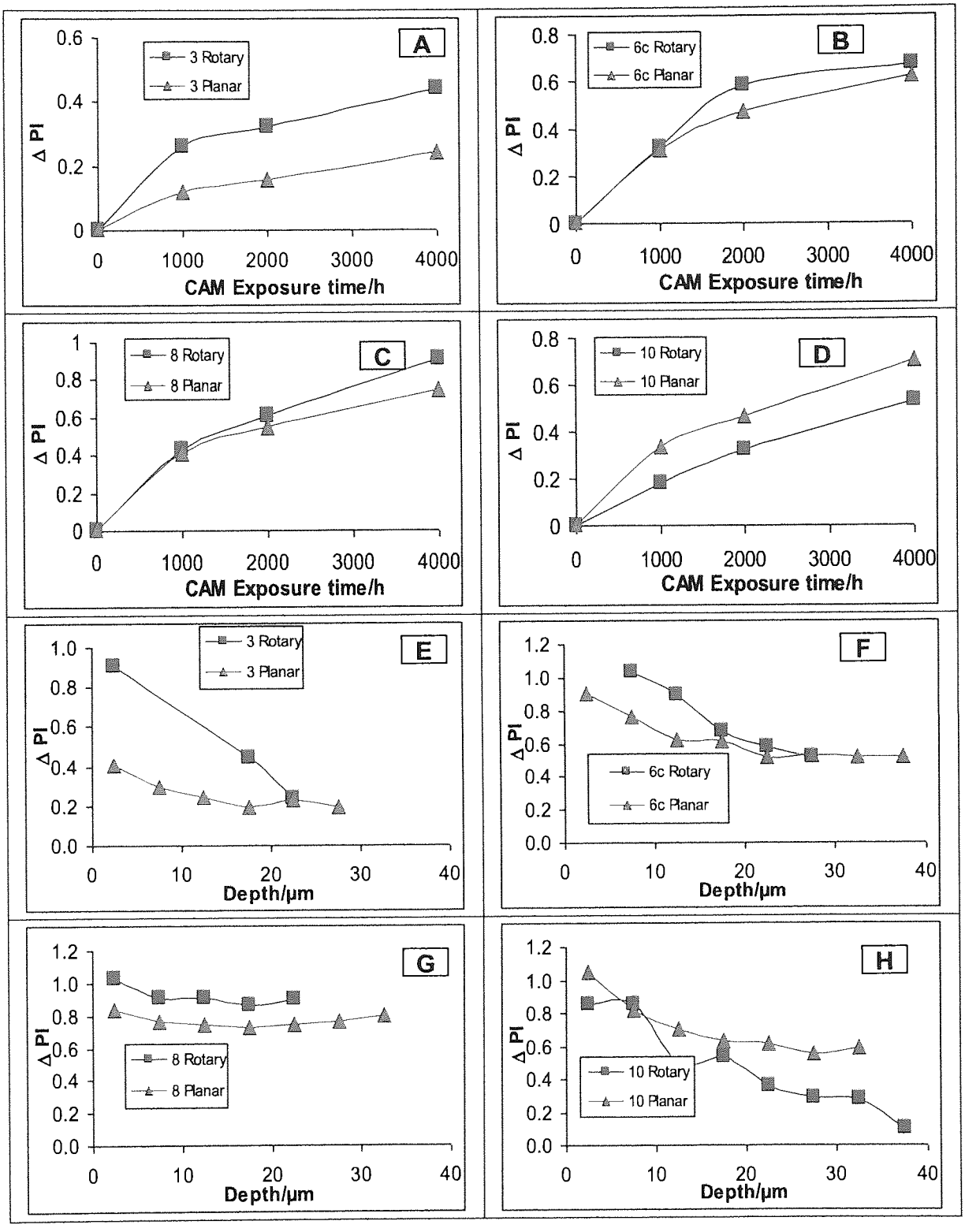

Figure 3.25 Comparison of the methods of calculating ΔPI_{OH} data (rotary and planar microtomed slices), for **Systems 3, 6c, 8 and 10** with CAM exposure time and nominal microtomed depth of 17.5μm at CAM 4000 hours exposure.

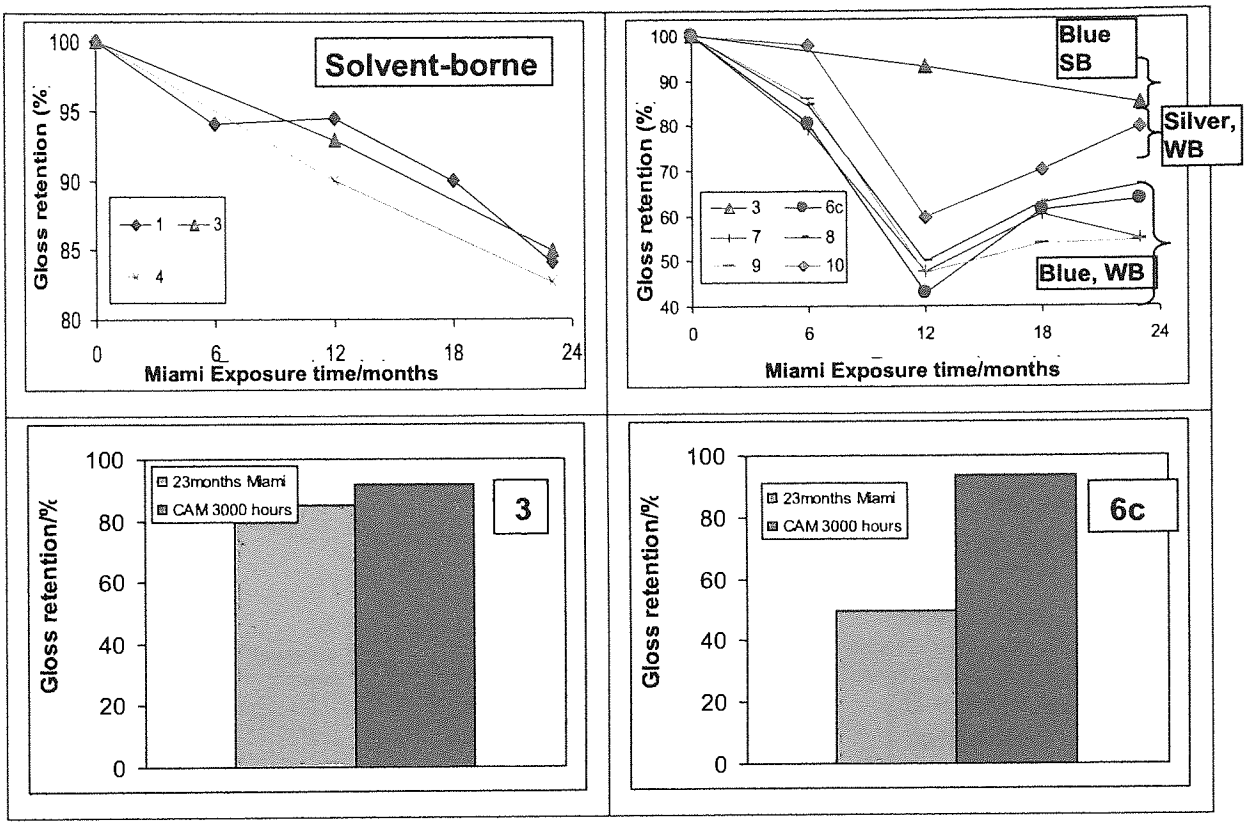

Figure 3.26 Percentage Gloss retention for water-borne and solvent-borne clearcoat systems with natural weathering (in Miami) and artificial accelerated (CAM) weathering.

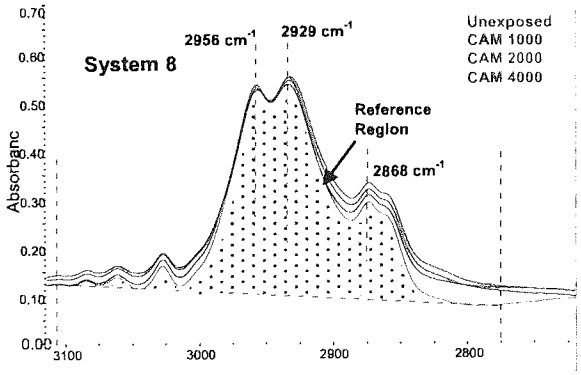

Figure 3.27 FTIR reference region for **System 8** used in deducing the mode of photoxidation

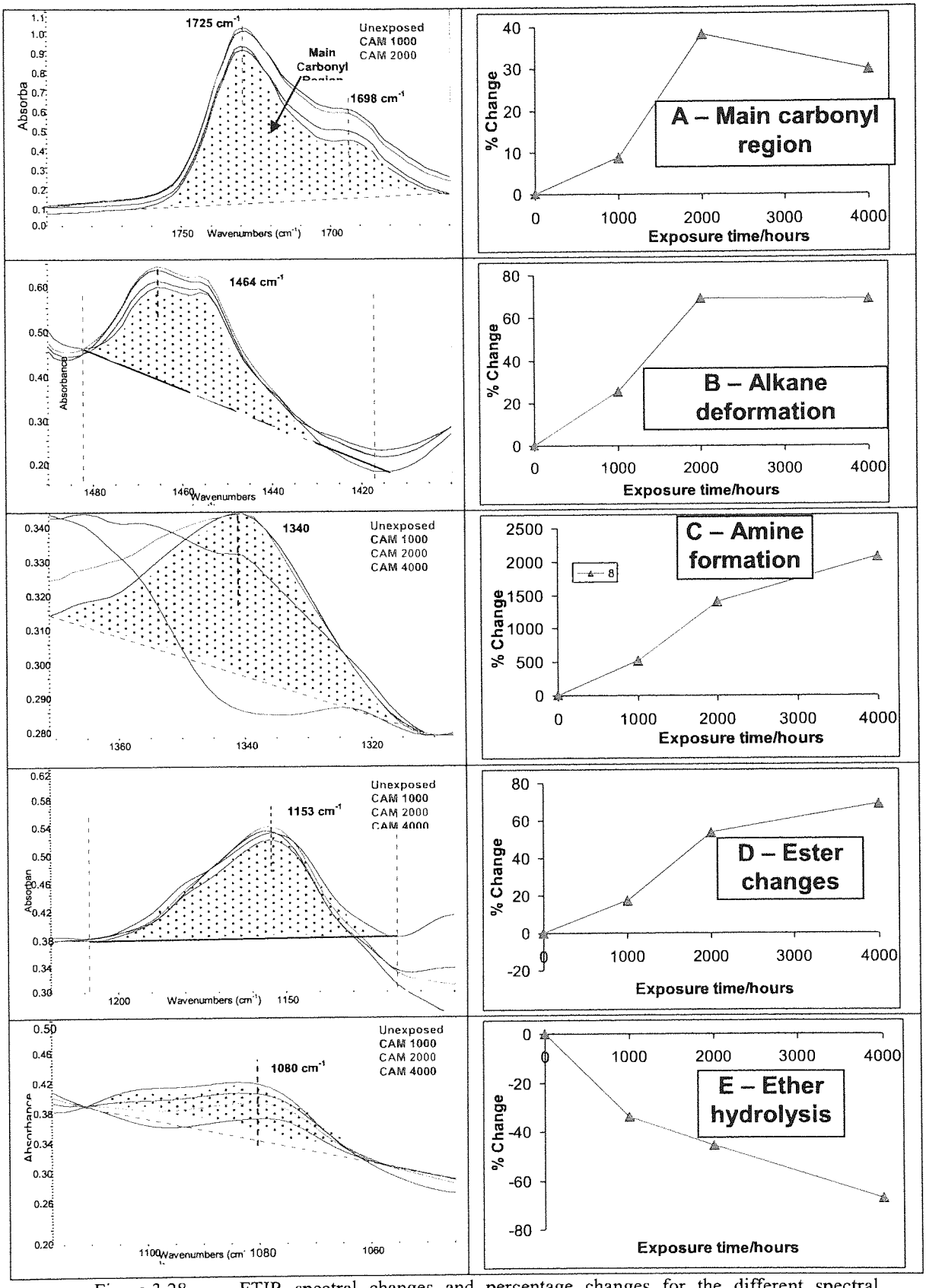

Figure 3.28 FTIR spectral changes and percentage changes for the different spectral regions for **System 8** unexposed and after artificial accelerated CAM weathering, for the third microtomed layer.

A, Main carbonyl region **B,** Alkane deformation
C, Amine Formation **D,** Ester change
E, Ether hydrolysis.

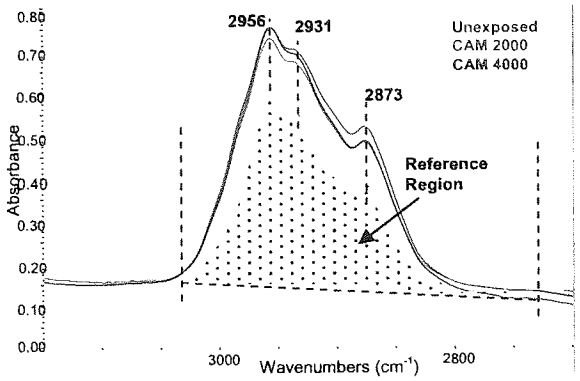

Figure 3.29 FTIR reference region for **System 3** used in deducing the mode of photoxidation.

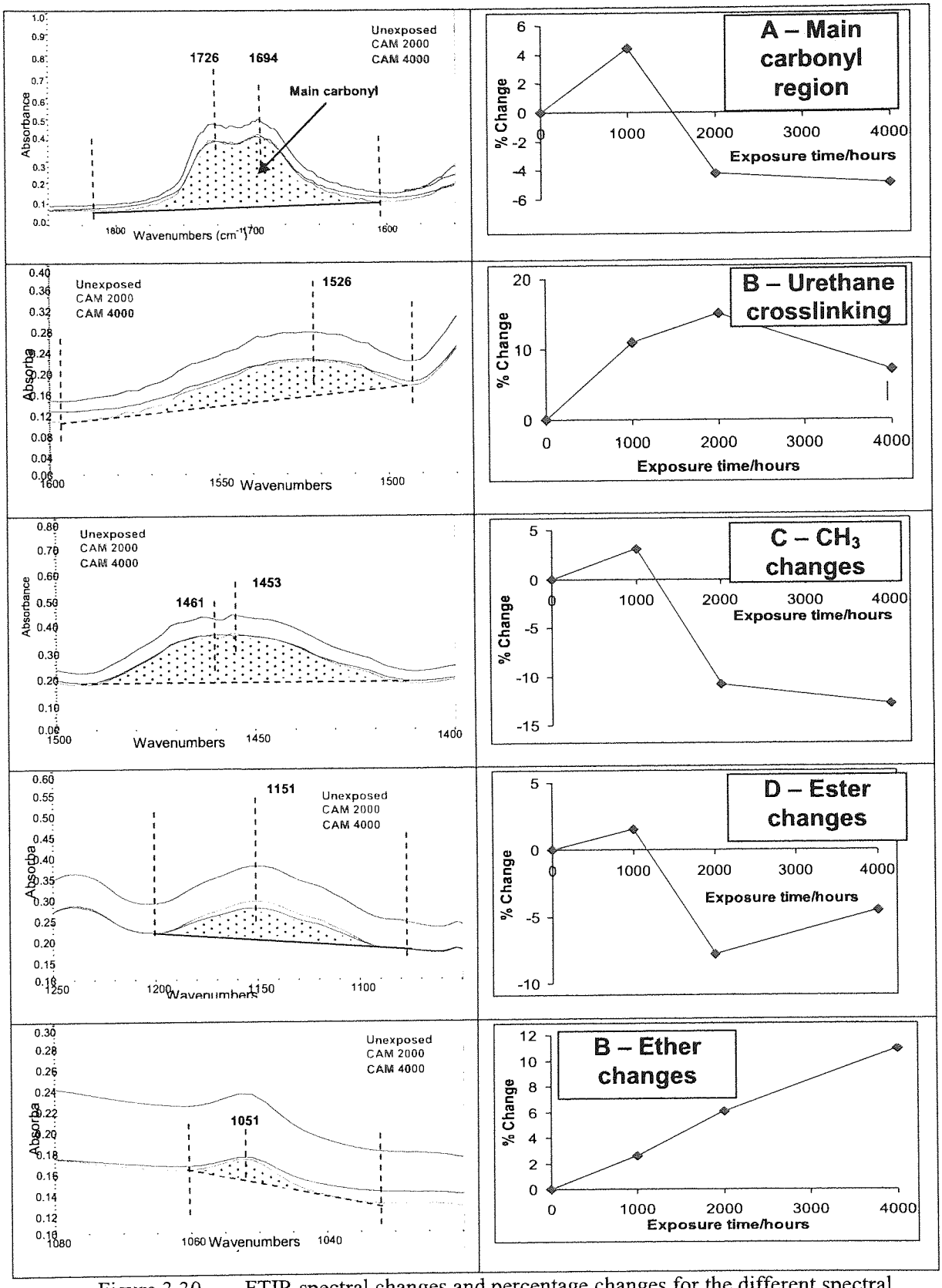

Figure 3.30 FTIR spectral changes and percentage changes for the different spectral regions for **System 3** unexposed and after artificial accelerated CAM weathering. **A,** Main carbonyl region **B,** Urethane crosslinking **C,** Alkane deformation **D,** Ester changes **E,** Ether hydrolysis.

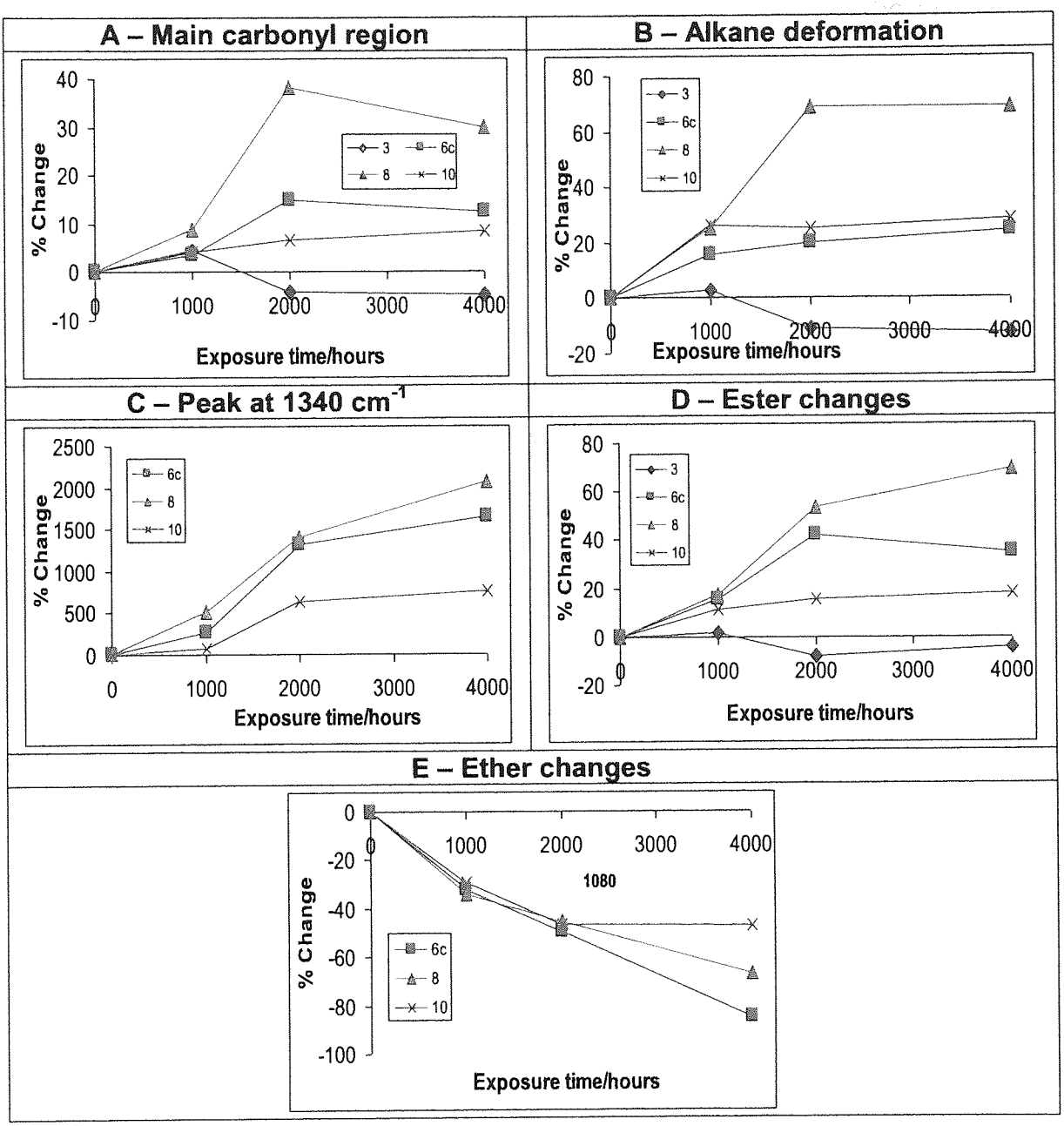

Figure 3.31 FTIR-ATR % area changes for the different spectral regions of Systems **3, 6c, 8 and 10** after artificial accelerated CAM weathering.

A Main carbonyl region at 1725 cm^{-1}
B Alkane deformation at 1464 cm^{-1}
C Peak at 1340 cm^{-1}
D Ester changes at 1153 cm^{-1}
E Ether changes at 1080 cm^{-1}

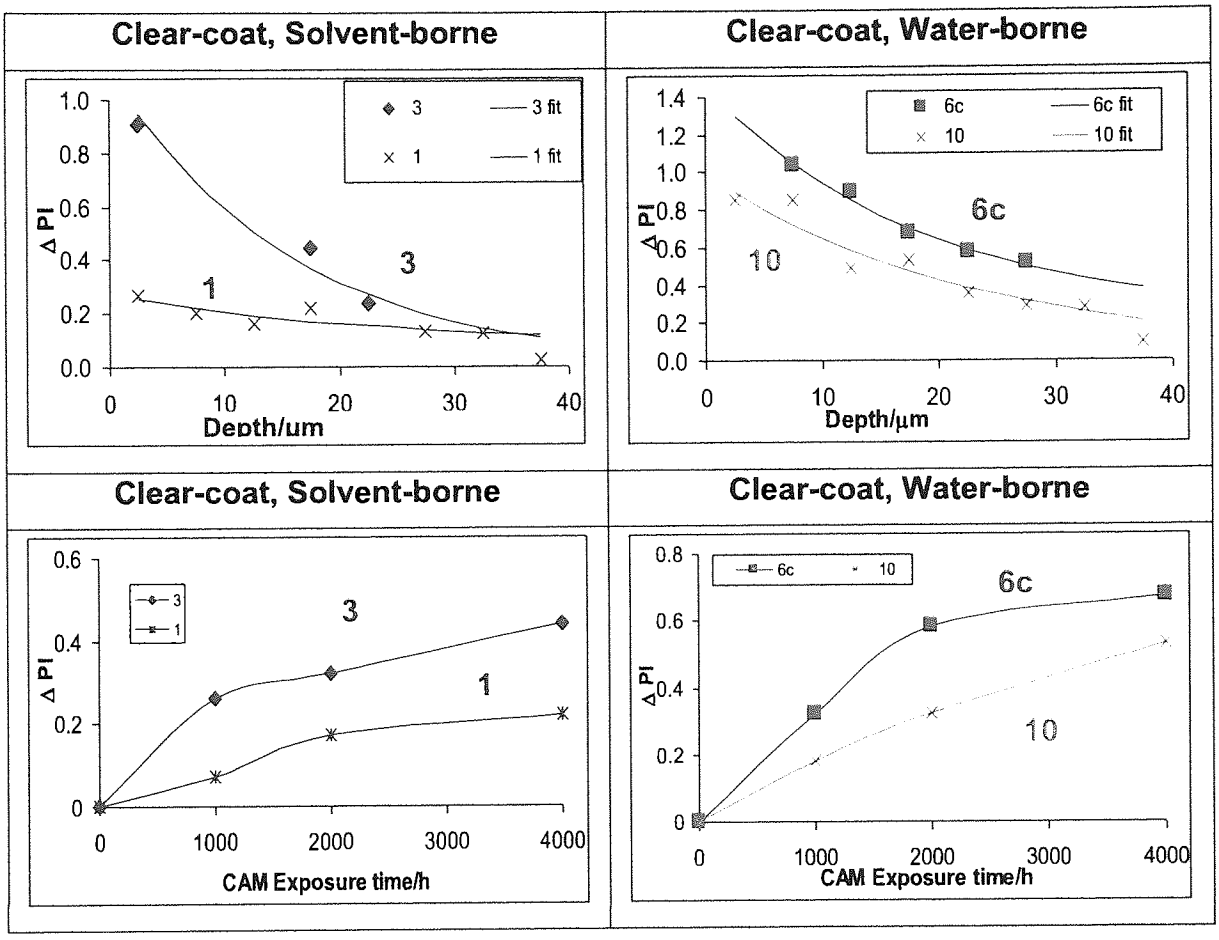

Figure 3.32 Depth profiling showing rotary microtomed PI changes in **1, 3, 6c and 10** under artificial weathering CAM where;

$\Delta PI_{OH} = \Delta PI_{OH\ t=t} - \Delta PI_{OH\ t=0}$. The points are the experimental data are calculated from curve fitting, see section 2.6.4.

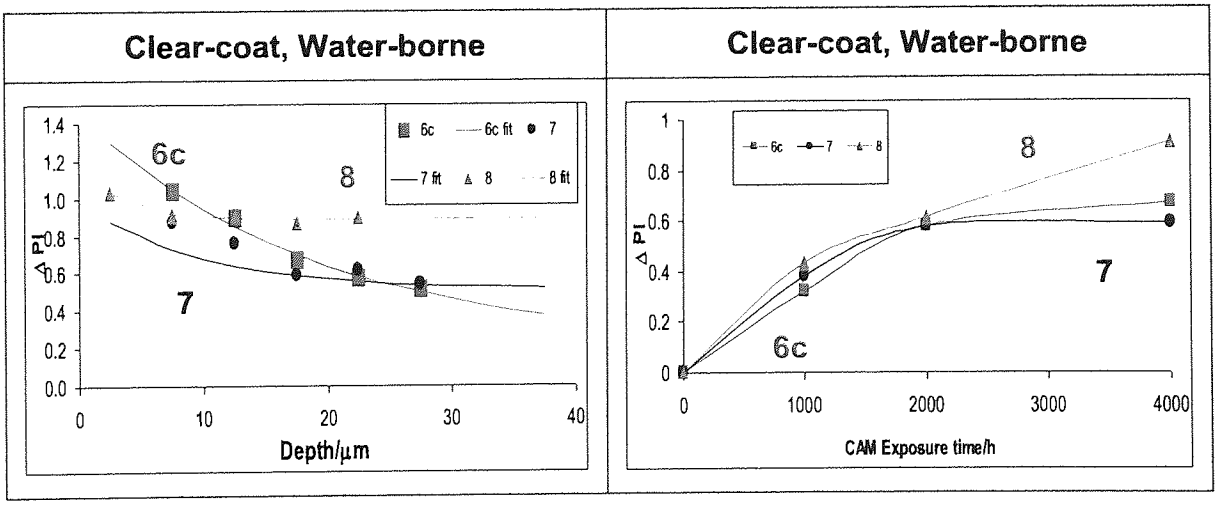

Figure 3.33 Depth profiling showing rotary microtomed PI changes in 6c, 7 and 8 (differences in UVA levels) under artificial weathering CAM where;

$\Delta PI_{OH} = \Delta PI_{OH\ t=t} - \Delta PI_{OH\ t=0}$. The points are the experimental data are calculated from curve fitting, see section 2.6.4.

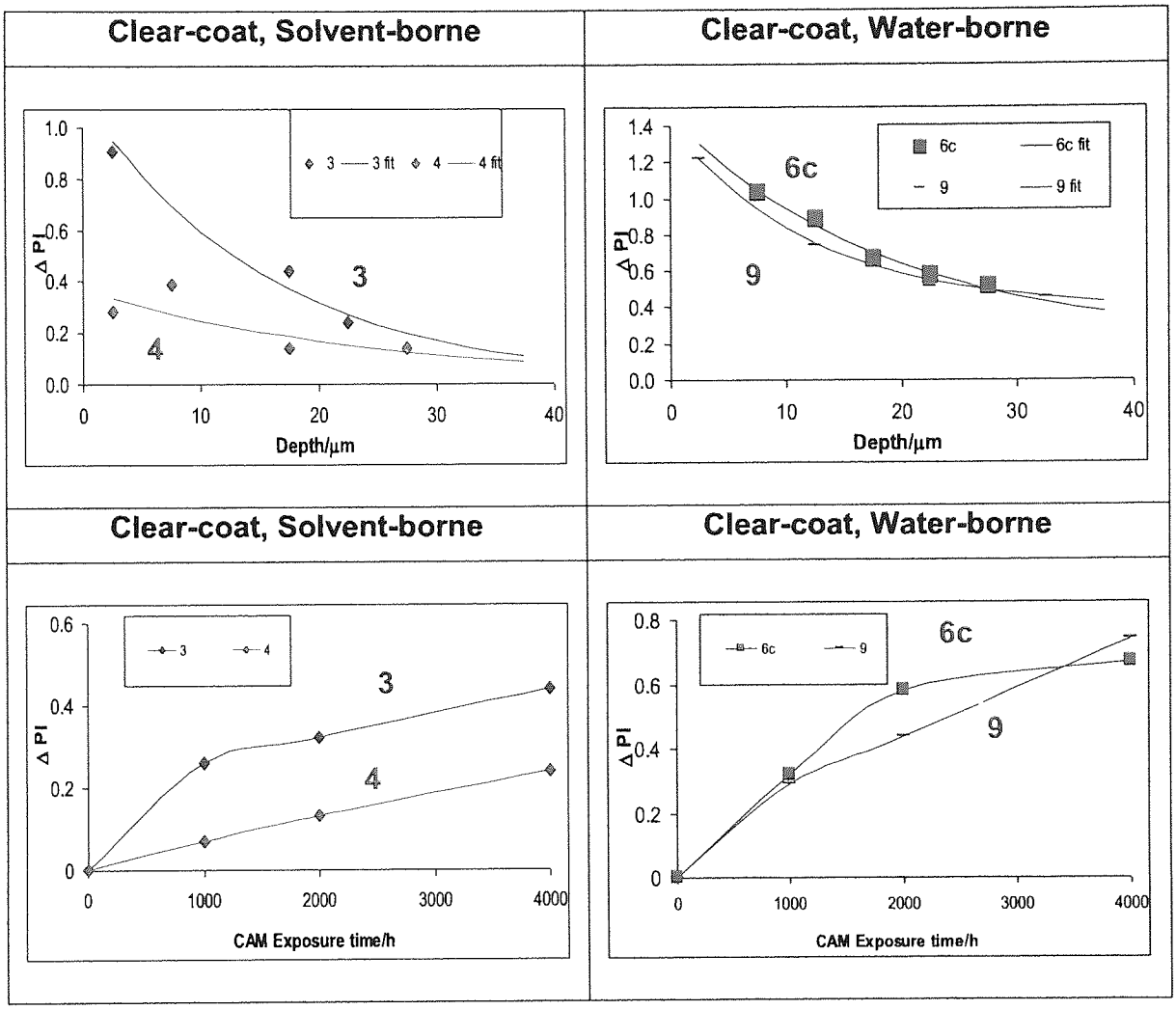

Figure 3.34 Depth profiling showing rotary microtomed PI changes in **3, 4 and 6c, 9** (differences in UVA types) under artificial weathering CAM where;

$\Delta PI_{OH} = \Delta PI_{OH\ t=t} - \Delta PI_{OH\ t=0}$. The points are the experimental data are calculated from curve fitting, see section 2.6.4.

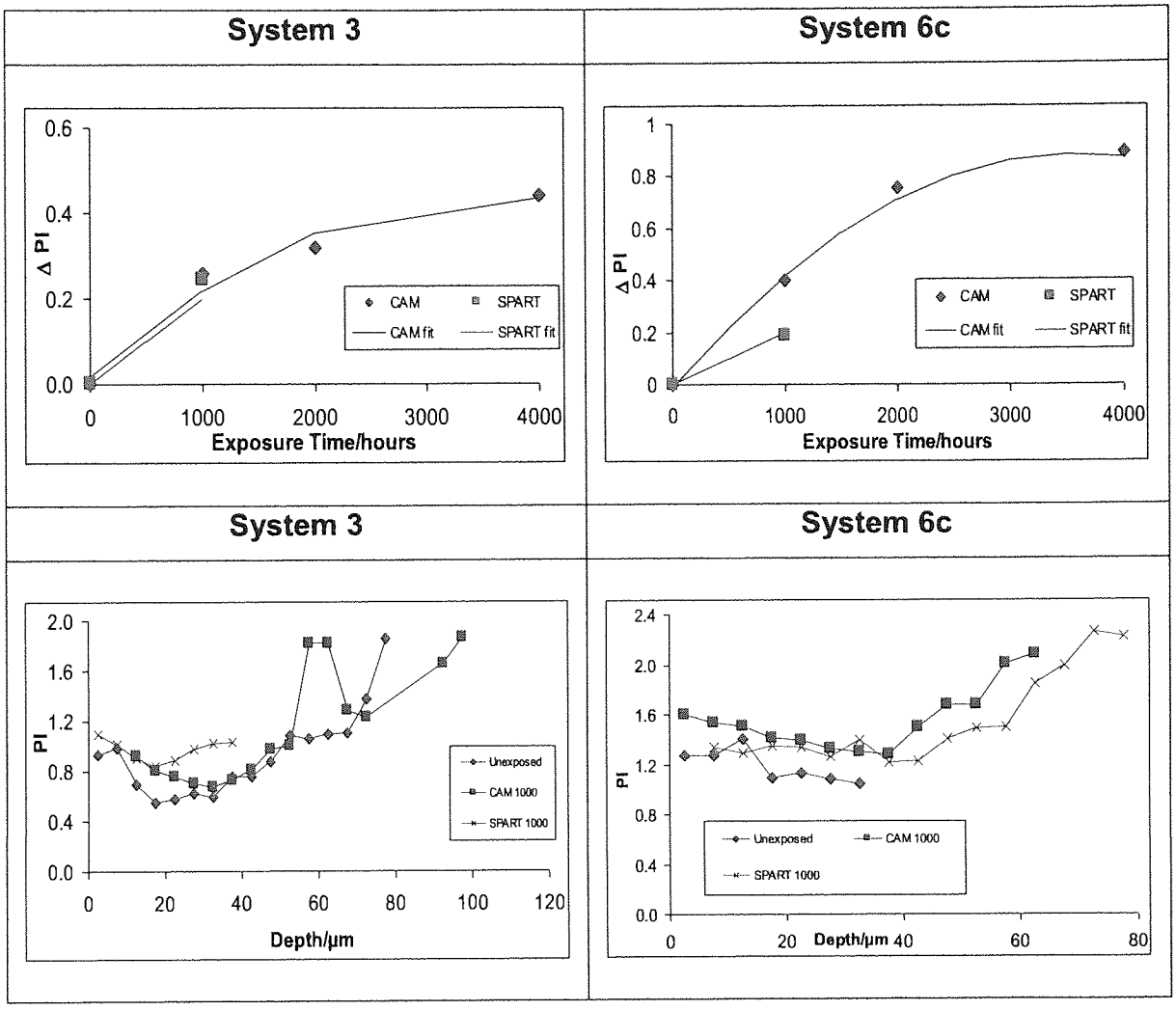

Figure 3.35 Depth profiling showing rotary microtomed PI changes in **3 and 6c** (differences in clear-coats) under artificial weathering CAM and SPART where;

$\Delta PI_{OH} = \Delta PI_{OH\ t=t} - \Delta PI_{OH\ t=0}$. The points are the experimental data are calculated from curve fitting, see section 2.6.

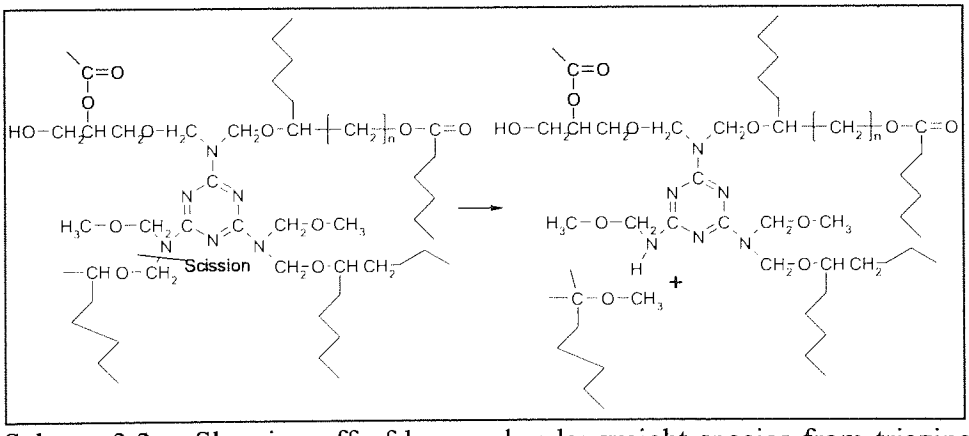

Scheme 3.2 Shearing off of low molecular weight species from triazine ring in the water-borne clear-coat.

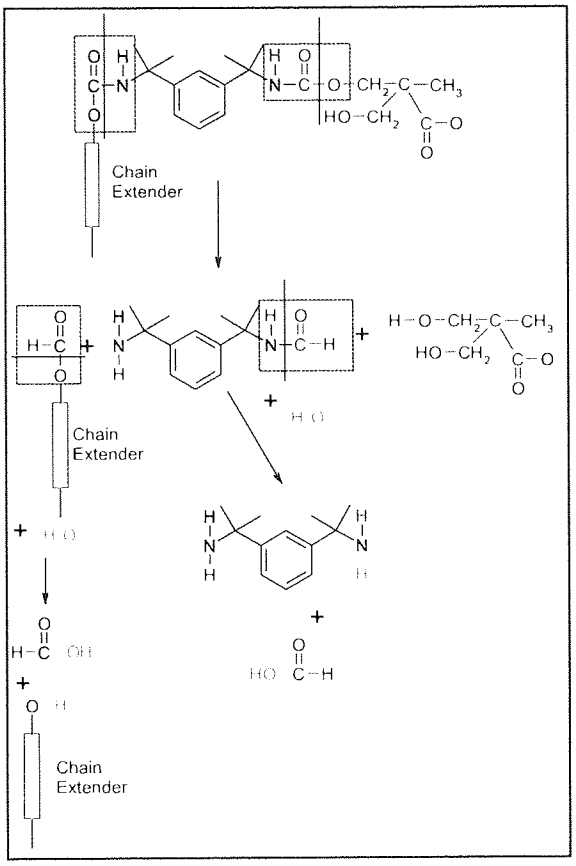

Scheme 3.3 Urethane degradation in the water-borne clear-coat

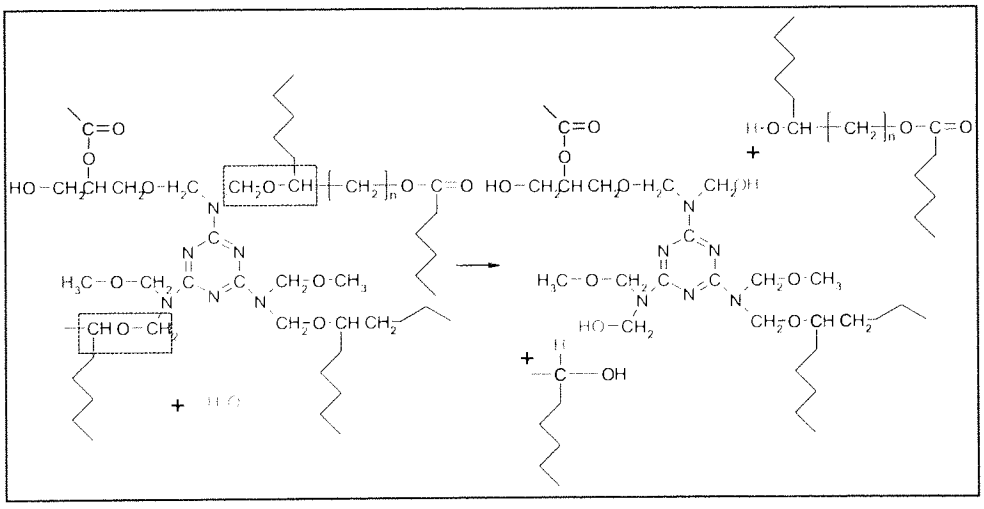

Scheme 3.4 Possible ether hydrolysis in the water-borne clear-coat

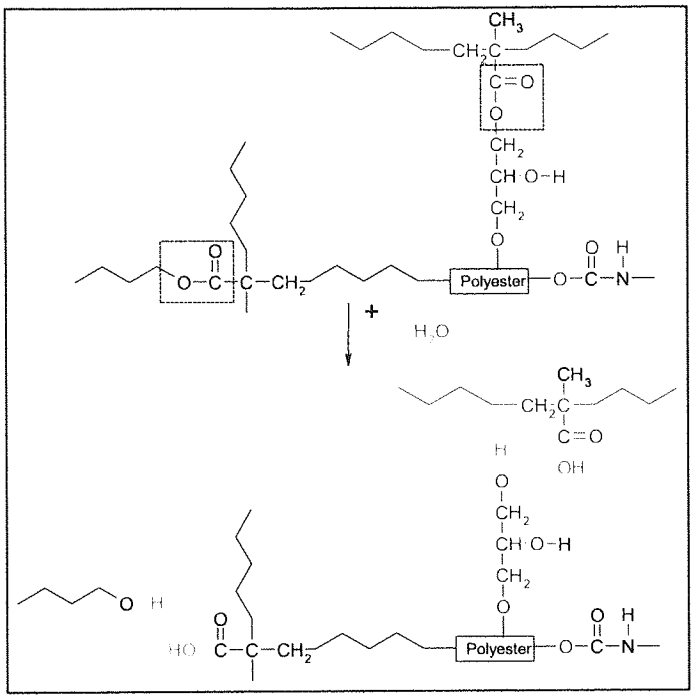

Scheme 3.5 Possible ester hydrolysis in the solvent--borne clear-coat

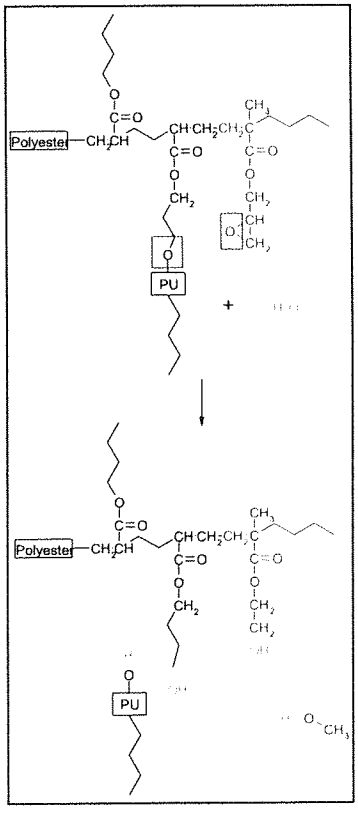

Scheme 3.6 Possible ether hydrolysis in the solvent-borne clear-coat.

CHAPTER 4: EFFECTS OF WEATHERING IN THE DEGRADATION OF AUTOMOTIVE COATINGS: NON-CONVENTIONAL METHODS OF ANALYSIS

CHAPTER 4: EFFECTS OF WEATHERING IN THE DEGRADATION OF AUTOMOTIVE COATINGS: NON-CONVENTIONAL METHODS OF ANALYSIS

4.1 Objectives and Methodology

The aim of the work described in this chapter was to investigate the use of Dynamic Mechanical Analysis (DMA) as a suitable method for investigating weathering-induced degradation that occurs at the early stages of exposure in various water-borne and solvent-borne automotive coatings used in this work. There is a very small volume of literature on the application of DMA in paint coating systems in spite of the fact that DMA is widely used for polymers and polymer blends typically for the purpose of structure determination **[89-92].** One of the reasons for the lack of information, particularly for its use in investigating degradation in paint systems during weathering, is associated with the difficulty in performing the DMA test on such coatings which are not only very thin (around 5-20μm) but also are often coated on a stainless steel surface. Further problems are associated with deterioration of the quality of the sample and possible erosion of the surfaces during weathering which would increase the difficultly in handling and clamping the samples during the DMA measurement.

DMA analysis performed in this work on coating (paint) systems involved the application of sinusoidal stress and measurement of the phase lagging deformation as a function of temperature (**Figure 4.1**). The measurements were carried out on microtomed slices (depth profiling) and also on full coating systems (not microtomed) before and after artificial accelerated weathering (CAM and SPART conditions, see section 2.4.1 for details) and natural weathering (in Miami, USA see section 2.4.2 for details). Tension analysis was carried out on the microtomed slices, throughout the depth of the coating systems, whereas bending analysis was carried out on the unmicrotomed coatings. Weathering-induced changes were investigated with respect to both exposure time (the third microtomed slices) and across the depth of the coating systems. **Table 4.1** gives a description of the coating systems discussed in this chapter.

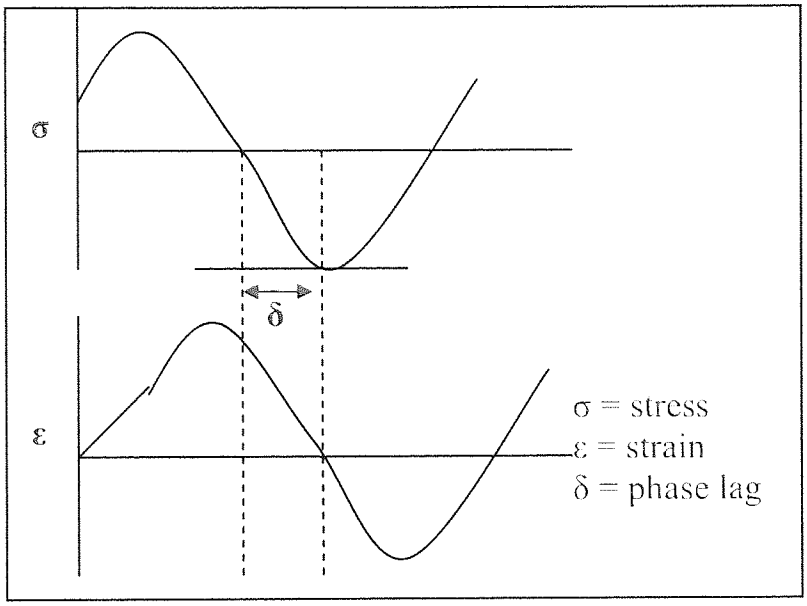

Figure 4.1 Illustration of DMA sinusoidal phase lag.

Table 4.1 Comparison of coating systems discussed in this chapter.

Layer Composition of various automotive coatings								
System Code Number		EC on aluminium substrate	Primer (WB-P)	Base 1	Base 2	Clearcoat (CC) Type	CC- UVA (level)	CC- HALS (level)
Solvent-borne	3	Yes	WB-Anthracite	No	Blue	SB	Cyasorb 1164 (level 1)	Sanduvor 3055 (level 1)
	4	Yes	WB-Anthracite	No	Blue	SB	KB 353 (level 1)	Sanduvor 3055 (level 1)
Water-borne	6c	Yes	No	Anthracite	Blue	WB	Cyasorb 1164 (level 1)	Sanduvor 3055 (level 1)
	7	Yes	No	Anthracite	Blue	WB	Cyasorb 1164 (level 3)	Sanduvor 3055 (level 1)
	8	Yes	No	Anthracite	Blue	WB	No	Sanduvor 3055 (level 1)
	9	Yes	No	Anthracite	Blue	WB	KB 353 (level 1)	Sanduvor 3055 (level 1)
	10	Yes	No	Light Grey	Silver	WB	Cyasorb 1164 (level 1)	Sanduvor 3055 (level 1)

4.2 Results

4.2.1 Tension analysis of microtomed paint coating films

DMA tension analysis was carried out on microtomed films of the coating systems, 3 (solvent-borne, blue, UVA level 1), 6c (water-borne, blue, UVA level 1), and system 10 (water-borne, silver, UVA level 1) before and after exposure to different weathering regimes. Samples for depth-profiling were produced by a project partner using a planar microtome, and used here for DMA analysis at a heating rate of 2°C/minute. Samples used to determine the changes in the clear-coats with weathering (times of exposure) were produced at Aston using a rotary microtome and analysed by DMA using a heating rate of 5°C/minute.

4.2.1.1 Characterisation by depth profiling of the solvent-borne and water-borne coating systems

Figure 4.2A and **B** show the depth profiling DMA results (for the microtomed slices) of the solvent-borne blue system 3 showing tan δ response (the peak maximum taken as the glass-transition temperature, Tg) and the elastic modulus (E') with temperature for the unexposed sample. It was possible to differentiate the different layers in the coating systems by examining both their tan δ and E' responses to the DMA heating programmes. The clear-coat layers showed a Tg around 140^{0}C, with the outermost layer having a slightly higher Tg than the inner layers. The base-coat and primer layers had lower Tg's at around 105^{0}C, the effect of coating slices present at the interface between two different layers was also clearly seen ('wedges', a result of microtoming). The differences in the E' responses of the different layers of the coating system were also seen (**Figure 4.2D**).

Figure 4.2 also shows the depth profiling results (for the microtomed slices) for the tan δ response and the elastic modulus (E') with temperature for the unexposed coating for the water-borne blue system 6c. Again the differences in the different layers were clearly seen, and in this case the clearcoat had a lower Tg at around 80^{0}C, with the outermost layers having the lowest Tg values. The base-coat layers had also a Tg at around 80^{0}C but the height of the curves were much lower than for the clear-coat layers.

The electro-coat layers showed a much higher Tg at 118^{0}C. The differences in the different coating layers were also observed in the E'min curves (also **Figure 4.2**).

Figure 4.3 shows the depth profiling DMA results for the tan δ response and the elastic modulus (E') at different temperatures for unexposed coating for the water-borne silver system number 10. The overall DMA behaviour of the silver system 10 was similar to that of the blue system 6c with the clear-coat Tg at around 80^{0}C, in both systems but the height of the Tg curves of the base-coat was much lower than that of the clear-coat and the electro-coat layer (72.5μm) in both systems had a much higher Tg of around 118^{0}C. The layer differences were also observed in the E'min curves with the electro-coat showing the largest difference compared to the other layers, (also **Figure 4.3**).

The solvent-borne and water-borne coating systems showed different characteristics across their depths in terms of their glass transition temperatures and in the relative level of their cross-link density. **Figure 4.4** shows that the clear-coat and the lower layers of the solvent-borne blue system 3 has a much higher glass transition temperature than the corresponding water-borne blue system 6c. However, the electro-coat layers of both water and solvent-borne systems gave similar glass transition temperatures. The difference in Tg across the depth of the blue and silver water-borne systems 6c and 10 was very small confirming the similarity in the overall chemistry of the different water-borne coating systems. The initial relative level of the cross-link density (determined from the E'min values) from both solvent-borne and water-borne systems were shown to be similar throughout the depth of the coating systems.

4.2.1.2 DMA Tension analysis to determine changes in the depth profiles of unexposed and weathered coating systems

DMA tension analysis was also carried out on the weathered coating systems to determine if weathering-induced changes could be detected in the depth profiles. **Figure 4.5** shows the DMA responses in the solvent-borne blue system 3 which was exposed to 4000 hours artificial accelerated weathering (CAM, SAE J1960) and after 23months of natural weathering, (Miami), (compared with results of unexposed

samples, see **Figure 4.1).** The two sets of curves (CAM or Miami exposure) are very similar, with the different layers of the coating systems being clearly distinguished.

Figure 4.6 shows the DMA charts for the water-borne blue system 6c exposed to 2500 hours artificial accelerated weathering (CAM, SAE J1960) and after 23months of natural weathering (in Miami), (compared with **Figure 4.2** for the unexposed sample). Changes in Tg and E'min are examined later in this chapter. Similarly **Figure 4.7** gives the DMA results for the silver water-borne system 10 exposed to artificial accelerated weathering for 4000 hours (CAM, SAE J1960) and for 1000 hours under SPART conditions, as well as for samples exposed to 23months of natural weathering (in Miami).

From the DMA responses, values of the glass transition temperature (Tg) and E'_{min} (a relative measure of the cross-link density) were determined throughout the different depths of the coatings, the full results are shown in appendix section A4.2, the results are given to ±0.6, (see appendix section A4.3 for details). **Figure 4.8** shows the changes in Tg, ΔTg, E'_{min} and $\Delta E'_{min}$ across the depths of the coatings for the unexposed and weathered (both artificial and natural) solvent-borne system 3. Changes in the glass transition temperature could be used to distinguish the different types of coating (clear-coat, base-coat, primer or electro-coat). The clear-coat gives the highest glass transition temperature which appeared to increase slightly after weathering. However, overall, the glass transition temperature decreased throughout the whole depth of the coating system, except for the electro-coat where it remained unchanged. Relative changes in the cross-link density of the slices were less easy to determine with large changes occurring at the interfaces between the different layers. A positive Δ change indicated that the relative cross-link density of the clear-coat slice had increased with respect to an average of the clear-coat slices of the unexposed sample (for the particular coating system examined).

The changes in Tg, ΔTg, E'_{min} and $\Delta E'_{min}$ across the depths of the coating for the water-borne blue system 6c before and after weathering (artificial) are shown in **Figure 4.9**. It was seen that the glass transition temperatures of the clearcoat, basecoat layer 2 and basecoat layer 1 decreased after weathering, although the glass transition temperature of

the electrocoat did not change. The greatest level of change in the glass transition of the clearcoat occurred at the very surface of the coating system (**Figure 4.9A and C**).

The Tg and E'_{min} changes across the depths of the water-borne silver coating system 10 before and after weathering (both natural and artificial) are shown in **Figure 4.10**. It is clear again that the electrocoat had a much higher glass transition temperature than the other coating layers. The glass transition temperature decreased in the clear-coat upon weathering with the greatest change occurring at the surface of the coating (**Figure 4.10A and C).** The glass transition temperature of the base-coat and electro-coat layers did not change greatly across the depth of the coating system. The relative level of the cross-link density decreased in the clear-coat with weathering indicating some polymer degradation. However at the interface with the silver base-coat-2 layer (around 40μm depth) the relative level of the cross-link density showed a large increase and this also increased with weathering (**Figure 4.10B).** The level of E'_{min} (relative cross-link density) decreased in the lower layers below the silver base-coat 2.

The glass transition temperature and relative level of the cross-link density of the solvent-borne and water-borne coating systems are compared at 2500 hours of CAM exposure, **Figure 4.11**. The solvent-borne system 3 shows very different results to those of the water-borne systems 6c and 10 in that there is a more pronounced decrease in its Tg especially in the clear-coat layers. Also, the relative level of the cross-link density especially in the clear-coat was always greater in the solvent-borne system 3 (see **Figure 4.12D).**

4.2.1.3 DMA Tension analysis to determine changes in the surface layers of the unexposed and weathered coating systems

The changes in tan δ (Tg) and elastic modulus (E') measured for a surface layer with a nominal depth of 17.5μm before and after accelerated ageing (using both CAM and SPART for different time periods) and after natural weathering (23 months in Miami) for the blue solvent-borne coating system number 3, and the water-borne systems blue 6c and silver 10 shown in **Figure 4.12**. In the case of the solvent-borne system 3, **Figure 4.12** shows clearly that both the maximum height of the tan δ peak and the Tg values increase with weathering (both accelerated and natural) with the coating

becoming less elastic with exposure. However, in the case of the water-borne blue (6c) and the silver (10) systems, both the maximum height of the tan δ peak and the Tg values are shown to decrease with weathering (both accelerated and natural), see **Figure 4.12** and the coatings became less elastic with exposure. **Figure 4.13** shows the changes in both glass transition temperature and elastic modulus of both systems 3 and 6c.

Changes in the glass transition temperatures upon accelerated (CAM) weathering of the solvent-borne systems 1 and 3 and the water-borne systems 6c, 7, 8, 9 and 10 are shown in **Figure 4.14**. It is clear that the solvent-borne coatings have consistently shown a much higher glass transition temperature than the water-borne coatings with the former giving an overall lower extent of change. In the solvent-borne coatings, the silver coloured system number 1 showed an even less change compared to the blue system number 3 **(Figure 4.14C and G).** In the case of the water-borne coatings on the other hand, the 'unstabilized' (with respect to UVA) blue system number 8 showed by far the greatest change in its glass transition temperature with exposure time showing an increase in Tg of up to 5°C (**Figure 4.14H**). The silver, stabilized, system number 10 showed the least extent of reduction in glass transition temperature whereas system number 9 containing a cross-linkable UV stabiliser showed more changes than system 6c containing a standard UV stabiliser. **Figure 4.15** gives the changes with exposure time in the relative cross-link density (E'min) for the same coating systems. The solvent-borne system 3 showed much greater increase in the cross-link density with weathering compared to the water-borne systems. The unstabilized, water-borne blue system number 8 showed the greatest decrease in cross-link density with weathering indicating the highest level of degradation.

The relative initial stiffness of the coating systems as determined from the storage modulus (E') determined at room temperature is given in **Figure 4.16**. The solvent-borne systems 1 and 3 generally showed a slightly lower initial stiffness that the water-borne coating systems (**Figure 4.16A**). but the values increased with weathering, while that of the water-borne systems generally decreased with weathering (**Figure 4.16F**). The highly stabilized blue, water-borne system 7 showed the least changes with weathering, followed by the silver system 10. The blue system 9, with the cross-linked

UVA showed the greatest decrease in stiffness at room temperature with weathering (**Figure 6.16H**).

4.2.2 DMA bending analysis to determine changes in the coating systems after weathering, without microtoming

The DMA analysis by bending mode was carried out on the full, unmicrotomed coating systems. **Figure 4.17A** shows the repeatability of the DMA bending analysis carried out on system 6c. The method gave reproducible results in terms of both E' and tan delta responses of the coatings. For the water-borne system, in the tan delta curve, two glass transition temperatures can be clearly seen; the lower value (at around 70^0C) is that for the clearcoat and the higher temperature (at around 120^0C) for the electrocoat. **Figure 4.17** also shows the E' and tan delta response curves for water-borne systems 6c (stabilized) and 8 (unstabilized) for the unexposed and CAM exposed (for 4000 hours) samples using bending mode. There is a clear glass transition temperature shift after weathering (for example from 116.1°C to 123.3°C for the upper transition temperature after 4000 hours of CAM weathering in system 8, **Table 4.3**), the relative cross-link density (E'min) also showed a shift with weathering (for example in system 6c from 1.2 * 10^{10} Pa to 1.8 * 10^{10} Pa after 4000 hours of CAM weathering. The higher (electro-coat) glass transition temperature increased with weathering, for the water-borne coating systems. The lower glass transition temperature of the clear-coat was not seen in the full (not microtomed) solvent-borne system 3, whereas for the water-borne systems, it again decreased with weathering (**Table 4.3**). The relative level of the cross-link density (E'min), increased with weathering, again more in the water-borne system 3 than in the solvent-borne system 3.

4.3 Discussion

4.3.1 Characterization of the paint systems using DMA tension analysis

Before any weathering exposures were carried out on the coating systems, DMA tension analysis was carried out on microtomed layers to characterize the behaviour of the different layers of the different unexposed coating systems with regard to their tan δ (glass transition temperature) and storage modulus curves (E', relative cross-link

density), (**Figure 4.18, Table 4.2**). DMA tension analysis was chosen for the microtomed layers of coatings since this is the only method that has been previously used for films with a thickness less than 60μm **[17]**, and no further sample preparation is needed for the microtomed slices, although handling of the very thin (around 5μm) slices proved quite challenging. The E'min value was used to give an indication of the relative values of the cross-link density of the coating systems. This was shown to give a good measure of the changes that occur in the polymer network structure caused by weathering **[17]**.

DMA analysis in terms of both the glass transition temperature and the E' values have made it possible to distinguish between the different layers of the coatings systems since the different layers gave very different and distinct glass transition temperatures, see **Table 4.2**. The clear-coats of the solvent-borne systems (for example number 3) showed a higher glass transition temperature (around 144°C) than the base-coat and primer layers (105°C), with the value of the electro-coat falling in the middle of the two (113°Csee **Figure 4.18D**). Also the results showed clearly that overall the glass transition temperatures of the solvent-borne systems were higher than those of the water-borne systems (**Figure 4.18D**). The glass transition temperature of a coating system depends upon the amount of thermal energy needed to keep the polymer chains moving, thus the solvent-borne systems which have higher glass transition temperatures (more energy is required to move the chains) must have a more rigid polymer structure. Indeed this was confirmed, for example, in the case of the solvent-borne system 3 which showed clearly a much higher E'min reflecting a higher extent of cross-linking than the respective water-borne system, **Figure 4.18H, Table 4.2.**

4.3.2 Determination of the extent of erosion caused by weathering using DMA tension analysis

The tension analysis carried out by DMA of the weathered samples was further correlated with the photographs and FTIR spectra of the microtomed sliced (see section 3.4.4) to corroborate the extent of erosion of the clear-coats. This was achieved using the depth profiling results, the charts of the glass transition temperature at the different depths, for the different exposure periods. The first layer of the electro-coat was assigned (as seen by the large increase in glass transition temperature) and then

counting the slices from this point back towards to the top of the clear-coat, thus the change was determined between the exposed and unexposed samples. The results confirmed that system 3 was shown to have eroded by 5μm after 4000 hours of the CAM weathering) as reflected by the shift in the position of the first electro-coat layer in the weathered sample compared to the unexposed counterpart, **Figure 4.19**. The Miami (exposed for 23 months) results were shown to be similar to those obtained after 1000 hours of CAM exposure for sample 10 (**Figure 4.19**), although this may not be highly predictable, as been found previously with natural weathering **[46]** due to the uncertainty of natural weather patterns. The 1000 hours SPART weathering (for sample 10, **Figure 4.19**) was found to be similar to the equivalent time period for the CAM weathering.

For the water-borne blue system 6c, the coating was seen to have eroded by 5μm after only 2500 hours of artificial accelerated, CAM weathering (**Figure 4.19**) due to the shift in the depth of the first electro-coat as determined by the change in glass transition temperature. Unfortunately samples exposed for 4000 hours were not available for DMA measurements. System 10 was seen to have eroded by 15μm after 4000 hours of CAM weathering (**Figure 4.19**), by the same method. These results indicate that the solvent-borne system 3 was more resistant to erosion than the water-borne systems, the stability of which will be discussed further below. The level of erosion was also investigated using the relative values of the cross-link density. The E'min values of system 3 did not show any conclusive results between the different layers. However, the E'min values of 6c and 10 appeared to decrease in the clearcoat layers after weathering, however the E'min layers appeared to increase after weathering in the deeper coating layers, with large 'spikes' occurring at interfaces between the different coating layers (**Figure 4.11** shows systems 3, 6c and 10).

The extent of erosion has been previously discussed in chapter 3, using the photographs of the microtomed slices. The erosion data from the pictures of the microtomed slices were compared to the results from the DMA analysis (**Figure 4.20**), and were used as a measure of the resistance of the coating system to the damaging effects of weathering. Both methods showed that the solvent-borne blue system (3) was the most resistant to weathering, showing the least amount of erosion than the water-borne systems, and the

unstabilized (with respect to the level of UVA) water-borne blue system (8) showed the highest level of erosion (**Figure 4.20**).

4.3.3 Use of DMA tension analysis to determine the resistance of the different automotive paint systems to weathering

The effects of weathering on the different coating systems were compared after up to 4000 hours of artificial accelerated (CAM) exposure. The differences in the glass transition temperatures between the different clearcoats were seen, with the solvent-borne system 3 showing less weathering induced changes than the water-borne systems 6c and 10 (**Figure 4.14E**). The DMA tension analysis was used as it was previously found to be able to distinguish between the ability of the different coating systems to resist weathering **[89].** The water-borne systems may have had incomplete curing regimes (cured at lower temperatures for less time) which would be consistent with a lower measured glass transition temperature than that of the comparable solvent-borne system (**Figure 4.14B**) and this was also shown to be the case for other systems described in the literature **[19].**

It was seen in all the systems that most of the changes in glass transition occurred at the surface of the coating systems as this was the part that was exposed to maximum radiation (**Figures 4.8-10C and D** for systems 3, 6c and 10). Thus, the more degraded material was at the surface of the coating, the same place where the stresses would be expected to be at their highest. The CAM weathering regime contained regular water-cycles, thus water uptake of the coatings would almost certainly have occurred. This could lead to the breaking of intermolecular hydrogen bonds between the polar groups, increasing the mobility of each polar group. Thus, the water uptake may have caused the decrease in glass transition temperatures observed in the coating systems particularly in the top clear-coat layers. The decreases in glass transition temperature of the clear-coat (measured in the third microtomed slice from the top) after weathering (**Figure 4.11D**) may also be due to cracking of the coating; this may be a result of an increase in the magnitude of the stress on the top clear-coat layers of the coating systems **[90].**

The differences in the changes in the glass transition temperature between the solvent-borne and water-borne coating systems may also have been due to different types of chemical changes occurring in the different clear-coats (**Figure 4.14A, E**). It has been suggested **[18]** that in the water-borne systems side reactions in the coating systems occur, such as esterification of hydroxyl groups in the polyols and in the alkoxy groups of the melamine resin (which do not occur in the solvent-borne system, 3) **[18],** see **Scheme 4.1.** The DMA results also showed differences in the relative cross-link density of the different coating systems, with system 3 showing less changes in the relative cross-link density than the water-borne systems, and less 'spikes' at the interfaces between the different coating layers (**Figures 4.8-10** for systems 3, 6c and 10), particularly between the clear-coat and base-coat layers. Beneath the clear-coat, water-borne systems (6c and 10) had a far higher level of the relative cross-link density than was the case for the solvent-borne system 3 (**Figure 4.8B**). For coating systems that contain isocyanates (as in this case for all systems examined), the cross-link density has been shown to increase with weathering **[18, 89],** however this did not occur in all systems examined here, particularly in systems 6c and 10 (**Figures 4.9 and 4.10**), possibly due to the presence of other chemical groups in the polymer chains, **Scheme 4.2** shows the different groups present in the complex water-borne coating systems. With an increased level in the relative cross-link density, the hardness of coating systems has been found to increase, as observed in the literature **[68],** and also here in the solvent-borne system 3, see chapter 3, Figure 3.4). The changes in the cross-link density have been found to be caused by photo-oxidation (see section 3.5), which can further lead to embrittlement of the coatings. The weathering reactions can give rise to non-uniform degradation of the clear-coats, which themselves contain heterogeneous structures with high or low cross-link density domains. Weathering may cause development of local stresses in the clearcoats, enlarging the pathway passages of water resulting in a reduction in the barrier properties and an increase in water uptake **[91].** The changes in cross-link density may also relate to chemical changes in the coating systems, the scission on the acrylic/melamine cross-links in the clear-coat of the water-borne systems can lead to the formation of melamine methylol groups. These groups may self-condense further to form melamine-melamine cross-links (see **Scheme 4.3**).

The differences between the solvent-borne system 3 and the water-borne 6c have already been mentioned, with the solvent-borne coatings being more resistant to

weathering. For the solvent-borne coatings, system 1 (silver) and 3 (blue), and in the water-borne systems system 10 (silver) and 6c (blue), the silver coating systems and had lower extent of change in their glass transition temperature and relative cross-link density changed less than the corresponding blue system indicating that the silver base-coat conferred greater stability than the blue base-coat (**Figure 4.14 and 4.15, F and H**), possibly because the silver aluminium particles reflect the damaging UV radiation away from the coating system, and the lower temperatures of the blue systems when compared to the silver systems (**Table 3.7,** chapter 3 shows a difference of up to 7°C). In the water-borne coating systems, the effect of the presence and amount of UVA in the water-borne coatings was investigated (see **Figure 4.14, D**). The effects of the existence and level of UVA also discussed in the ΔPI measurements seen in chapter 3, (see Figure 3.32) which showed that the silver systems (solvent-borne 1 and water-borne 10) are most resistant to photodegradation compared to the equivalent blue systems (solvent-borne 3 and water-borne 6c respectively).

It was seen that the glass transition temperature changed differently with weathering in the presence and in the absence of UVA; the glass transition temperature of system 8 (no UVA) increased with weathering (**Figure 4.14B, D**), while the glass transition temperature of the other systems containing UVA decreased with weathering. This may be due to the protecting action of the UVA in the clear-coat, which prevents the radiation from penetrating further in the depth of the coating. It has previously been found that in systems containing no UVA, the glass transition temperature of the coating increased with weathering **[17]**. The greatest change in the glass transition temperature occurring at the surface of the coating systems, where the coating surface was most exposed to the greatest amount of the damaging radiation (**Figure 4.11C**). The system that did not contain UVA (system 8), also showed the greatest changes in its photoxidation index (ΔPI) (**chapter 3, Figure 3.34**). The weathering behaviour of the water-borne system containing the cross-linkable UVA (system 9) did not show any difference to the changes observed in the corresponding system (number 6c) containing standard UVA.

System 3 showed the greatest increase in the relative cross-link density with weathering, indicating weathering caused the dominance of cross-linking reactions, see **Figure 4.15, F**. The unstabilized, water-borne, blue system 8 showed the greatest

decrease in cross-link density with weathering, followed by system 9 (with the cross-linkable UVA) and 6c (with the standard UVA), again showing that the cross-linkable UVA did not seem to increase the resistance to weathering of the coating. The different coating systems were shown to have different stiffness at room temperature (**Figure 4.15**). The solvent-borne systems showed a lower initial stiffness than the water-borne coating systems, further indicating the differences of the water-borne and solvent-borne coating systems. The increase in the stiffness of the solvent-borne systems with weathering is possibly due to an increase in the extent of cross-linking and similarly the decrease in the case of the water-borne systems (6c and 8) suggest a dominance of chain scission reactions during weathering (this was also seen by the changes in the hardness of the coatings after weathering in chapter 3 (section 3.3.1)). The changes in the initial stiffness after weathering again showed importance of stabilizing the coating systems with UVA (**Figure 4.16H**).

4.3.4 Changes in the thermal characteristics in the coating systems using bending analysis by DMA

The results from the bending analysis were shown to be consistent for duplicate samples. The use of bending analysis has several advantages over the use of tension measurements, the main advantage being the coating was tested in-situ (there was no need to slice the coating into sections), thus the coating system was able to retain the same structure (composition profile, morphology and internal stresses). However, variable results have been found, these reflect the complexity of the coating systems (a low modulus coating applied to a thicker substrate of higher modulus), thus, the mechanical stiffness of the sample may have been dominated by the substrate **[19]**. Thus, the modulii found from the bending results are composites for the coating systems (due to the system containing several different layers (clear-coat, base-coat, primer, electro-coat) which may individually have different characteristics).

The higher glass transition temperature at around 120°C (originated primarily from the electrocoat) generally did not change with weathering; except for system 8 which did not contain any UVA and thus showed (**Figure 4.17C** for system 8) greater weathering effects. The lower glass transition temperature at around 70°C originating from the clear-coat decreased with ageing (**Figure 4.17**), in the same way as was seen from the

tension analysis (for example in **Figure 4.14**. for the different coating systems). The relative values of the cross-link density from the bending analysis increased for all systems, a greater change was seen in the water-borne 6c than in the solvent-borne 3, again as shown in the results from the tension analysis (**Figure 4.17**).

4.3.6 Overview of the differences in weathering behaviour of the solvent-borne and water-borne coating systems and the effect of the different analytical techniques used in assessing their resistance to weathering

Several different methods have now been used to analyse the responses of the different coating systems to the weathering regimes, ranging from the simple optical microscopy (OM) showing the visual changes to the surfaces of the coatings to depth profiling using thermal analysis showing the changes in the glass transition temperature of the different layers of the coating after weathering. This section aims to compare the different techniques that have been used to assess how the different coating systems react to weathering. At the end of chapter 5, a further section will compare the performance of the different coating systems after weathering (with particular reference to comparing the solvent-borne and water-borne coating systems).

The simple optical microscopy (OM) method showed the visual changes to the surface of the coating but was found to be only qualitative and very subjective [**57**]. The surface gloss measurement which is a commonly used method for assessing automotive coatings [**1, 2, and 53**] enabled differences in the performance of the solvent-borne and water-borne coatings to be seen. However, differences between the water-borne clear coatings that contained different levels of stabilisers were too small for the gloss readings to be able to distinguish between their performances (see **Figure 3.26**) which is a major disadvantage of this method. Additionally, problems were encountered when measuring the gloss of the naturally weathered samples by the growth of mildew on the panels. The hardness measurements conducted on the full coating systems gave the first indications of the different types of reactions caused by weathering in the solvent-borne and water-borne clear-coats, with the solvent-borne system 3 showing increased hardness after weathering whereas the hardness of the water-borne systems 6c decreased (**Figure 3.4**). It is thought that the observed increase in hardness in the

solvent-borne system 3 with weathering is most likely to be due to an increase in the extent of cross-linking and similarly the decrease in the case of the water-borne systems (6c and 8) suggests a dominance of chain scission reactions during weathering. This is supported by literature results which illustrate the clear competition between these two types of reactions **[53].**

Both FTIR spectroscopic methods (ATR on the surface of the full systems, **Figures 3.16 and 3.17** and transmission on the microtomed slices (depth profiling), **Figures 3.18-3.25, 3.30, 3.13**) proved very useful in assessing the performance of the different coating systems after weathering. The measurement of the photoxidation index (Δ PI) were used to compare the photoxidation resistance of the different coating families **[8]** with the assumption that the long-term weathering performance of coatings is determined mainly by the coatings' ability to resist photodegradation **[12].** The DMA tension analysis of the microtomed films enabled changes in physical properties (of the glass transition temperature and the relative level of cross-linking) to be determined in all of the coating systems and was very useful in distinguishing the differences caused by weathering in the different coating systems and the level of erosion was also determined and gave similar answers to the erosion determined by the photographs of the microtomed slices (**Figure 3.8** for **FTIR 4.19** for DMA).

Thus the methods used were all useful in determining differences between the different systems after weathering and can be compared. Relationships were seen between the measurements of the photoxidation index and the glass transition temperature (using the third microtomed slice for both methods, **Figure 4.21**). For all of the systems examined (except the unstabilized system 8), the ΔTg decreased after the CAM weathering, while the ΔPI increased. The ΔPI was a measure of the chemical changes undergone by the coating systems after weathering, whereas the glass transition temperature is a physical property of the coating (but is also related to the chemical structure of the coating), so it was useful to see a strong relationship between the two parameters, although care must be taken when assessing a coating that does not contain UVA (such as system 8), due to the differences in the change in glass transition temperatures observed.

The increase in ΔPI after weathering was also compared with the hardness of the coatings after 1000 hours of weathering (**Figure 4.22**). However, although the change

in hardness of the coating after weathering depended upon whether the clear-coat was solvent-borne or water-borne, the ΔPI always increased after weathering. The ΔPI is a generic measure of the level of the photoxidation reactions in the coating and the change in hardness is related to the changes in the structure of the clear-coat of the coating system caused by weathering. The main advantage of the hardness tests were that they were carried out on the full coating system and thus microtoming was not required and a difference in the weathering behavior of the solvent-borne and water-borne coating systems was seen. Finally the changes in ΔPI were also compared to the level of erosion (determined by the photographs of the microtomed slices, **Figure 4.23**). It was clearly seen for all the systems examined that with weathering both the level of photoxidation and erosion increased. This was expected as the photodegradation of a coating system may cause erosion to occur, so thus as more photoxidation and erosion occurred in the water-borne, unstabilized (with respect to UVA) blue system 8, and the least erosion and photoxidation was seen in the solvent-borne, blue, stabilized system 3. However both methods relied on using the same fragile microtomed slices, so any resultant damage caused to them would influence both sets of results.

The results from the two main thermal parameters determined from the thermal analysis were also compared; the glass transition temperature and the relative cross-link density (**Figure 4.24**). Although the glass transition temperature fell after weathering for both systems examined, the changes in the relative cross-link density were less clear, for the solvent and water-borne systems. Thus the DMA method was very useful as it allowed different factors of the weathering of the coating systems to be examined, where the systems may behave differently for the parameters (for example, it was shown that the glass transition temperature of the unstabilized system 8 (with respect to the level of UVA) fell after weathering, whereas for all other systems after weathering the glass transition temperature increased (**Figure 4.14**).

All of the methods used showed that the changes occurring in the automotive clear-coats after weathering could be assessed in different ways. The ΔPI was very useful of assessing the generic photoxidation of different coating types, whereas the DMA allowed both the level of erosion, the glass transition temperature and the relative cross-link density of the different coating systems to be determined.

Table 4.2 Depth profiling data of tan δ (Tg) and elastic modulus (E'min) for the unexposed and weathered (4000 hours of CAM exposure, except for 6c, which was 2500 hours) for systems 3 (solvent-borne), 6c and 10 (both water-borne). The depths are the nominal layer depths in μm.

Unexposed

Layer	Clear-coat			Base-coat			Primer			Electro-coat		
System	Depth/ μm	Tg/°C	Av. Tg/°C	Depth/ μm	Tg/°C	Av. Tg/°C	Depth/ μm	Tg/°C	Av. Tg/°C	Depth/ μm	Tg/°C	Av. Tg/°C
3	7.5	145.5	142.5	32.5	117	111.0	67.5	106.0	105.0	87.5	115.0	115.5
	17.5	141.0		47.5	107.5		77.5	104.0		97.5	116.0	
	27.5	141.0		57.5	107.5							
6c	12.5	76.0	76.0	42.5	71.5	72.0	57.5	72.5	72.5	67.5	117.5	117.5
	17.5	74.0		47.5	72.0		62.5	72.5				
	27.5	78.0										
	37.5	76.0										
10	7.5	76.0	72.0	52.5	67.5	67.5	62.5	69.0	69.0	77.5	113.0	113.0
	17.5	71.0										
	27.5	70.5										
	37.5	70.5										

Layer	Clear-coat			Base-coat			Primer			Electro-coat		
System	Depth/ μm	E'min MPa	Av. E'min/ Mpa	Depth/ μm	E'min MPa	Av. E'min/ Mpa	Depth/ μm	E'min MPa	Av. E'min/ Mpa	Depth/ μm	E'min MPa	Av. E'min/ Mpa
3	7.5	26000	22333	32.5	36000	33667	67.5	30000	38000	87.5	25000	28500
	17.5	29000		47.5	35000		77.5	46000		97.5	32000	
	27.5	12000		57.5	30000							
6c	12.5	22000	21250	42.5	45000	38500	57.5	45000	43500	67.5	36000	36000
	17.5	25000		47.5	32000		62.5	42000				
	27.5	15000										
	37.5	23000										
10	7.5	27000	24500	52.5	43000	43000	62.5	44000	44000	77.5	31000	31000
	17.5	24000										
	27.5	24000										
	37.5	23000										

CAM Weathered

Layer	Clear-coat			Base-coat			Primer			Electro-coat		
System	Depth /μm	Tg/°C	Av. Tg/°C	Depth /μm	Tg/°C	Av. Tg/°C	Depth /μm	Tg/°C	Av. Tg/°C	Depth /μm	Tg/°C	Av. Tg/°C
3	17.5	144.0	139.0	37.5	90.0	96.5	67.5	97.0	95.0	82.5	112.0	112.0
	22.5	138.0		47.5	101.0		77.5	93.0				
	27.5	135.0		57.5	98.0							
6c	7.5	75.5	72.5	37.5	70.5	68.5	52.5	68.5	68.5	62.5	115.5	115.5
	17.5	70.5		47.5	66.0		57.5	69.0				
	27.5	70.5										
	32.5	72.5										
10	7.5	72.5	67.5	32.5	69.0	71.0	47.5	70.5	70.5	57.5	113.0	113.5
	17.5	64.0		37.5	72.5					67.5	114.0	
	27.5	66.0										

Layer	Clear-coat			Base-coat			Primer			Electro-coat		
System	Depth/ μm	E'min MPa	Av. E'min/ Mpa	Depth/ μm	E'min MPa	Av. E'min/ Mpa	Depth/ μm	E'min MPa	Av. E'min/ Mpa	Depth/ μm	E'min MPa	Av. E'min/ Mpa
3	17.5	28000	26333	37.5	25000	32333	67.5	23000	25000	82.5	27000	27000
	22.5	30000		47.5	35000		77.5	27000				
	27.5	21000		57.5	37000							
6c	7.5	16000	17500	37.5	61000	11200 0	52.5	51000	50500	62.5	51000	51000
	17.5	20000		47.5	51000		57.5	50000				
	27.5	15000										
	32.5	19000										
10	7.5	20000	17667	32.5	24000	72000	47.5	89000	89000	57.5	33000	29500
	17.5	18000		37.5	12000 0					67.5	26000	
	27.5	15000										

Table 4.3 DMA responses for systems 3, 7, 6c and 8 for unexposed and weathered samples using single cantilever bending mode.

Exposure type and time	Tg/^{0}C Upper (EC)	Tg/^{0}C Lower (CC)	E'minE*10 Pa (at 160^{0}C)
System 3			
CAM 1000	116.2	Not seen	1.2
CAM 2000	115.8	Not seen	1.4
System 7			
CAM 666	120.2	76.9	1.4
CAM 1000	119.6	76.9	1.4
CAM 2000	122	76	1.4
System 6c			
Unexposed	119	73.8	1.2
CAM 4000	122.6	70.9	1.8
System 8			
Unexposed	116.1		
CAM 4000	123.3	70.8	

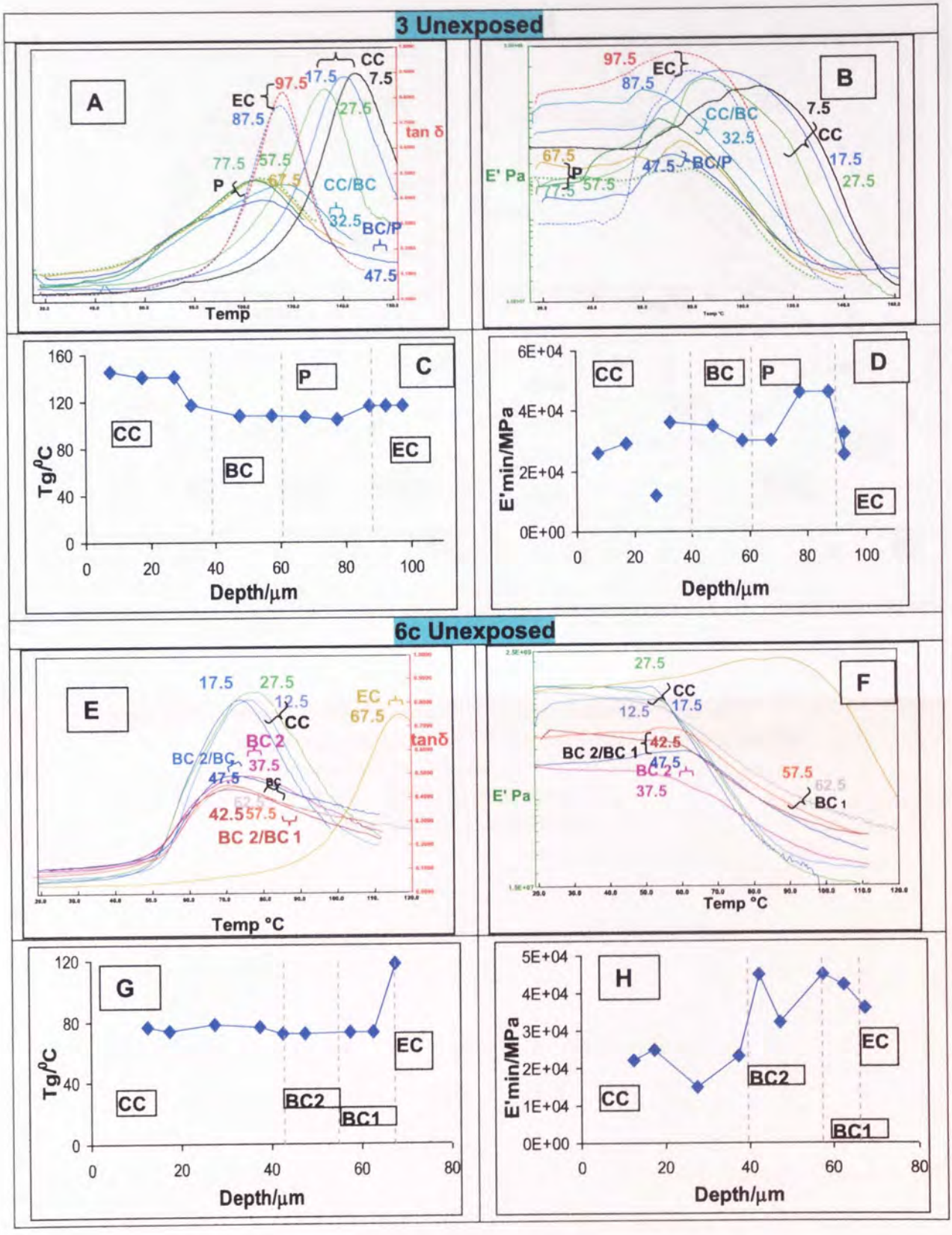

Figure 4.2 Depth profiling of tan δ (Tg) and elastic modulus (E') for unexposed Systems 3 (SB) and 6c (WB). Numbers on curves are the nominal layer depths in μm.

A, C, E, G DMA Tg responses

B, D, F, H DMA E'min responses

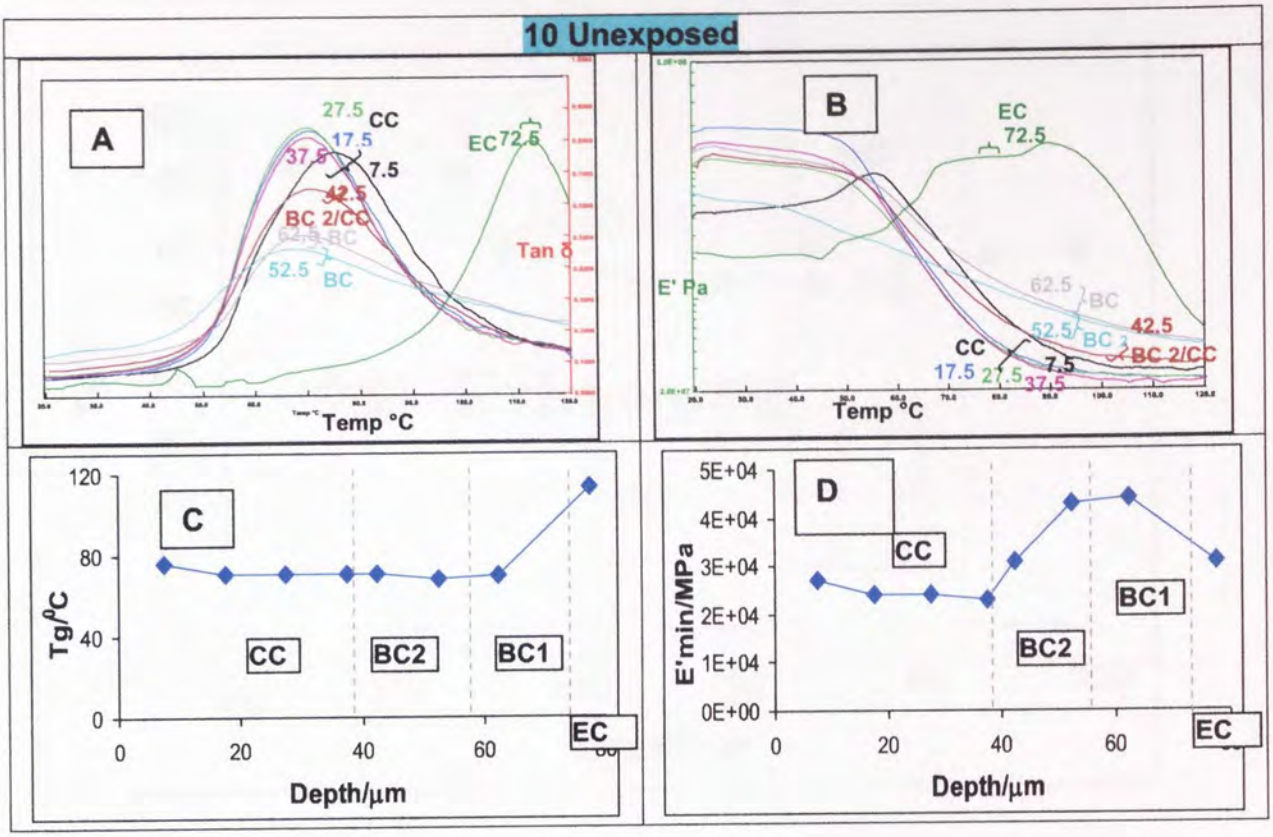

Figure 4.3 Depth profiling of tan δ (Tg) and elastic modulus (E') for unexposed System10 (WB). Numbers on curves are the nominal layer depths in µm.

A, C DMA Tg responses

B, D DMA E'min response

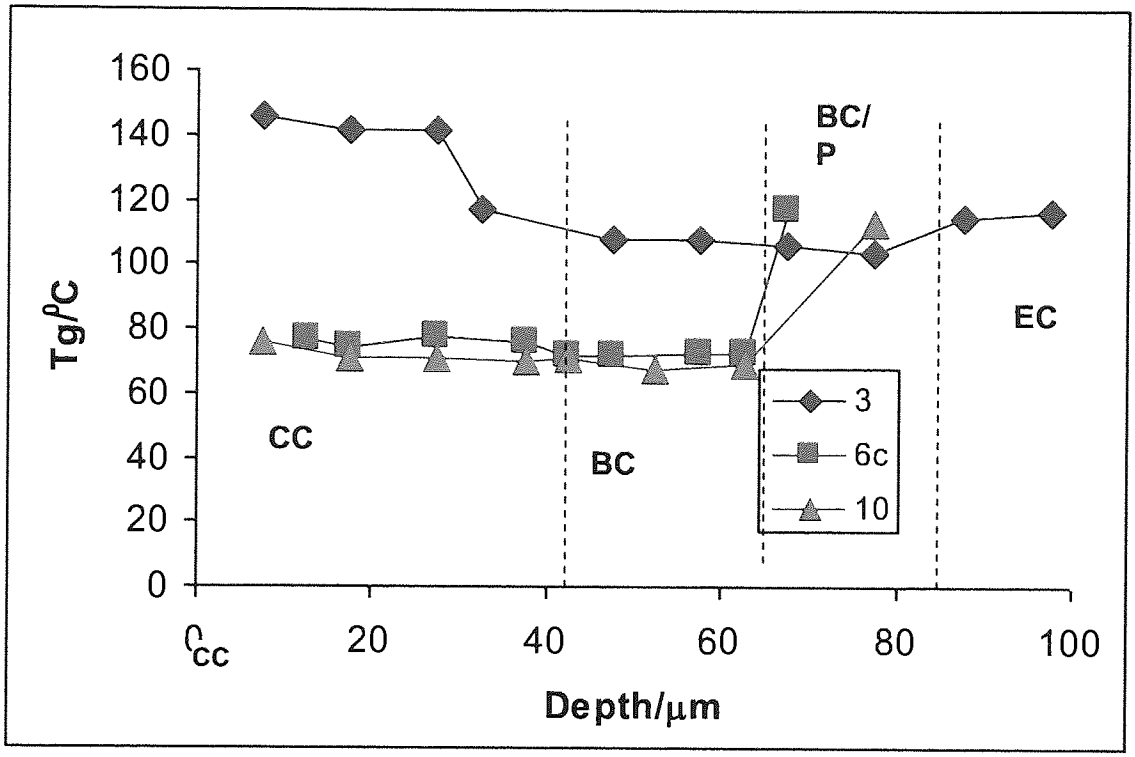

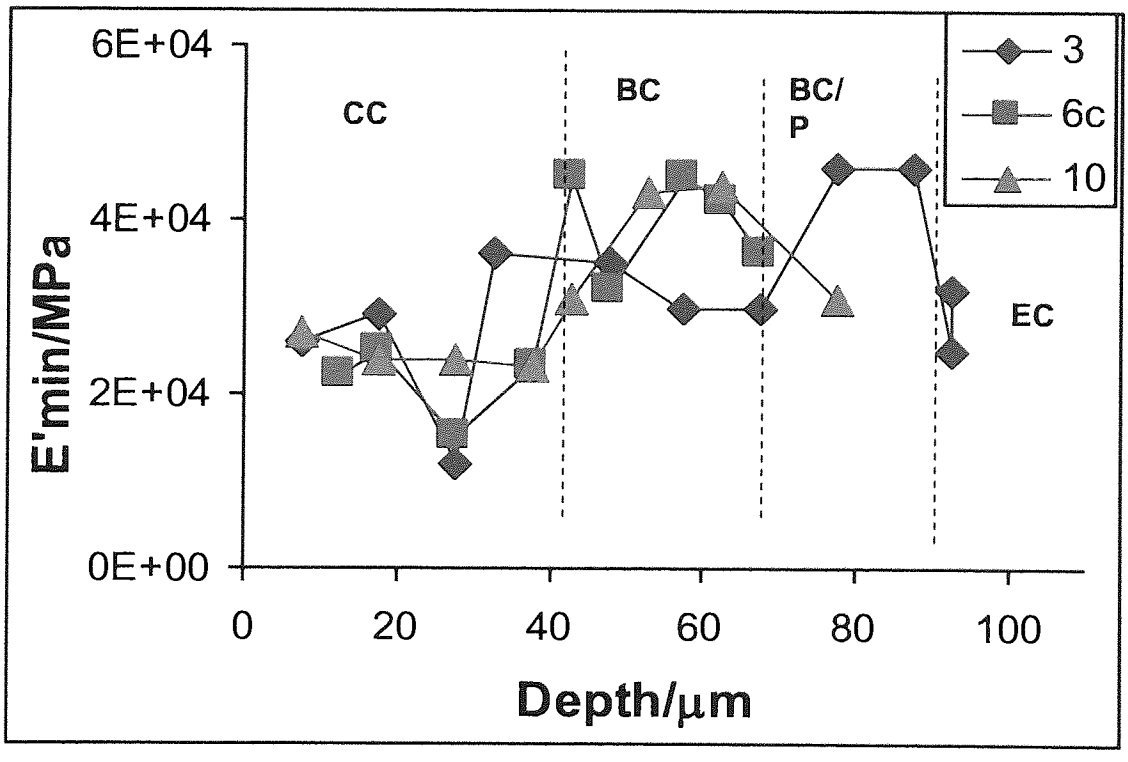

Figure 4.4 Differences in the glass transition temperature and relative level of the cross-link density of the different systems (3, 6c and 10), before weathering experiments.

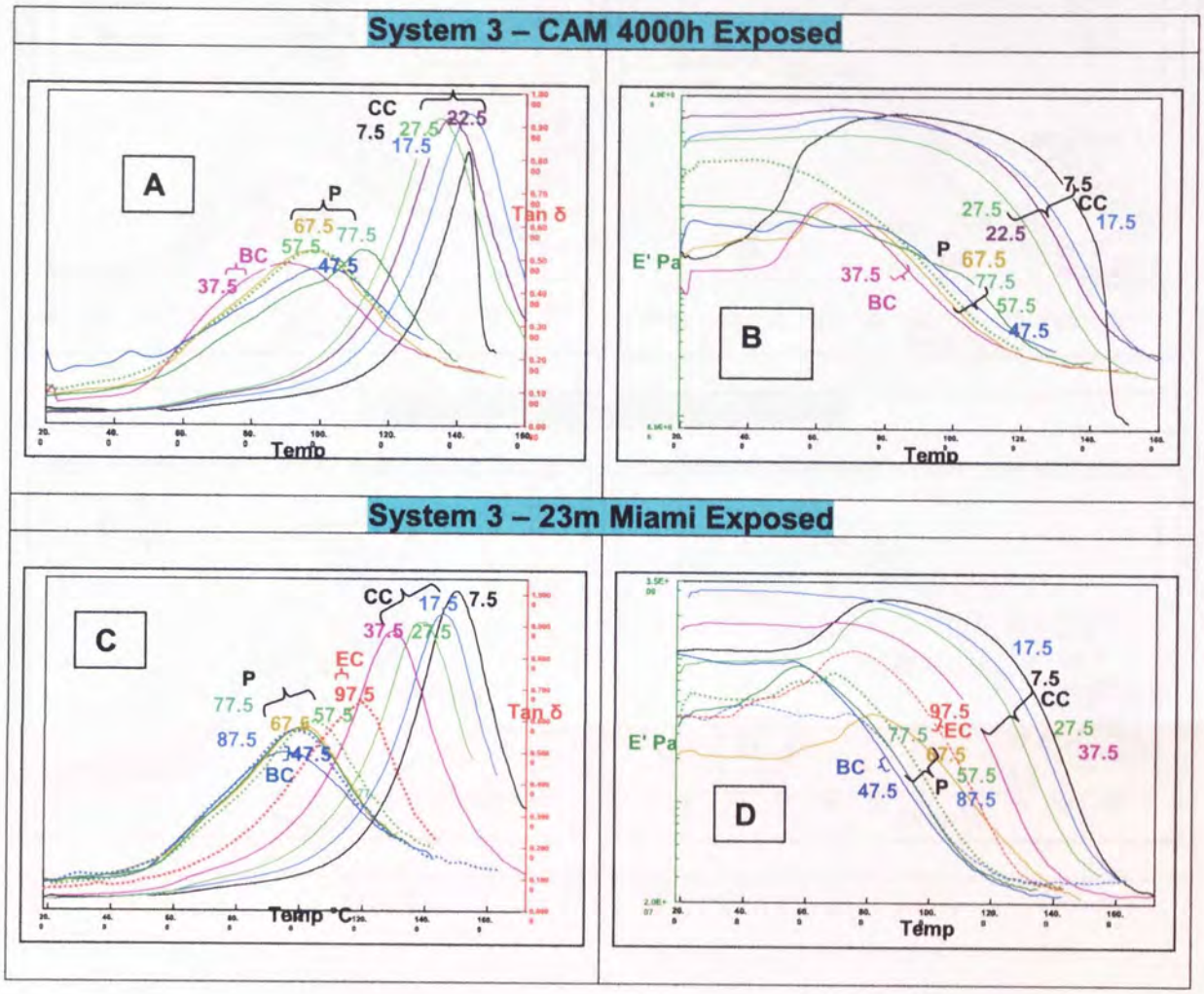

Figure 4.5 Depth profiling of tan δ (Tg) and elastic modulus (E') for exposed microtomed slices of System 3 (SB). Numbers on curves are the nominal layer depths in μm.

A, B 4000 artificial accelerated CAM Exposure

C, D 23months natural weathering in Miami.

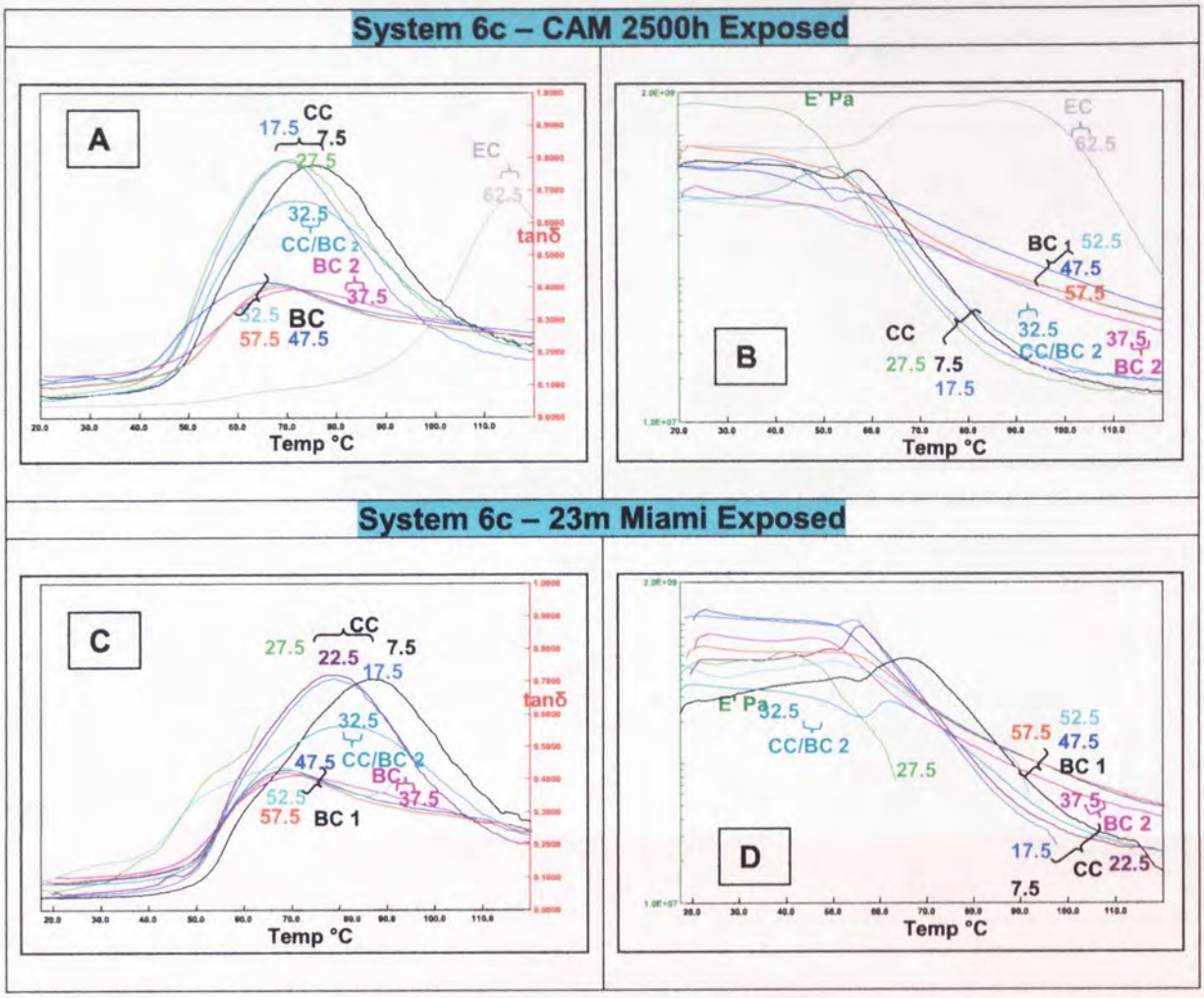

Figure 4.6 Depth profiling of tan δ (Tg) and elastic modulus (E') for exposed microtomed slices of System 6c (WB). Numbers on curves are the nominal layer depths in μm.

A, B 2500 artificial accelerated CAM Exposure

C, D 23months natural weathering in Miami.

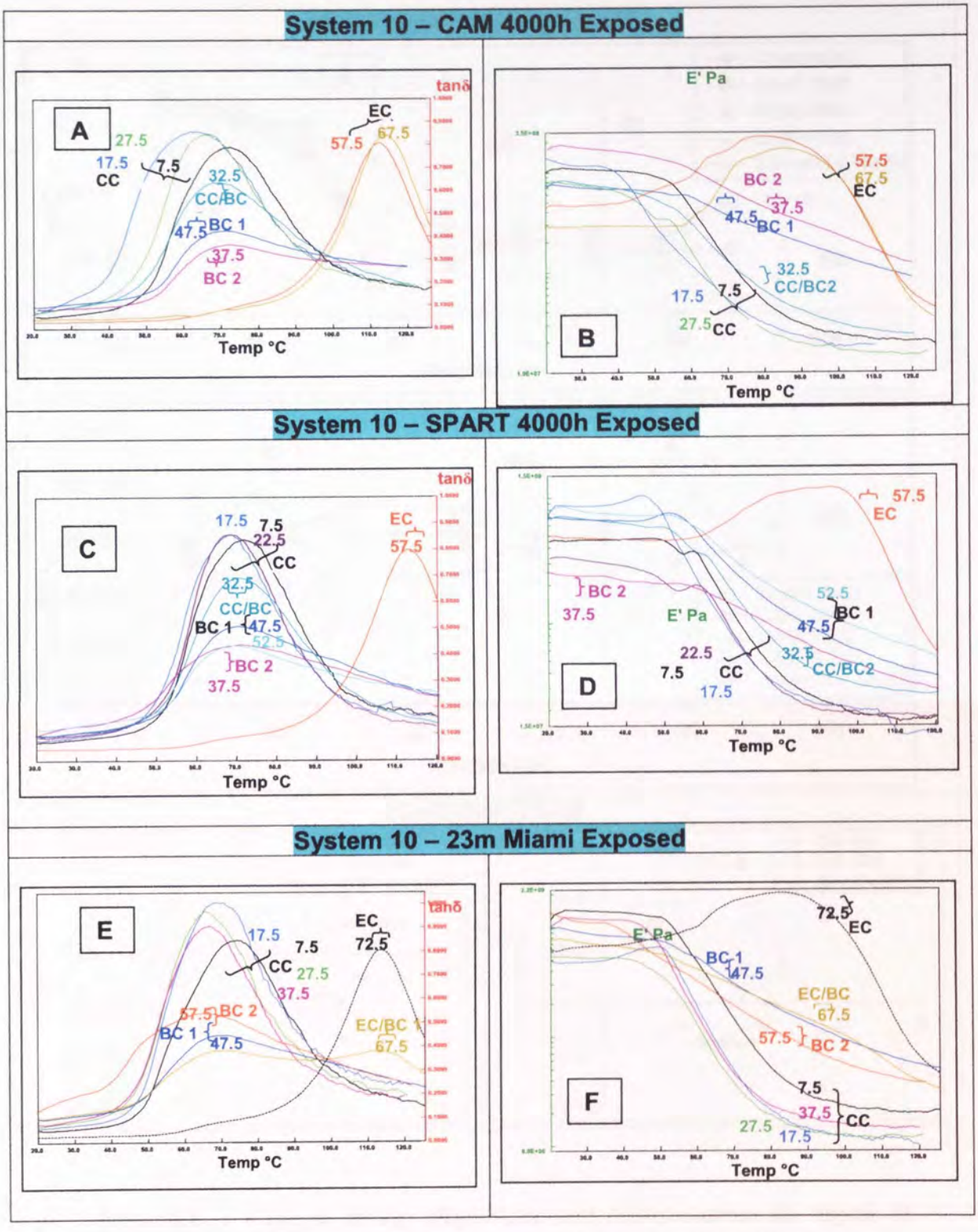

Figure 4.7 Depth profiling of tan δ (Tg) and elastic modulus (E') for exposed microtomed slices of System 10 (WB). Numbers on curves are the nominal layer depths in μm.

A, B 2500 artificial accelerated CAM Exposure
C, D 1000 artificial accelerated SPART Exposure
E, F 23months natural weathering in Miami.

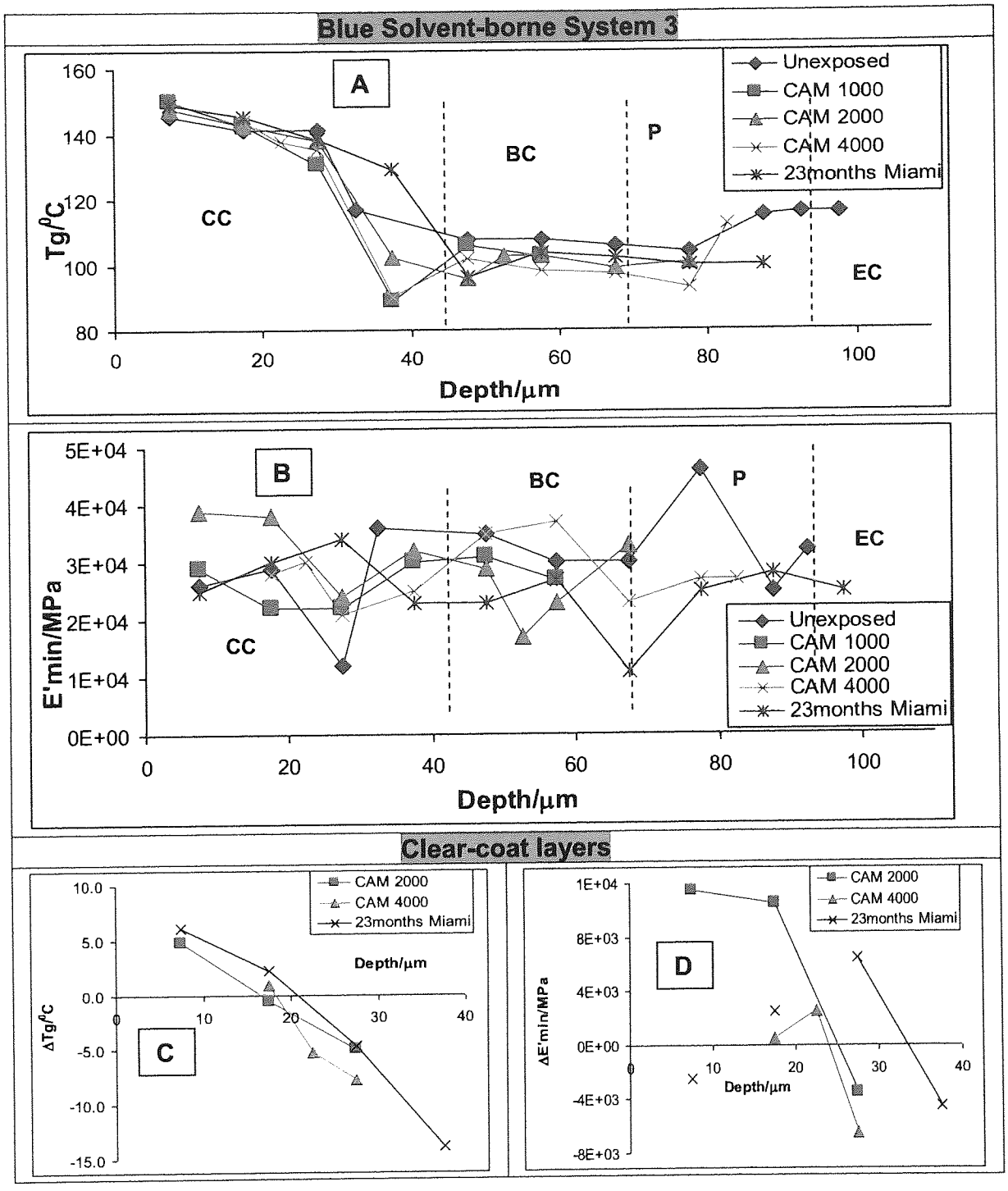

Figure 4.8 Changes in Tg, ΔTg, E'min and ΔE'min across the depths of the coating for system 3 unexposed, and weathered (both artificial and natural). The depths are the nominal layer depths in μm.

$\Delta Change = value_{time=t} - value_{average\ across\ the\ clearcoat\ at\ t=0}$

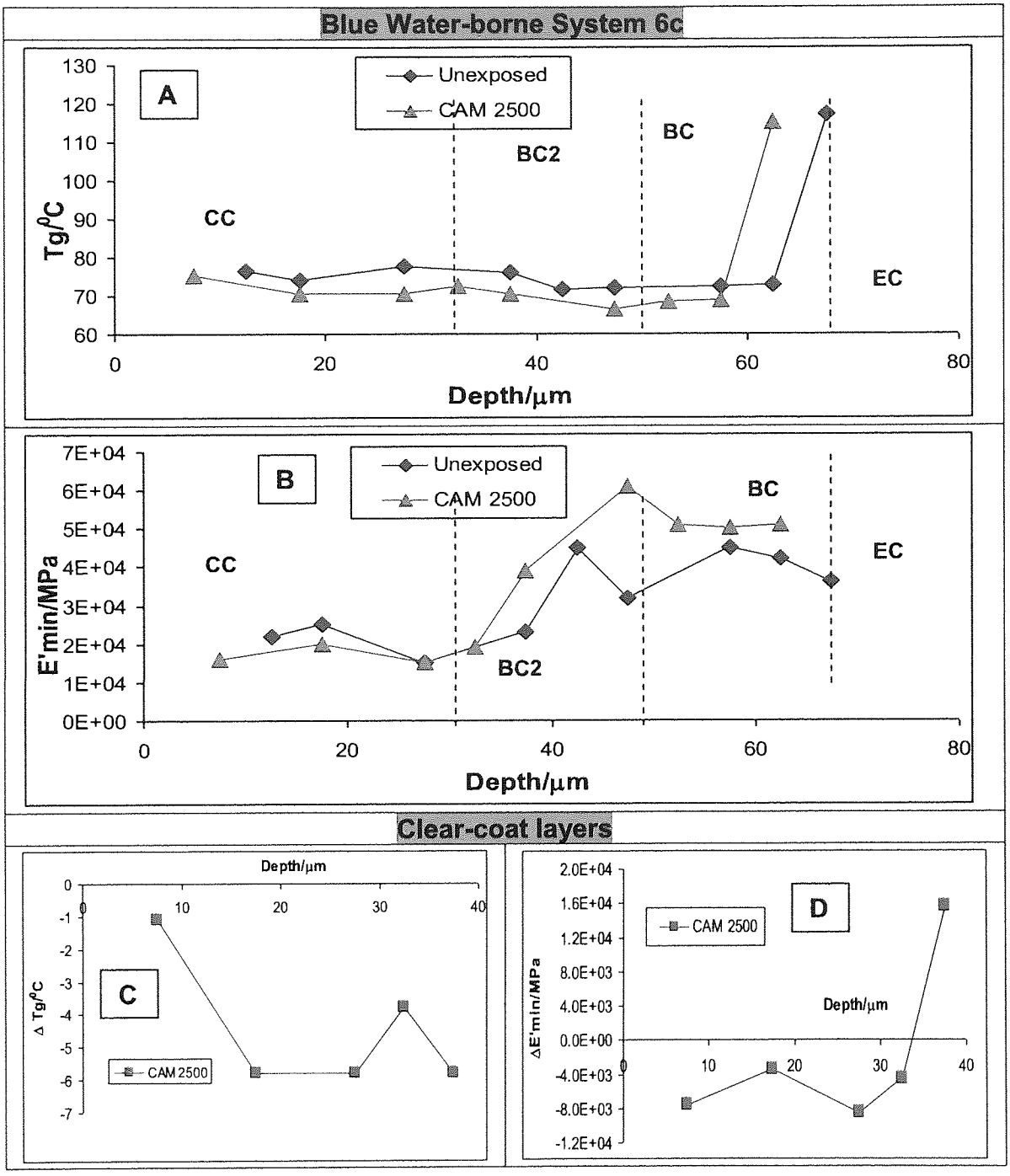

Figure 4.9 Changes in Tg, ΔTg, E'min and ΔE'min across the depths of the coating for system 6c unexposed, and weathered. The depths are the nominal layer depths in µm.
ΔChange = $value_{time=t} - value_{average\ across\ the\ clearcoat\ at\ t=0}$

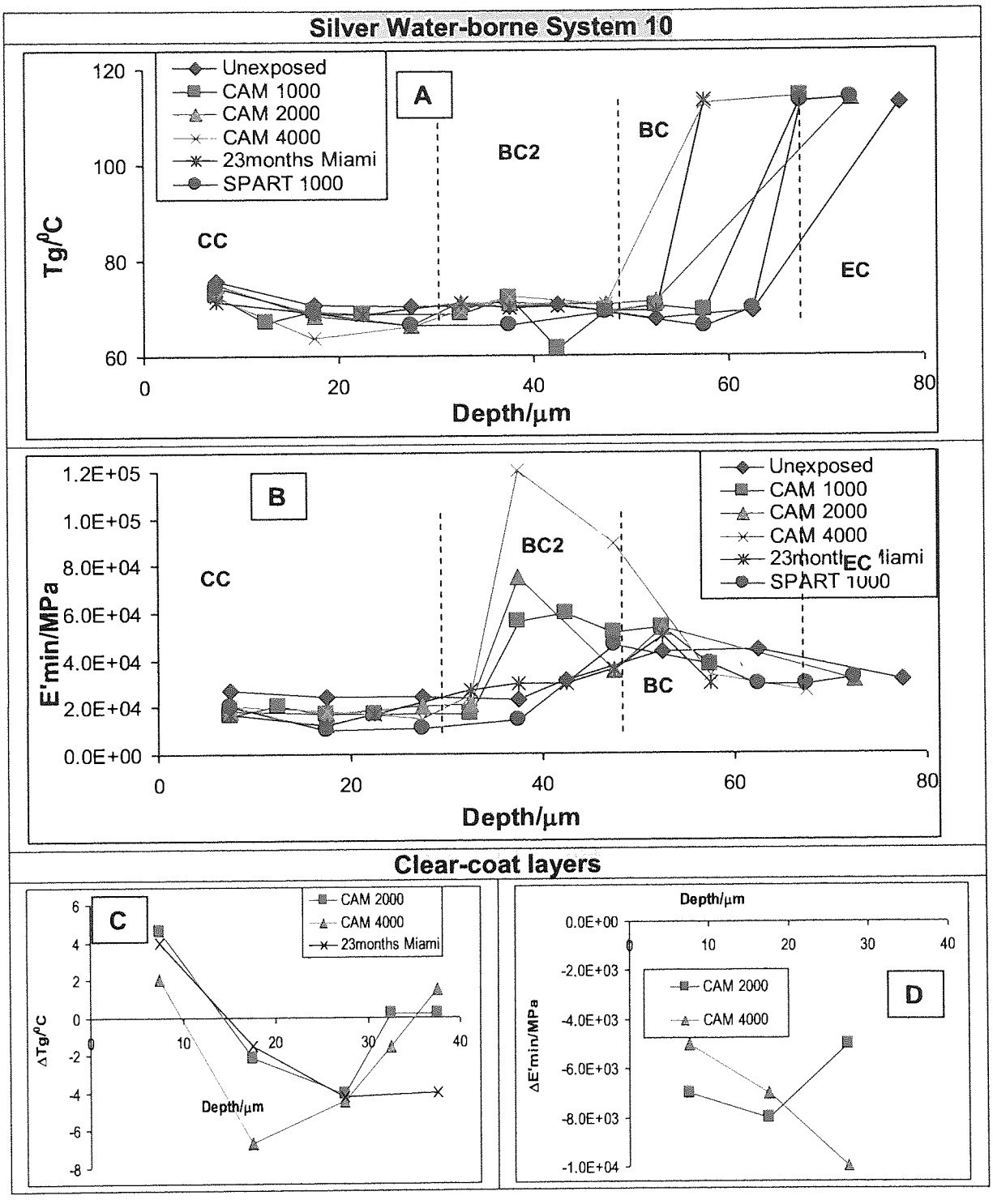

Figure 4.10 Changes in Tg, ΔTg, E'min and ΔE'min across the depths of the coating for system 10 unexposed, and weathered. The depths are the nominal layer depths in µm.
ΔChange = $value_{time=t}$ – $value_{average\ across\ the\ clearcoat\ at\ t=0}$

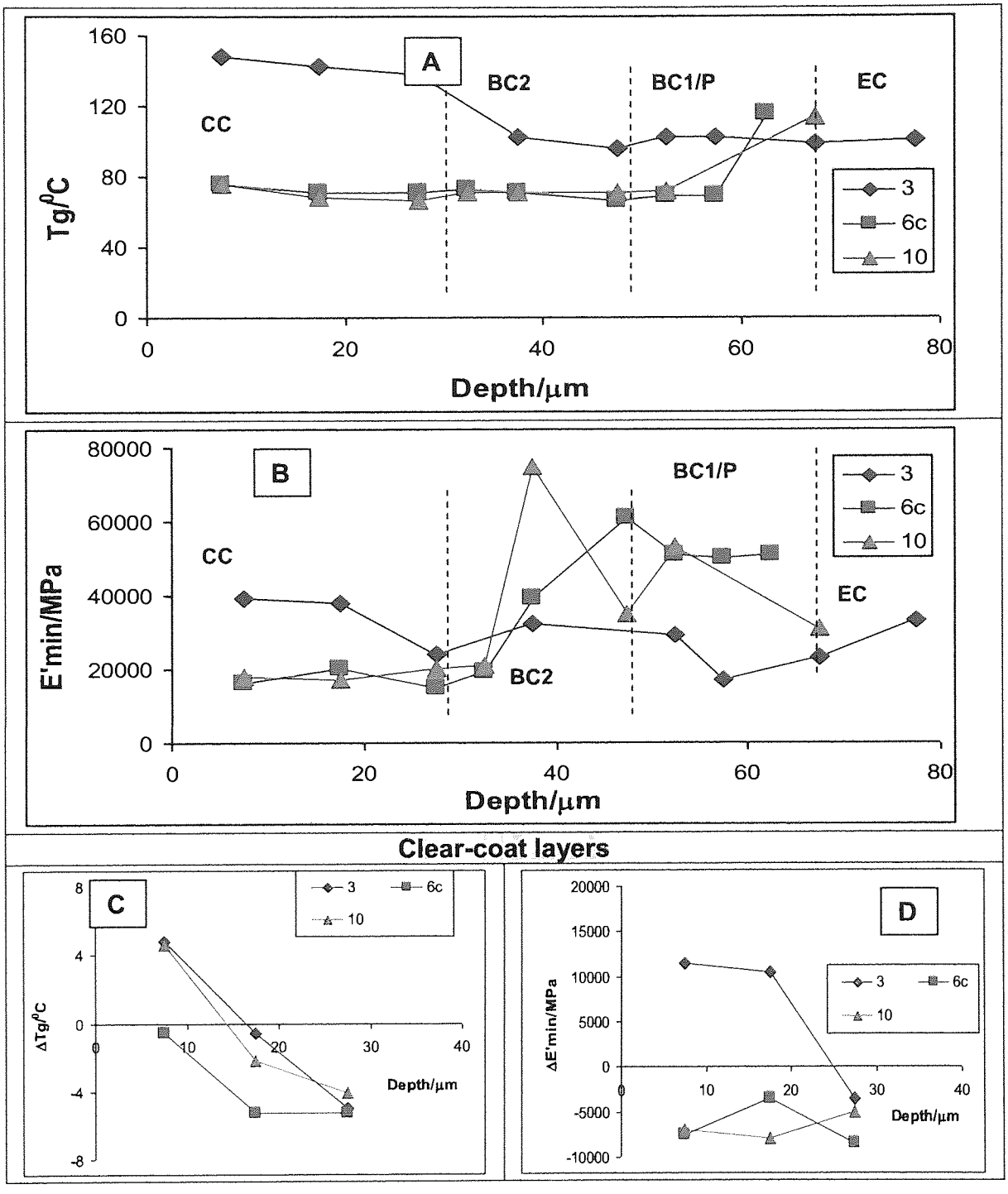

Figure 4.11 Changes in Tg, ΔTg, E'min and ΔE'min across the depths of the coating for systems 3, 6c and 10 after 2500 hours of CAM exposure. The depths are the nominal layer depths in µm.
ΔChange = $value_{time=t}$ – $value_{average\ across\ the\ clearcoat\ at\ t=0}$

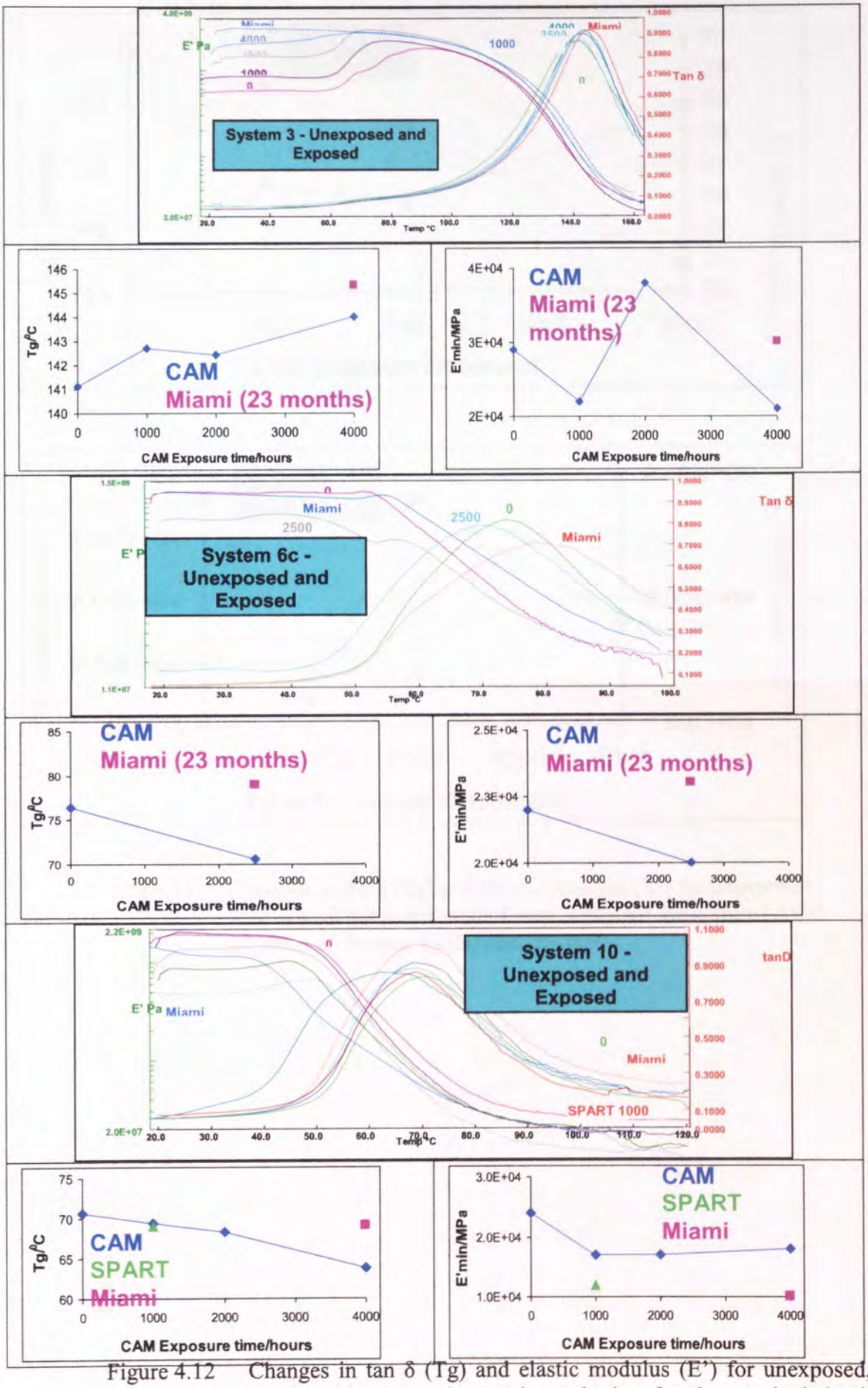

Figure 4.12 Changes in tan δ (Tg) and elastic modulus (E') for unexposed, accelerated aging and natural weathering for the nominal depth of 20μm of System 3 (SB) and 6c (WB). Numbers on curves are the hours of CAM exposure.

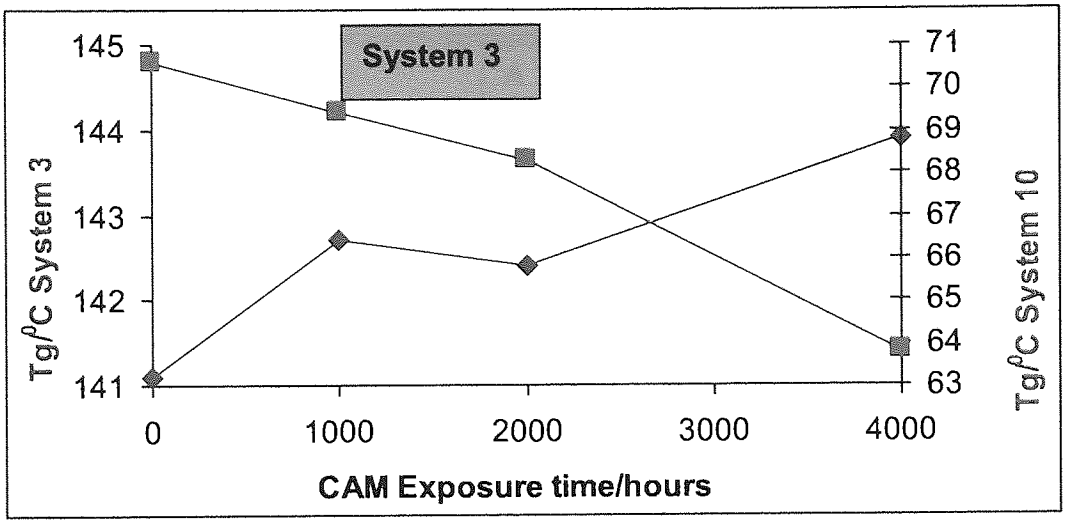

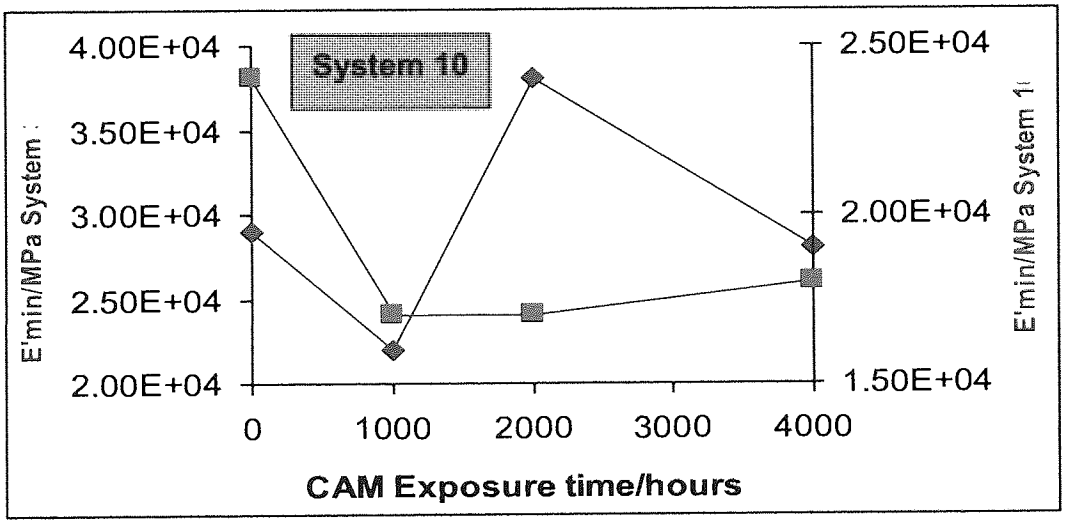

Figure 4.13 Changes in tan δ (Tg) and elastic modulus (E') for unexposed, accelerated aging and natural weathering for the nominal depth of 20μm of System 3 (SB) and 10 (WB).

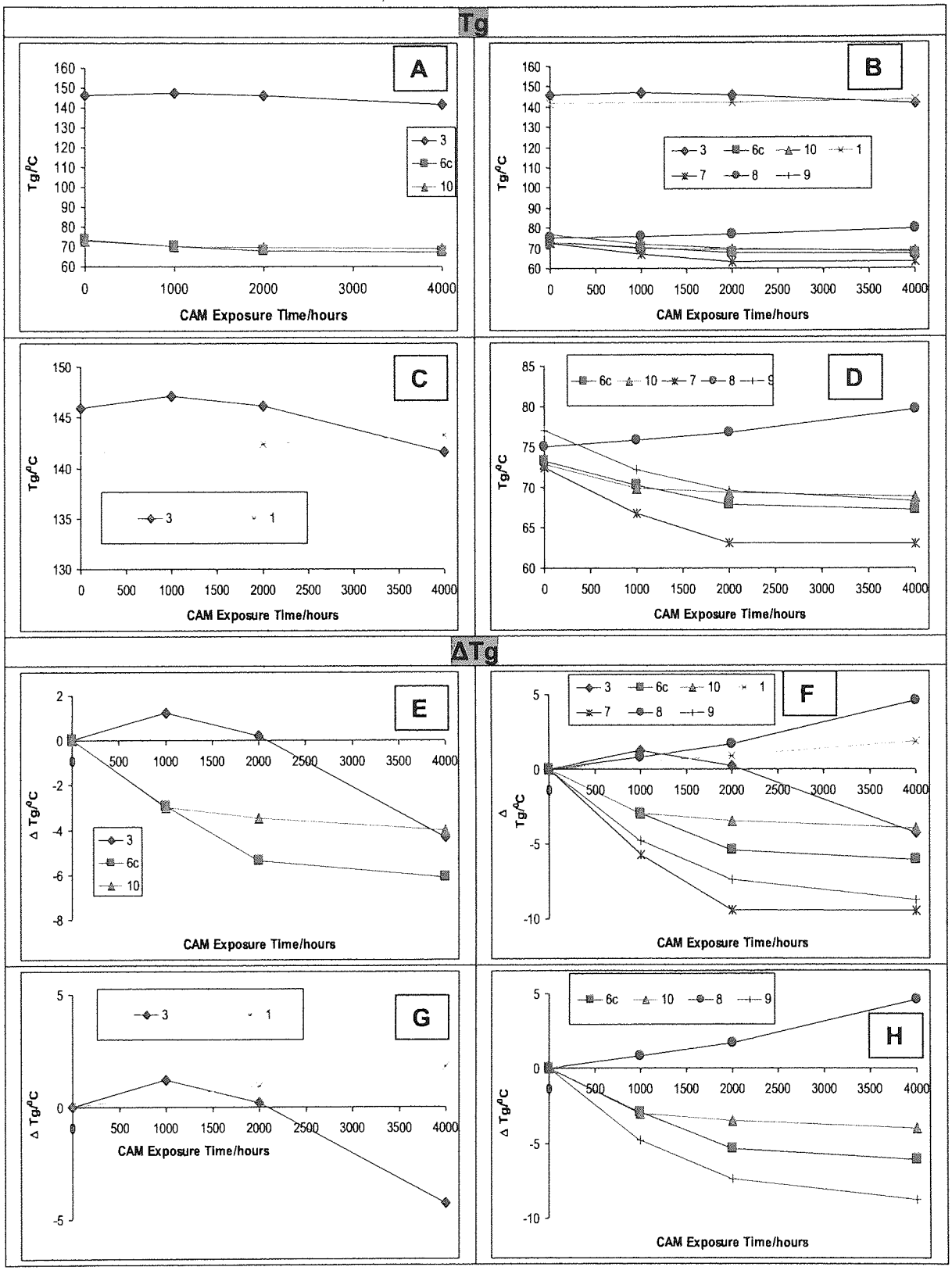

Figure 4.14 Changes in Tg and ΔTg, for the 3rd microtomed slice of systems 1, 3, 6c, 7, 8, 9 and 10 up to 4000 hours of CAM exposure.
$\Delta Change = value_{time=t} - value_{average\ across\ the\ clearcoat\ at\ t=0}$

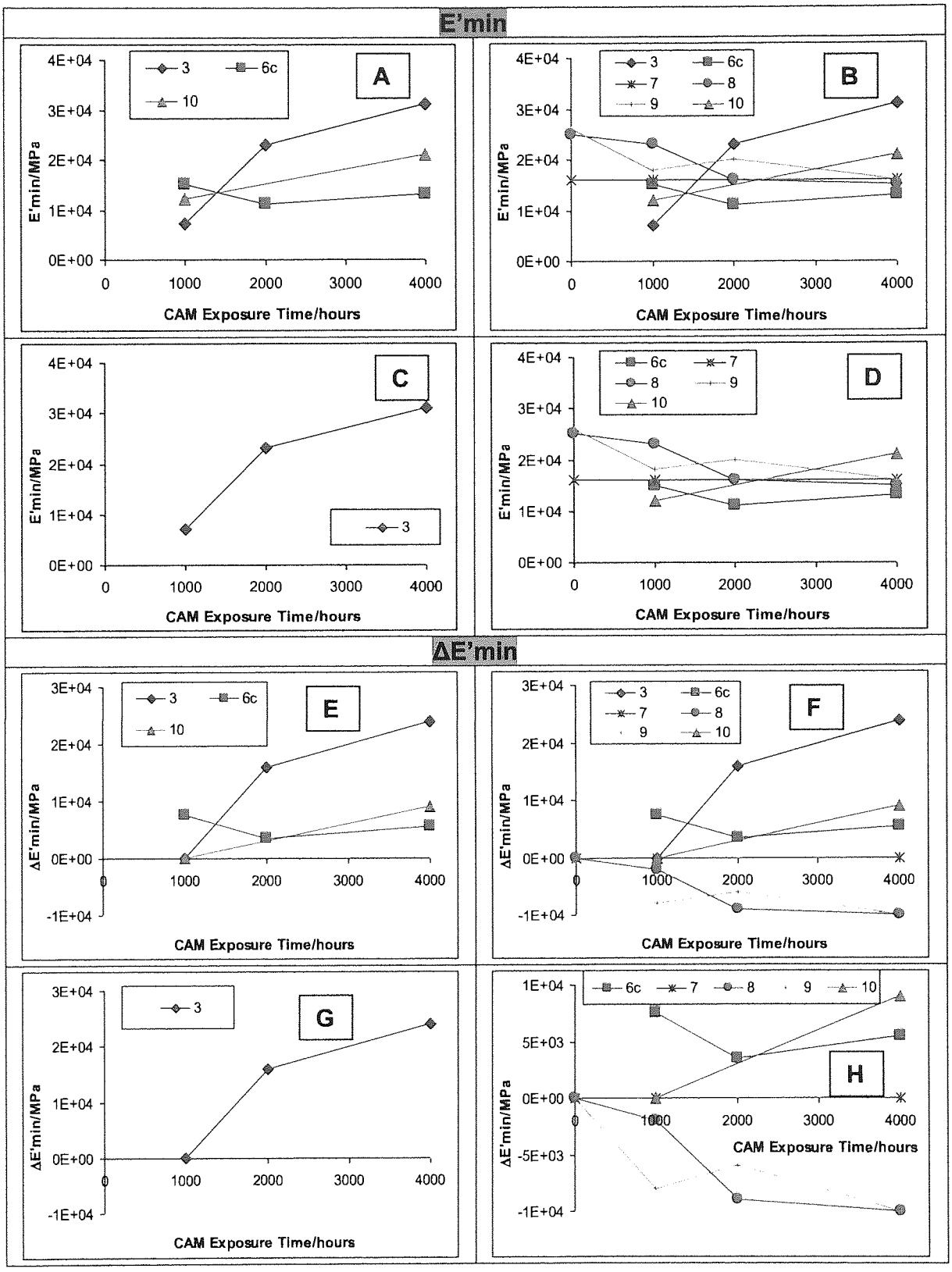

Figure 4.15 Changes in E'_{min} and $\Delta E'_{min}$, for the clear-coat determined from the 3rd microtomed slice of systems 1,3, 6c, 7, 8, 9 and 10 up to 4000 hours of CAM exposure.
$\Delta Change = value_{time=t} - value_{average\ across\ the\ clearcoat\ at\ t=0}$

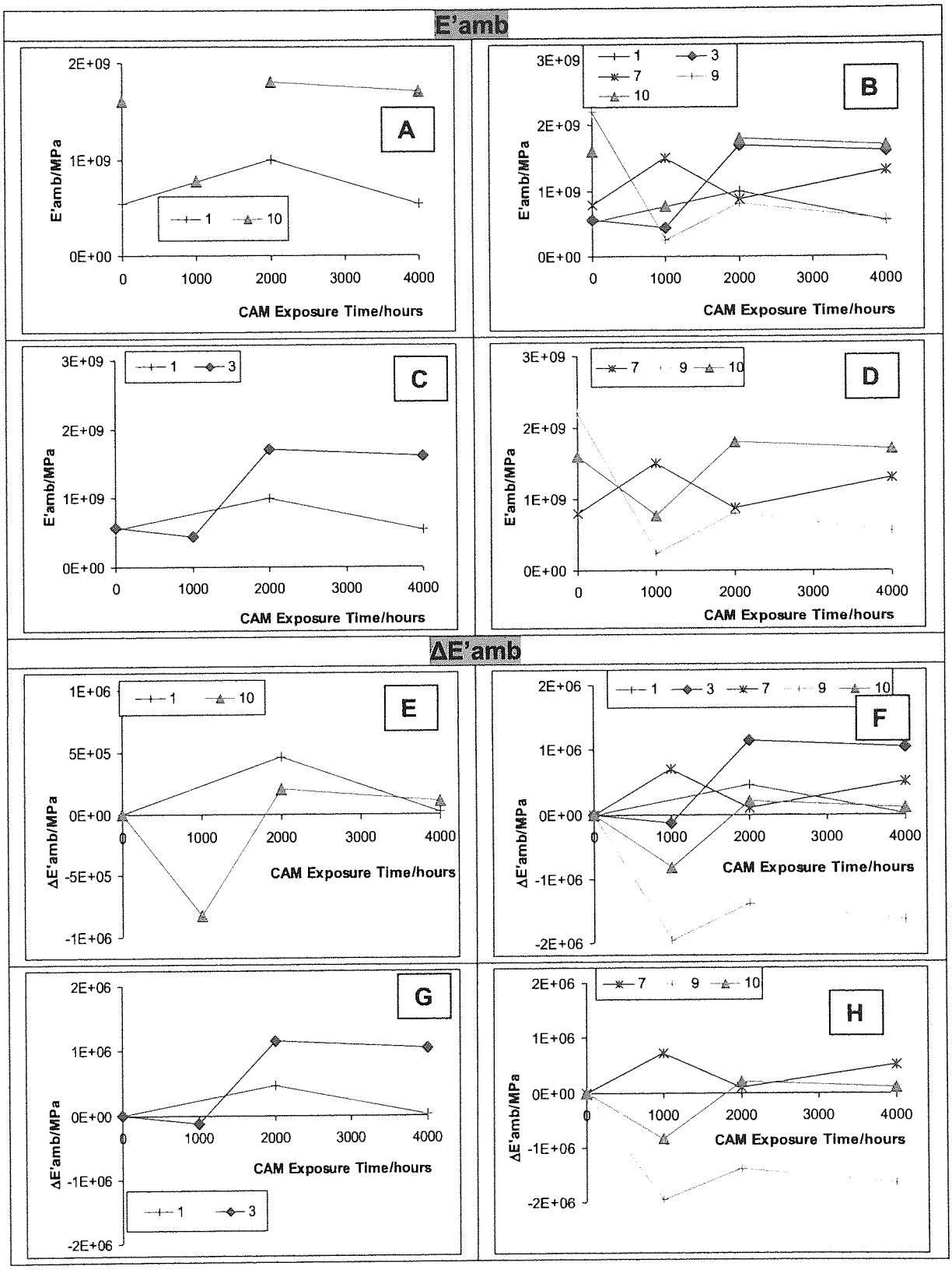

Figure 4.16 Changes in E'_{amb} and $\Delta E'_{amb}$, for the 3rd microtomed slice of systems 1,3, 6c, 7, 8, 9 and 10 up to 4000 hours of CAM exposure.
$\Delta Change = value_{time=t} - value_{average\ across\ the\ clearcoat\ at\ t=0}$

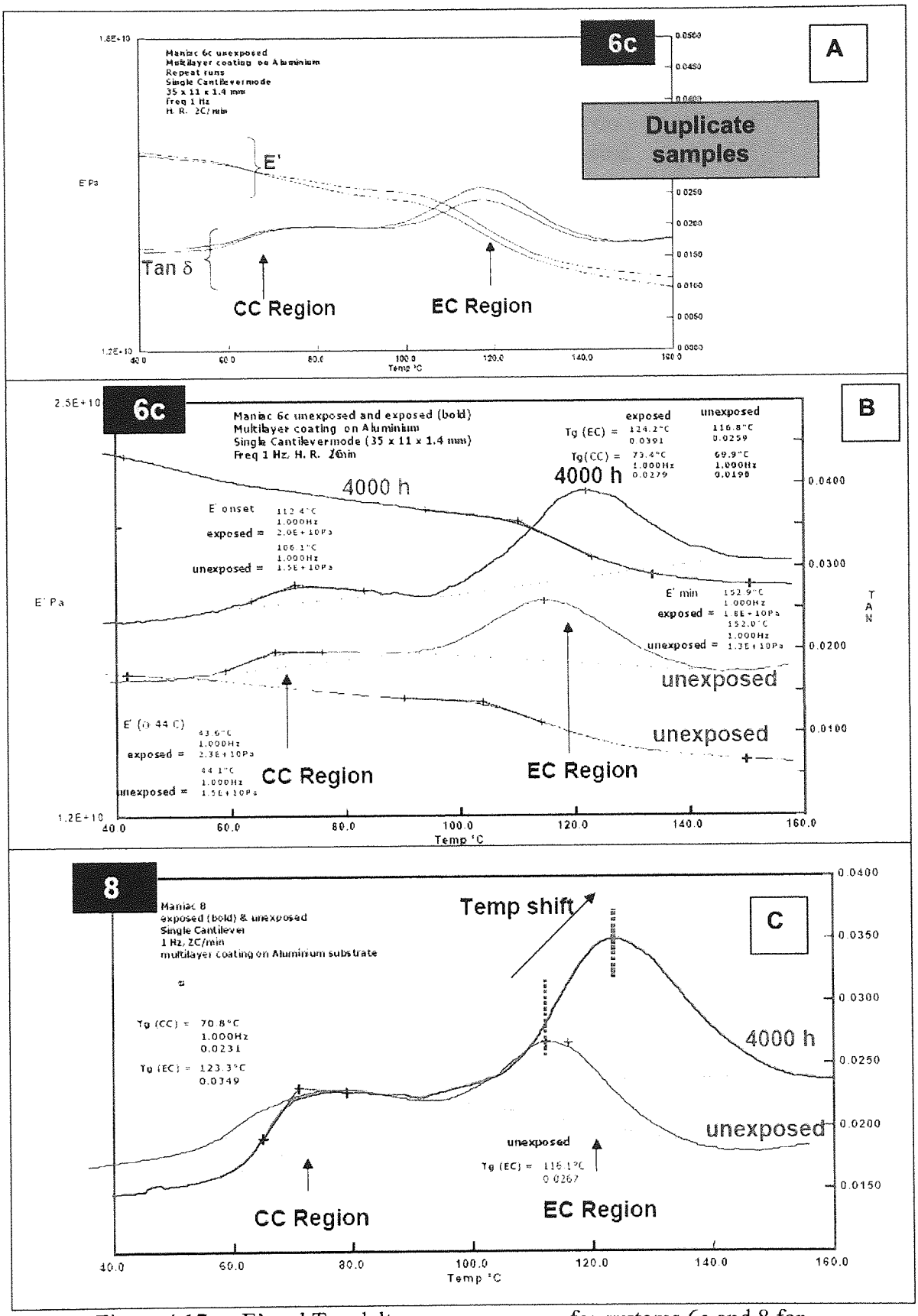

Figure 4.17 E' and Tan delta response curves for systems 6c and 8 for unexposed and weathered samples using single cantilever bending mode, carried out on the full coating systems (not microtomed)

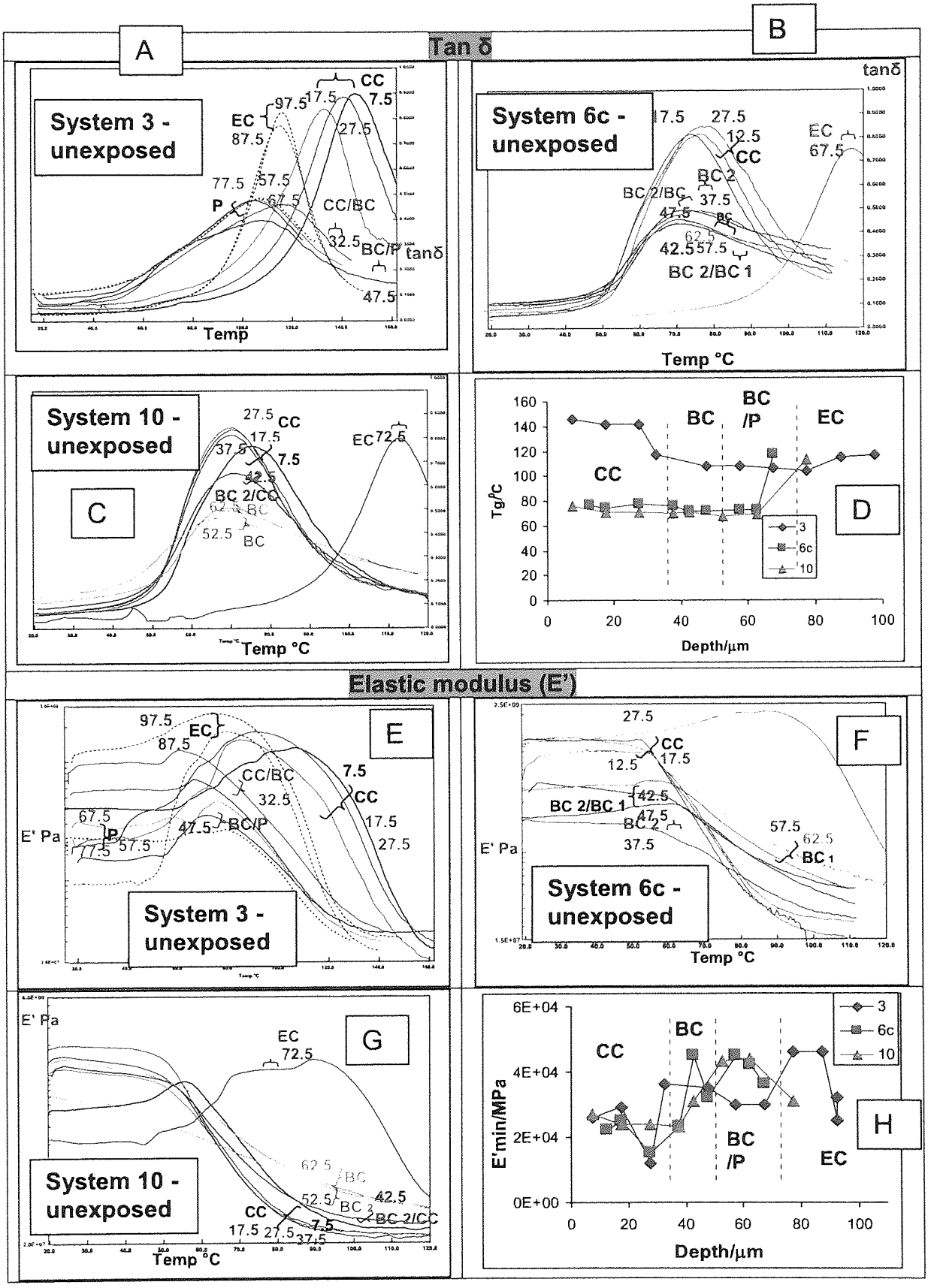

Figure 4.18 Depth profiling of tan δ (Tg) and elastic modulus (E') for unexposed Systems 3 (SB), 6c and 10 (WB) Numbers on curves are the nominal layer depths in µm.

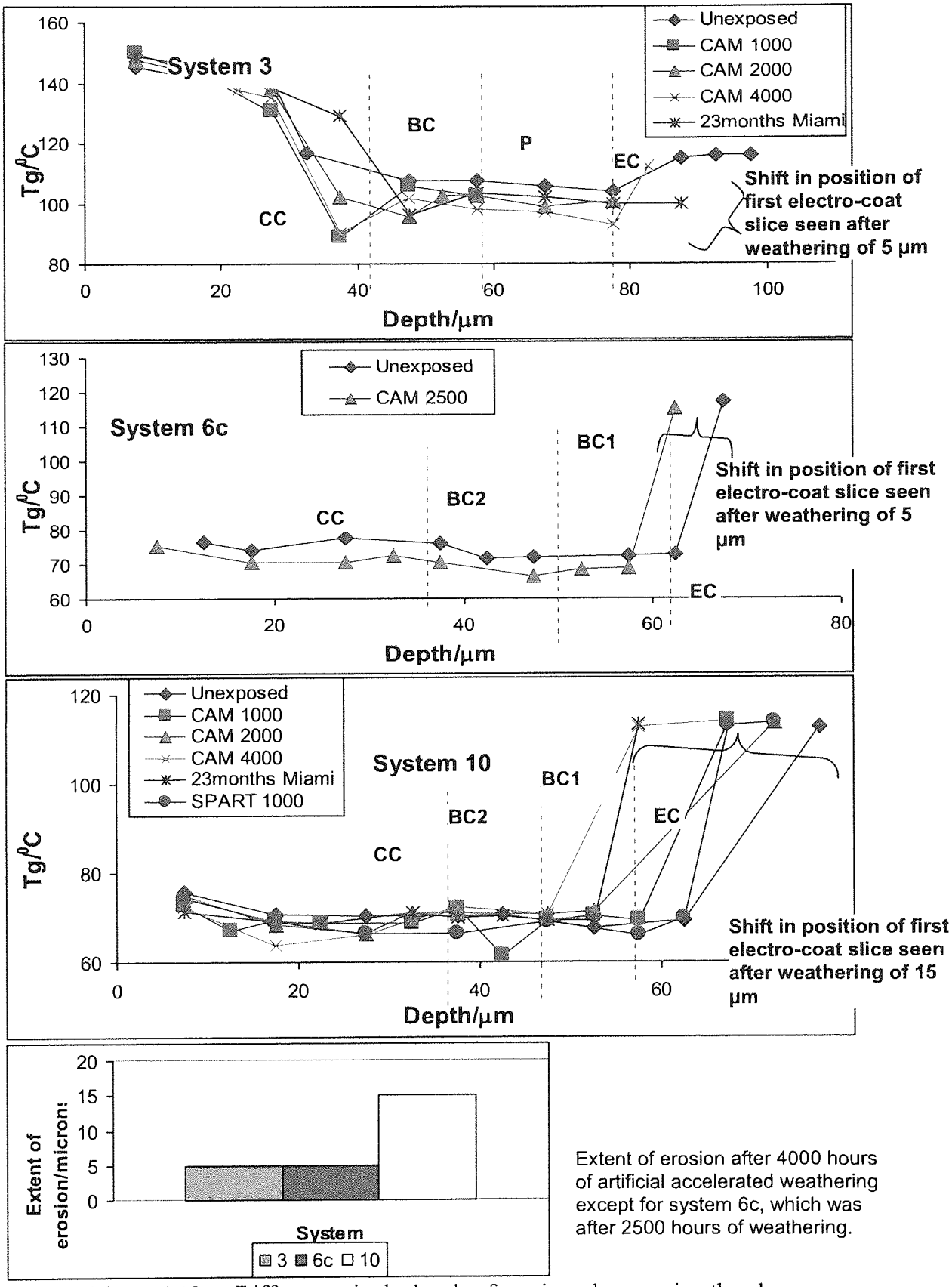

Figure 4.19 Differences in the levels of erosion, shown using the glass transition temperature of the different coating systems (3, 6c and 10). The values of shift were taken as the shift of the first electro-coat slice after weathering compared to the unexposed counterpart.

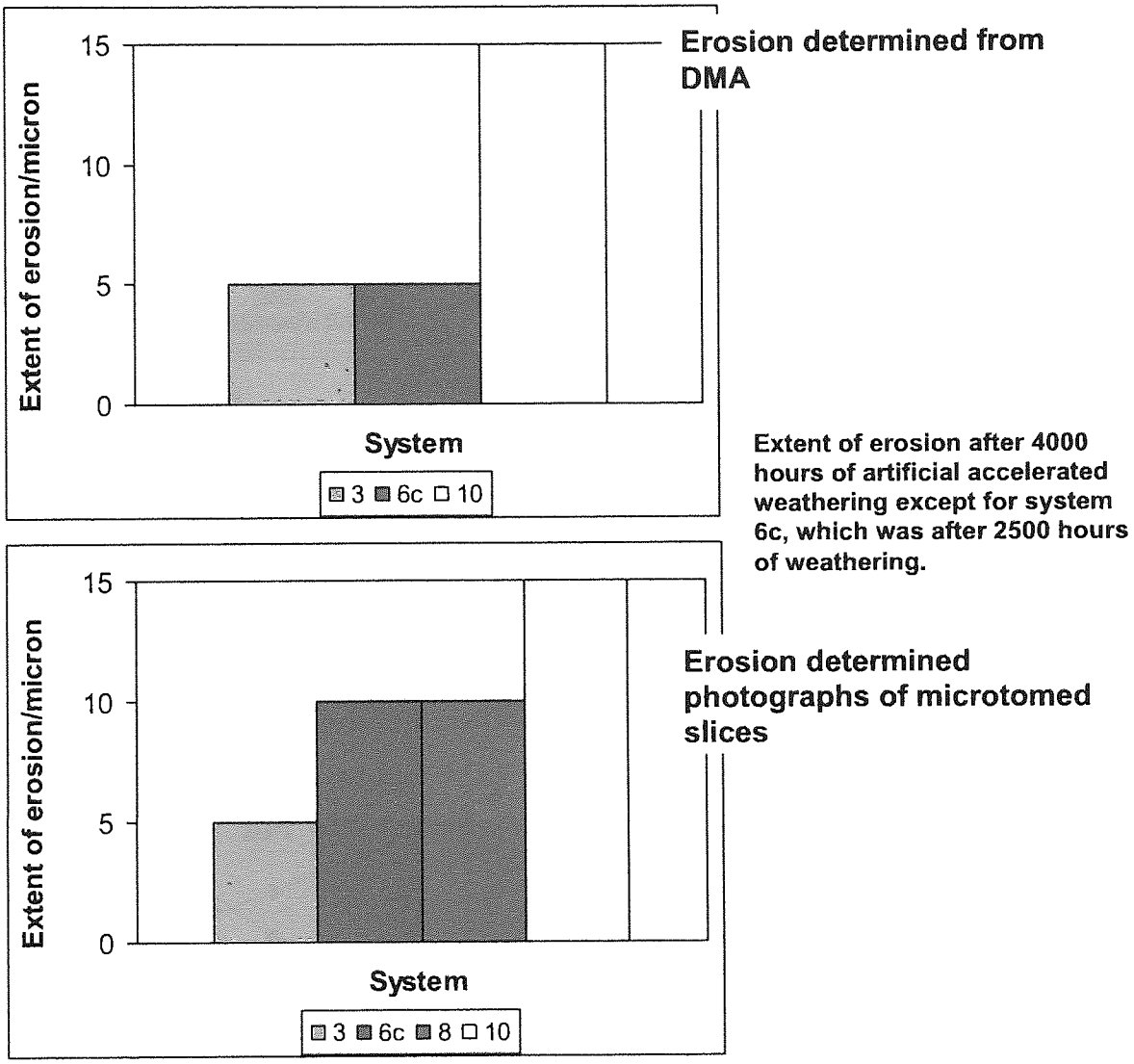

Figure 4.20 Differences in the levels of erosion, shown using the glass transition temperature or the photographs of the microtomed slices of the different coating systems (3, 6c, 8 and 10). The values of shift were taken as the shift of the first electro-coat slice after weathering compared to the unexposed counterpart.

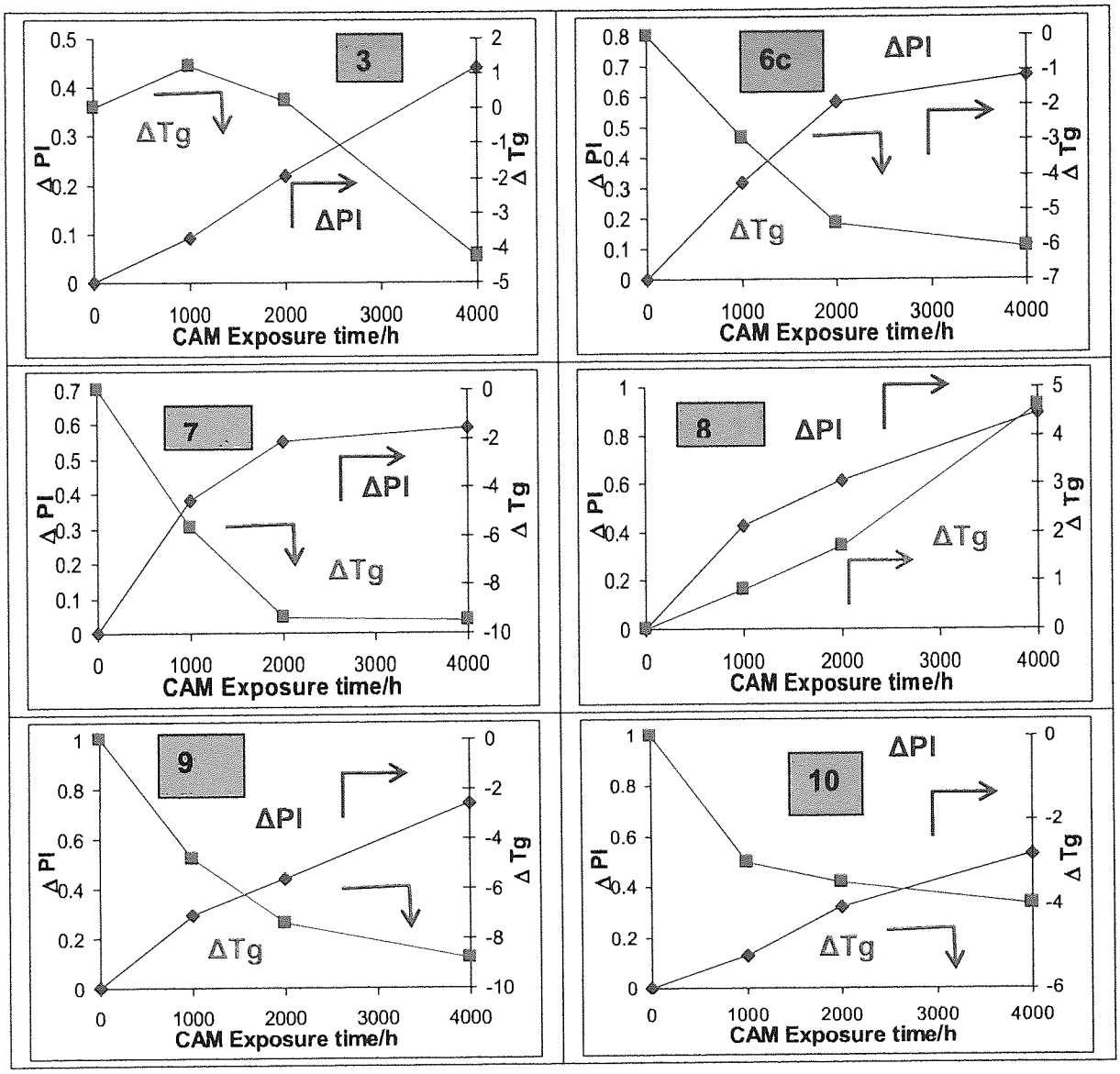

Figure 4.21 Comparison of the changes in ΔTg (from DMA analysis) and ΔPI (transmission mode) CAM weathering for the third microtomed slice systems **3, 6c, 7, 8, 9 and 10.**

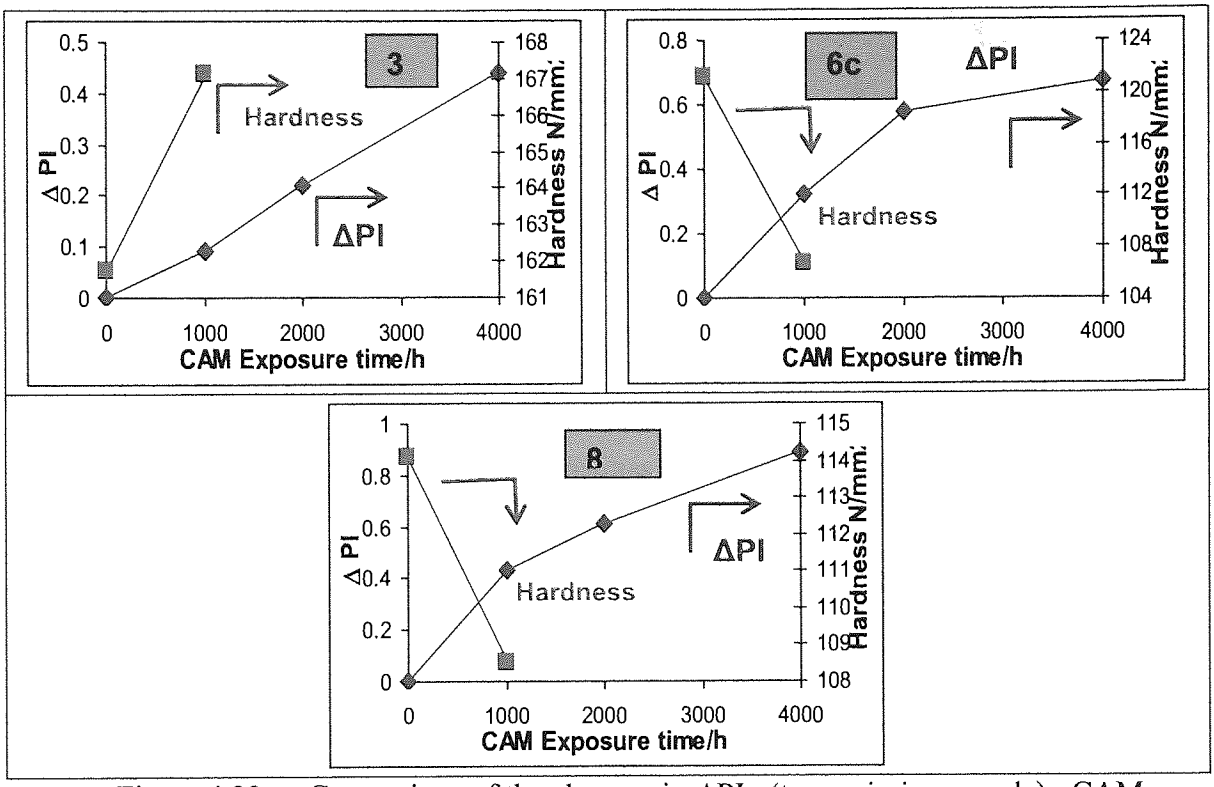

Figure 4.22 Comparison of the changes in ΔPI (transmission mode) CAM weathering for the third microtomed slice systems with hardness loading for systems **3, 6c and 8.**

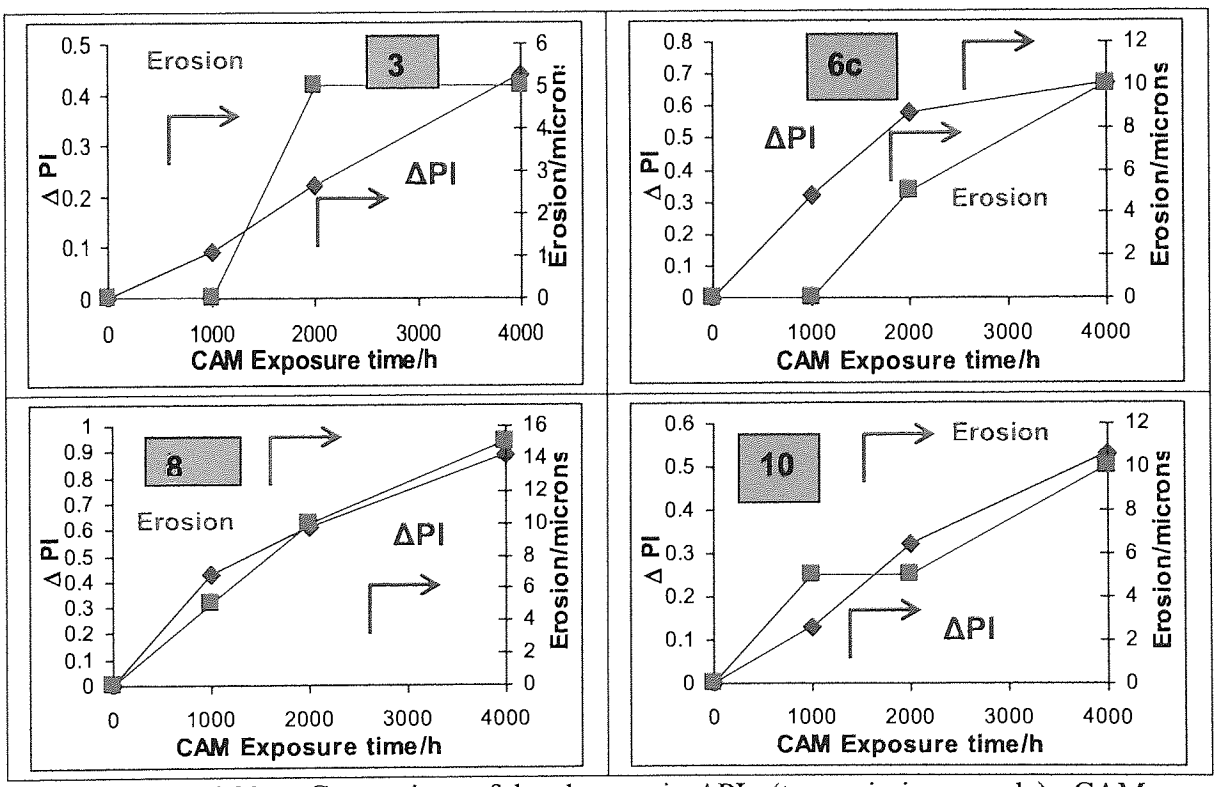

Figure 4.23 Comparison of the changes in ΔPI (transmission mode) CAM weathering and the level of erosion for systems **3, 6c, 8 and 10.**

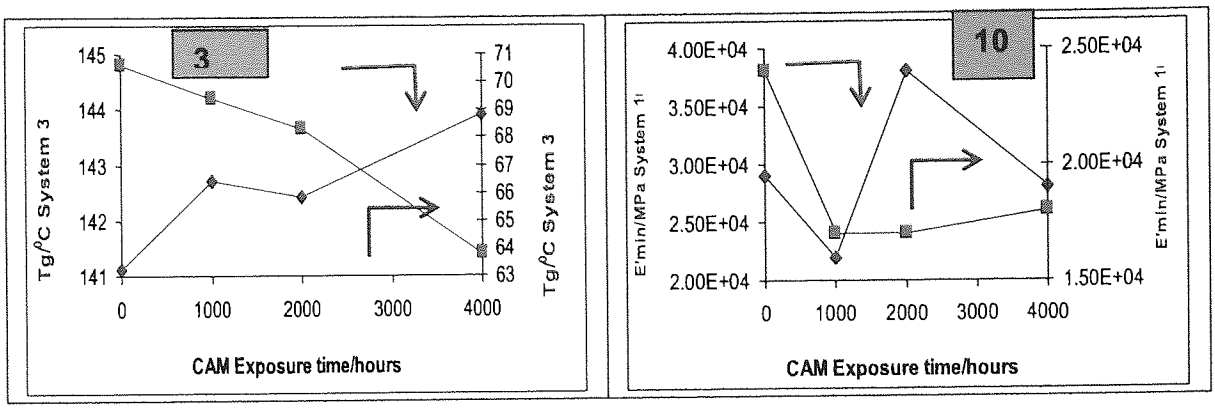

Figure 4.24 Comparison of the changes in the glass transition temperature (Tg) and the relative cross-link density after CAM weathering for systems **3 and 10.**

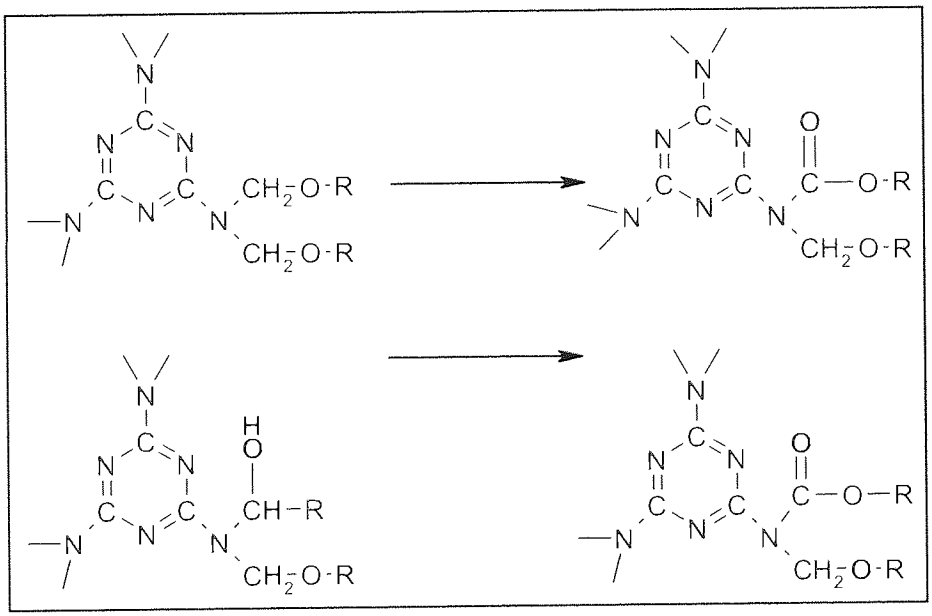

Scheme 4.1 Possible esterification of the alkoxy groups in the melamine resin and in the hydroxyl group.

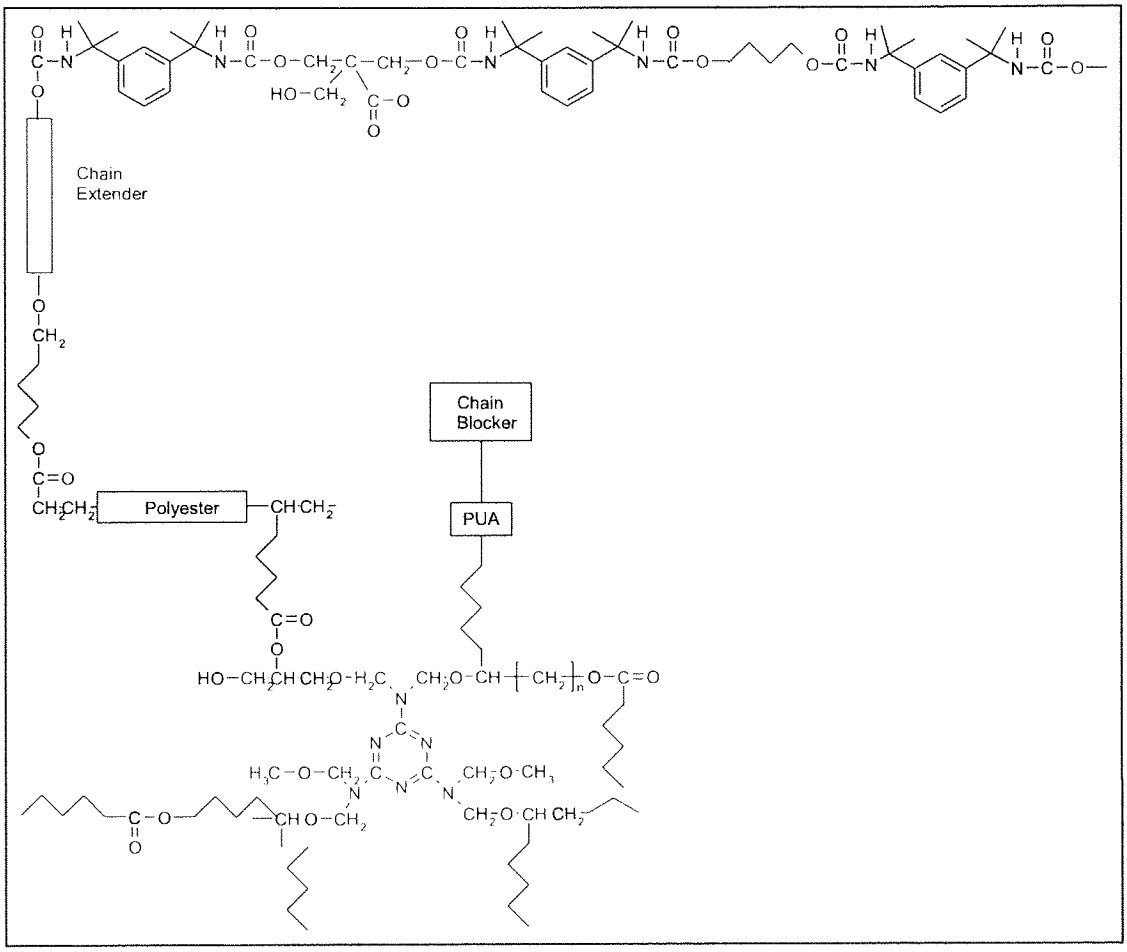

Scheme 4.2 Groups present in the water-borne clear-coat

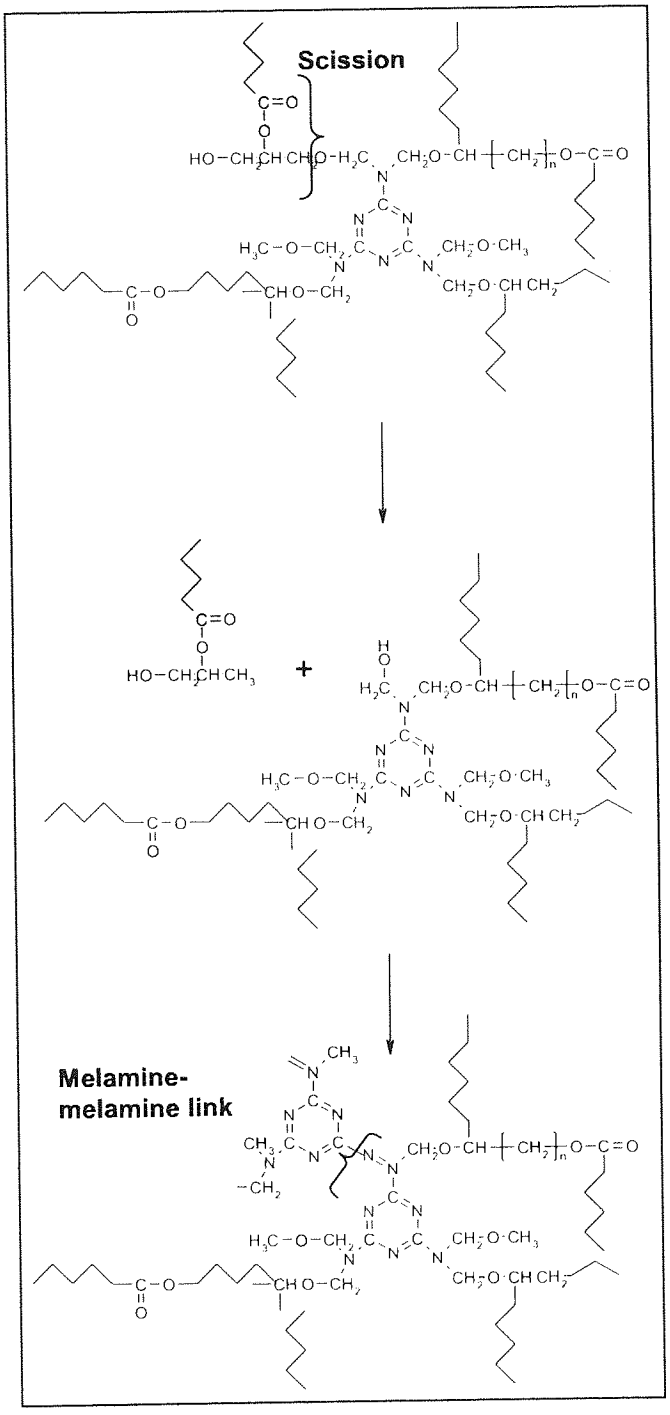

Scheme 4.3 Possible scission acrylic/melamine cross-link in water-borne clear-coat leading to melamine methylol groups.

CHAPTER 5: EFFECTS OF WEATHERING ON THE MIGRATION BEHAVIOUR OF UV STABILISERS IN WATER-BORNE AND SOLVENT-BORNE AUTOMOTIVE COATINGS

CHAPTER 5: EFFECTS OF WEATHERING ON THE MIGRATION BEHAVIOUR OF UV STABILISERS IN WATER-BORNE AND SOLVENT-BORNE AUTOMOTIVE COATINGS

5.1 Objectives and Methodology

The aim of the work described in this chapter was to investigate the effect of weathering on the changes in concentration of the UV stabilisers Cyasorb 1164 (UVA) and Sanduvor 3055 (HALS) which have been incorporated in the clear-coats of both solvent-borne and water-borne coating systems used in this work. The concentration of the UV stabilizers was examined both on the surface layers and across the depth of the coatings (depth profiling) in order to have a better understanding of the effect of the stabilisers on the differences observed in the overall weathering performance of the different coating systems examined here. The solubility and diffusion behaviour of the UVA stabiliser was also examined. **Table 5.1** gives the composition of the different coating systems used in this investigation and shows the structures of the investigated stabilisers.

Three different analytical methods were used to determine the concentration depth profiles of the two stabilisers in microtomed slices of the different coating systems before and after artifical accelerated (CAM and SPART) weathering conditions. These are; 1), Direct absorbance UV-Vis spectroscopy (both transmission mode and diffuse reflectance (DRA, see section 2.6.6)) used only for the UVA concentration in the clear-coat, 2), solvent extraction followed by HPLC-MS-MS used for both the UVA and HALS to determine their concentrations across the whole depths of the coating systems (depth profiling) and 3), solvent extraction method followed by GC-MS was also used to determine the concentration profile for both the UVA and HALS across the entire depth of the coating systems (the latter two measurements were carried out by a project partner); all values determined for the additives are given as an average of three measurements (see **Scheme 5.1** for details).

The solubility and diffusion characteristics of the UVA in the clearcoat were determined using either a traditional "cell" method **[20]** in which the additive diffuses through the layers of the clear-coat, or by using a heated ATR attachment with FTIR

where the solubility and diffusion values were measured at different temperatures. The presence of the UVA in the clear-coat layers was also determined by MALDI-ToF analysis conducted on the full (not microtomed) coating systems.

Table 5.1 Structure and Properties of the stabilisers used in the different automotive clearcoats and a summary of the coating systems presented in this chapter.

Stabiliser Code and Supplier	**Structure**	**Physical Properties and State**
Sanduvor 3055 (Clariant) **(HALS)**	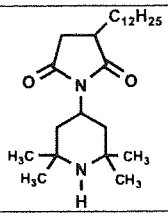	• Yellow viscous liquid • MW = 407 • Mpt = -15^{0}C • Bpt = 212^{0}C • Purity = 91%
Cyasorb 1164 (Cytec) **(UVA)**	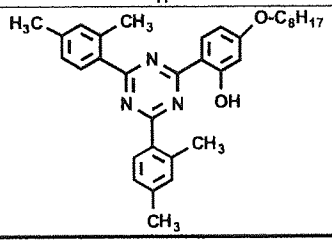	• Yellow powder • MW = 510 • Mpt = 88–91^{0}C • Purity = 96%(min)

Layer Composition of various automotive coatings								
System Code Number		**EC on aluminium substrate**	**Primer (WB-P)**	**Base 1**	**Base 2**	**Clearcoat (CC) Type**	**CC- UVA (level)**	**CC- HALS (level)**
Solvent-borne	**3**	Yes	WB-Anthracite	No	Blue	SB	Cyasorb 1164 (level 1)	Sanduvor 3055 (level 1)
Water-borne	**6c**	Yes	No	Anthracite	Blue	WB	Cyasorb 1164 (level 1)	Sanduvor 3055 (level 1)
	7	Yes	No	Anthracite	Blue	WB	Cyasorb 1164 (level 3)	Sanduvor 3055 (level 1)
	10	Yes	No	Light Grey	Silver	WB	Cyasorb 1164 (level 1)	Sanduvor 3055 (level 1)

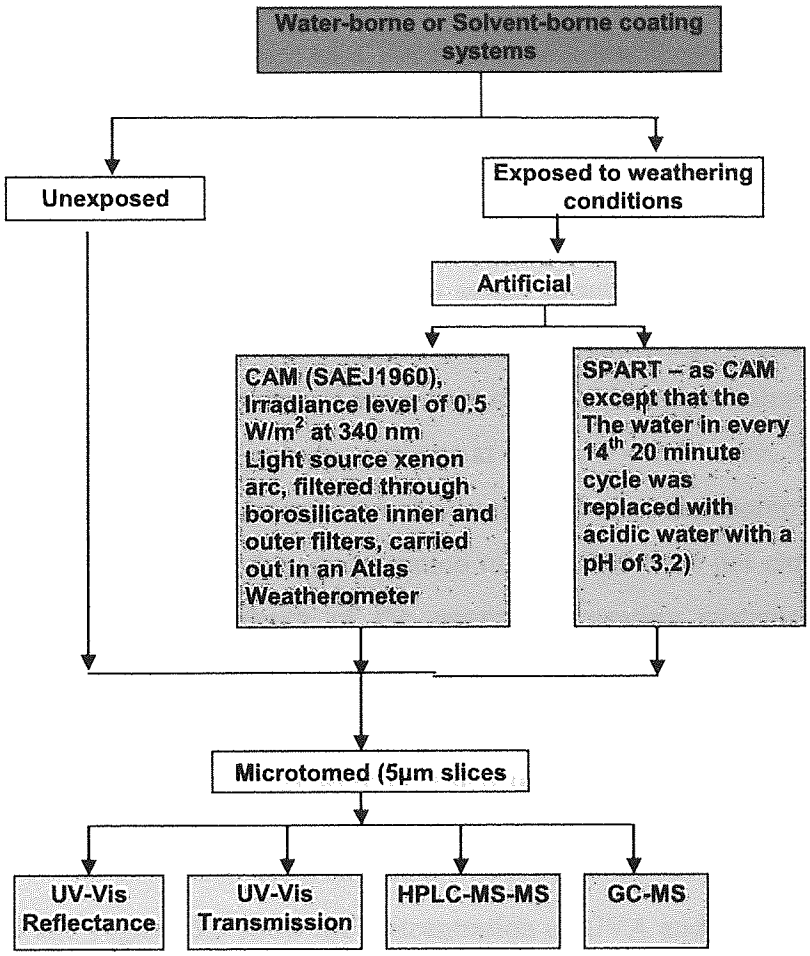

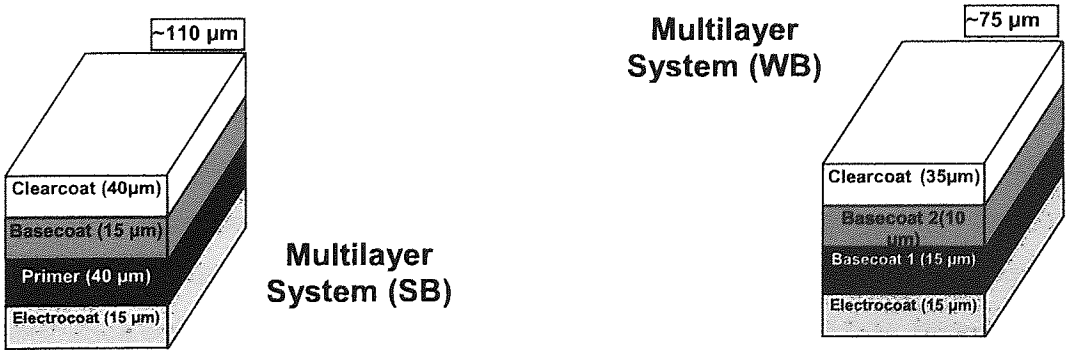

Scheme 5.1 Schematic illustration of methods used to investigate changes in stabilizer levels in automotive coatings after weathering.

5.2 Results

5.2.1 Concentration profiles of UVA and HALS stabilisers across the depths of the coating systems

The concentration level one (**Table 5.1**) of UVA used in all clear-coat formulations of both water-borne and solvent-borne coating systems (except for system 7 which contained level 3) was compared with its actual measured concentration (by UV-Vis transmission analysis) after curing and before weathering exposure. The actual measured concentration was found to be very close to the target value (level 1) used in both solvent-borne and water-borne systems at around 1.4-1.6 w/w%. Furthermore, it is shown that in the case of unexposed clear-coat of both water-borne (system 6c) and solvent-borne (3) systems, the concentration of the UVA does not change to any great extent across the entire depth of the unexposed coating systems (**Figure 5.1C**). However after 4000 hours of CAM exposure, the UVA level in system 3 decreased slightly more rapidly than was the case in the water-borne system 6c (**Figure 5.1E**, see also **Table 5.2**). Similar results were obtained from a second method of concentration measurements using DRA UV-Vis spectroscopy (**Figure 5.2**).

Table 5.3 and **Figure 5.3** show the concentration of UVA and HALS determined from HPLC-MS-MS analysis of extracted solutions from microtomed slices across the depth of the whole water-borne coating system 6c before and after accelerated (CAM and SPART) weathering, (exposure for 1000 hours). It is clear that UVA and HALS concentrations were fairly stable in the clear-coat of the unexposed samples. The concentration however decreased after the CAM or SPART weathering exposures, both weathering regimes giving similar results. Since both stabilizers were originally applied only in the clear-coat layers of the automotive coatings it is quite clear that they have migrated to the base-coat layers and to a lesser extent to the electro-coat layers (see stabilization concentration profile for unexposed samples in **Figure 5.3**). However, both stabilizers seem to migrate at a much higher concentration in the base-coat layers during CAM experiment weathering exposures.

Closer examination of the concentration profile obtained by GC-MS analysis of the extracted solutions of the UVA and HALS stabilizers in the microtomed layers across

the full depths of the solvent-borne 3 and water-borne systems number 6c and 7 coating systems (system 7 has a UVA concentration level of 3, compared to a concentration level of 1 in system 6c) reveals that in the case of the solvent-borne system, while the concentration of the stabilisers decreased steadily with exposure times, the maximum amount of decay occurred at the surface layers with low concentrations remaining in the base-coat layers (see **Figure 5.4A**). The water-borne systems 6c and 7 behaved differently in that while the stabilizer concentrations also reduced with exposure time across the depth of these systems, their concentration level in the base-coats is shown to be similar to their concentration in the clear-coat layers with the major drop occurring in the deeper electro-coat layers (**Figure 5.4C, E and G**). Although, system 7 contained UVA stabilizer at a concentration level 3 compared to level 1 in system 6c, the concentration profile across the depth of the coating in both systems was very similar, except for the much higher overall initial concentration in system 7.

A more clear comparison of the concentration profiles across the depths of the solvent-borne 3 and water-borne 6c and 7 coating systems (from GC-MS extracts) is shown in **Figure 5.5**. The figure also compares the normalized extent of reduction of UVA and HALS in the clear-coat (in a layer of nominal depth 7.5μm) after 4000 hours of CAM exposure in both solvent-borne 3 and water-borne 6c and 7 coating systems. It is clear that the HALS is consumed much more rapidly compared to UVA in all systems. Furthermore both the UVA and HALS are retained to a much lower extent in the solvent-borne system 3 compared to the water-borne 6c (both systems were formulated with the same level of UVA, level 1).

5.2.2 Solubility and Diffusion of the UVA Stabilisers in the coating systems

The solubility and diffusion characteristics of the UVA (Cyasorb 1164) in a prepared water-borne clear-coat were determined at different temperatures (from 30-80°C) using the traditional method of a stack of clear-coat films **[20]**, see **Table 5.7** for a summary of results and **Table 5.8** and **Figure 5.6** for the resulting Arrhenius plots for the solubility and diffusion of the UVA in the clear-coat. The activation energy from the solubility (heat of solution) of UVA in the water-borne clear-coat films was found to be **81 J mol^{-1}** and the activation energy from the diffusion data was found to be **6700 J mol^{-1}** with the diffusion coefficient at 80°C as **$1.0 * 10^{-11}$ cm^2/s.**

Figure 5.7 shows a comparison of the experimental results from the FTIR ATR method with the theoretical curve, which was calculated using equation 2.10

$$\frac{A_t}{A_\infty} = 1 - \frac{8\gamma}{\pi[1-\exp(-2\gamma L)]} \sum_{n=0}^{\infty} \left[\frac{\exp(g)[f\exp(-2\gamma L) + (-1)^n (2\gamma)}{(2n+1)(4\gamma^2 + f^2)} \right] \qquad (2.10)$$

$$g = \frac{-D(2n+1)^2 \pi^2 t^2}{4L^2} \qquad (2.11)$$

$$f = \frac{(2n+1)\pi}{2L} \qquad (2.12)$$

Where;

A_t = absorbance at time=t

A_0 = absorbance at t = equilibrium

γ = $1/d_p$ (d_p is the depth of penetration of the ATR crystal)

The experimental results are also plotted in **Figure 5.8** and are shown in **Table 5.9.** The slope of the line includes the D term and thus allows the calculation of the diffusion coefficient, D.

Slope = $D\pi^2 / 4L^2$

Slope = $9 * 10^{-5}$

L = 0.00017 cm

D = $1.0 * 10^{-13}$ m^2/s (at 80°C).

5.2.3 MALDI-TOF-MS / Laser Desorption Ionization-TOF-MS

The UVA stabilizer in the coating system (not microtomed) was seen to have a high absorption at the emission frequency of the nitrogen laser used in the MALDI-TOF resulting in high sensitivity for the direct detection of the outermost surface concentration of the UVA without the need for special sample handling and preparation

methods. For high UV absorbers, it was necessary to limit the laser energy to threshold levels so as to limit the extent of fragmentation. Although the HALS used in the coating systems (Sanduvor 3055) absorbed the laser light only slightly, compared to the UVA molecule, it was also possible to detect this species by this approach albeit at very much attenuated signal levels. It was not possible to detect, by this simple approach, neither the UVA nor the HALS species at the surface of unexposed, (i.e. before weathering), paint panels but the surface distribution (by 1D-mapping) of both HALS and UVA in WB-paint system 7 could be closely detected after 1000h artificial accelerated (CAM) exposure (from laser-desorption-ionization-Tof-MS spectra) see **Figure 5.9.**

5.3 Discussion

5.3.1 Concentration profiles of the UVA and HALS across the depths of the coating systems

Very little work has been published on concentration profiles of UVA stabilisers across the full depth of automotive coating systems exposed to weathering. The UVA Cyasorb 1164 was added to the clear-coat in order for the paint to become resistant to the penetration of the UV light (the light is allowed to pass through the clear-coat in order to reveal the colour of the base-coat). Thus, as the UV stability of the clear-coat decreases, the solar radiation can penetrate deeper and deeper into the multilayer paint coating system and would contribute to photoxidation of the paint. Using the Beer-Lambert law, the peak height (at 342 nm) from microtomed slices was used to calculate the UVA concentration, however if after weathering the UVA degraded to form products that would also absorb in the UV region, it has been shown that the shape of the spectra and the ratio of the peaks (at 290 and 342nm for Cyasorb 1164, see Chapter 2, **Figure 2.15**) may change **[11].** If little change is seen in the ratio of the peaks, the UV spectra of the clear-coat can then be used to determine the amount of UVA that remains intact in the coating system. The loss of the UVA from the coating can be due to; volatility, physical incompatibility and low photostability **[11].** However, it has also been suggested that the root cause of loss of UVA stabilisers from coatings is due to chemical destruction as well as physical loss **[12].** UV-Vis analysis can be used on different types of clear-coats (for example water-borne and solvent-borne) as long as the additive is visible in the UV absorption region (unfortunately the absorbance of the HALS stabilizer used in this work was too weak to be measured). The UV-Vis

absorption method was also only useful in assessing the clear-coat and not the lower coating layers due to scattering issues. There were also handling issues due to the small size and fragility of the slices; it was difficult to position the films in the correct position in the UV-Vis spectrometer; however stabilizing the films with a long-chain terminal alcohol has been found to be useful in keeping the films in the correct position **[5, 6].**

The advantages and limitations of the different analytical methods used in examining the concentration profiles and stabilization in the clear-coats of automotive paint systems are outlined below. As mentioned previously, UV-Vis analysis (both in transmission mode and DRA) was only useful in examining the top clear-coats and the prepared clear-coat microtomed slices were difficult to handle. **Figure 2.19** (chapter 2) shows how the DRA spectra from the entrance and exit ports obtained from the DRA were added, essentially removing the effects of scattering and reflection. The HPLC-MS-MS method also involved the use of microtomed slices but these were first solvent extracted. This method has a number of advantages, first it did not matter if the slices became damaged during handling as the amount of the additive present would remain the same in the extracts. Another advantage is that the method is equally applicable to all layers of the multilayered system, not just the clear-coat as long as an appropriate solvent can be found to extract the additive (solvents such as methylene chloride and DCM have previously been used **[5]),** in this work methylene chloride was used. Thus this method is only suitable if the additives are capable of being extracted. Some UVA stabilisers have been found to be difficult to extract as they become covalently bonded to the clear-coat matrix during the curing stage **[13].** Another great advantage of this method is that the concentrations of both UVA and HALS could be investigated separately and the extract solutions could be further analysed using methods such as UV-Vis analysis, however it must be ensured that the signal responses are normalized to the weight of the material extracted in order for comparison to be made with the additive concentration present in the other layers.

GC-MS analysis of extracted solutions of the stabilisers present in the microtomed layers of the coating systems was also used to give the concentration depth profiles of the UVA and HALS. This method was again only suitable if the additives were capable of being extracted. The presence of UVA and HALS was again seen in all of the layers

further indicating that migration of the additives had occurred from the clear-coat to the deeper layers if the paint. After the weathering regimes, the concentrations of both UVA and HALS decreased with the greatest change occurring at the surface of the coating systems as these layers were closest to the damaging radiation (**Figures 5.4 and 5.5**).

In the unexposed samples, more of the UVA was found to be present in the lower layers of the water-borne 6c compared to its concentration in these layers in the solvent-borne system 3 (**Figure 5.5**). This may be attributed to the wet-on-wet curing regime used in the water-borne systems, or to a greater migration of the additives in the water-borne coating matrix. It is well known that many HALS and UVA additives are capable of migrating freely between the clear-coat layers **[13, 43]** particularly during wet-on-wet curing regimes. However, it has also been thought that an efficient stabiliser should be able to diffuse freely through the polymer matrix, providing sufficient mobility of the additive within the coating layers while keeping physical losses low **[74]**. It has also been suggested that due to the nature of photodegradation processes in the polymers there must be some requirement for some degree of mobility of the additive.

Figure 5.5 shows that the effect of weathering (accelerated CAM exposure) is to reduce the concentration of both UVA and HALS with the level of these UV stabilisers decreasing more rapidly in the solvent-borne system 3 compared to the water-borne system. The higher concentration of UVA (e.g. in system 7) led to a lower extent of loss during weathering. The two different accelerated weathering regimes (CAM and SPART) resulted in similar concentration profiles of the UVA and HALS across the depth of the coating systems when compared at the same exposure time of 1000 hours, see **Figures 5.3 and 5.4**. This observation was also seen in the FTIR analysis of the coating systems (chapter 3). It is thought that the acid in the SPART regime would begin to etch the surface of the coatings, causing erosion and revealing new undamaged coating, thus similar concentration profiles were obtained under both the CAM and SPART exposure regimes.

5.3.2 Solubility and Diffusion of the UVA stabilizer in the coating systems

The diffusion coefficient of Cyasorb 1164 was calculated using the stack method and was found to be 9.8 * 10^{-14} m^2/s at 60°C and 1.0 * 10^{-15} m^2/s at 80°C, the latter was based on the FTIR-ATR method. These values are reasonably close to each other although there is a difference. Previous authors **[23]** have found that the D values measured with the ATR technique do compare favorably with values obtained from traditional stack methods (at ambient temperatures) in other polymer systems. The value of D determined here can be extrapolated to room temperature and has been found to be useful in dealing with the storage of the material, and are often assumed to follow the Arrhenius law **[22].**

The ATR method worked well although more method development is needed. The main advantage of the FTIR-ATR method was the time needed to produce results was in hours as opposed to days/weeks with the traditional stack method. Another disadvantage of the traditional method compared to the FTIR method is the separation and handling of the fragile prepared coating films in the stack necessary for analysis. The additive must however have a distinctive IR absorption peak for the ATR-FTIR method to be suitable. However, the traditional method does produce reliable results and the UV measurements method have previously been seen to produce good fits to Fickian curves **[21].** It was also found that the most reliable diffusion values for the diffusion coefficient were obtained when the k value was around 0.15 **[20].**

The migration characteristics of additives in coating systems are important due to the effects of possible additive loss on the stability and service life of the coatings [**20, 21**]. The rates of additive loss are controlled mainly by the rate of additive diffusion and the solubility in the polymer. Thus, understanding the changes in these physical parameters for stabilisers used in automotive coatings could be directly related to the behaviour of the coatings. Additive solubility in a polymer is determined by the free energy change associated with the transfer of the additive from a pure material into the polymer matrix. Measurements of solubility of additives in polymers require a true equilibrium to be established between the additive and the polymer. However, it is known that many HALS and UVA additives can migrate between clear-coat and base-coat layers during cure, particularly in wet-on-wet applications [**8, 43**]. Although, as it is common

practice, different levels of HALS and UVA are used in different amounts in each of the coating layers, the additive content of an isolated clear-coat layer may not match its additive content in practice. Furthermore, the polymers and cross-linkers used to formulate the paint systems may be comparable to the molecular weight of the HALS and UVA additives used, making it possible for these components to also migrate during cure [8]. Thus, the results from this study have shown that the UVA is capable of diffusing through the clear-coat layers and consequently the additive contents of the isolated clear-coats before and after weathering previously determined and reported in this chapter using methods such as HPLC-MS-MS (**Figures 5.4 and 5.5).**

5.3.3 MALDI-TOF-MS / Laser Desorption Ionization-TOF-MS

MALDI-TOF-MS / Laser Desorption Ionization-TOF-MS was used as a method to detect the presence of both UVA and HALS in coating systems. **Figure 5.9** showed that the distribution of both the HALS and UVA was not uniform and furthermore the additives were virtually absent in some spots across the sample. The signal levels or intensity (counts) that was shown in the various measured spots (d, e, f, h, i, j, k) could be used for comparative purposes in a semi-quantitative way because of the extremely high sensitivity of detection achievable with the UVA species by this approach. The non-uniform distribution of both HALS and UVA may have been due to inhomogeneous distribution of the additives on the surface of the paint panel produced during preparation, or possibly caused by the development of specific defects and localized sites of weaknesses following the depletion of the additives upon weathering. TOF-MS has been previously used to analyse coatings and has been shown to be a powerful tool with a high sensitivity and can give information about the outermost surface of a sample **[5].** A great advantage of the method was that no microtoming was needed and sample preparation was minimal. Examination of coating surfaces by this method can be seen as a complementary method of analysis of paint systems following weathering to that of optical microscopy, but more method development is needed to quantify the results.

5.3.4 Critical evaluation of the performance of the different automotive coating systems

Following on from the final section of chapter 4, this section compares the weathering performance of the different coating systems (with particular reference to the water-borne and solvent-borne systems), using the different methods already discussed in the previous chapters.

A large emphasis of this work has focused on discussing the differences in the durability after weathering between the blue solvent-borne (3) and water-borne coating systems (6c) and the silver systems, solvent-borne (1) and the corresponding water-borne coating system (10). This is particularly important as the emphasis of most new coating developments is based on water-borne coatings due to environmental concerns but very little test data is available for water-borne systems compared to much larger volumes of work for existing solvent-borne coating systems. Results from all tests have shown that the solvent-borne systems are consistently more resistant to weathering than the corresponding water-borne systems. This is even applicable when using the traditional gloss measurements where differences between the solvent-borne and water-borne systems were clearly seen, **Figure 5.10**. The results reinforce why gloss measurements are still used to assess the performance of the coating systems; although the method only gives information about the changes on the surface of the coating. However, attempts have been made to try to correlate gloss readings with spectral changes to coating systems [2]. The advantage of the photoxidation measurements (from FTIR spectroscopy) is that not only information can be obtained about the changes that take place on the surface of the coating, but also for the deeper layers (depth profiling). **Figure 5.11** shows that even throughout the depth of the clear-coat, the solvent-borne system 3 was always more resistant to photoxidation than the corresponding water-borne 6c. It is known that photoxidative degradation plays a key role in determining the long-term weathering performance of clear-coat/base-coat systems. In many cases, traditional methods (such as gloss) provide little information that catastrophic failure of the coating is about to occur (for instance by peeling). A further advantage of the FTIR photoxidation measurement method is that it is applicable not only to different types of coatings (for example solvent-borne and water-

borne in this case), but also to different stabilization packages. The photoxidation of the melamine based clear-coats involves hydrolysis reactions leading to cross-linking or chain-scission with the predominance of each depends upon the prevailing conditions. Changes in the photoxidation are observed before seeing appearance-based changes such as gloss. The differences between the solvent and water-borne coatings were also seen by the changes in the concentration of the stabilizers (UVA and HALS) in the different levels of the coatings (**Figure 5.12**). The effects of the different cure regimes between the coating types were also seen. An advantage of the water-borne cure process was the shorter time needed and consequently lowers emissions, however lower film thicknesses are also seen. The lower film thickneses can be critical in exposure tests for durability and migration behaviour of additives in the formulations. The water-borne systems had both a lower cross-link density with a higher migration tendency of the additives and also lower molecular weight resin components. Only the GC-MS results showed that in the water-borne systems the stabilisers have migrated almost uniformly across the CC-layers and into the lower layers of the multilayer coating systems (in BC2, BC1 and EC) during the wet-on-wet application of the coating systems. The concentration of the UVA (and HALS) decreased with exposure time in the outer CC-layers but the inner BC-layers retained the concentration of the originally migrated stabilizers. In contrast, the reference solvent-borne system 3 showed that the concentration of the stabilisers decreased rapidly across the depth of the CC-layers with much smaller amount migrating to the inner base-coat layers and the trend of concentration decrease across the depth of the coating was paralleled by a similar decrease with exposure time, **Figure 5.12.** The loss of HALS during the accelerated weathering was greater than that of the UVA. This is to be expected as the HALS is the primary antioxidant which is a powerful radical scavenger, whereas the UVA is primarily a UV-screen to protect the HALS and binder system from the damaging UV light. The HALS is used up as the coating is protected.

The DMA experiments further allowed differences between the solvent-borne and water-borne coatings to be explored (**Figure 5.13**) and property changes were measured on a molecular level. It was presumed that apart from any external stresses introduced during microtoming, the thin films examined would retain the compositional profile, morphology and internal stresses of the respective fully baked system. It was further presumed that the baked systems had been fully cured, in that the thermal conditions

used for the DMA experiments would not contribute to the developments of further cross-links. Thus the changes in the parameters measured could be interpreted in terms of the chemistry of the binder systems during weathering. The cross-linking of the water-borne systems (which was based on wet-on-wet cure) would lead to a lowering of the glass transition temperature of the clear-coat. After weathering, greater changes were seen in the glass-transition temperatures of the water-borne coatings compared to the solvent-borne coatings. The temperature during the weathering experiments may rise to a value close to, or even higher than, the glass transition temperature of the coatings (particularly the water-borne), suggesting that the lightly cross-linked polymer network of the binder system may have been sufficiently mobile to allow post curing processes to take place during weathering.

Another important respect of this work illustrated the influence of the different colours of the coating systems on the weathering resistance of the overall coating, (comparing solvent-borne silver system 1 with the blue system 3, and the water-borne systems, blue system 3 with the silver system 10). Both **Figure 5.14** (for the photoxidation results) and **Figure 5.15** (DMA tension results for both glass transition temperature and relative cross-link density) show that the silver system 10 is always more durable than the blue system 6c (and similarly system 1 is more durable than system 3). This indicates the importance of the presence of aluminium-flakes in the silver base-coat layer of systems 1 and 10 which contributes to both reflecting away the harmful light (artificial or sunlight) and to giving rise to lower temperatures (cooler) throughout the upper layers (of up to 7°C). Small changes in the glass transition temperature indicate greater resilience of the crosslinked network to weathering effects and this also correlates well with the extent of drop in E'_{min} during exposure, i.e. breaking down of crosslinks on ageing, see **Figure 5.15.**

The effect of the type and concentration of UV stabilization package was also investigated in this work, (see **Figure 5.15** for the photoxidation results and **Figure 5.16** for the DMA tension results). For the DMA results, it was clear that in the absence of UVA (system 8) the glass transition temperature increased with exposure time causing the development of a more brittle clear-coat structure through the formation of cross-linked structures, on ageing, i.e. higher glass transition material was observed.

This increase in the glass transition temperature correlates well with greater increase in photoxidation index obtained from FTIR. It was also clear from **Figure 5.17** that the glass transition temperature is affected by the presence of UVA; compare the glass transition temperature of the unexposed samples containing UVA, 6c, 10, and 7 (around 73°C) with that of 8 (around 75 0C); this lowering of the glass transition temperature is not the result of plasticisation. Further examination of the glass transition temperatures of the clear-coats of unexposed systems 6c, 10 and 7 tend to indicate that higher concentrations of UVA as in sample 7 (level 3) produces a lower glass transition temperature. It is also important to note from **Figure 5.17** that the clear-coat of the unexposed **sample 9**, which contains crosslinkable UVA, shows a much higher glass transition temperature value (77 °C) than those containing a similar but non-crosslinkable UVA (samples 6c, 7, 10). This confirms the crosslinkable nature of the UVA which results in a more rigid network structure of the clear-coat, hence the slightly higher glass transition temperature values observed. The large drop in the glass transition temperatures in sample 7 (UVA at level 3) compared to sample 6c (UVA at level 1) on UV-exposure further supports the excellent role of UVA in protecting the clear-coat layers on prolonged exposures from crosslinking reactions that appear to be light-initiated/catalysed, thus the competing hydrolytic reactions that lead to chain scission would predominate under these conditions. These results in a more flexible structure responsible for the lower Tg values observed.

Table 5.2 UVA concentration in microtomed slices of the clear-coat in systems 3, 6c and 10 before and after artificial accelerated (CAM) weathering determined by both transmission mode and DRA UV-Vis spectroscopy

System 3				
Nominal Depth of clear-coat/μm	UV-Vis Transmission		UV-Vis DRA	
	Unexposed [UVA] w/w%	CAM Exposure Time/hours 4000 [UVA] w/w%	Unexposed [UVA] w/w%	CAM Exposure Time/hours 4000 [UVA] w/w%
2.5		1.1		1.2
7.5	1.5		1.6	1
12.5	1.4	1.1	1.5	
17.5	1.3	1.1		1.2
22.5	1.6	0.9	1.4	1
27.5	1.4		1.2	1.2

System 6c					
Nominal Depth of clear-coat/μm	UV-Vis Transmission		UV-Vis DRA		
	Unexposed [UVA] w/w%	CAM Exposure Time/hours 4000 [UVA] w/w%	Unexposed [UVA] w/w%	CAM Exposure Time/hours 1000 [UVA] w/w%	CAM Exposure Time/hours 2000 [UVA] w/w%
2.5	1.7	1.5	1.8	1.4	
7.5	1.8	1.6	1.8	1.4	1.3
12.5		1.5			1.3
17.5	1.6	1.5	1.7	1.5	1.3
22.5	1.5	1.6	1.6	1.6	1.4
27.5		1.4		1.5	1.4
32.5		1.4			

System 3			System 10		
Nominal Depth of clear-coat/μm	UV-Vis DRA		UV-Vis DRA		
	Unexposed [UVA] w/w%	CAM Exposure Time/hours 4000 [UVA] w/w%	Unexposed [UVA] w/w%	CAM Exposure Time/hours 1000 [UVA] w/w%	CAM Exposure Time/hours 2000 [UVA] w/w%
2.5		1.2		1.1	
7.5	1.6	1	1.5	1.2	
12.5	1.5		1.7	1.3	
17.5		1.2		1.7	1.4
22.5	1.4	1	1.6	1.6	
27.5	1.2	1.2	1.8	1.6	1.7
32.5			1.3	1.6	
37.5				1.6	

Table 5.3 Concentration of UVA and HALS stabilisers in microtomed slices of the clear-coat of system 6c, before and after artificial accelerated (CAM) weathering, determined using HPLC-MS-MS of extracted solutions (carried out by project partner – Clariant).

System 6c							
				CAM Exposure Time/hours		SPART Exposure Time/hours	
	Nominal Depth/μm	Unexposed		1000		1000	
Layer		UVA w/w%	HALS w/w%	UVA w/w%	HALS w/w%	UVA w/w%	HALS w/w%
CC	2.5	2.57	0.46	1.73	0.45	1.50	0.48
CC	7.5	1.61	0.57	1.82	0.55	1.63	0.52
CC	12.5	1.57	0.59	1.89	0.59	1.69	0.53
CC	17.5	1.77	0.67	2.06	0.79	1.72	0.81
CC	22.3	1.97	0.75	1.95	0.80	1.52	0.52
CC	27.5	1.63	0.58	1.88	0.96	1.60	0.56
CC	32.5	1.48	0.57	1.81	0.80	1.46	0.49
BC2	37.5	1.58	0.53	1.89	1.21	1.40	0.48
BC2	42.5	1.79	0.65	2.56	0.94	1.66	0.59
BC2	47.2	1.56	0.53	2.89	0.89	1.80	0.56
BC1	52.5	1.85	0.66	2.7	1.15	1.72	0.49
BC1	57.5	1.82	0.53	2.52	0.90	1.96	0.40
BC1	62.5	1.72	0.53	1.2	0.45	1.70	0.44
EC	67.3	0.71	0.19			0.50	0.11

Table 5.4 Concentration of UVA and HALS stabilisers in microtomed slices of the clear-coat of system 3, before and after artificial accelerated (CAM and SPART) weathering, using GC-MS of extracted solutions (carried out by project partner – Clariant).

Concentrations from GC-MS for System 3									
				CAM Exposure Time/hours				SPART Exposure Time/hours	
	Nominal Depth/ μm	Unexposed		1000		4000		1000	
Layer		UVA w/w%	HALS w/w%	UVA w/w%	HALS w/w%	UVA w/w%	HALS w/w%	UVA w/w%	HALS w/w%
CC	2.5	1.35	0.58	0.89	0.14	0.50	0.06	0.98	0.18
CC	7.5	1.36	0.63	0.97	0.17	0.56	0.07	1.03	0.20
CC	12.5	1.33	0.64	1.09	0.19	0.68	0.09	1.12	0.22
CC	17.5	1.27	0.64	1.10	0.22	0.63	0.10	1.09	0.22
CC	22.3	1.27	0.62	1.10	0.22	0.51	0.13	1.02	0.21
CC	27.5	1.20	0.59	0.74	0.19	0.36	0.15	0.90	0.19
CC	32.5	1.08	0.53	0.64	0.20	0.37	0.21	0.77	0.19
BC	37.5	0.83	0.41	0.53	0.22	0.31	0.19	0.64	0.17
BC	42.5	0.56	0.29	0.47	0.24	0.25	0.16	0.51	0.17
BC	47.2	0.45	0.26	0.42	0.25	0.24	0.15	0.44	0.19
BC	52.5	0.48	0.26	0.42	0.25	0.22	0.14	0.39	0.20
P	57.5	0.42	0.23	0.34	0.24	0.21	0.14	0.36	0.21
P	62.5	0.32	0.24	0.31	0.22	0.21	0.14	0.41	0.25
P	67.5	0.32	0.24	0.27	0.21			0.27	0.22
P	72.5	0.29	0.24	0.32	0.24			0.27	0.23
EC	77.5	0.29	0.26	0.24	0.18			0.28	0.23

Table 5.5 Concentration of UVA and HALS stabilisers in microtomed slices of the clear-coat of system 6c, before and after artificial accelerated (CAM and SPART) weathering, using GC-MS of extracted solutions (carried out by project partner – Clariant).

Concentrations from GC-MS for System 6c										
	Unexposed		CAM Exposure Time/hours						SPART Exposure Time/hours	
			1000		2000		4000		1000	
Nominal Depth/µm	UVA w/w%	HALS w/w%	UVA w/w%	HALS w/w%	UVA w/w%	HALS w/w%	UVA w/w%	HALS w/w%	UVA w/w%	HALS w/w%
2.5	1.40	0.58	1.12	0.34	1.05	0.27	0.88	0.21	1.30	0.46
7.5	1.44	0.62	1.07	0.38	0.94	0.30	0.89	0.23	1.31	0.50
12.5	1.40	0.62	1.16	0.47	1.05	0.37			1.47	0.59
17.5	1.39	0.62	1.16	0.48	1.11	0.43	1.03	0.32	1.42	0.59
22.5	1.36	0.62	1.19	0.50	1.06	0.42	1.01	0.31	1.40	0.59
27.5	1.26	0.58	1.21	0.51	1.14	0.47	1.03	0.34	1.33	0.57
32.5	1.22	0.55	1.14	0.52	1.18	0.52	1.10	0.40	1.29	0.56
37.5	1.31	0.56	1.27	0.54	1.31	0.58	1.30	0.44	1.24	0.55
42.5	1.34	0.56	1.41	0.57	1.53	0.61	1.39	0.43	1.40	0.59
47.5	1.36	0.53	1.38	0.48	1.40	0.50	1.43	0.38	1.43	0.57
52.5	1.44	0.51	1.44	0.46	1.51	0.47	1.40	0.34	1.49	0.54
57.5	0.97	0.36	1.28	0.40			1.24	0.29	1.49	0.50
62.5	0.23	0.10	1.19	0.38	1.51	0.47	0.71	0.18	1.42	0.47
67.5			0.40	0.12					1.10	0.36
72.5			0.19	0.07					0.35	0.11

Table 5.6 Concentration of UVA and HALS stabilisers in microtomed slices of the clear-coat of system 7, before and after artificial accelerated (CAM and SPART) weathering, using GC-MS of extracted solutions (carried out by project partner – Clariant).

Concentrations from GC-MS for System 7					
Layer		Unexposed		CAM Exposure Time/hours	
				4000	
	Nominal Depth/µm	UVA w/w%	HALS w/w%	UVA w/w%	HALS w/w%
CC	2.5	4.69	0.71	3.47	0.25
CC	7.5	4.14	0.59	3.55	0.20
CC	12.5	4.23	0.60	3.53	0.20
CC	17.5	4.21	0.61	3.64	0.21
CC	22.5	4.16	0.60	3.76	0.23
CC	27.5	4.04	0.59	3.57	0.24
CC	32.5	3.90	0.56	4.26	0.29
CC	37.5	3.68	0.54	5.01	0.33
BC2	42.5	3.53	0.53	4.62	0.24
BC2	47.5	4.16	0.55	4.65	0.23
BC2	52.5	4.55	0.52	1.32	0.13
BC1	57.5	4.36	0.50	0.53	0.07
BC1	62.5	2.29	0.27	0.23	0.04
BC1	67.5	0.87	0.11		
EC	72.5	0.30	0.06		
EC	77.5	0.09	0.04		

Table 5.7 Summary of diffusion and solubility data of the UVA (Cysaorb 1164), in the water-borne clear-coat obtained using both the stack method and the FTIR-ATR method. Traditional refers to curve fitting to the theoretical curve; graphical refers to using the gradient of the line.

Temperature/^{0}C	Temperature/K	Maximum Solubility of the UVA %w/w	Method	D, cm^2/s
30	303	2.5	Stack-Traditional	2.1×10^{-11}
			Stack-Graphical	**8.3×10^{-11}**
45	273	2.6	Stack-Traditional	-*
			Stack-Graphical	**2.6×10^{-10}**
60	273	2.7	Stack-Traditional	2.3×10^{-10}
			Stack-Graphical	**9.8×10^{-10}**
80	293		FTIR-ATR	**1.0×10^{-11}**

* Off scale, could not fit to theoretical curve

Table 5.8 Arrhenius data for the solubility and diffusion characteristics of the UVA (Cyasorb 1164) in the clear-coat obtained using the stack method.

Solubility				Diffusion			
Log S	Maximum Solubility w/w%	1/T	T/°C	Log D	Diffusion coefficient, m^2/s	1/T	T/°C
0.40	2.5	0.0033	30	-14.1	8.3×10^{-15}	0.0033	30
0.41	2.6	0.0031	45	-13.6	2.6×10^{-14}	0.0031	45
0.43	2.7	0.0030	60	-13.0	9.8×10^{-14}	0.0030	60

Activation energies for Cyasorb 1164, J mol^{-1}	
Solubility	81
Diffusion	6700

Table 5.9 Example raw data for FTIR ATR method for calculation of the diffusion coefficient of the UVA (Cyasorb 1164) in the water-borne clear-coat, measured at 80°C.

Time	A_t	A_t/A_{ref}	A_t/A_{eq}	$1-A_t/A_{eq}$	$\ln(1-A_t/A_{eq})$
0	0	0	0	1	0
1200	0.0144	0.032034	0.0506	0.9494	-0.05192
2400	0.0902	0.200658	0.316951	0.683049	-0.38119
3600	0.135	0.30032	0.474372	0.525628	-0.64316
4800	0.165	0.367058	0.579788	0.420212	-0.86699
6000	0.182	0.404876	0.639523	0.360477	-1.02033
7200	0.199	0.442694	0.699259	0.300741	-1.20151
8400	0.207	0.460491	0.72737	0.27263	-1.29964
9600	0.218	0.484962	0.766022	0.233978	-1.45253
10800	0.223	0.496085	0.783592	0.216408	-1.53059
12000	0.231	0.513881	0.811703	0.188297	-1.66973
13200	0.233	0.518331	0.81873	0.18127	-1.70777
14400	0.239	0.531678	0.839813	0.160187	-1.83142
15600	0.24	0.533903	0.843327	0.156673	-1.8536
16800	0.246	0.54725	0.864411	0.135589	-1.99812
18000	0.248	0.5517	0.871438	0.128562	-2.05135
19200	0.251	0.558373	0.88198	0.11802	-2.1369
20400	0.253	0.562823	0.889008	0.110992	-2.19829
21600	0.254	0.565047	0.892521	0.107479	-2.23046
22800	0.258	0.573946	0.906577	0.093423	-2.37062
24000	0.26	0.578395	0.913605	0.086395	-2.44882
25200	0.262	0.582844	0.920632	0.079368	-2.53366
26400	0.265	0.589518	0.931174	0.068826	-2.67617
27600	0.268	0.596191	0.941716	0.058284	-2.84242
28800	0.269	0.598416	0.945229	0.054771	-2.9046
30000	0.271	0.602865	0.952257	0.047743	-3.04193
31200	0.274	0.609539	0.962799	0.037201	-3.29141

Where;

A_t = Absorbance at time t

A_{ref} = Absorbance of the reference peak

A_{eq} = Equilibrium absorbance = 0.284587

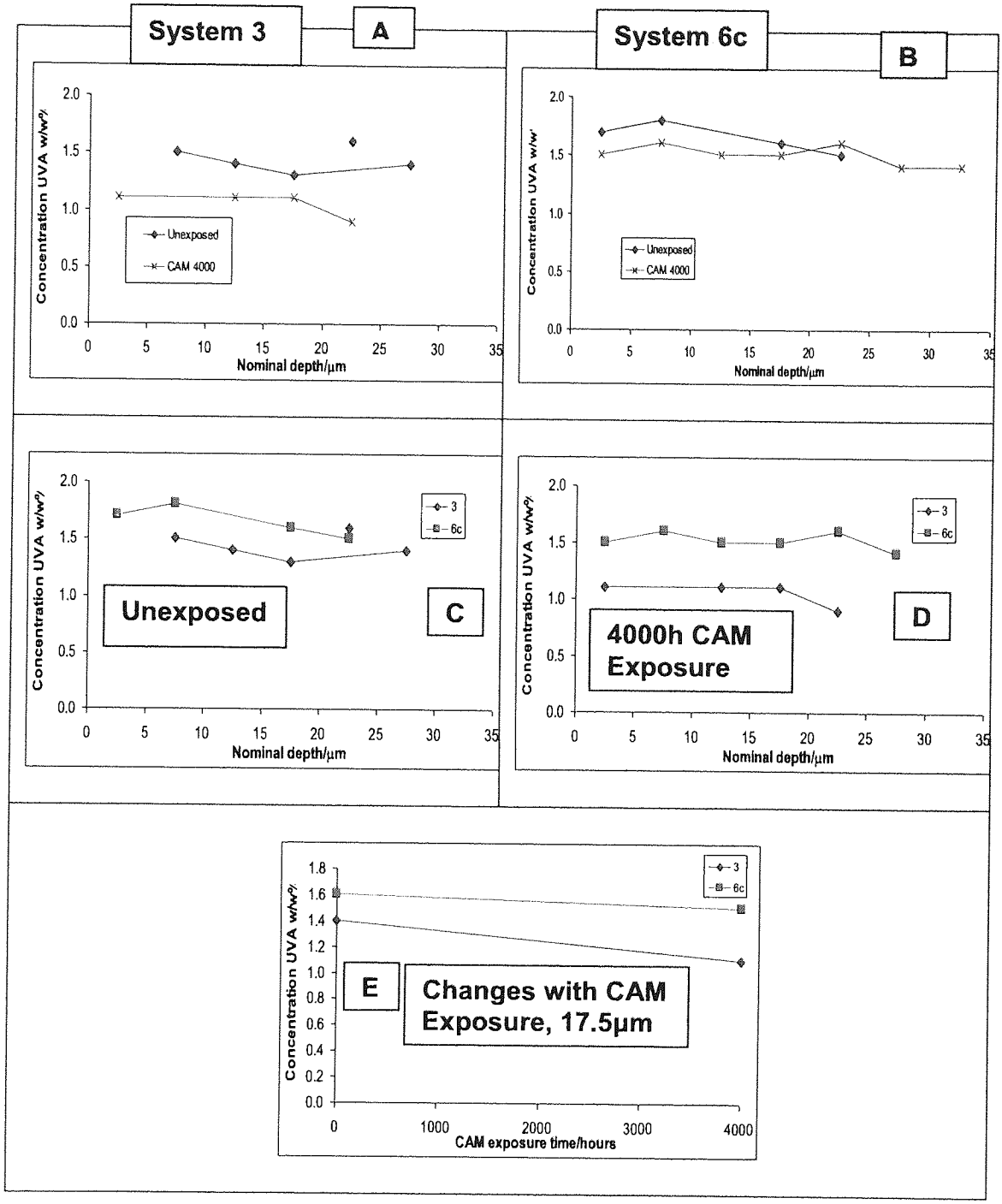

Figure 5.1 UVA concentration in microtomed slices of clear-coats of systems 3 and 6c, before and after 4000 hours accelerated (CAM) weathering, using transmission mode UV-Vis spectroscopy (A-D). Changes with CAM exposure time of a layer of nominal microtomed depth of 17.5µm for both systems 3 and 6c are also shown (E).

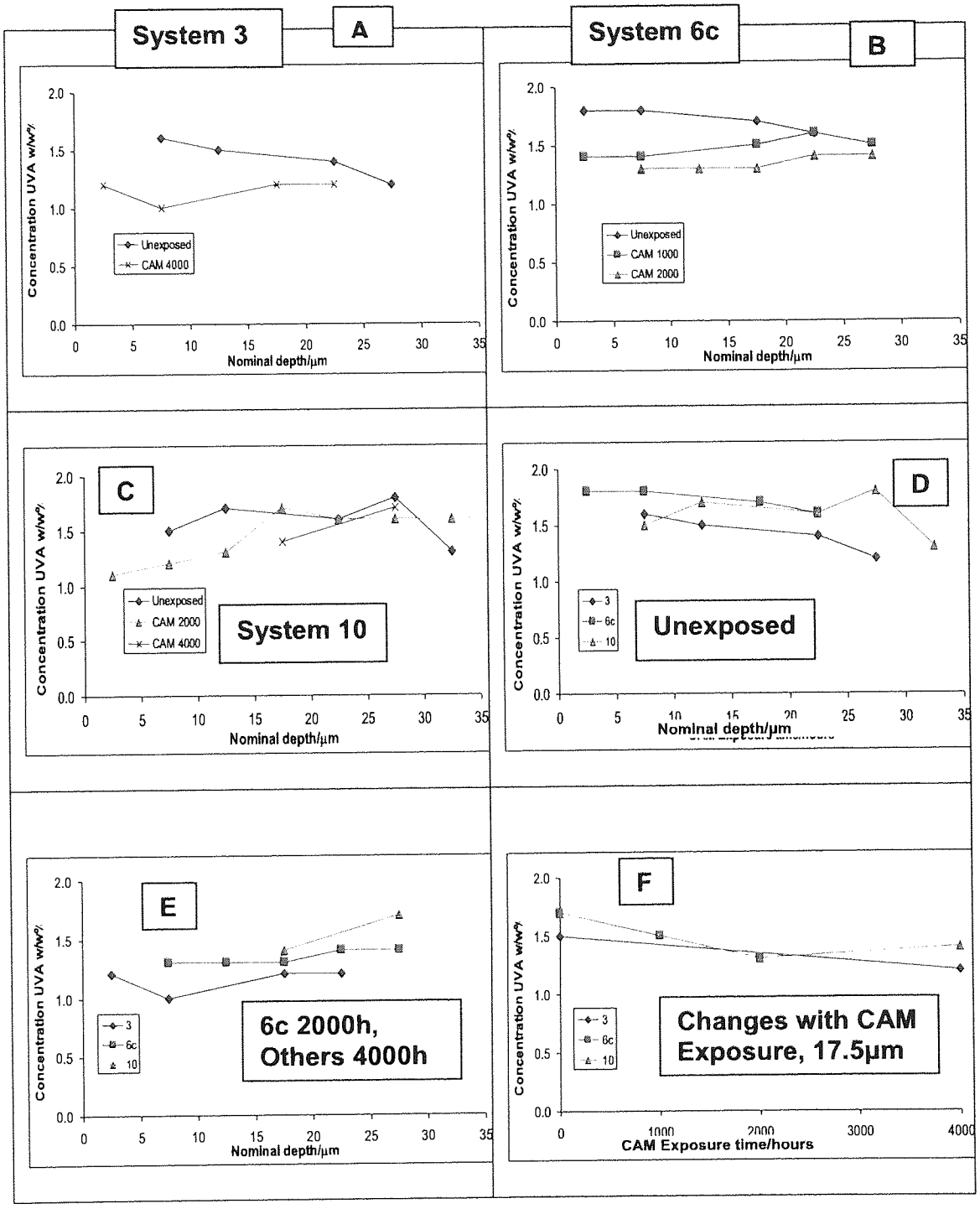

Figure 5.2 UVA concentration in microtomed slices of clear-coats of systems 3, 6c and 10 before and after accelerated (CAM) weathering, using diffuse reflectance UV-Vis spectroscopy (A-E). Changes with CAM exposure time at a nominal microtomed depth of 17.5µm for the systems are also shown (F).

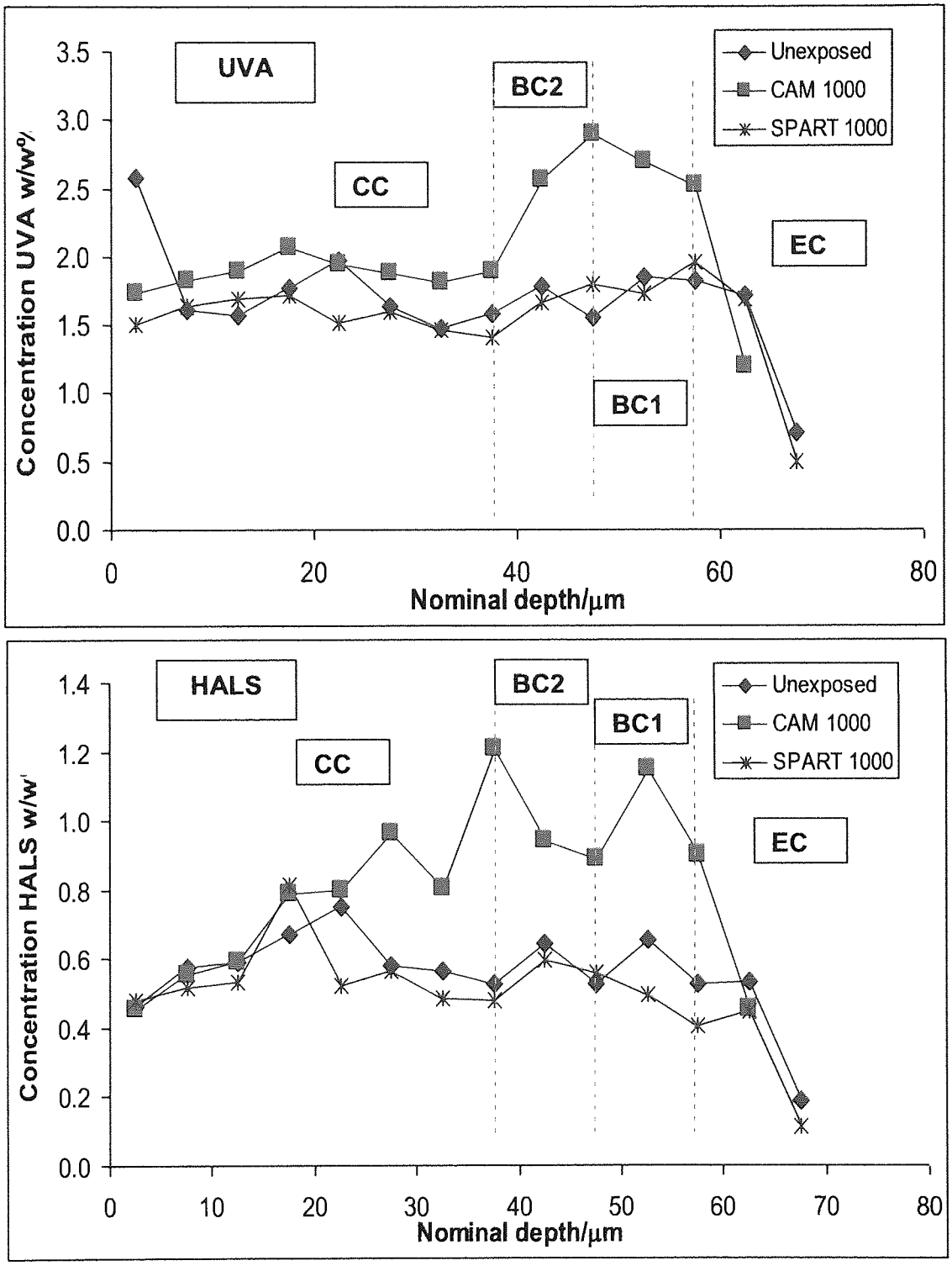

Figure 5.3 Concentration profiles of UVA and HALS in microtomed slices of the clear-coat of system 6c, before and after artificial accelerated (CAM and SPART) weathering for 1000 hours, the UVA level was determined using HPLC-MS-MS analysis of extracted solutions from the coating systems.

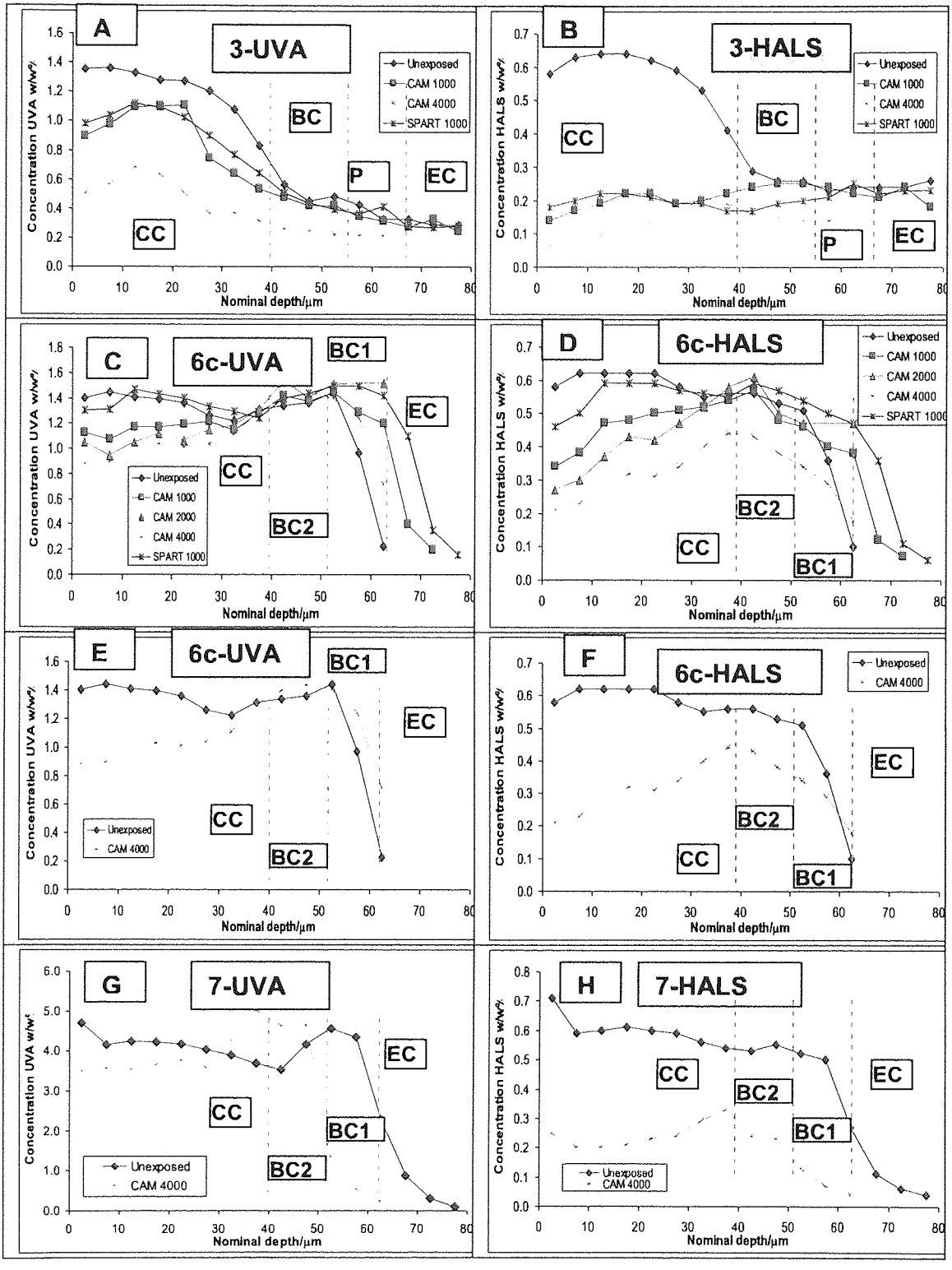

Figure 5.4 UVA and HALS concentration in microtomed slices of the clear-coat of systems 3 (A, B) 6c (C, D, E, F) and 7 (G, H) before and after artificial accelerated (CAM and SPART) weathering, the UVA level was determined using GC-MS analysis of extracted solution.

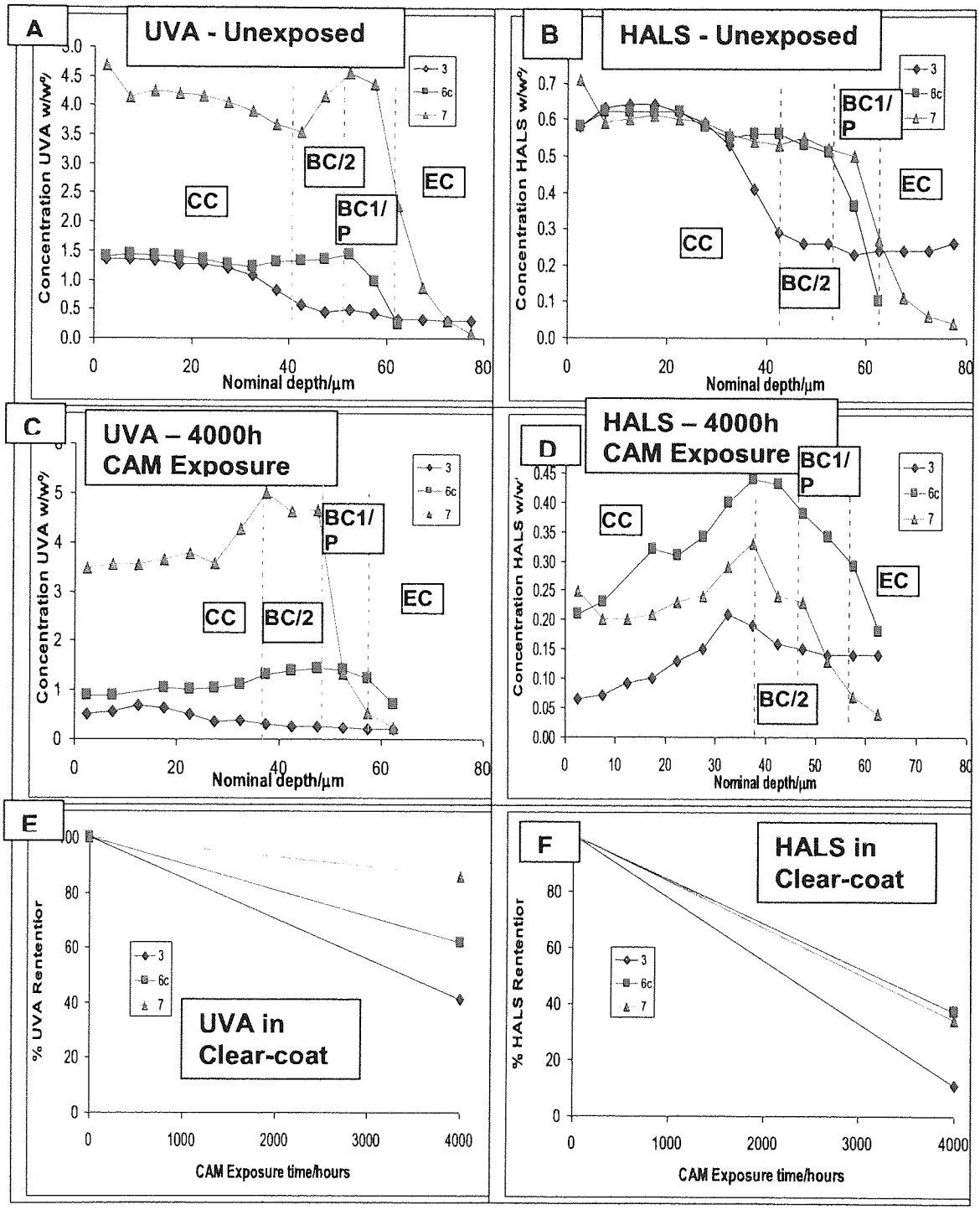

Figure 5.5 UVA and HALS concentration comparisons for microtomed slices of the clear-coats of systems 3, 6c and 7 and 6c, before and after artificial accelerated (CAM) weathering, the UVA level was determined using GC-MS. Results for the different depths at unexposed and 4000 hours of CAM exposure (A, B, C, D), and changes with CAM exposure at a nominal depth of 17.5µm (E, F).

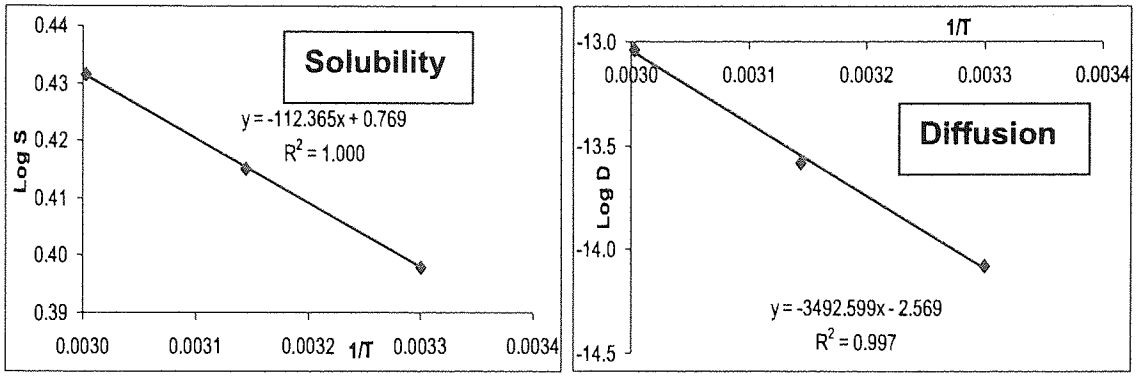

Figure 5.6 Arrhenius plots for the solubility and diffusion characteristics of the UVA (Cyasorb 1164) in the clear-coat obtained using the stack method.

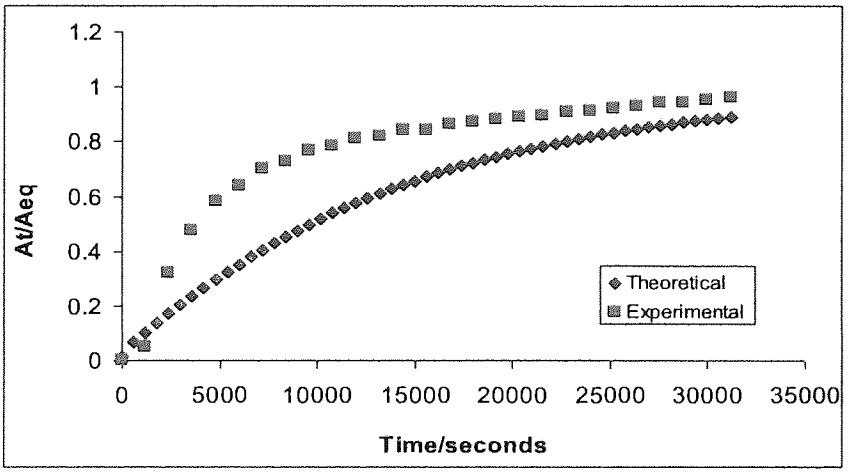

Figure 5.7 Comparison of the theoretical curve (blue) to the actual experimental diffusion results (pink) of the UVA (Cyasorb 1164) in the water-borne clear-coat at 80°C from the FTIR-ATR method (theoretical D for calculations = $8.3*10^{-15}$ m^2/s).

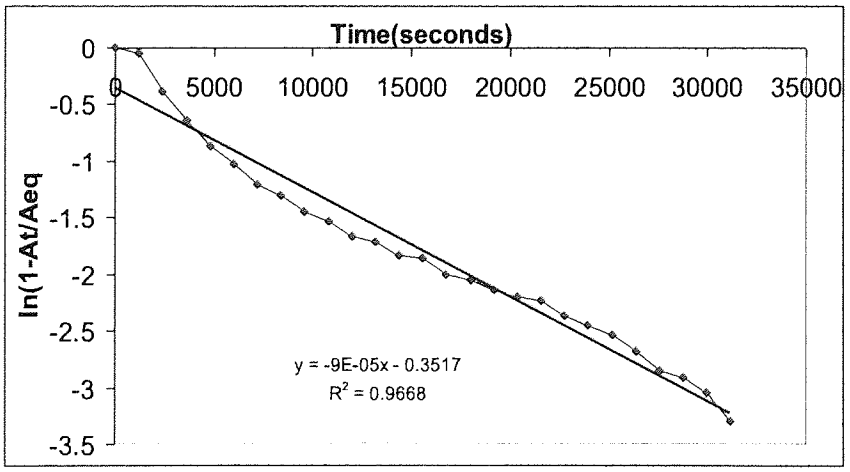

Figure 5.8 Experimental results (blue) for calculation of the diffusion coefficient of the UVA (Cyasorb 1164) in the water-borne clear-coat at 80°C from the FTIR-ATR method, shown with a line of best fit.

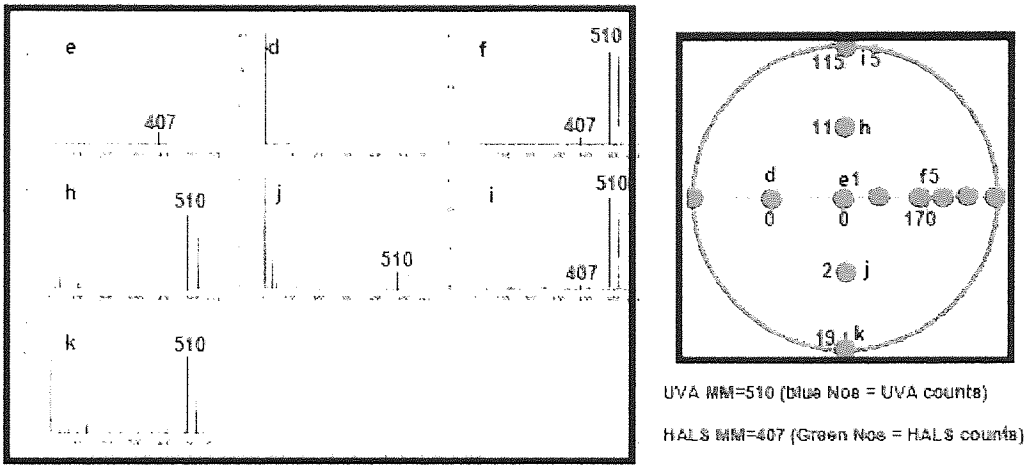

Figure 5.9 LDI-TOF-MS spectra of surface mapping of an area 1*1mm of WB-system 7 after 1000 hours of CAM exposure. Each measurement spot was identified alphabetically (mass spectrum) and numerically (count). The peak at 407 was thought to be due to the Sanduvor 3055 and the peak at 510 due to the Cyasorb 1164.

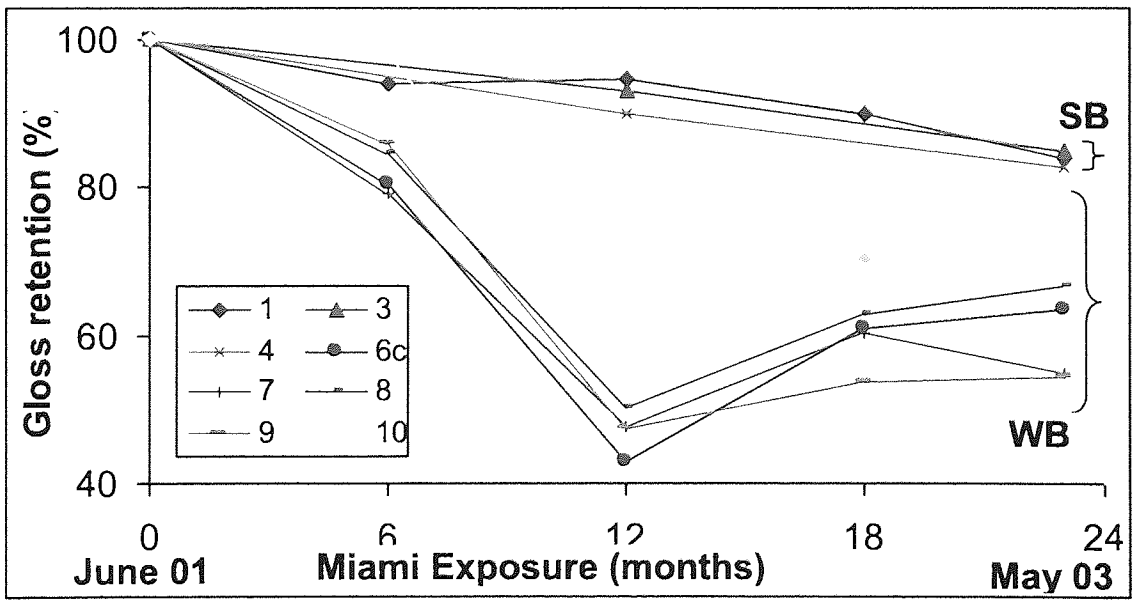

Figure 5.10 Percentage Gloss retention for natural weathering (in Miami, USA).

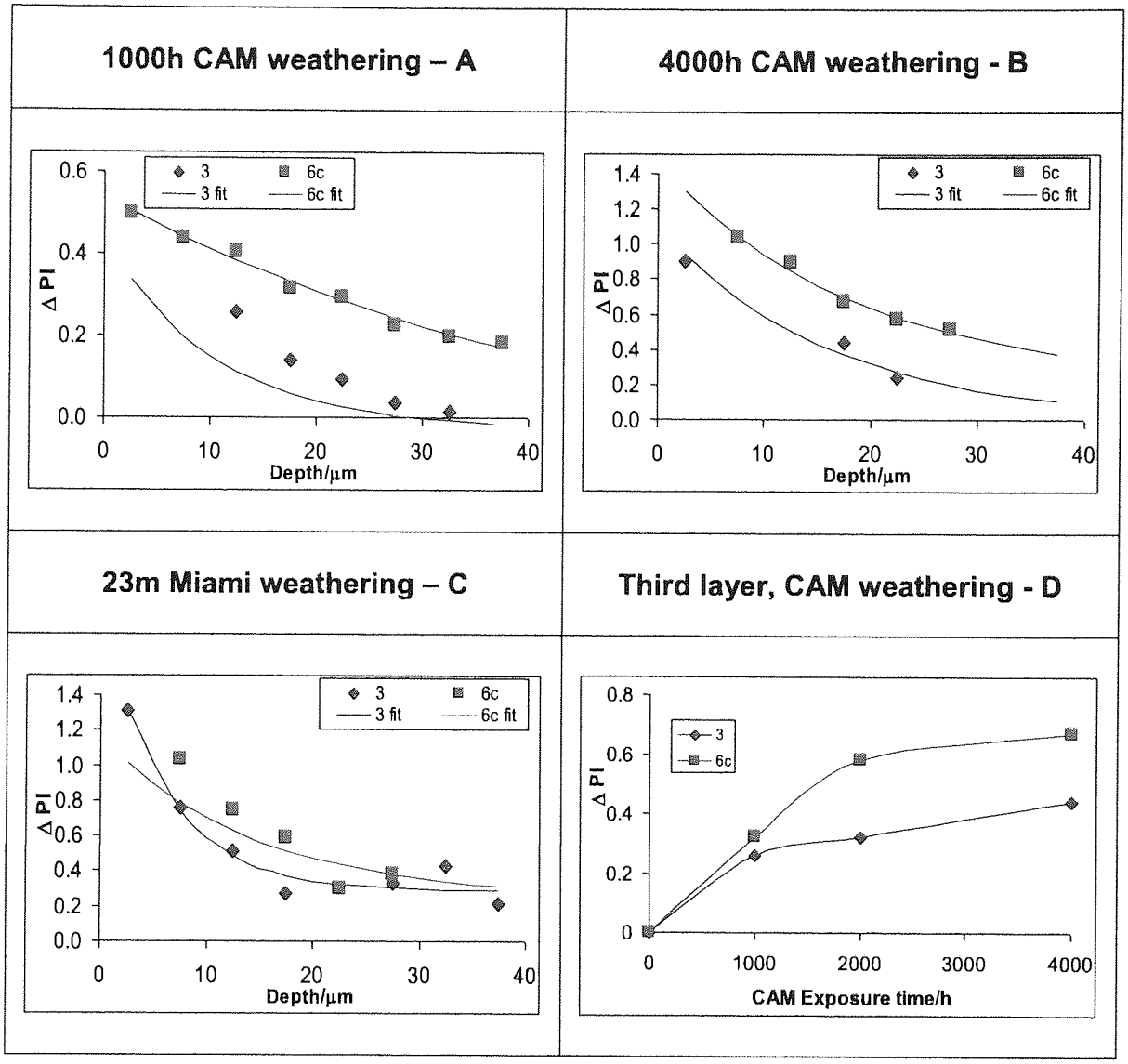

Figure 5.11 Depth profiling showing rotary microtomed PI changes in **Systems 3 and 6c** under natural weathering (Miami) and artificial weathering (CAM and SPART), where;

$\Delta PI_{OH} = \Delta PI_{OH\ t=t} - \Delta PI_{OH\ t=0}$. The points are the experimental data and lines are calculated from curve fitting, see section 2.6.4.

A ΔPI_{OH} changes after 1000 hours of CAM weathering
B ΔPI_{OH} changes after 4000 hours of CAM weathering
C ΔPI_{OH} changes after 23months of natural weathering in Miami
D ΔPI_{OH} changes with weathering of the 3rd clear-coat slice

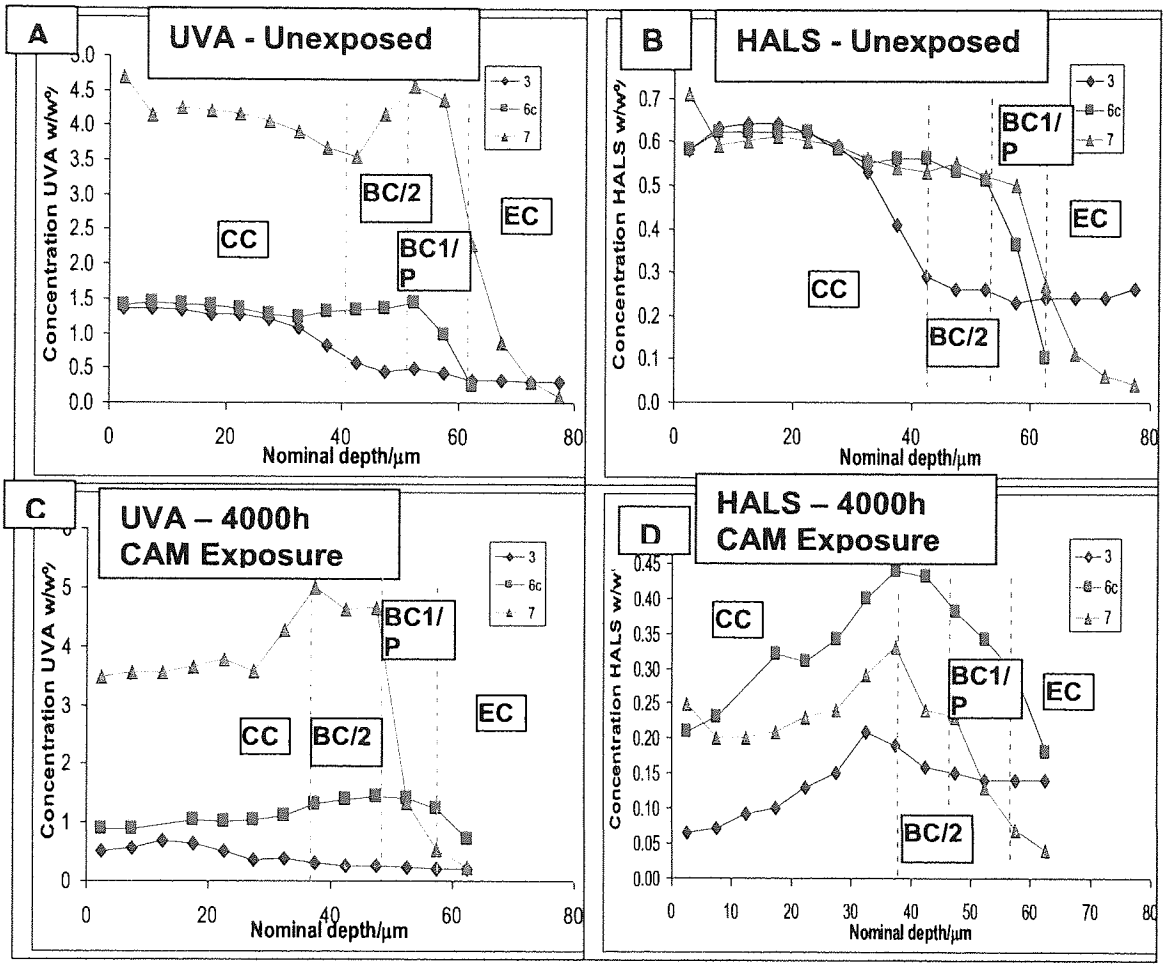

Figure 5.12 UVA and HALS concentration comparisons for microtomed slices of the clear-coats of systems 3, 6c and 7 and 6c, before and after artificial accelerated (CAM) weathering, the UVA level was determined using GC-MS. Results for the different depths at unexposed and 4000 hours of CAM exposure (A, B, C, D).

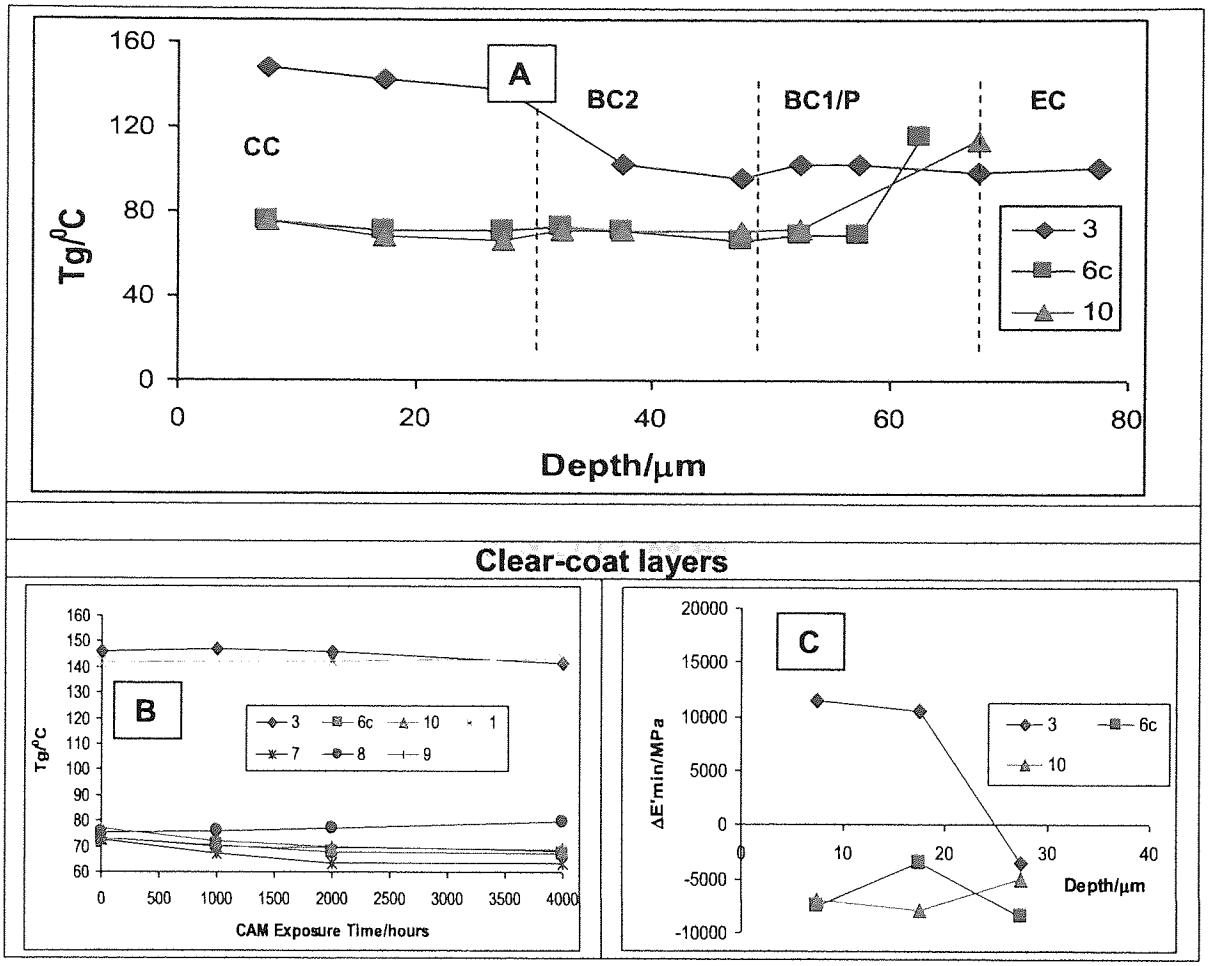

Figure 5.13 Changes in Tg, ΔE'min across the depths of the coating for systems 3, 6c and 10 after 2500 hours of CAM exposure. The depths are the nominal layer depths in µm. ΔChange = $value_{time=t}$ – $value_{average\ across\ the\ clearcoat\ at\ t=0}$

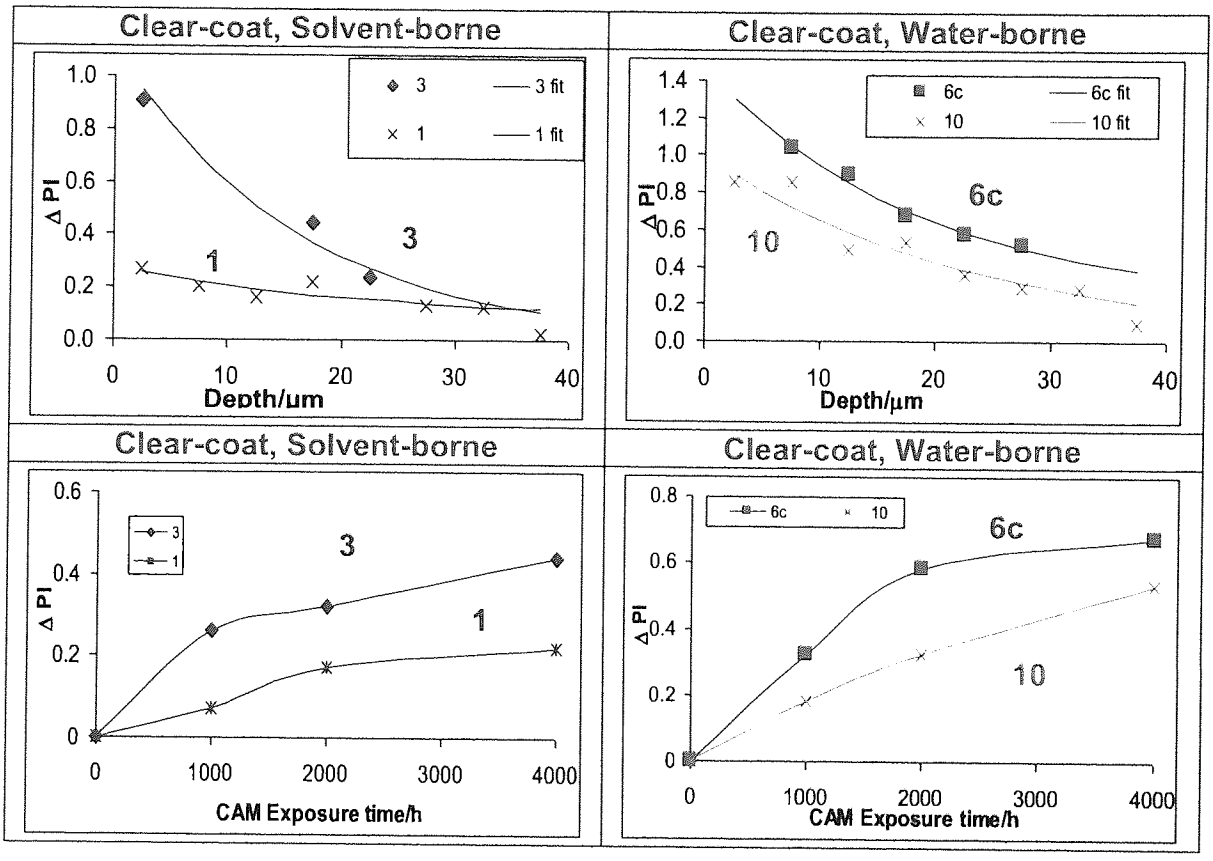

Figure 5.14 Depth profiling showing rotary microtomed PI changes in **1, 3, 6c and 10** under artificial weathering CAM where; $\Delta PI_{OH} = \Delta PI_{OH\ t=t} - \Delta PI_{OH\ t=0}$. The points are the experimental data are calculated from curve fitting, see section 2.6.4

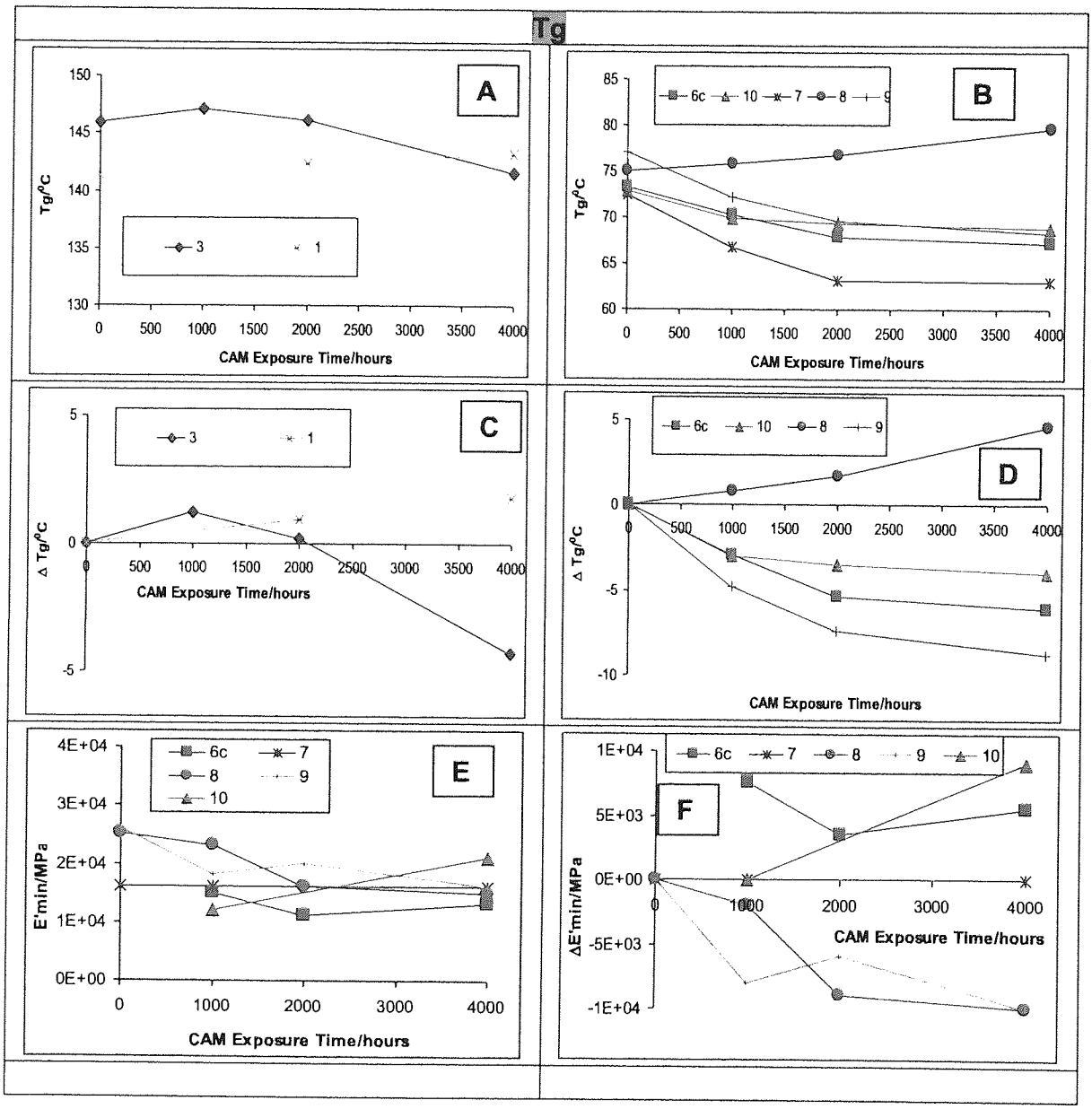

Figure 5.15 Changes in Tg, ΔTg, E'min Δmin and for the 3rd microtomed slice of the blue and silver systems up to 4000 hours of CAM exposure.
ΔChange = $value_{time=t}$ – $value_{average\ across\ the\ clearcoat\ at\ t=0}$

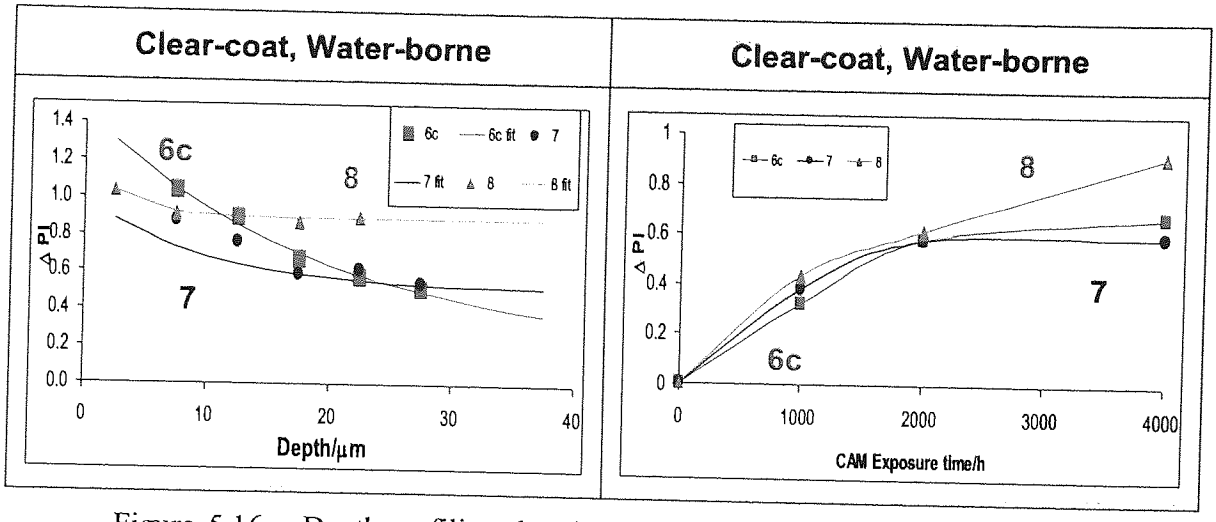

Figure 5.16 Depth profiling showing rotary microtomed PI changes in **6c, 7 and 8** (differences in UVA levels) under artificial weathering CAM where;

$\Delta PI_{OH} = \Delta PI_{OH\ t=t} - \Delta PI_{OH\ t=0}$. The points are the experimental data are calculated from curve fitting, see section 2.6.4.

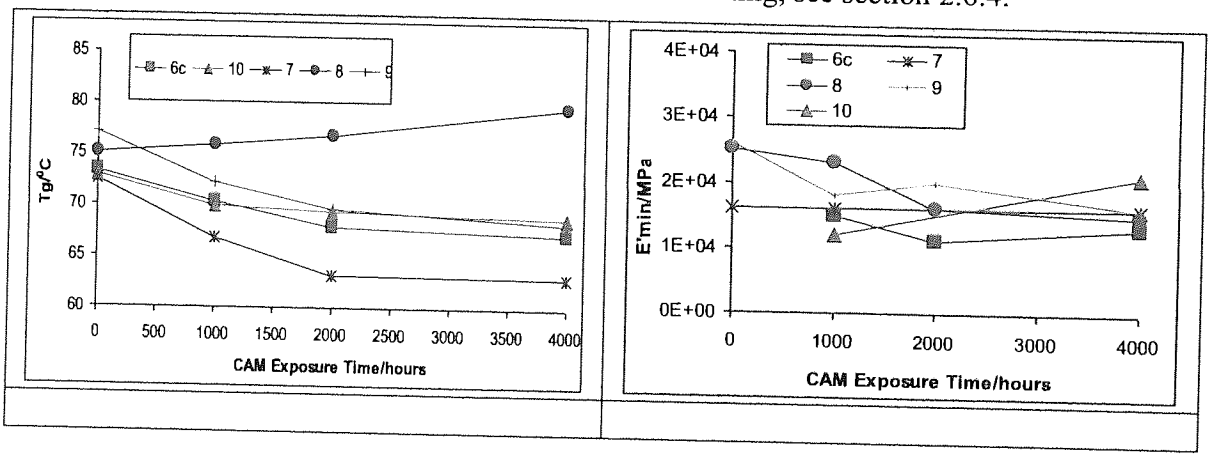

Figure 5.17 Changes in Tg and E'_{min}, for the clear-coat determined from the 3rd microtomed slice of the water-borne systems up to 4000 hours of CAM exposure.
$\Delta Change = value_{time=t} - value_{average\ across\ the\ clearcoat\ at\ t=0}$

CHAPTER 6: CONCLUSIONS AND RECOMMENDATIONS FOR FURTHER WORK

CHAPTER 6: CONCLUSIONS AND RECOMMENDATIONS FOR FURTHER WORK

6.1 Conclusions

From the results discussed in **Chapters 3 to 5**, several conclusions can be made;

6.1.1 In all work carried out in this project the water-borne coating systems were found to be less resilient to weathering compared to the corresponding solvent-borne systems. This information was important as the emphasis of most new coating developments is based on water-borne coatings but very little test data is available for water-borne systems compared to a much larger volume of work for existing solvent-borne systems. The differences in the structures of the materials used in the coating systems caused differences in the properties of the coating systems. The lesser resilience of the water-borne systems was found to be due to the different chemistry of the solvent-borne systems with different reactions occurring after weathering, and also to the use of the wet-on-wet curing regime of the water-borne systems as opposed to the full-bake used between coating layers of the solvent-borne systems. Initially, the results from hardness analysis indicated that the solvent-borne coatings underwent more cross-linking after weathering whereas the water-borne coatings underwent more chain scission (section 3.3.1, **Figure 3.4**) and this was further confirmed from the photoxidation results (section 3.3.2, **Figures 3.18-3.24**) and the DMA analysis (section 4.3.3, **Figure 4.14**).

6.1.2 The method of looking at the changes in the photoxidation index (ΔPI), from FTIR transmission analysis on microtomed automotive coating slices was found to be a useful tool in determining initial weathering-induced changes in the automotive coating systems, before traditional physical methods such as gloss were used, and was found to be a useful way of comparing the durability after weathering of the different types of automotive coatings (for example in the case comparing the solvent-borne and water-borne coatings, and the blue and silver coatings, section 3.3.2). The method was applicable to all layers of the coating

systems; from the top clear-coat layers right down to the electro-coat (section 3.3.2, **Figures 3.18-3.24**). Additionally, ΔPI measurements obtained from FTIR-ATR analysis can be used to compare the resistance to weathering of the coating systems of only the very top layer of the clear-coat if microtoming is not available (section 3.3.2, **Figure 3.16**).

6.1.3 The migration potential of the UV stabiliser (particularly with respect to the UVA) was found to be very important when examining the resistance of the automotive coating systems to weathering. In particular, the changes in UVA concentration levels in the different layers of the coatings were followed by depth profiling using different methods (section 5.3.1, **Figures 5.3-5.5**) It was found that in the water-borne systems, the UVA migrates between the coating layers (for example from the clear-coat into the base-coat) as a consequence of both the wet-on-wet curing regime (in contrast to a full bake between the layers in the solvent-borne systems), and the lower level of cross-linking in the binder matrix of the water-borne systems.

6.1.4 The method of dynamic mechanical analysis (DMA) carried out on microtomed coating films was found to give useful information on the physical changes that took place (in terms of both the glass transition temperature and the relative cross-link density) after weathering (section 4.3.3, **Figures 4.8-4.10),** This method again gave important information observed before changes in physical properties such as changes in gloss and hardness could be measured. The measurements showed that most changes occurred at the surface of the coatings. The changes in glass transition temperatures and the relative cross-link densities were interpreted in terms of the chemistry of the binder systems during weathering. The DMA measurements also allowed for the differences in the coating systems throughout the coating layer depths to be compared (for example solvent-borne vs. water-borne and the effects of the different colours of the coating systems). Furthermore, the effects of erosion of the top layer of the clear-coats after weathering were inferred from changes in the glass transition temperatures of the particular coating layers which were distinct (section 4.3.2, **Figure 4.19**) and these were correlated with photographs of the microtomed slices used to investigate the effects of weathering on erosion.

6.1.5 The results from all the methods of analyses also indicated that the colour of an automotive coating has a major effect on the exterior durability of the coatings. The photoxidation results (section 3.2.3, **Figure 3.3.2**) showed that the silver systems are more resistant to photodegradation than the equivalent blue systems. This was due to, firstly, the silver base-coats contained aluminium particles that reflected the damaging UV radiation away from the coatings. Secondly, the temperature of the exposed blue coatings was higher than that of the silver coatings helping to accelerate the photoxidation reactions and giving rise to the higher extent of photoxidation change. This effect was further seen from DMA results (section 4.3.3, **Figures 4.14-4.15 F and H**) showing the importance of the presence of the aluminium flakes in the case of the silver coatings.

6.1.6 The level of the UV stabiliser was also found to have an effect on the durability to weathering of the different coatings systems. The photoxidation results (section 3.3.3, **Figure 3.33**) showed that the unstabilised (with respect to the UVA stabiliser) water-borne system 8 had the greatest changes in photoxidation index after weathering, whereas system 7 which has three times the concentration of UVA compared to system 6c gave a slightly lower photoxidation index value, showing that the use of UVA at higher concentrations in automotive coatings results in better resistance to weathering. The glass transition temperature from the DMA analysis also changed differently in the presence and absence of the UVA stabiliser (section 4.3.3, **Figure 4.18 B, D**). The effect of weathering was to reduce the concentrations of both the HALS and UVA stabilisers (section 5.3.1, **Figure 5.5**), with the higher concentration of UVA (in system 7) leading to a lower extent of loss during weathering.

6.1.7 The natural weathering (in Miami, USA) and artificial accelerated (CAM, SAE J1960) weathering regimes gave rise to similar patterns of degradation profiles. This was seen by the changes in photoxidation index results (section 3.3.3, **Figure 3.22**) where the CAM accelerated weathering exposures gave information about the extent of photodegradation at a much reduced time scale compared to the Miami weathering. The wavelength range used in the CAM

weathering was similar to that of natural weathering thus the degradative profiles can be expected to be similar. The advantage of the outdoor weathering exposure gives information about the actual effects of photodegradation in the end-use service environment of the automotive coatings, thus it is still advisable to use both accelerated weathering and outdoor weathering tests where possible.

6.2 Recommendations for Further Work

6.2.1 The effects of the two colours investigated (blue and silver) were found to have a great effect upon the exterior durability of the coating systems. Thus, it may be useful to investigate other colours; for example black and white which will reach very different temperatures after weathering and the consequences of the use of metallic flakes in the base-coat (for example taking the same coating but in the absence and presence of metallic flakes).

6.2.2 It would be useful to further continue the developed MALDI-Tof analysis work to track the distribution and movement of the UVA/HALS stabilisers in the complete coating systems before and after weathering, as the method requires no microtoming and is applicable for different coating systems.

6.2.3 The changes caused by weathering to the coating systems were also seen by the DMA bending method and this analysis could be extended to all the systems investigated after different weathering regimes. This method also has the advantage that no microtoming is required and minimal samples preparation is needed.

6.2.4 The analytical methods used in this work (for example photoxidation index, concentration profiles of the UV-stabilisers, DMA analysis) are also applicable to different types of automotive coatings (for example different binder chemistries with different stabilisation packages) and thus the analysis could be carried out on these and the results for different coating systems compared.

REFERENCES

1. N. Tahmassebi, S. Moradian, 'Predicting the Performances of Basecoat-Clearcoat Automotive Paint Systems by the use of Adhesion, Scratch and Mar Resistance Measurements', Poly. Deg. Stab, **83,** 405-410, (2004).

2. K.M. Wenstahl, 'Service Life Prediction of Automotive Coatings, Correlating IR Measurements and Gloss Retention', Poly. Deg. Stab, **54,** 57-65, (1996).

3. D.J. McEwan, M.H. Verma, R.O. Turner, 'Accelerated Weathering of Automotive Paints Measured by Gloss and IR Spectroscopy', J. Coatings Tech, **59, 755,** 64-74, (1987).

4. J. Musil, F. Kunc, H. Zeman, H. Polakova, 'Relationships between hardness, Young's Modulus and Elastic Recovery in hard nanocomposite coatings', Surface Coatings and Technology, **154,** 304-313, (2002).

5. K. Adamsons, 'Chemical Surface Characterization and Depth Profiling of Automotive Coating Systems', Prog. Polm Sci, **25,** 1363-1409, (2000).

6. K. Adamsons, 'Chemical Depth Profiling of Multilayer Automotive Coating Systems', Prog. Org. Coatings, **45,** 69-81, (2002).

7. C.M. Seubert, M.E. Nichols, V.A. Cooper, J.L. Gerlock, 'The Long-Term Weathering Behaviour of UV Curable Clearcoats, I. Bulk Chemical and Physical Analysis', Poly. Deg. Stab, **81,** 103-115, (2003).

8. J.L. Gerlock, C.A. Smith, V.A. Cooper, T.G. Dusbiber, W.H. Weber, 'On the use of FTIR and UV Spectroscopy to Assess the Weathering Performance of Isolated Clearcoats from Different Chemical Families', Poly. Deg. Stab, **62,** 225-234, (1998).

9. C. Decker, K. Zahouily, 'Photodegradation and Photoxidation of Thermoset and UV-cured acrylate polymers', Poly. Deg. Stab, **64,** 293-304, (1999).

10. K. Adamsons, 'Chemical Depth Profiling of Automotive Coating Systems using Slab Microtome Sectioning with IR/UV-Vis Spectroscopy and Optical Microscopy', J. Coatings Tech, **74, 925,** 47-54, (2002).

11. R. Iyengar, B. Schellenburg, 'Loss Rate of UV Absorbers in Automotive Coatings', Poly. Deg. Stab, **61,** 151-159, (1998).

12. J.L. Gerlock, A.V. Kucherov, 'M.E. Nichols, On the Combined Use of UVA, HALS, Photoxidation and Fracture Energy Measurements to

Anticipate the Long-term Weathering Performance of Clearcoat-Basecoat Automotive Paint Systems', J. Coatings Tech, **73, 918,** 45-54, (2001).

13. C.A. Smith, J.L. Gerlock, R.O. Carter III, 'Determination of ultraviolet light longevity and distribution in automotive paint systems using ultra-violet micro-spectroscopy', Poly. Deg. Stab, **72,** 89-97, (2001).

14. S.E. Strawn, J.M. White, G.W. Marshall, L. Gee, H.E. Goodis, S.J. Marshall, 'Spectroscopic Changes in Human dentine exposed to various storage solutions - short term', Journal of Dentistry, **24, 6,** 417-423, 1996).

15. K. Moller, T. Gevert, 'A Solid State Investigation of the Desorption/Evaporation of Hindered Phenols from LDPE using FTIR and UV Spectroscopy with Integrating Sphere:the Effect of Molecular Size on the Desorption', J. Applied Poly. Sci, **61**, 1149-1162, (1996).

16. K. P. Menard, Dynamical Mechanical Analysis: A Practical Introduction, RC Press, Florida, (1999).

17. W. Schesing, M. Buhk, M. Osterhold, 'DMA in the Coatings Industry', Prog. Org. Coatings, **49**, 197-208, (2004).

18. M. Osterhold, P. Glockner, 'Influence of Weathering on Physical Properties of Clearcoats', Prog. Org. Coatings, **41**, 177-182, (2001).

19. G. M. Spinks, Z. Liu, H. Brown, M. Swain, H. See, E. Evans, 'Paint Layer Thermomechanical Properties determined by in-situ Dynamic Mechanical Analysis in 3 point bending', Prog. Org. Coatings, **49**, 95-102, (2004)

20. R-J. Roe, HE Bair, C. Gieniewski, 'Solubility and Diffusion Coefficient of Antioxidants in Polyethylene', J. Applied Poly. Sci, **18**, 843-856, (1974).

21. L. Lazare, N.C. Billingham, 'Diffusion of a UV-Absorbing Stabiliser in some poly(ester-block-ether) copolymers', Polymer, **42**, 9461-9467, (2001).

22. G. Ferrara, M. Bertoldo, M. Scoponi, F. Ciardelli, 'Diffusion coefficient and activation energy of Irganox 1010 in Poly(propylene-co-ethylene) copolymers', Poly. Deg. Stab, **73,** 411-416, (2001).

23. C.M. Balik, W. Simendinger, 'An attenuated total reflectance cell for analysis of small molecule diffusion in polymer thin films with FTIR', Polymer, **39 20**, 4723-4728, (1998).

24. G.T. Fieldson and T.A. Barbari, 'The use of FTIR-ATR spectroscopy to characterize penetrant diffusion in polymers', Polymer, **34**, 1146-1153, (1993).

25. S. Papasavva, S. Kia, J. Claya, R. Gunther, 'Characterization of Automotive Paints: an Environmental Impact Analysis, Prog. Org. Coatings. **43**, 193-203, (2001).

26. www.brian-jones.co.uk/puchem.shtml
Accessed 23/09/05.

27. B. Vogt-Birnbrich, 'Novel Synthesis of low VOC Polymeric Dispersions and their Application in Waterborne Coatings, Prog. Org. Coatings. **29**, 31-38, (1996).

28. K. D. Weiss, 'Paints and Coatings: A Mature Industry in Transition, 'Prog. Polm Sci, **22**, 203-245, (1997).

29. A. T. Chen, R. T. Wojick, 'Polyurethane Coatings for Metal and Plastic Substrates,' Olin Corp, Cheshire, Conn.

30. T. Nabuurs, D. Pears, A. Overbeek, 'Defect Free Coatings from Two-pack Isocyanate Curable Acrylic Dispersions', Prog. Org. Coatings. **35**, 129-140, (1999).

31. S. Subramani, Y. Park, Y.-Soo Lee, J. Kim, 'New Development of Polyurethene Dispersion Derived from Blocked Aromatic Diisocyanates',Prog. Org. Coatings, **48**, 71-79, (2003).

32. K. Rink, B. Mayer, 'Water-based coatings for Automotive Refinishing', Prog. Org. Coatings, **34**, 175-180, (1998).

33. E. Schmid, Chapter 3, 'Exterior Durability of Organic Coatings', Redhill, FMJ International Publications Ltd, Surrey, 1988.

34. Z. Wicks, D. Wicks, J. Rosthauser, 'Two Package Water-borne Urethane Systems', Prog. Org. Coatings, **44**, 161-183, (2002).

35. R. G. Coogan, 'Post-crosslinking of Waterborne Urethanes, Prog. Org. Coatings. **32**, 51-63, (1997).

36. David A. Ley, D. Fiori, R. Quinn, 'Optimization of Acrylic Polyols for Low VOC Two-Component Water Reducible Polyurethane Coatings Using Tertiary Isocyanate Crosslinkers', Prog. Org. Coatings, **35**, 109-116, (1999).

37. P. Geurink, T. van't Veer, R. Buter, I. Rood, J. Schlief, L. Van der Van, R. Leijzer, 'Binder Systems for Water-borne two-pack products for automotive refinish application', Prog. Org. Coatings, **48**, 153-160, (2003).

38. W. Collong, A. Gobel, B. Kleuser, W. Lenard, M. Sonnlag, '2K Water-borne Clear-coats - A Competition between Cross-linking and side reactions', Prog. Org. Coatings, **45,** 205-209, (2002).

39. R. G. Coogan, 'Post-crosslinking of Waterborne Urethanes, Prog. Org. Coatings. **32,** 51-63, (1997).

40. J. Pospisil, S. Nespurek, 'Photostabilisation of Coatings: Mechanisms and Performance', Prog. Polm Sci, **25,** 1261-1335, (2000).

41. J. Fried, Chapter 6, 'Polymer Science and Technology', Prentice Hall Professional Technical Reference, New Jesey, (2003).

42. www.specialchem.com
Accessed 24.9.05.

43. Cangelosi, Davis, Gray, Stretanski, Jakiela, 'UV Stabilisers in the Encyclopedia of Polymer Science and Technology, John Wiley and Sons, (2002), Accessed from,
www.mrw.interscience.com/epst/articles/pst379/frame.html
Article online posting date: July 15, 2002.

44. M. E. Nichols, J. L. Gerlock, 'Rates of photooxidation induced crosslinking and chain scission in thermoset polymer coatings II. Effect of hindered aminelight stabilizer and ultraviolet light absorber additives', Poly. Deg. Stab, **69,** 197-207, (2000).

45. J. Sampers, 'Importance of Weathering Factors other than UV Radiation and temperature in Outdoor Exposure', Poly. Deg. Stab, **76,** 455-465, (2002).

46. J.E. Picket and M.M. Gardner, 'Reproducibility of Florida Weathering Data,' Poly. Deg. Stab, **In press**, (2005).

47. Atlas Material Testing Solutions, 'Network of Weathering Products and Services,' printed in the USA, 2002.

48. L. F. E. Jacques, 'Accelerated and Outdoor/Natural Exposure Testing of Coatings', 'Prog. Polm Sci, **25,** 1337-1362, (2000).

49. SAE J1976

50. SAE J1960 JUN89, 'Accelerated exposure of automotive materials using a controlled irradiance water cooled xenon arc apparatus,'

51. U. Schulz, P. Trubiroha, U. Schernau, H. Baumgart, 'The Effects of Acid Rain on the Appearance of Automotive Paint Systems Studied

outdoors and in a new Artificial Weathering Test', Prog. Org. Coatings. **40,** 153-159, (2000).

52. Downloaded from Finishing.com, Letter #31707 SAE J1960: How does it correlate to Florida Exposure? Allen Zielnik, Atlas Materials Testing Technology LLC, Chicago, (2004), www.finishing.com.

53. F.X. Perrin, M. Irigoyen, E. Aragon, J.L. Vernet, 'Evaluation of Accelerated Weathering Tests for three paint systems: a comparative study of their aging behaviour', Poly. Deg. Stab, **72,** 115-124, (2001).

54. M.E. Nichols, C.A. Darr, C.A. Smith, M.D. Thoules, E.R. Fischer, 'Fracture Energy of Automotive Clearcoats -1. Experimental Methods and Mechanics', Poly. Deg. Stab, **60,** 291-299, (1998).

55. J. A. Sims, 'Acceleration Shift Factor and its Use in Evaluating Weathering Data', J. Coatings Tech, **59, 748,** 45-53, (1987).

56. M. Sadati, N. Mohammadi, N. Taheri Qazvini, N. Tahmasabi, S. Koopahi, 'Evalution of Scratch Resistance of an acrylic-melamine clear-coat based on its fracture energy', Prog. Org. Coatings. **53, 1,** 23-28 (2005).

57. K. Adamsons, G. Blackman, B. Gregorovich, L. Lin, R. Matheson, 'Oligomers in the Evolution of Automotove Clearcoats: Mechanical Performance Testing as a Function of Exposure', Prog. Org. Coatings. **34,** 64-74, (1998).

58. Downloaded from the National Physical Laboratory, www.npl.com, Accessed 12.07.2005.

59. M. Osterhold, G. Wagner, 'Methods for Characterizing the Mar Resistance', Prog. Org. Coatings. **45,** 365-371, (2002).

60. M. Vitali, 'Development of a Semi-quantitative ATR IR Spectroscopy Analysis for the Study of Compatibility of HAS in PE Films', Poly. Testing, **20,** 293-304, (2001).

61. N. S. Allen, M. Edge, A. Ortega, C. M. Liauw, J. Stratton, R. B. McIntyre, 'Behaviour of nanoparticle (ultrafine) Titanium dioxide Pigments and Stabilisers on the photoxidative Stability of Waterborne Acrylic and Isocyanate based acrylic Coatings', Poly. Deg. Stab, **78,** 467-478, (2002).

62. R. P. Singh, N. Tomer, S. Bhadraiah, 'Photoxidation Studies on Polyurethane Coatings; Effect of Additives on Yellowing of Polyurethane', Poly. Deg. Stab, **73,** 443-446, (2001).

63. M. Horgnies, E. Darque-Ceretti, R. Combarieu, 'Influence of Additives Segregation on Surface Composition of Automotive Coatings:effects of ethanol cleaning', Prog. Org. Coatings. **47,** 156-163, (2003).

64. A. Zmihorska-Gotfryd, 'Coating Compositions based on Modified phenol-formaldehyde Resins and Urethane Polymers', Prog. Org. Coatings. **49,** 109-114, (2004).

65. S.J. Marrs, R.M. Head, M.J. Cowling, T. Hodgkiess, J. Davenport, 'Spectrophotometric Evaluation of Micro-algal Fouling on Marine Optical Windows', Estaurine, Coastal and Shelf Science', **48,** 137-141, (1999).

66. J. Bart, 'Polymer Additive Analysis at the Limits', Poly. Deg. Stab, **82,** 197-205, (2003).

67. T Murayama, 'DMA of polymeric materials', Elsevier, Amsterdam, (1978).

68. D. K. Chattopadhyay, S. S. Panda, K.V.S.N. Raju, 'Thermal and Mechanical Propertites of epoxy acrylate/methacrylate UV Cured Coating,' Prog. Org. Coatings. **54,** 10-19, (2005).

69. X. Ramis, A. Cadenate, J. M. Morancho, J.M. Salla, 'Curing of a Thermosetting Powder Coating by means of DMTA, TMA and DSC', Polymer, **44,** 2067-2079, (2003).

70. S. Tasic, B. Bozic, B. Dunjic, 'Synthesis of new hyperbranched urethane acrylates and evaluation in UV-Curable coatings', Prog. Org. Coatings. **51,** 321-328, (2004).

71. C.M. Seubert, M.E. Nichols, 'Alternative Curing Methods of UV Curable Automotive Clearcoats', Prog. Org. Coatings. **48,** 218-224, (2004).

72. C. M. Guttman, 'Mass Spectrometry in the Encyclopaedia of Polymer Science and Technology, John Wiley and Sons, (2002), Accessed from, www.mrw.interscience.com
Article online posting date: October 22, 2001.

73. www.pslc.ws/macrogcss/maldi.html
Accessed 12/12/2006

74. J. Malik, G. Ligner, L. Avar, 'Polymer bounds HALS – expectations and possibilities', Poly. Deg. Stab, **60,** 205-213, (1998).

75. J. Y Moisan, Chapter 4, 'Effects of Oxygen Permeation and the Mathematics of Diffusion', in Polymer Permeability, Elsevier Applied Science Publishers, London, (1986).

76. J. Crank, The Mathematics of Diffusion, 2nd edition, Clarendon Press, Oxford, (1975).

77. J. Comyn, Chapter 1, 'Introduction to Polymer Permeability and the Mathematics of Diffusion', in Polymer Permeability, Elsevier Applied Science Publishers, London, (1986).

78. L. Mascia, Thermoplastics, Materials Engineering, 2nd edition, Chapman and Hall, Hampshire, (1989).

79. M.D.R.J. Goonetilleka, 'Migration of Additives from Thermoplastic Polymers', Ph.D. Thesis, PPP Research Unit, SEAS, Aston University, (1988).

80. O-W. Lau, S-K. Wong, 'Review Paper; Contamination in Food from Packaging Material', Journal of Chromatography A, **882,** 255-270, (2000).

81. J. Crank, Diffusion in Polymers, Academic Press, (1968).

82. P. Vink, Chapter 4, 'Loss of UV Stabilisers from polyolefins during photoxidation', in Developments in Polymer Stabilisation, **Volume 3,** G Scott (editor), Applied Science Publishers, London, (1981).

83. B Murphy, P Kirwan, P McLoughlin, 'Investigation in polymer diffusant interaction using ATR-FTIR Spectrscopy', Vibrational Spectroscopy, **33,** 75- 82, (2003).

84. http://scholar.lib.vt.edu/theses/available/etd-73197-10251/unrestricted/ETD.PDF

85. J. Luston, Chapter 5, 'Physical Loss of Stabilisers from Polymers', in Developments in Polymer Stabilisation, **Volume 2,** G Scott (editor), Applied Science Publishers, London, (1980).

86. Pictures from SP, a project partner.

87. C. Decker, F. Masson, R. Schwalm, 'Weathering Resistance of water-based UV-cured polyurethane-acrylate coatings', Poly. Deg and Stab, **83,** 309-320 (2004).

88. D. Wicks, Z. Wicks, 'Autoxidizible Urethane Resins' Prog. Org. Coatings, **54,** 141-149, (2005).

89. L. W. Hill, H. M. Korzeniowski, M. Ojunga-Andrew, R. C. Wilson, 'Accelerated Clearcoat Weathering studied by Dynamic Mechanical Analysis', Prog. Org. Coatings, **24,** 147-173, (1994).

90. M. E. Nichols, J. L. Gerlock, C. A. Smith, C. A. Darr, 'The Effects of Weathering on the Mechanical Performance of Automotive Paint Systems', Prog. Org. Coatings, **35**, 153-159, (1999).

91. N. Tahmassebi, S. Moradian, S. M. Mirabedino, 'Evaluation of Basecoat-clearcoat Automotive paint systems by electrochemical properties measurements', Prog. Org. Coatings, **54**, 384-389, (2005).

92. M. E. Nichols, J. L. Gerlock, C. A. Smith, C. A. Darr, 'The Effects on the Mechanical Performance of Automotive Paint Systems', Prog. Org. Coatings, **35**, 153-159, (2005).

APPENDICES

APPENDICES: CHAPTER 3

A3.1. Optical Microscopy

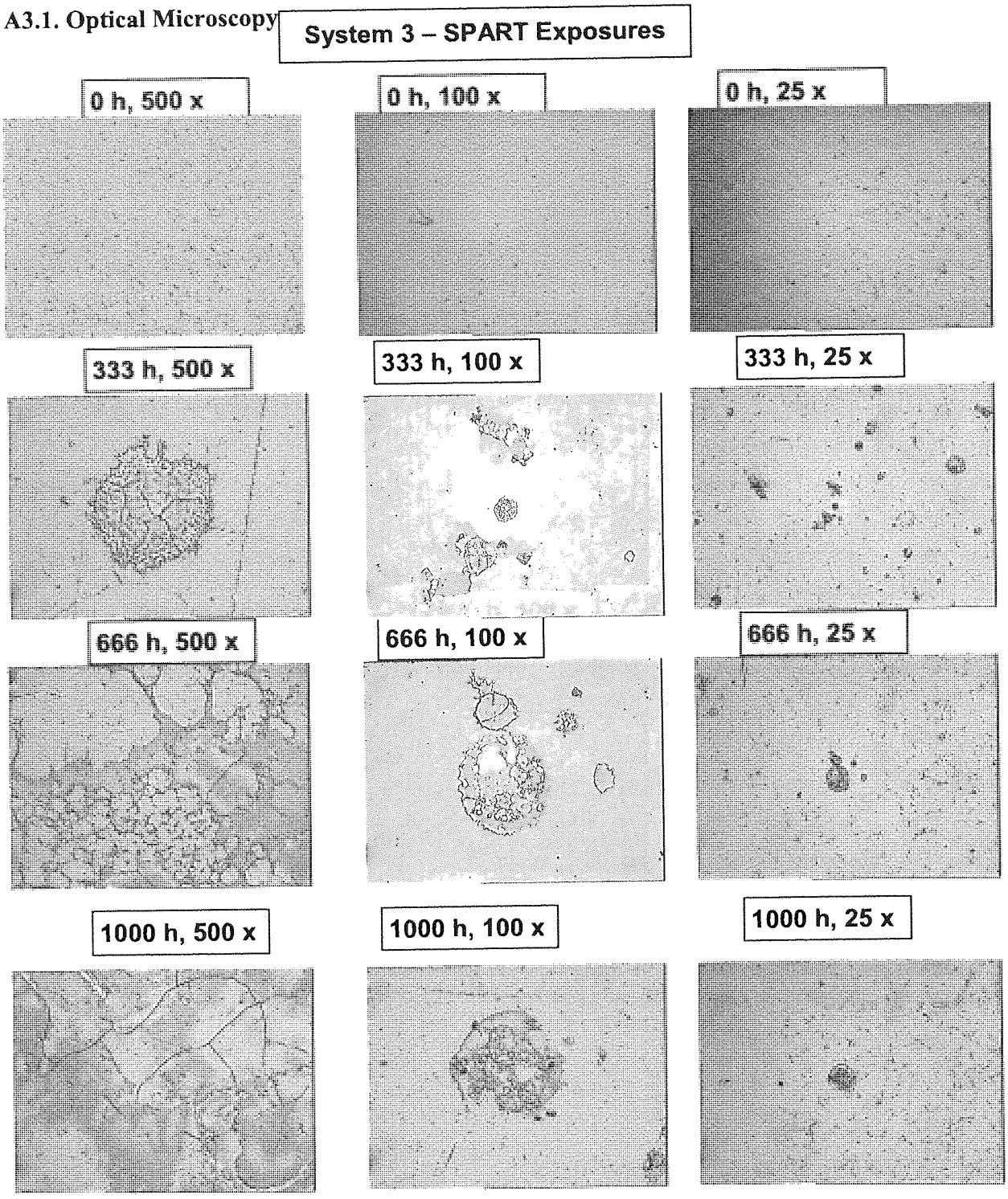

Appendix A3.1.1 Optical micrographs of System 3, with Artificial Accelerated Weathering (SPART), 333, 666 and 1000 hours and magnifications of 500, 100 and 25 for each exposure period, under reflectance.

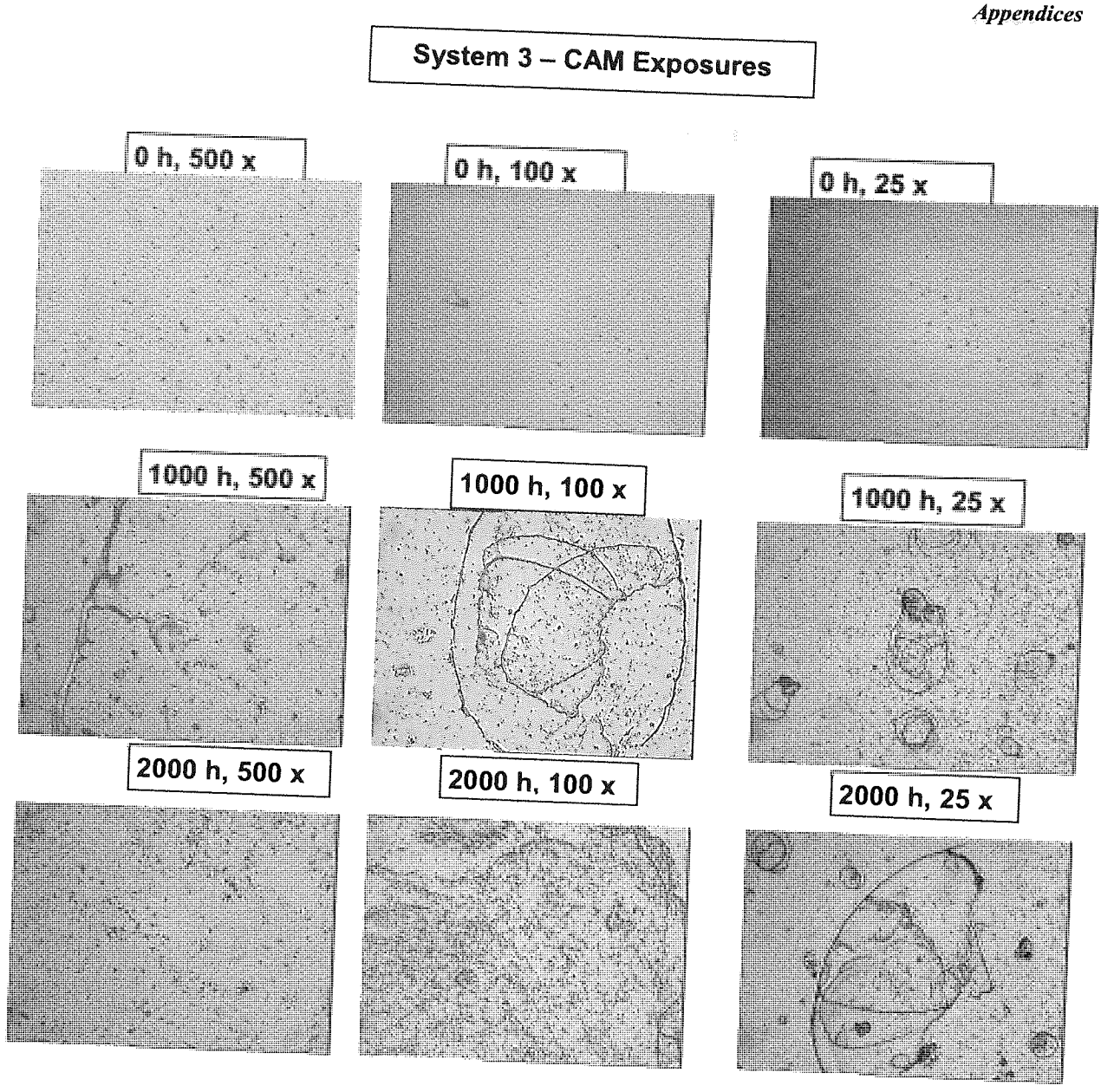

Appendix A3.1.2 Optical micrographs of System 3, with Artificial Accelerated Weathering (CAM), 1000 and 2000 hours and magnifications of 500, 100 and 25 for each exposure period.

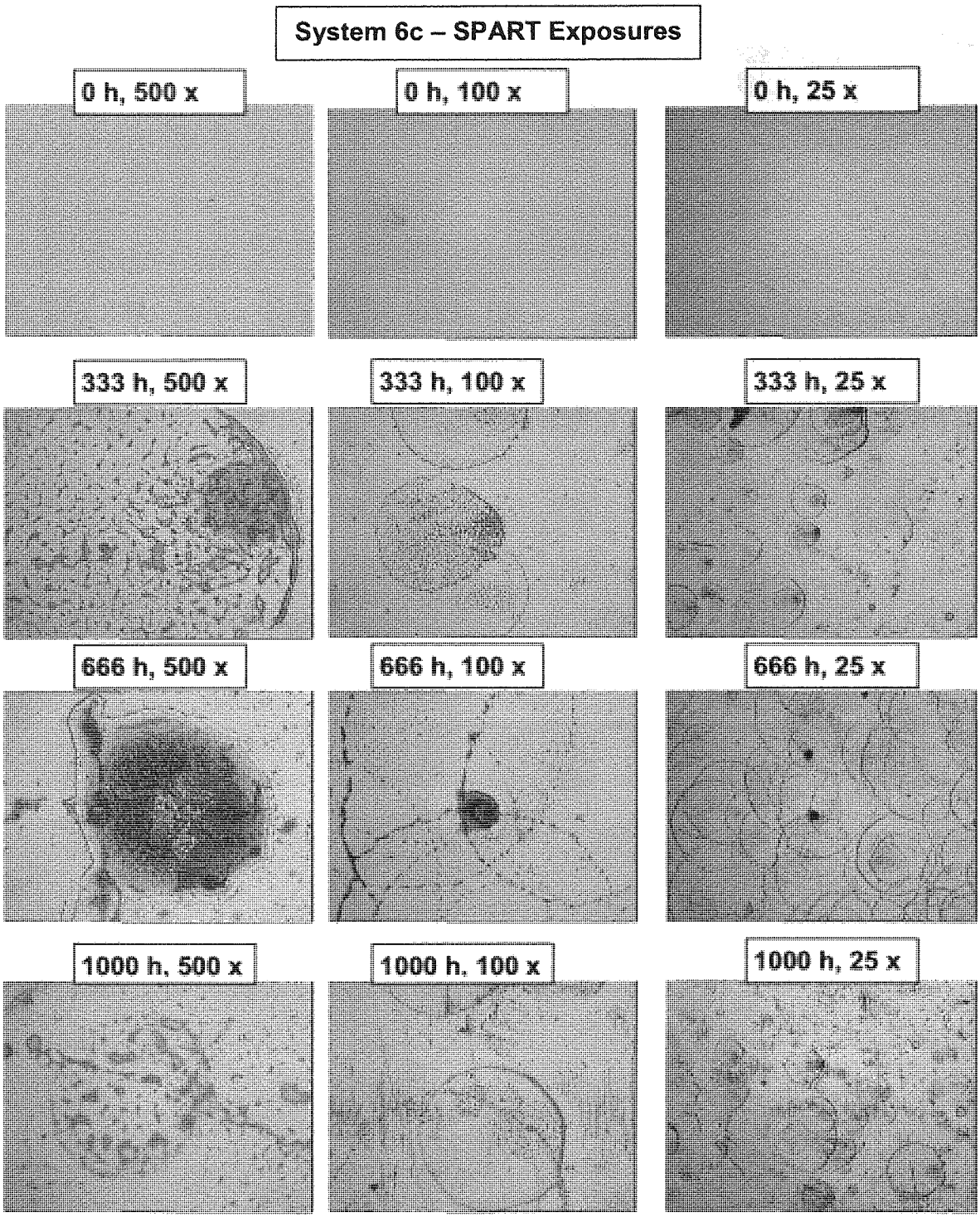

Appendix A3.1.3 Optical micrographs of System 6c, unexposed and with Artificial Accelerated Weathering (SPART), 333, 666 and 1000 hours and magnifications of 500, 100 and 25 for each exposure period, under reflection.

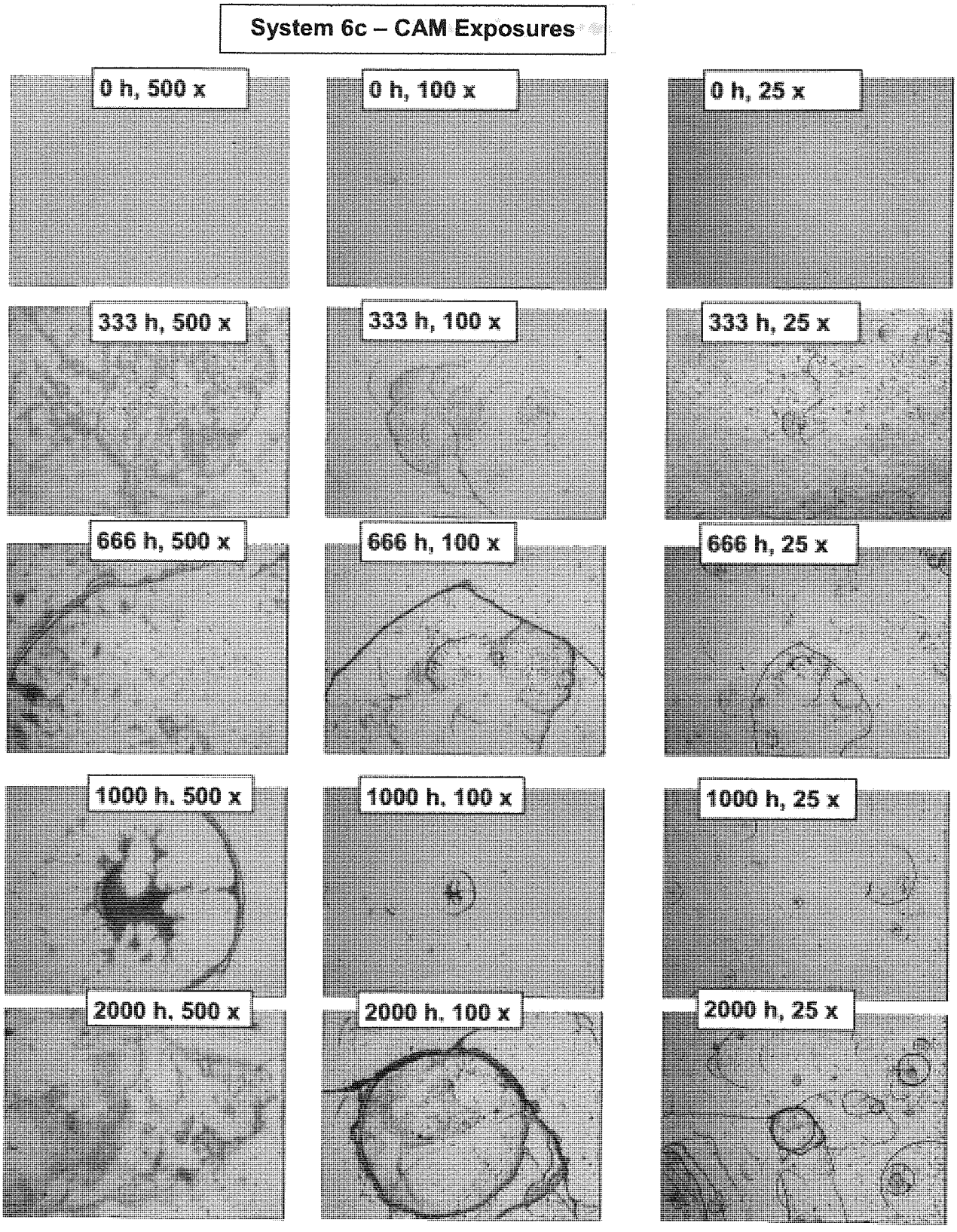

Appendix A3.1.4 Optical micrographs of System 6c, unexposed and with Artificial Accelerated Weathering (CAM), 333, 666, 1000 and 2000 hours and magnifications of 500, 100 and 25 for each exposure period.

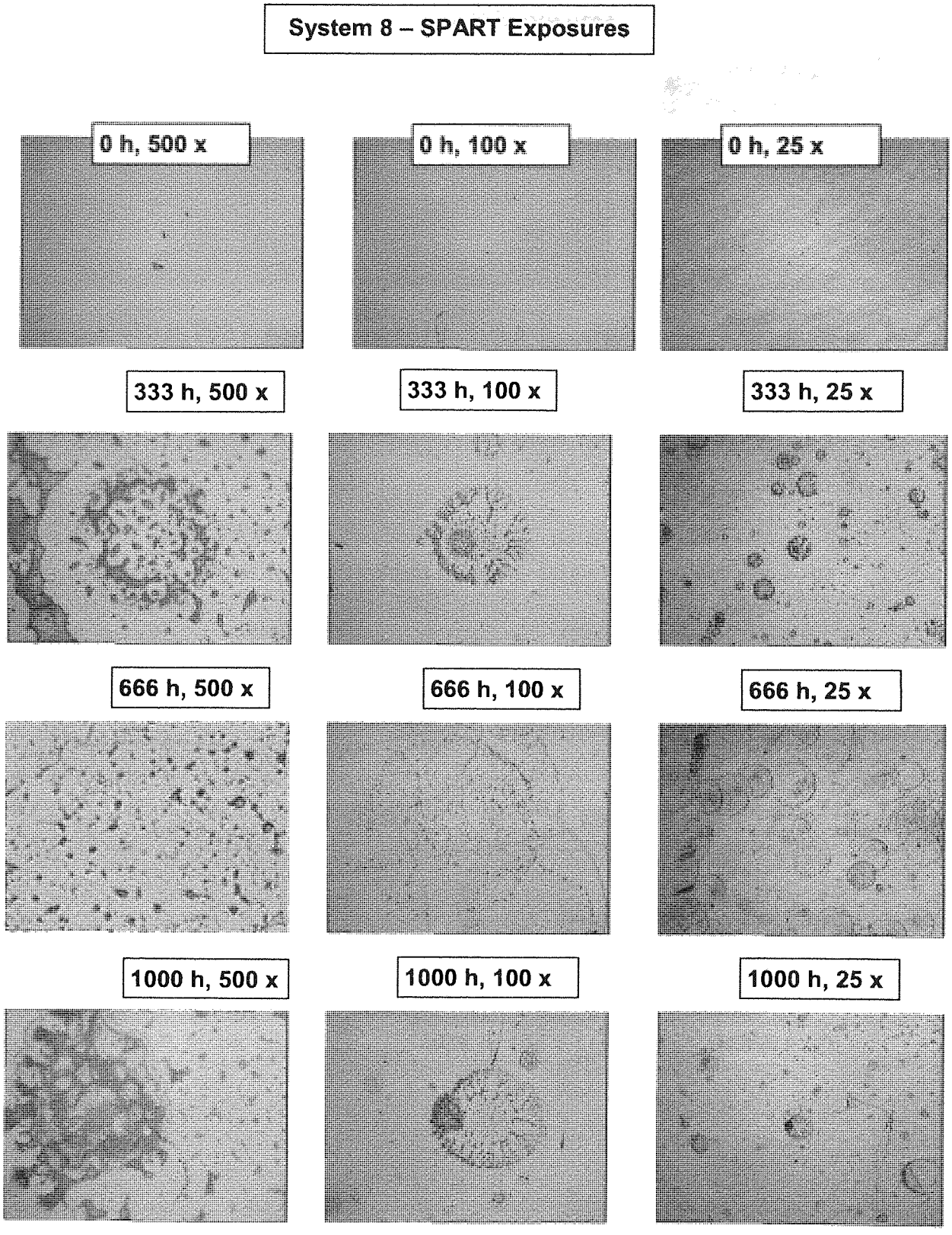

Appendix A3.1.5 Optical micrographs of System 8, with Artificial Accelerated Weathering (SPART), 333 and 666 hours and magnifications of 500, 100 and 25 for each exposure period, under reflection.

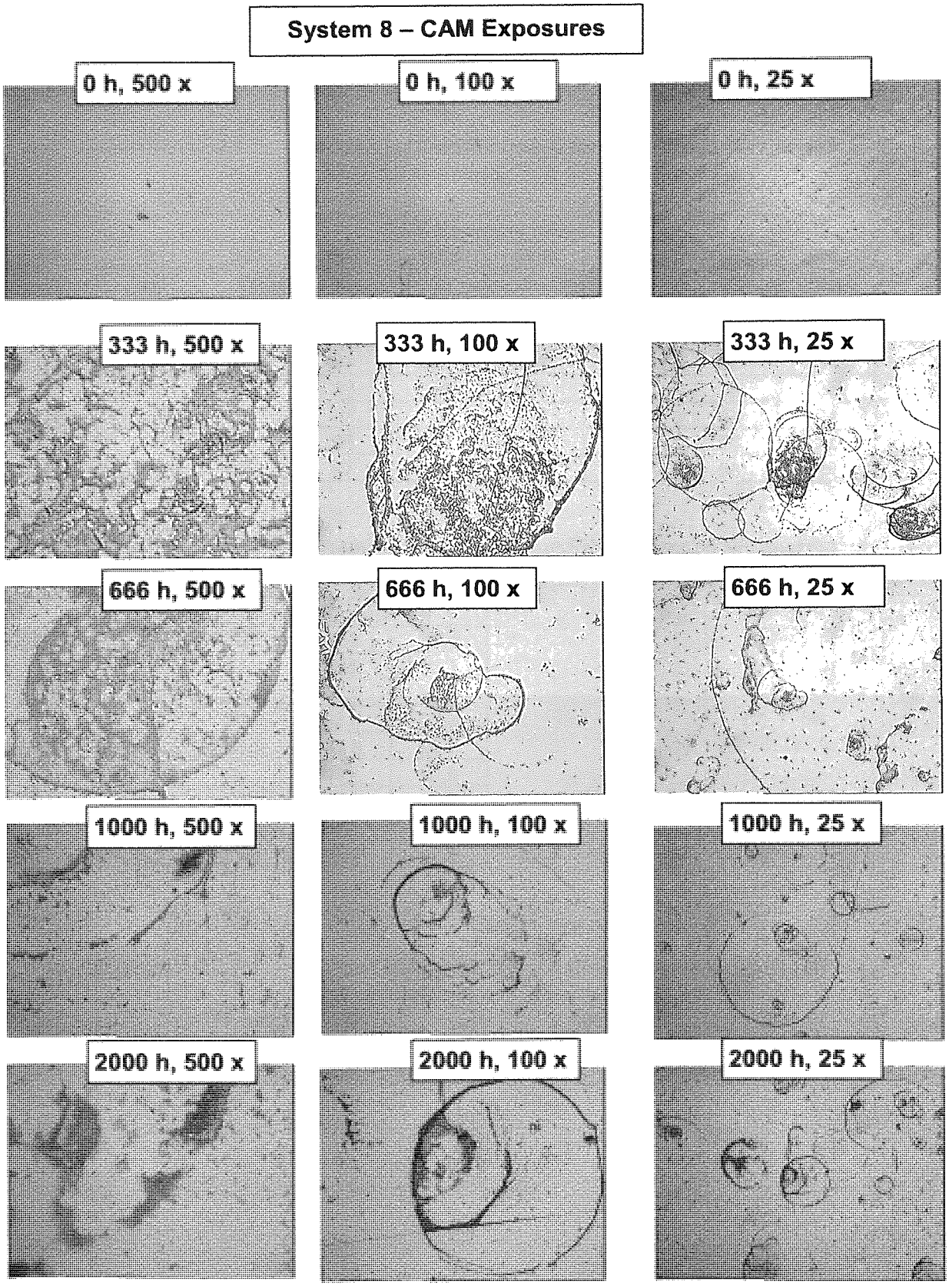

Appendix A3.1.6 Optical micrographs of System 8, with Artificial Accelerated Weathering (CAM), 333 and 666 hours and magnifications of 500, 100 and 25 for each exposure period, under reflection.

A3.2 Gloss Results

Appendix A3.2.1 Percentage Gloss Retention for Accelerated Weathering (CAM), for systems 1, 3, 4, 6c, 7, 8, 9 and 10.

System	CAM Exposure time/h							
	0	333	666	1000	1500	2000	2500	3000
1	100	97	97	96	94	94	93	93
3	100	97	96	95	91	92	92	92
4	100	97	96	95	92	91	87	86
6c	100	98	98	98	96	96	96	94
7	100	99	98	98	97	97	96	94
8	100	98	97	98	97	97	96	94
9	100	98	98	98	96	96	95	94
10	100	98	97	97	97	96	96	94

Appendix A3.2.2 Percentage Gloss Retention for Accelerated Weathering (SPART), for systems 1, 3, 4, 6c, 7, 8, 9 and 10.

System	SPART Exposure time/hours			
	0	333	666	1000
1	100	97.6	98.2	95.1
3	100	97.8	97.0	96.8
4	100	98.4	98.4	97.9
6c	100	97.5	97.8	96.6
7	100	97.1	96.7	97.0
8	100	96.8	96.9	96.4
9	100	96.8	97.1	96.9
10	100	97.7	97.7	97.6

Appendix A3.2.3 Sample Calculation of 95% Confidence limit for sample 6c CAM 2000h exposed (water-borne, blue).

Sample	Gloss	Average	Standard Deviation	Relative Standard Deviation	95% Confidence
6c CAM 2000h Exposed	87.6	88.3	0.354	0.401	88.0 ± 0.5
	88.0				
	88.5				

A3.3 Photographs of the microtomed slices, unexposed and after weathering

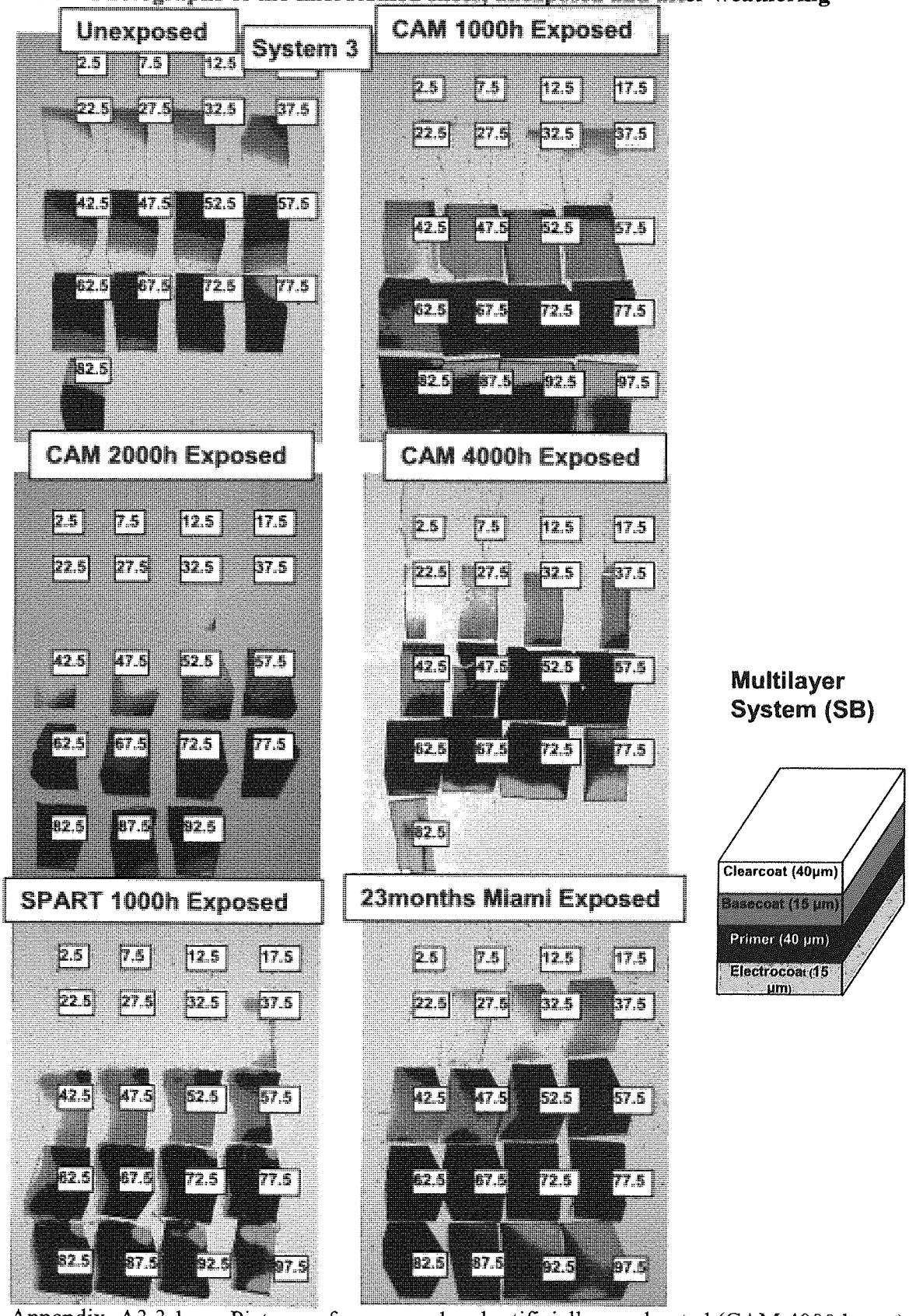

Appendix A3.3.1 Pictures of unexposed and artificially accelerated (CAM 4000 hours) exposed microtomed 5µm thick slices of systems 3 (SB), produced on a rotary microtome. Number on slices are the nominal depths in µm

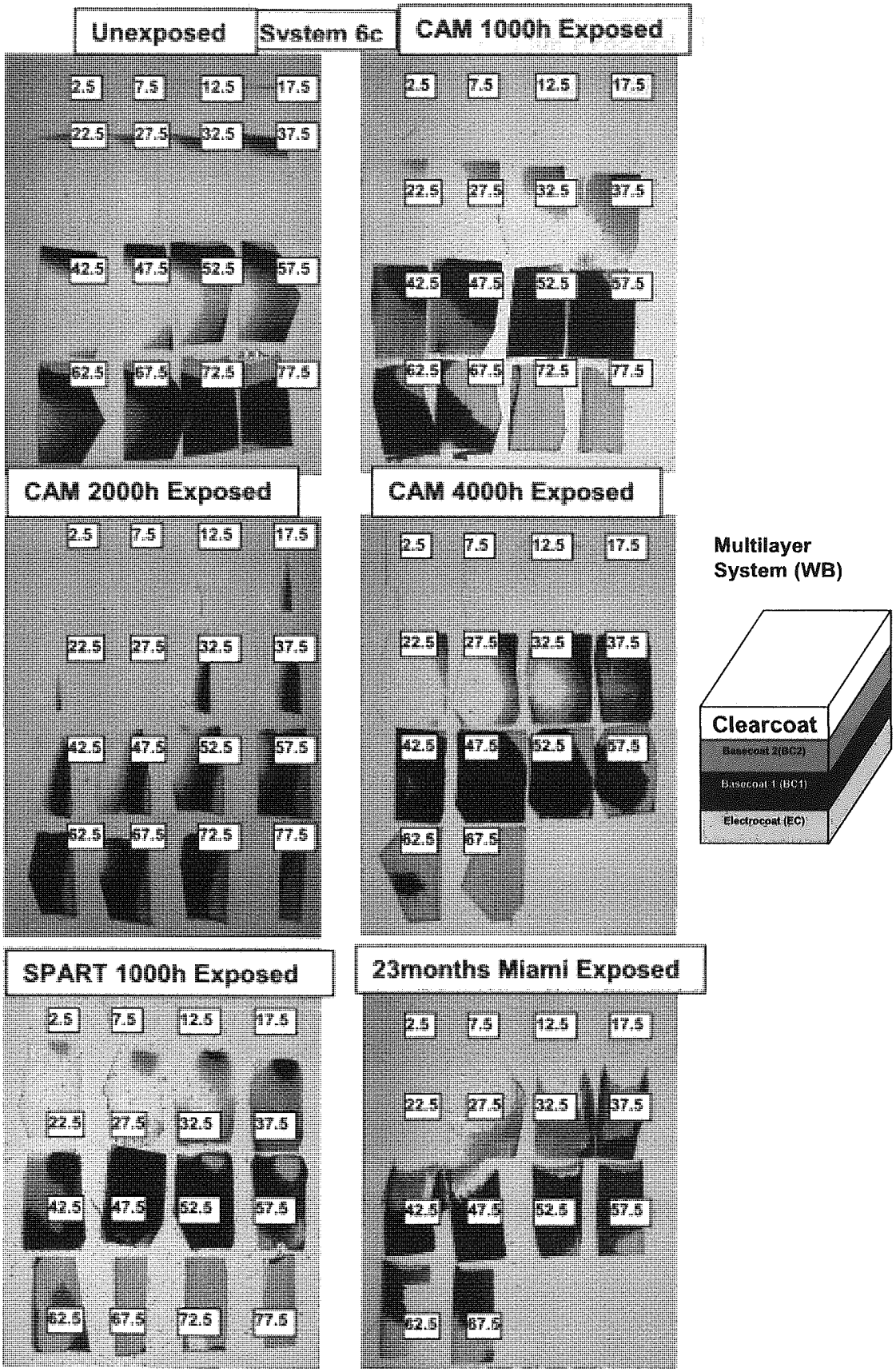

Appendix A3.3.2 Pictures of unexposed and artificially accelerated (CAM 4000 hours) exposed microtomed 5μm thick slices of systems 6c (WB), produced on a rotary microtome. Number on slices are the nominal depths in μm.

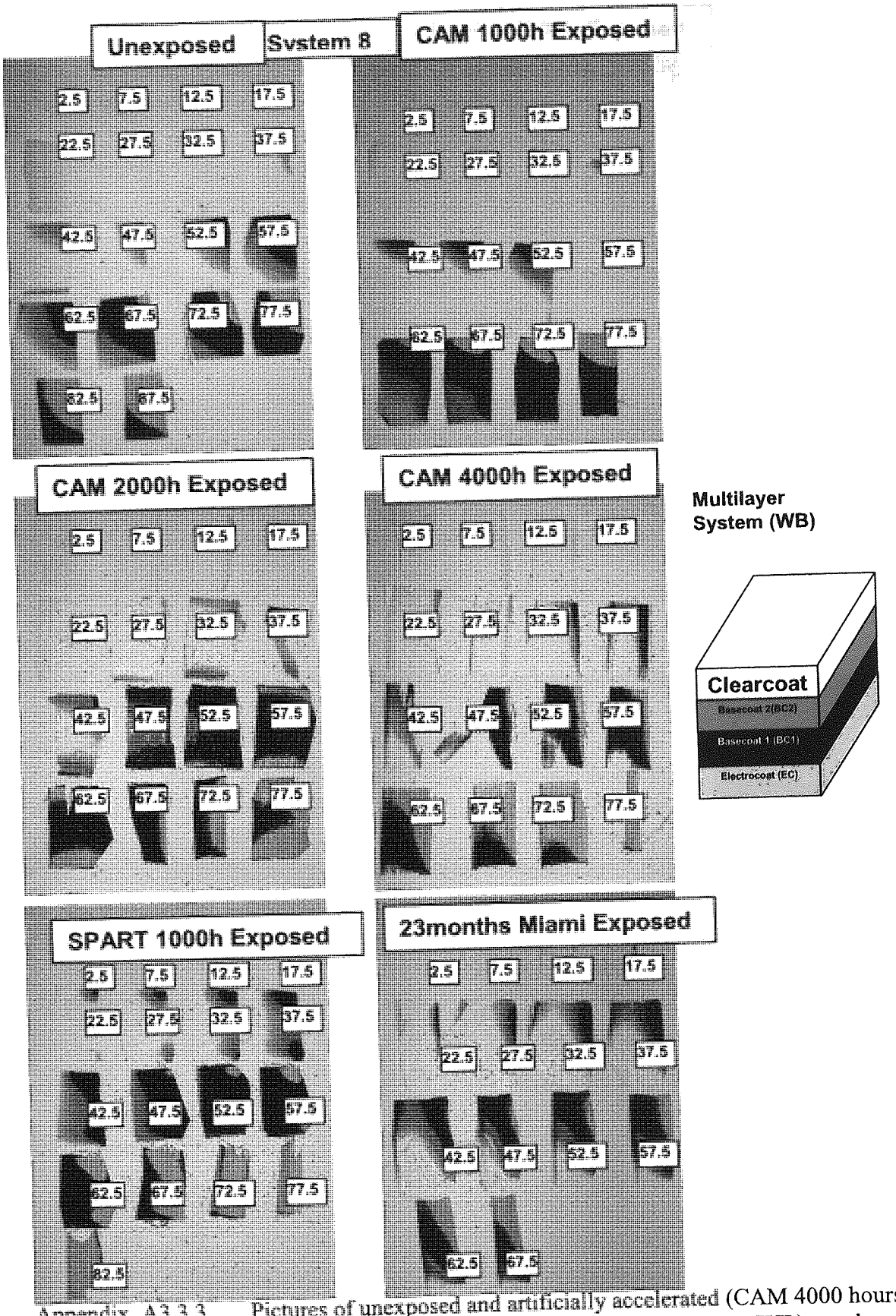

Appendix A3.3.3 Pictures of unexposed and artificially accelerated (CAM 4000 hours) exposed microtomed 5µm thick slices of systems 8 (WB), produced on a rotary microtome. Number on slices are the nominal depths in µm.

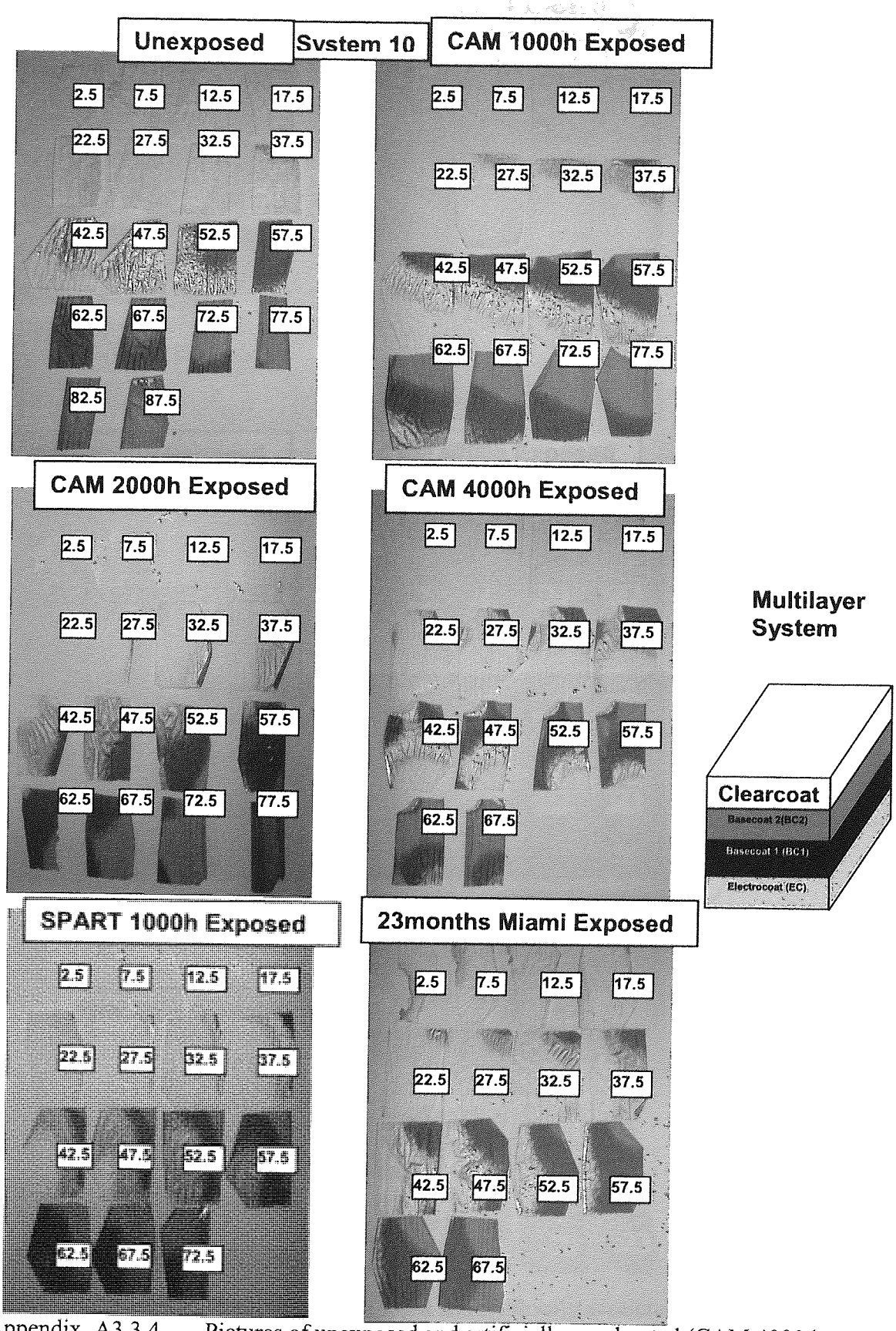

Appendix A3.3.4 Pictures of unexposed and artificially accelerated (CAM 4000 hours) exposed microtomed 5μm thick slices of systems 10 (WB), produced on a rotary microtome. Number on slices are the nominal depths in μm.

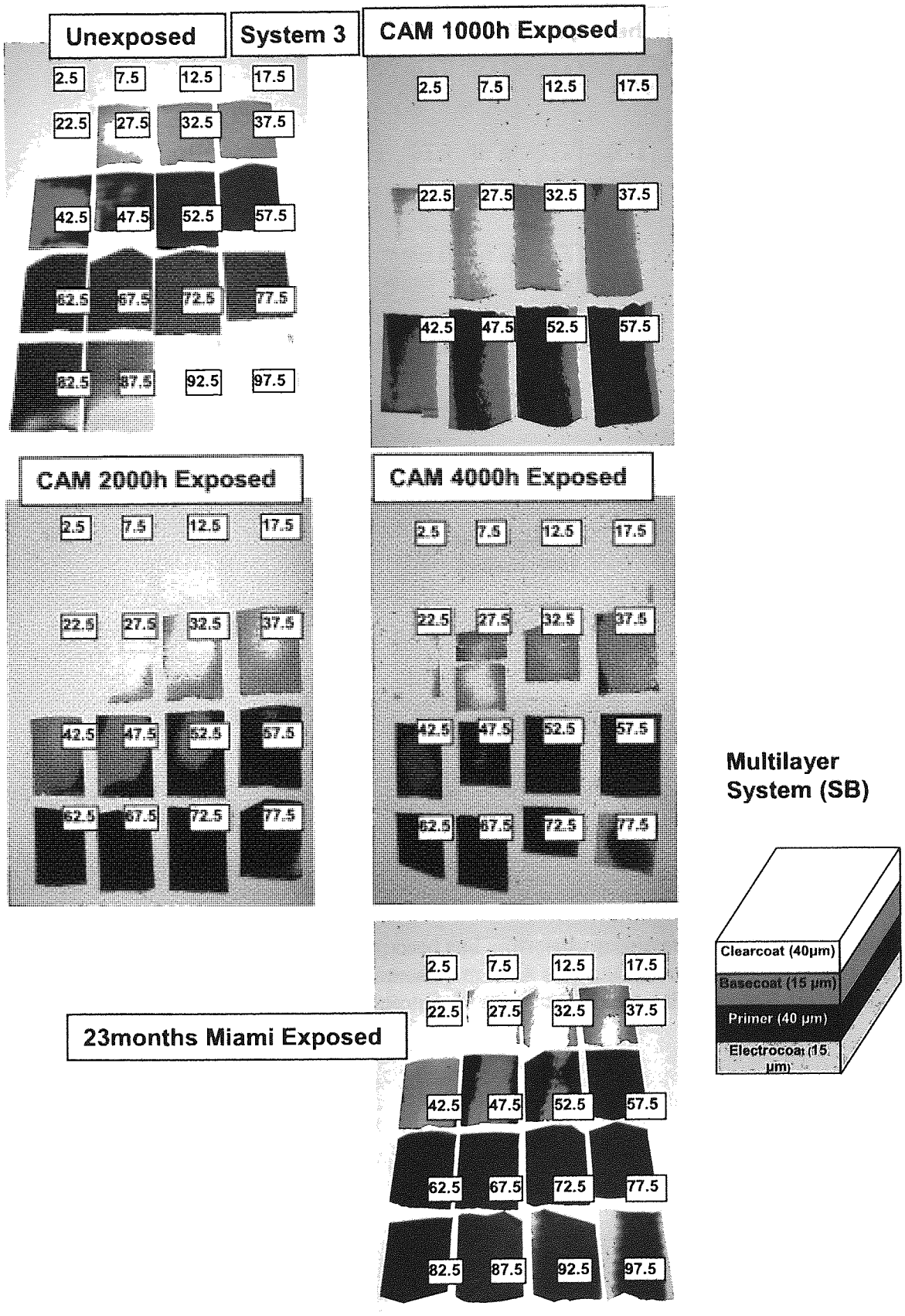

Appendix A3.3.5 Pictures of unexposed and artificially accelerated (CAM 4000 hours) exposed microtomed 5µm thick slices of systems 3 (SB), produced on a rotary microtome. Number on slices are the nominal depths in µm.

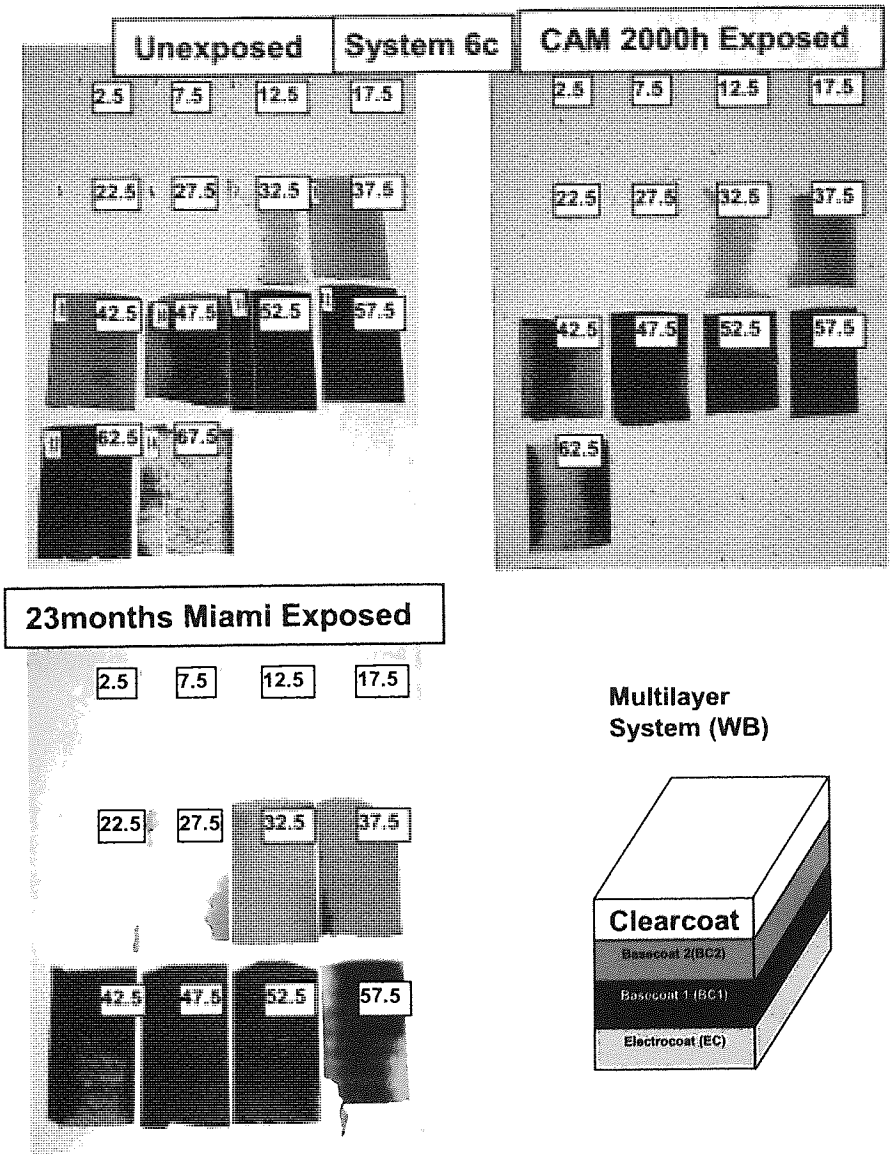

Appendix A3.3.6 Pictures of unexposed and artificially accelerated (CAM 4000 hours) exposed microtomed 5µm thick slices of systems 6c (WB), produced on a rotary microtome. Number on slices are the nominal depths in µm.

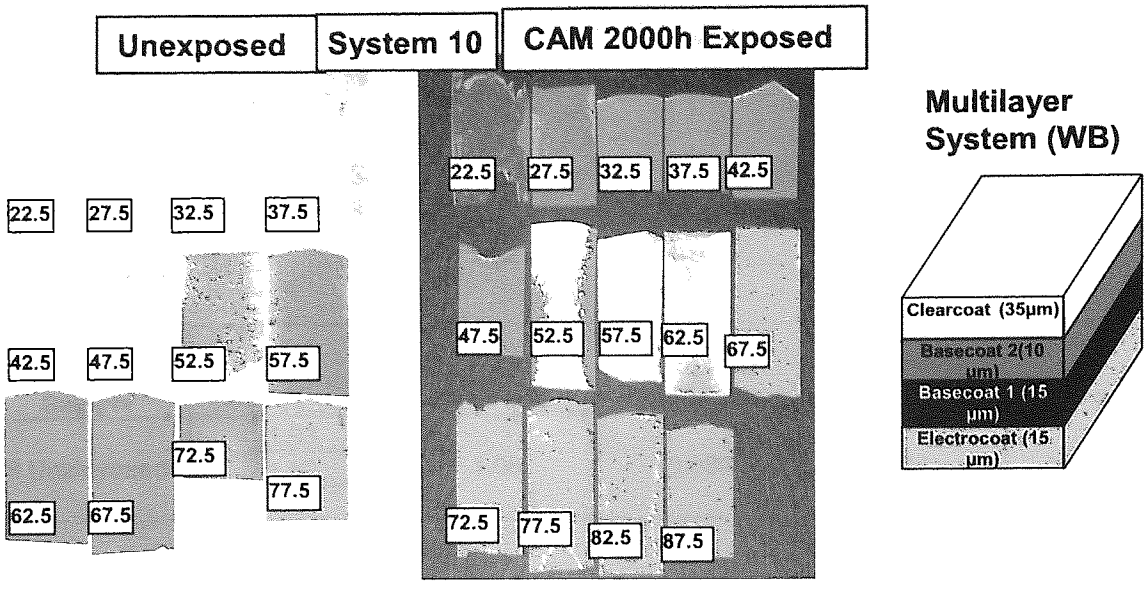

Appendix A3.3.7 Pictures of unexposed and artificially accelerated (CAM 4000 hours) exposed microtomed 5µm thick slices of systems 10 (WB), produced on a rotary microtome. Number on slices are the nominal depths in µm.

A3.4 FTIR ATR PI Results

Appendix A3.4.1 Sample Calculation of 95% Confidence limit for the water-borne, blue systems.

Sample	Gloss	Average	Standard Deviation	Relative Standard Deviation	95% Confidence
WB, Blue systems	0.41	0.41	0.063	3.98	0.41±0.02
	0.43				
	0.39				
	0.41				

A-3.5 FTIR PI Results

Appendix A3.5.1 Sample Calculation of 95% Confidence limit for systems 3, 6c, 8 and 10.

Sample	PI	Average	Standard Deviation	Relative Standard Deviation %	95% Confidence
8 Unexposed	1.03	1.08	0.099	9.14	1.08 ± 0.11
	1.02				
	1.20				
6c Unexposed	1.18	1.16	0.20	1.5	1.16 ± 0.20
	1.42				
	1.14				
	0.92				
3 Unexposed	0.62	0.65	0.018	2.83	0.65 ± 0.02
	0.67				
	1.46				
	0.66				
	0.66				
	0.64				
10 Unexposed	1.00	1.09	0.074	6.84	0.07
	1.17				
	1.16				
	1.11				
	1.03				
Average Unexposed					**0.10**

Appendix A3.5.1 Sample Calculation of 95% Confidence limit for systems 3, 6c, 8 and 10 (cont).

Sample	PI	Average	Standard Deviation	Relative Standard Deviation %	95% Confidence
3 CAM 1000h	0.91	0.87	0.093	10.7	0.87 ± 0.09
	0.89				
	0.74				
	0.96				
3 CAM 4000h	0.60	0.79	0.16	20.5	0.79 ± 0.18
	0.88				
	2.04				
	0.88				
3 23m Miami	1.18	1.12	0.080	7.14	1.12 ± 0.11
	1.06				
6c CAM 1000h	1.50	1.35	0.21	15.7	1.35 ± 0.29
	1.20				
6c CAM 4000h	1.99	1.78	0.31	17.5	1.78 ± 0.43
	1.56				
6c 6m Miami	1.65	1.51	0.19	12.5	1.51 ± 0.26
	1.38				
6c 23m Miami	1.53	1.61	0.10	6.38	1.61 ± 0.14
	1.68				
8 CAM 1000h	1.71	1.47	0.17	11.4	1.47 ± 0.15
	1.41				
	1.35				
	1.31				
	1.56				
8 CAM 4000h	1.96	2.03	0.092	4.52	2.03 ± 0.13
	2.09				
8 23m Miami	1.92	1.89	0.051	2.68	1.89 ± 0.07
	1.85				
10 CAM 1000h	1.23	1.39	0.21	15.1	1.39 ± 0.24
	1.31				
	1.63				
10 CAM 4000h	1.36	1.67	0.28	16.8	1.67 ± 0.28
	1.58				
	2.03				
	1.72				
10 23m Miami	1.42	1.42	0.0011	0.0789	1.42 ± 0.00
	1.42				
Average Exposed					**0.20**

Appendix A3.5.2 Rotary PI Data for system 1, unexposed artificial weathering (CAM and SPART), for 5μm thick microtomed slices at the nominal depths indicated.

Rotary 1					
		CAM Exposure time/hours			SPART Exposure time/hours
	Unexposed	1000	2000	4000	1000
Depth/μm	PI_{OH}	PI_{OH}	PI_{OH}	PI_{OH}	PI_{OH}
2.5					0.94
7.5	0.58			0.86	0.87
12.5	0.74			0.82	0.77
17.5	0.67	0.72		0.88	0.84
22.5	0.55	0.73	0.83	1.07	0.73
27.5	0.60	0.81	1.01	0.79	0.80
32.5	0.84	0.67		0.78	0.82
37.5	0.68	0.68		0.69	0.82
42.5	1.03	0.64	1.08	0.97	0.77
47.5	0.99	0.81		0.93	0.77
52.5	1.19	1.09	1.07	1.55	0.82
57.5	1.07	1.51		1.49	1.17
62.5	1.30	1.54		1.39	
67.5	1.16	1.39		1.29	1.24
72.5	1.20	1.35		1.26	1.22
77.5	1.23	1.28			1.20
82.5		1.18			1.18
87.5		1.18			
92.5		1.15			

Appendix A3.5.3 Rotary PI Data for system 3, unexposed artificial weathering (CAM and SPART), for 5μm thick microtomed slices at the nominal depths indicated.

Rotary 3							
		CAM Exposure time/hours			SPART Exposure time/ hours	Miami Exposure Time/months	
	Unexposed	1000	2000	4000	1000	18	23
Depth/μm	PI_{OH}	PI_{OH}	PI_{OH}	PI_{OH}	PI_{OH}	PI_{OH}	PI_{OH}
2.5	0.93			1.57	1.09	1.14	1.97
7.5	0.98				1.01	1.18	1.42
12.5		0.92			0.90	0.86	1.17
17.5	0.69	0.80		1.10	0.84	0.82	0.93
22.5	0.54	0.75	0.75	0.90	0.88	0.80	
27.5	0.58	0.70	0.88		0.97	0.81	0.99
32.5	0.61	0.67	0.78		1.02	0.86	1.09
37.5	0.59	0.73		1.47	1.03	1.00	0.87
42.5	0.75	0.81	0.65	1.29		1.09	0.96
47.5	0.76	0.97	0.79	1.39		1.13	
52.5	0.87	1.00	0.96	1.54		1.25	1.32
57.5	1.08	1.81	1.08	1.53		1.38	2.03
62.5	1.06	1.82	1.14	1.45		1.42	1.55
67.5	1.09	1.28	1.32	1.40		1.39	1.53
72.5	1.10	1.23	1.43	1.62			1.53
77.5			1.38	1.58			1.53
82.5			1.63	1.89			1.51
87.5	1.37		1.34				1.51
92.5	1.85	1.66	1.69				1.52
97.5		1.86					1.67
102.5							2.03

Appendix A3.5.4 Rotary PI Data for system 4, unexposed artificial weathering (CAM and SPART), for 5μm thick microtomed slices at the nominal depths indicated.

Rotary 4						
		CAM Exposure time/hours			SPART Exposure time/ hours	Miami Exposure Time/ months
	Unexposed	1000	2000	4000	1000	18
Depth/μm	PI_{OH}	PI_{OH}	PI_{OH}	PI_{OH}	PI_{OH}	PI_{OH}
2.5	0.66			0.94		0.85
7.5	0.52	0.80		1.05	0.90	0.85
12.5	0.68	0.73	0.92	0.77	0.78	0.75
17.5	0.68	0.77	1.01	0.80	0.83	
22.5	0.75	0.67	1.07	0.76	0.84	0.71
27.5	0.78	0.66	0.79	0.80	0.81	
32.5	0.82	0.71	0.80	0.99	0.78	
37.5	1.04	0.72	0.89	1.25	0.79	
42.5	0.78	0.83	0.89	1.40	0.85	0.96
47.5	0.92	0.82	0.88	1.39	0.90	1.13
52.5	1.10	0.88	1.25	1.55	1.03	1.08
57.5	1.41		1.13	1.51	1.19	1.28
62.5	1.34	1.05		1.74	1.51	1.36
67.5	1.35	1.29	1.83	1.47	1.44	1.57
72.5	1.47	1.91		1.65		1.37
77.5	1.59	1.29	1.74	1.84		1.36
82.5	1.80	1.66	1.84	1.67		1.39
87.5	2.10	1.55	2.30	1.90		
92.5	1.99		1.91			
97.5	1.97		2.14			

Appendix A3.5.5 Rotary PI Data for system 6c, unexposed artificial weathering (CAM and SPART), for 5μm thick microtomed slices at the nominal depths indicated.

Rotary 6c							
		CAM Exposure time/hours			SPART Exposure time/ hours	Miami Exposure Time/months	
	Unexposed	1000	2000	4000	1000	18	23
Depth/μm	PI_{OH}	PI_{OH}	PI_{OH}	PI_{OH}	PI_{OH}	PI_{OH}	PI_{OH}
2.5	1.27	1.60	1.84	2.18	1.53	1.87	2.13
7.5	1.27	1.54	1.83	2.13	1.34	1.95	1.84
12.5	1.40	1.50	1.86	1.99	1.29	1.44	
17.5	1.09	1.42	1.68	1.77	1.35	1.34	1.68
22.5	1.13	1.39	1.66	1.67	1.34	1.26	
27.5	1.08	1.33	1.74	1.61	1.27	1.28	1.40
32.5	1.04	1.30	1.72	1.69	1.39	1.27	1.48
37.5	0.92	1.28	1.70	1.94	1.22	1.25	1.57
42.5	1.14	1.49	1.70	1.85	1.22	1.24	1.73
47.5		1.67	1.59	2.00	1.40	1.08	1.81
52.5		1.67	1.79	1.95	1.49	1.14	1.31
57.5		2.00	1.90	1.95	1.50	1.37	1.64
62.5		2.08	1.94		1.84	1.38	1.62
67.5			2.01		1.99	1.35	1.48
72.5					2.26	1.45	
77.5					2.22		

Appendix A3.5.6 Rotary PI Data for system 7, unexposed artificial weathering (CAM and SPART), for 5μm thick microtomed slices at the nominal depths indicated.

Rotary 7							
		CAM Exposure time/hours			SPART Exposure time/ hours	Miami Exposure Time/months	
	Unexposed	1000	2000	4000	1000	18	23
Depth/μm	PI_{OH}	PI_{OH}	PI_{OH}	PI_{OH}	PI_{OH}	PI_{OH}	PI_{OH}
2.5				1.97	1.48	1.46	1.86
7.5	1.11	1.59	1.81	1.86	1.56	1.30	1.74
12.5	1.13	1.48	1.65	1.69	1.36	1.27	1.53
17.5	1.09	1.56	1.68	1.72	1.25	1.26	1.36
22.5	1.10	1.53	1.57	1.65	1.27	1.27	1.21
27.5	1.12	1.52	1.52	1.70	1.24	1.29	1.23
32.5	1.15	1.58	1.58	1.72	1.27	1.25	1.33
37.5	1.04	1.29	1.58	2.01	1.19	1.13	1.29
42.5	1.04	1.46	1.65	2.33	1.24	1.23	1.26
47.5	1.12	1.76	1.59	2.19	1.32	1.47	1.33
52.5	1.20	1.70	1.79	2.30	1.24	1.40	1.44
57.5	1.33	1.85	1.94		1.33	1.58	1.51
62.5					1.70	1.96	1.48
67.5							1.89

Appendix A3.5.7 Rotary PI Data for system 8, unexposed artificial weathering (CAM and SPART), for 5µm thick microtomed slices at the nominal depths indicated.

Rotary 8							
		CAM Exposure time/hours			SPART Exposure time/ hours	Miami Exposure Time/months	
	Unexposed	1000	2000	4000	1000	18	23
Depth/µm	PI_{OH}	PI_{OH}	PI_{OH}	PI_{OH}	PI_{OH}	PI_{OH}	PI_{OH}
2.5	1.11	1.67	2.10	2.13	1.71	1.74	2.25
7.5	1.08	1.61	1.77	2.01	1.53	1.55	2.23
12.5	1.03	1.53	1.71	2.01	1.46	1.44	1.87
17.5	1.07	1.61	1.69	1.97	1.49	1.43	1.74
22.5	1.07	1.54	1.60	1.99	1.45	1.37	1.75
27.5	1.05	1.58	1.61	2.05	1.38	1.35	1.67
32.5	1.09	1.53	1.59	2.20	1.36	1.36	1.72
37.5	0.99	1.57	1.61	2.64	1.37	1.35	1.69
42.5	0.86	1.54	1.68	2.50	1.33	1.24	1.74
47.5	1.06	1.39	1.73	2.42	1.29	1.08	1.81
52.5	1.11	1.60	1.96	2.02	1.65	1.14	1.90
57.5	1.26	1.51	1.71	1.91	2.00	1.37	1.72
62.5	1.60	1.56	1.82	2.15		1.38	1.78
67.5		1.61	1.76	1.89		1.35	1.97

Appendix A3.5.8 Rotary PI Data for system 9, unexposed artificial weathering (CAM and SPART), for 5µm thick microtomed slices at the nominal depths indicated.

Rotary 9						
		CAM Exposure time/hours			SPART Exposure time/ hours	Miami Exposure Time/months
	Unexposed	1000	2000	4000	1000	18
Depth/µm	PI_{OH}	PI_{OH}	PI_{OH}	PI_{OH}	PI_{OH}	PI_{OH}
2.5	1.23	1.57			1.57	1.66
7.5	1.16	1.41	1.80	1.65	1.54	1.73
12.5	1.33	1.39	1.54	1.84	1.46	1.53
17.5	1.21	1.43	1.60	1.77	1.42	1.31
22.5	1.15	1.43	1.48	1.61	1.32	1.28
27.5	1.17	1.40	1.49	1.61	1.30	1.32
32.5	1.18	1.37	1.46	1.55	1.27	1.26
37.5	1.08	1.35	1.45	1.64	1.31	1.35
42.5	1.04	1.47	1.45	2.01	1.47	1.29
47.5	1.05	1.39	1.46	2.48	1.52	1.37
52.5	1.07	1.37	1.64	2.09	1.32	1.46
57.5	1.04	1.56	1.76	1.86	1.42	1.59
62.5	1.27	1.91	1.68	2.15	1.73	
67.5	1.74			2.15	1.81	

Appendix A3.5.9 Rotary PI Data for system 10, unexposed artificial weathering (CAM and SPART), for 5µm thick microtomed slices at the nominal depths indicated.

Rotary 10							
		CAM Exposure time/hours			SPART Exposure time/ hours	Miami Exposure Time/months	
	Unexposed	1000	2000	4000	1000	18	23
Depth/µm	PI_{OH}	PI_{OH}	PI_{OH}	PI_{OH}	PI_{OH}	PI_{OH}	PI_{OH}
2.5			1.65	1.95	1.70	1.64	1.56
7.5		1.28	1.56	1.96	1.63	1.38	1.48
12.5	1.02	1.23	1.37	1.59	1.63	1.36	
17.5	1.04	1.20	1.42	1.63	1.32	1.35	1.42
22.5	1.01	1.26	1.42	1.45	1.29	1.27	1.47
27.5	1.03	1.21	1.37	1.39	1.24	1.21	1.43
32.5	1.09	1.30	1.37	1.37	1.24	1.19	1.39
37.5	1.19	1.40	1.28	1.20	1.23	1.18	1.28
42.5	1.04	1.29	1.32	1.53	1.42	1.27	1.63
47.5	1.30	1.37	1.85	1.53	1.30	1.16	1.80
52.5	1.23	1.39	1.56	1.77	1.25	1.40	1.66
57.5	1.25	1.58	1.60	1.61	1.60	1.42	1.64
62.5	1.54	1.48	2.03	1.55	1.49	1.41	1.85
67.5	1.40	1.69	1.86	1.59	1.98	1.47	2.00
72.5	1.62		1.71				1.74

Appendix A3.5.10 Rotary PI Data for system 1 clearcoat only, artificial weathering (CAM and SPART), where; $\Delta PI_{OH} = \Delta PI_{OH\ t=t} - \Delta PI_{OH\ t=0}$ and, Calc ΔPI_{OH} = data for clearcoat fitted to an exponential equation, for 5µm thick microtomed slices at the nominal depths indicated.

Rotary 1						
	CAM Exposure Time/hours				SPART Exposure Time/hours	
	1000		4000		1000	
Depth/µm	ΔPI	Calc ΔPI	ΔPI	Calc ΔPI	ΔPI	Calc ΔPI
2.5			0.27	0.26	0.28	0.28
7.5		0.15	0.20	0.22	0.21	0.19
12.5		0.10	0.16	0.19	0.11	0.15
17.5	0.06	0.07	0.22	0.17	0.18	0.14
22.5	0.07	0.05		0.15	0.07	0.13
27.5		0.03	0.13	0.14	0.14	0.13
32.5	0.01	0.02	0.12	0.13	0.16	0.13
37.5	0.02	0.00	0.03	0.12	0.16	0.13

Appendix A3.5.11 Rotary PI Data for system 3 clearcoat only, artificial weathering (CAM and SPART), and natural weathering (Miami), where;

$\Delta PI_{OH} = \Delta PI_{OH\ t=t} - \Delta PI_{OH\ t=0}$ and, Calc ΔPI_{OH} = data for clearcoat fitted to an exponential equation, for 5µm thick microtomed slices at the nominal depths indicated.

Rotary 3												
	CAM Exposure Time/hours						SPART Exposure Time/hours		Miami Exposure Time/months			
	1000		2000		4000		1000		18		23	
Depth/ µm	ΔPI	Calc ΔPI	ΔPI	Calc ΔPI	ΔPI	Calc ΔPI	ΔPI	Calc ΔPI	ΔPI	Calc ΔPI	ΔPI	Calc ΔPI
2.5		0.33	0.49	0.49	0.90	0.95	0.43	0.44	0.48	0.53		1.32
7.5		0.20		0.42		0.69	0.35	0.32	0.52	0.37	0.76	0.74
12.5	0.26	0.11	0.46	0.36		0.51	0.24	0.25	0.20	0.27	0.51	0.49
17.5	0.14	0.06	0.32	0.30	0.44	0.37	0.18	0.21	0.16	0.21	0.27	0.37
22.5	0.09	0.02		0.25	0.24	0.27	0.22	0.19	0.14	0.17		0.32
27.5	0.04	0.00	0.22	0.21		0.20		0.18	0.15	0.15	0.33	0.30
32.5	0.01	-0.01	0.12	0.17		0.14		0.17	0.19	0.13	0.43	0.29
37.5		-0.02		0.13		0.11		0.17		0.12	0.21	0.29
42.5			0.12	0.10				0.16			0.30	0.29

Appendix A3.5.12 Rotary PI Data for system 4 clearcoat only, artificial weathering (CAM and SPART), and natural weathering (Miami),

where; $\Delta PI_{OH} = \Delta PI_{OH\ t=t} - \Delta PI_{OH\ t=0}$ and, Calc ΔPI_{OH} = data for clearcoat fitted to an exponential equation, for 5µm thick microtomed slices at the nominal depths indicated.

Rotary 4										
	CAM Exposure Time/hours						SPART Exposure Time/hours		Miami Exposure Time/months	
	1000		2000		4000		1000		18	
Depth/ µm	ΔPI	Calc ΔPI	ΔPI	Calc ΔPI	ΔPI	Calc ΔPI	ΔPI	Calc ΔPI	ΔPI	Calc ΔPI
2.5		0.25	0.26	0.32	0.28	0.33			0.19	0.23
7.5	0.14	0.14	0.35	0.26	0.39	0.27	0.24	0.24	0.19	0.23
12.5	0.07	0.08		0.21		0.22		0.15	0.09	0.23
17.5	0.11	0.06	0.13	0.17	0.14	0.18	0.17	0.15		0.23
22.5	0.01	0.05	0.14	0.13		0.15	0.18	0.15	0.05	0.23
27.5	0.00	0.04		0.11	0.14	0.12	0.14	0.15		0.23
32.5	0.05	0.04		0.09		0.10	0.12	0.15		
37.5	0.06	0.04		0.07		0.08	0.13	0.15		
42.5										

Appendix A3.5.13 Rotary PI Data for system 6c clearcoat only, artificial weathering (CAM and SPART), and natural weathering (Miami), where; $\Delta PI_{OH} = \Delta PI_{OH\ t=t} - \Delta PI_{OH\ t=0}$ and, Calc ΔPI_{OH} = data for clearcoat fitted to an exponential equation, for 5µm thick microtomed slices at the nominal depths indicated.

Rotary 6c												
	CAM Exposure Time/hours						SPART Exposure Time/hours		Miami Exposure Time/months			
	1000		2000		4000		1000		18		23	
Depth/ µm	ΔPI	Calc ΔPI	ΔPI	Calc ΔPI	ΔPI	Calc ΔPI	ΔPI	Calc ΔPI	ΔPI	Calc ΔPI	ΔPI	Calc ΔPI
2.5	0.50	0.50		0.88		1.30	0.43	0.43	1.03	0.87	1.03	1.01
7.5	0.44	0.44	0.73	0.75	1.03	1.04	0.24	0.24	0.74	0.60	0.74	0.78
12.5	0.40	0.38	0.76	0.68	0.89	0.85	0.19	0.23		0.43		0.62
17.5	0.32	0.33	0.58	0.64	0.67	0.70	0.25	0.23	0.58	0.31	0.58	0.51
22.5	0.29	0.28	0.56	0.62	0.57	0.58	0.24	0.23		0.23		0.43
27.5	0.23	0.24	0.64	0.60	0.51	0.50	0.17	0.23	0.30	0.18	0.30	0.38
32.5	0.20	0.20	0.62	0.60		0.43		0.23	0.38	0.15	0.38	0.34
37.5	0.18	0.17		0.59		0.38		0.23		0.12		0.31

Appendix A3.5.14 Rotary PI Data for system 7 clearcoat only, artificial weathering (CAM and SPART), and natural weathering (Miami), where;

$\Delta PI_{OH} = \Delta PI_{OH\ t=t} - \Delta PI_{OH\ t=0}$ and, Calc ΔPI_{OH} = data for clearcoat fitted to an exponential equation, for 5µm thick microtomed slices at the nominal depths indicated.

Rotary 7												
	CAM Exposure Time/hours						SPART Exposure Time/hours		Miami Exposure Time/months			
	1000		2000		4000		1000		18		23	
Depth/ µm	ΔPI	Calc ΔPI	ΔPI	Calc ΔPI	ΔPI	Calc ΔPI	ΔPI	Calc ΔPI	ΔPI	Calc ΔPI	ΔPI	Calc ΔPI
2.5				0.81		0.88	0.38	0.43	0.36	0.35	0.76	0.81
7.5	0.49	0.49	0.71	0.69	0.87	0.73	0.46	0.34	0.20	0.22	0.64	0.55
12.5	0.38	0.43	0.55	0.60	0.76	0.64	0.26	0.27	0.17	0.17	0.43	0.39
17.5	0.46	0.43	0.58	0.53	0.59	0.59	0.15	0.22	0.16	0.15	0.26	0.29
22.5	0.43	0.43	0.47	0.47	0.62	0.56	0.17	0.18	0.17	0.14	0.11	0.23
27.5	0.42	0.43	0.42	0.43	0.55	0.54	0.14	0.15	0.19	0.14	0.13	0.19
32.5	0.48	0.43		0.39		0.53	0.17	0.12	0.15	0.13	0.23	0.16
37.5		0.43		0.36		0.52	0.09	0.10	0.03	0.13	0.19	0.15

Appendix A3.5.15 Rotary PI Data for system 8 clearcoat only, artificial weathering (CAM and SPART), and natural weathering (Miami), where;

$\Delta PI_{OH} = \Delta PI_{OH\ t=t} - \Delta PI_{OH\ t=0}$ and, Calc ΔPI_{OH} = data for clearcoat fitted to an exponential equation, for 5µm thick microtomed slices at the nominal depths indicated.

Rotary 8												
	CAM Exposure Time/hours						SPART Exposure Time/hours		Miami Exposure Time/months			
	1000		2000		4000		1000		18		23	
Depth/ µm	ΔPI	Calc ΔPI	ΔPI	Calc ΔPI	ΔPI	Calc ΔPI	ΔPI	Calc ΔPI	ΔPI	Calc ΔPI	ΔPI	Calc ΔPI
2.5		0.57		0.78	1.03	1.03	0.61	0.59	0.64	0.64	1.15	1.21
7.5	0.51	0.50	0.67	0.68	0.91	0.92	0.43	0.46	0.45	0.45	1.13	0.97
12.5	0.43	0.47	0.61	0.61	0.91	0.89	0.36	0.39	0.34	0.35	0.77	0.82
17.5	0.51	0.46	0.59	0.56	0.87	0.89	0.39	0.34	0.33	0.30	0.64	0.72
22.5	0.44	0.46	0.50	0.53	0.89	0.89	0.35	0.31	0.27	0.28	0.65	0.65
27.5	0.48	0.46	0.51	0.51		0.89	0.28	0.29	0.25	0.26	0.57	0.61
32.5	0.43	0.46	0.49	0.50		0.89	0.26	0.28	0.26	0.25	0.62	0.58
37.5		0.46	0.51	0.49		0.89	0.27	0.28	0.25	0.25	0.59	0.56

Appendix A3.5.16 Rotary PI Data for system 9 clearcoat only, artificial weathering (CAM and SPART), and natural weathering (Miami), where;

$\Delta PI_{OH} = \Delta PI_{OH\ t=t} - \Delta PI_{OH\ t=0}$ and, Calc ΔPI_{OH} = data for clearcoat fitted to an exponential equation, for 5µm thick microtomed slices at the nominal depths indicated.

Rotary 9										
	CAM Exposure Time/hours						SPART Exposure Time/hours		Miami Exposure Time/months	
	1000		2000		4000		1000		18	
Depth/ µm	ΔPI	Calc ΔPI	ΔPI	Calc ΔPI	ΔPI	Calc ΔPI	ΔPI	Calc ΔPI	ΔPI	Calc ΔPI
2.5	0.47	0.47	0.62	0.67	1.22	1.22	0.47	0.49	0.56	0.63
7.5	0.31	0.31	0.70	0.58		0.94	0.44	0.41	0.63	0.50
12.5	0.29	0.31	0.44	0.52	0.74	0.76	0.36	0.35	0.43	0.40
17.5	0.33	0.31	0.50	0.47	0.67	0.63	0.32	0.30	0.21	0.31
22.5	0.33	0.31	0.38	0.42	0.51	0.55	0.22	0.26	0.18	0.24
27.5	0.30	0.31	0.39	0.39	0.51	0.49	0.20	0.22	0.22	0.18
32.5		0.31	0.36	0.36	0.45	0.45	0.17	0.19	0.16	0.13
37.5		0.31	0.35	0.34		0.43	0.21	0.17		0.10

Appendix A3.5.17 Rotary PI Data for system 10 clearcoat only, artificial weathering (CAM and SPART), and natural weathering (Miami), where; $\Delta PI_{OH} = \Delta PI_{OH\ t=t} - \Delta PI_{OH\ t=0}$ and, Calc ΔPI_{OH} = data for clearcoat fitted to an exponential equation, for 5µm thick microtomed slices at the nominal depths indicated.

Rotary 10												
	CAM Exposure Time/hours						SPART Exposure Time/hours		Miami Exposure Time/months			
	1000		2000		4000		1000		18		23	
Depth/ µm	ΔPI	Calc ΔPI	ΔPI	Calc ΔPI	ΔPI	Calc ΔPI	ΔPI	Calc ΔPI	ΔPI	Calc ΔPI	ΔPI	Calc ΔPI
2.5			0.55	0.56	0.85	0.89	0.60	0.64		0.34	0.46	0.44
7.5	0.18	0.18	0.46	0.41	0.86	0.72	0.53	0.51	0.28	0.29	0.38	0.41
12.5	0.13	0.13	0.27	0.34	0.49	0.58	0.53	0.40	0.26	0.25		0.38
17.5	0.10	0.12	0.32	0.31	0.53	0.47	0.22	0.31	0.25	0.21	0.32	0.35
22.5	0.16	0.12	0.32	0.29	0.35	0.38	0.19	0.23	0.17	0.18	0.37	0.32
27.5	0.11	0.12	0.27	0.28	0.29	0.31	0.14	0.18	0.11	0.14	0.33	0.29
32.5		0.12	0.27	0.27	0.27	0.25	0.14	0.13	0.09	0.10	0.29	0.26
37.5		0.12		0.27	0.10	0.20	0.13	0.09	0.08	0.06	0.18	0.23

Appendix A3.5.18 Planar PI Data for system 1 clearcoat only, artificial weathering (CAM and SPART), where;

$\Delta PI_{OH} = \Delta PI_{OH\ t=t} - \Delta PI_{OH\ t=0}$ and, Calc ΔPI_{OH} = data for clearcoat fitted to an exponential equation, for 5µm thick microtomed slices at the nominal depths indicated.

Planar 1								
	CAM Exposure Time/hours						SPART Exposure Time/hours	
	1000		2000		4000		1000	
Depth /µm	ΔPI	Calc ΔPI	ΔPI	Calc ΔPI	ΔPI	Calc ΔPI	ΔPI	Calc ΔPI
2.5	0.13	0.13	0.28	0.29	0.43	0.42	0.43	0.47
7.5	0.12	0.12	0.27	0.24	0.34	0.35	0.48	0.36
12.5	0.11	0.11	0.18	0.20	0.31	0.30	0.25	0.29
17.5	0.10	0.10	0.17	0.17	0.22	0.25	0.21	0.25
22.5	0.10	0.09	0.14	0.15	0.23	0.22	0.17	0.23
27.5	0.08	0.08	0.13	0.13	0.18	0.19	0.25	0.21
32.5	0.08	0.08	0.11	0.11	0.20	0.16	0.24	0.20
37.5	0.07	0.07	0.10	0.10	0.15	0.15		0.20

Appendix A3.5.19 Planar PI Data for system 3 clearcoat only, artificial weathering (CAM and SPART), where;

$\Delta PI_{OH} = \Delta PI_{OH\ t=t} - \Delta PI_{OH\ t=0}$ and, Calc ΔPI_{OH} = data for clearcoat fitted to an exponential equation, for 5µm thick microtomed slices at the nominal depths indicated.

Planar 3								
	CAM Exposure Time/hours						SPART Exposure Time/hours	
	1000		2000		4000		1000	
Depth /µm	ΔPI	Calc ΔPI	ΔPI	Calc ΔPI	ΔPI	Calc ΔPI	ΔPI	Calc ΔPI
2.5	0.18	0.18	0.27	0.28	0.40	0.40	0.19	0.19
7.5	0.13	0.13	0.24	0.21	0.30	0.29	0.12	0.12
12.5	0.12	0.12	0.15	0.17	0.24	0.24	0.10	0.09
17.5	0.12	0.12	0.12	0.14	0.19	0.22	0.05	0.07
22.5	0.12	0.12	0.13	0.12	0.23	0.20	0.05	0.07
27.5	0.12	0.12	0.10	0.10	0.19	0.20	0.06	0.06
32.5		0.12	0.10	0.09		0.20	0.07	0.06

Appendix A3.5.20 Planar PI Data for system 6c clearcoat only, artificial weathering (CAM and SPART), where;

$\Delta PI_{OH} = \Delta PI_{OH\ t=t} - \Delta PI_{OH\ t=0}$ and, Calc ΔPI_{OH} = data for clearcoat fitted to an exponential equation, for 5µm thick microtomed slices at the nominal depths indicated

Planar 6c								
	CAM Exposure Time/hours						SPART Exposure Time/hours	
	1000		2000		4000		1000	
Depth /µm	ΔPI	Calc ΔPI	ΔPI	Calc ΔPI	ΔPI	Calc ΔPI	ΔPI	Calc ΔPI
2.5	0.43	0.44	0.67	0.68	0.91	0.91	0.33	0.33
7.5	0.39	0.36	0.61	0.56	0.76	0.74	0.29	0.27
12.5	0.31	0.33	0.47	0.49	0.62	0.64	0.31	0.27
17.5	0.31	0.31	0.44	0.45	0.61	0.58	0.28	0.27
22.5	0.28	0.31	0.40	0.42	0.51	0.55	0.25	0.27
27.5	0.29	0.31	0.42	0.41	0.52	0.53	0.26	0.27
32.5	0.32	0.30	0.40	0.40	0.52	0.51	0.26	0.27
37.5	0.33	0.30	0.41	0.39	0.52	0.50	0.23	0.27

Appendix A3.5.21 Planar PI Data for system 7 clearcoat only, artificial weathering (CAM and SPART), where;

$\Delta PI_{OH} = \Delta PI_{OH\ t=t} - \Delta PI_{OH\ t=0}$ and, Calc ΔPI_{OH} = data for clearcoat fitted to an exponential equation, for 5µm thick microtomed slices at the nominal depths indicated.

Planar 7								
	CAM Exposure Time/hours						SPART Exposure Time/hours	
	1000		2000		4000		1000	
Depth /µm	ΔPI	Calc ΔPI	ΔPI	Calc ΔPI	ΔPI	Calc ΔPI	ΔPI	Calc ΔPI
2.5	0.40	0.40	0.58	0.58	0.70	0.71	0.29	0.30
7.5	0.28	0.27	0.41	0.41	0.54	0.51	0.21	0.19
12.5	0.21	0.21	0.34	0.34	0.39	0.42	0.13	0.14
17.5	0.16	0.17	0.31	0.30	0.38	0.38	0.08	0.12
22.5	0.14	0.15	0.27	0.28	0.34	0.37	0.11	0.11
27.5	0.16	0.14	0.27	0.27	0.38	0.36	0.12	0.11
32.5	0.13	0.13	0.27	0.27	0.39	0.36	0.12	0.10

Appendix A3.5.22 Planar PI Data for system 8 clearcoat only, artificial weathering (CAM and SPART), where;

$\Delta PI_{OH} = \Delta PI_{OH\ t=t} - \Delta PI_{OH\ t=0}$ and, Calc ΔPI_{OH} = data for clearcoat fitted to an exponential equation, for 5µm thick microtomed slices at the nominal depths indicated

Planar 8								
	CAM Exposure Time/hours						SPART Exposure Time/hours	
	1000		2000		4000		1000	
Depth/ µm	ΔPI	Calc ΔPI	ΔPI	Calc ΔPI	ΔPI	Calc ΔPI	ΔPI	Calc ΔPI
2.5	0.42	0.42	0.61	0.64	0.83	0.83	0.38	0.38
7.5	0.38	0.37	0.66	0.59	0.76	0.76	0.27	0.28
12.5	0.41	0.37	0.54	0.57	0.74	0.75	0.28	0.26
17.5	0.34	0.37	0.47	0.56	0.72	0.75	0.24	0.26
22.5	0.37	0.37	0.51	0.55	0.74	0.75	0.20	0.26
27.5	0.38	0.37	0.58	0.55	0.76	0.75	0.31	0.26
32.5	0.33	0.37	0.62	0.55	0.79	0.75	0.28	0.26

Appendix A3.5.23 Planar PI Data for system 10 clearcoat only, artificial weathering (CAM and SPART), where;

$\Delta PI_{OH} = \Delta PI_{OH\ t=t} - \Delta PI_{OH\ t=0}$ and, Calc ΔPI_{OH} = data for clearcoat fitted to an exponential equation, for 5µm thick microtomed slices at the nominal depths indicated.

Planar 10								
	CAM Exposure Time/hours						SPART Exposure Time/hours	
	1000		2000		4000		1000	
Depth/ µm	ΔPI	Calc ΔPI	ΔPI	Calc ΔPI	ΔPI	Calc ΔPI	ΔPI	Calc ΔPI
2.5	0.48	0.49	0.67	0.66	1.05	1.05	0.37	0.38
7.5	0.43	0.41	0.53	0.54	0.81	0.82	0.28	0.27
12.5	0.33	0.36	0.47	0.47	0.70	0.70	0.22	0.23
17.5	0.34	0.34	0.44	0.43	0.63	0.63	0.21	0.22
22.5	0.36	0.33	0.42	0.42	0.61	0.60	0.23	0.21
27.5	0.31	0.32	0.42	0.41	0.55	0.58	0.23	0.21
32.5	0.31	0.32	0.38	0.40	0.58	0.57	0.20	0.21

APPENDICES: CHAPTER 4

A4.1 DMA Charts at different weathering times

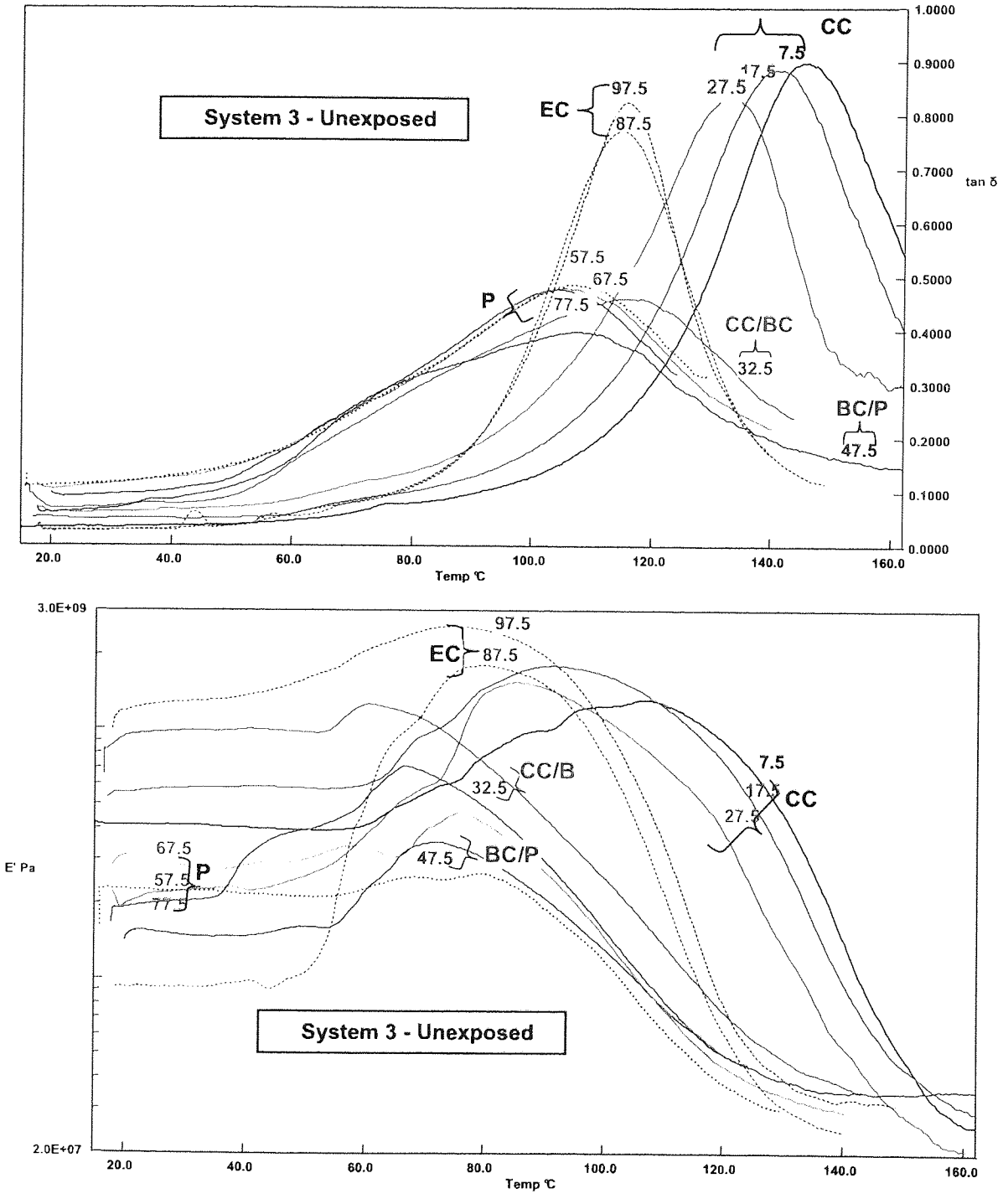

Appendix 4.1.1 Depth profiling of tan δ (Tg) and elastic modulus (E') for unexposed System 3 (SB). Numbers on curves are the nominal layer depths in μm.

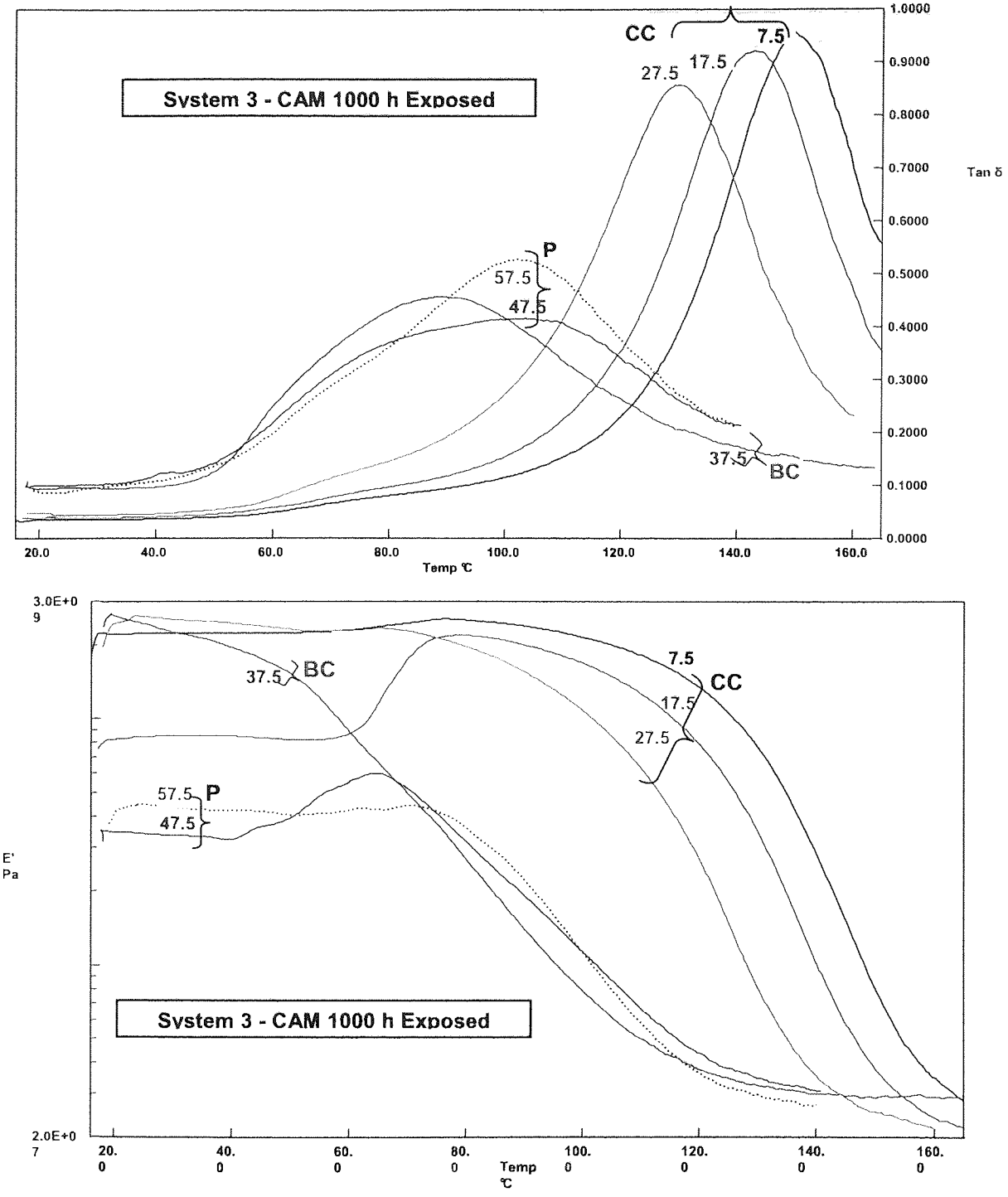

Appendix 4.1.2 Depth profiling of tan δ (Tg) and elastic modulus (E') for exposed (accelerated weathering – CAM 1000 h) of System 3 (SB). Numbers on curves are the nominal layer depths in μm.

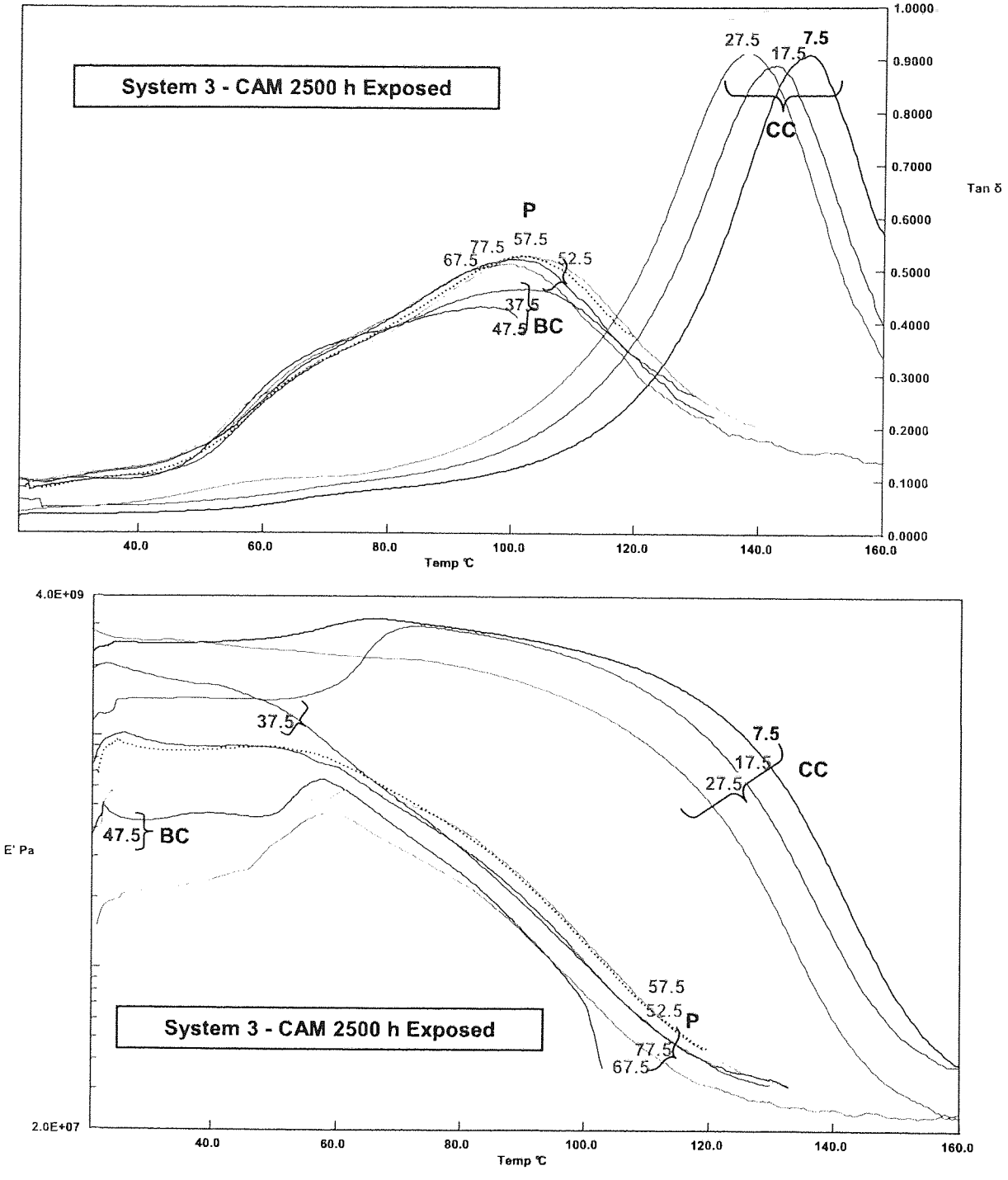

Appendix 4.1.3 Depth profiling of tan δ (Tg) and elastic modulus (E') for exposed (accelerated weathering – CAM 2500 h) of System 3 (SB). Numbers on curves are the nominal layer depths in μm.

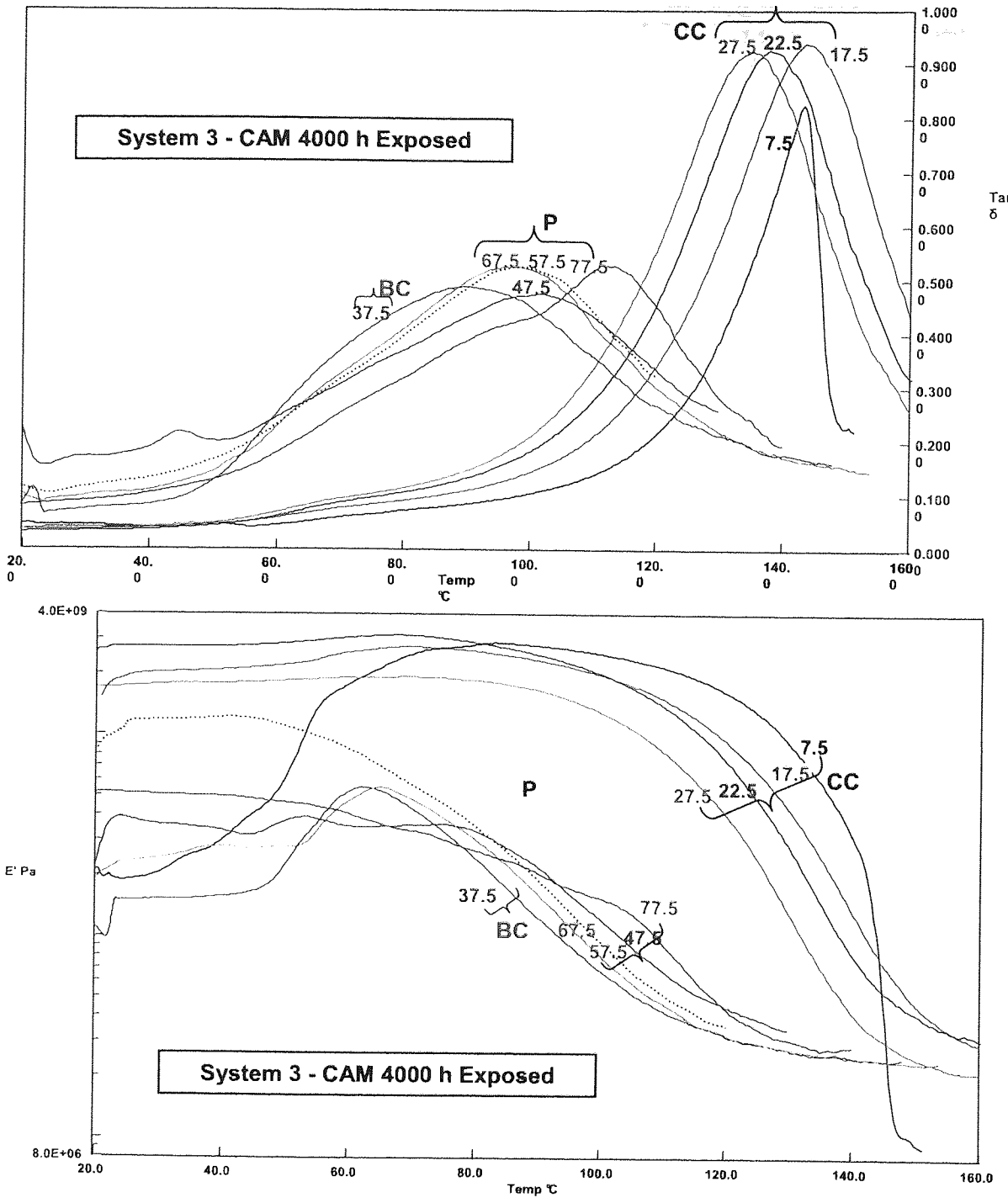

Appendix 4.1.4 Depth profiling of tan δ (Tg) and elastic modulus (E') for exposed (accelerated weathering – CAM 4000 h) of System 3 (SB). Numbers on curves are the nominal layer depths in μm.

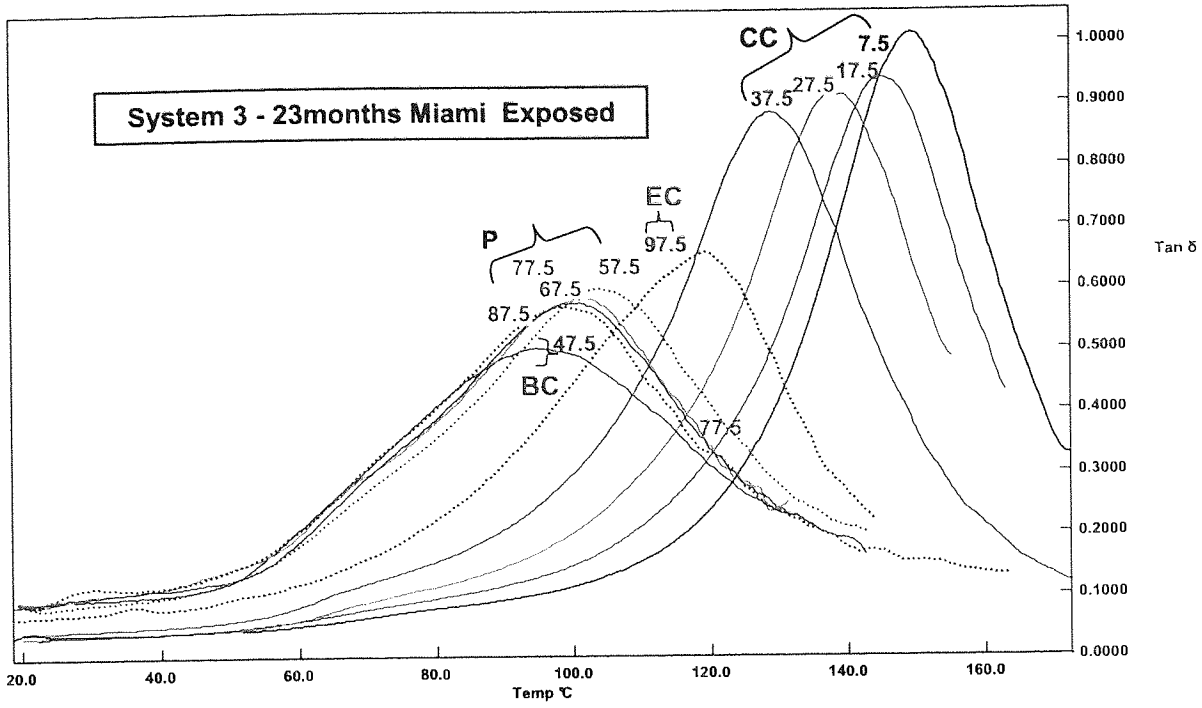

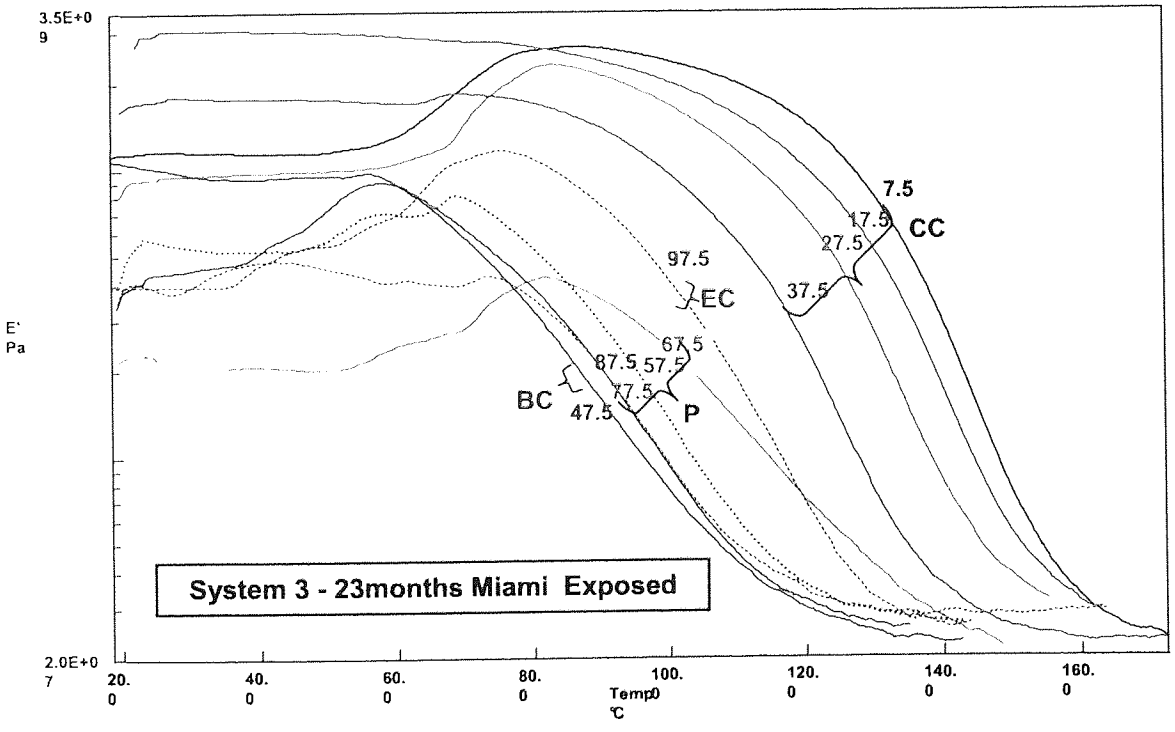

Appendix 4.1.5 Depth profiling of tan δ (Tg) and elastic modulus (E') for exposed (natural weathering –23 months Miami) of System 3 (SB). Numbers on curves are the nominal layer depths in μm.

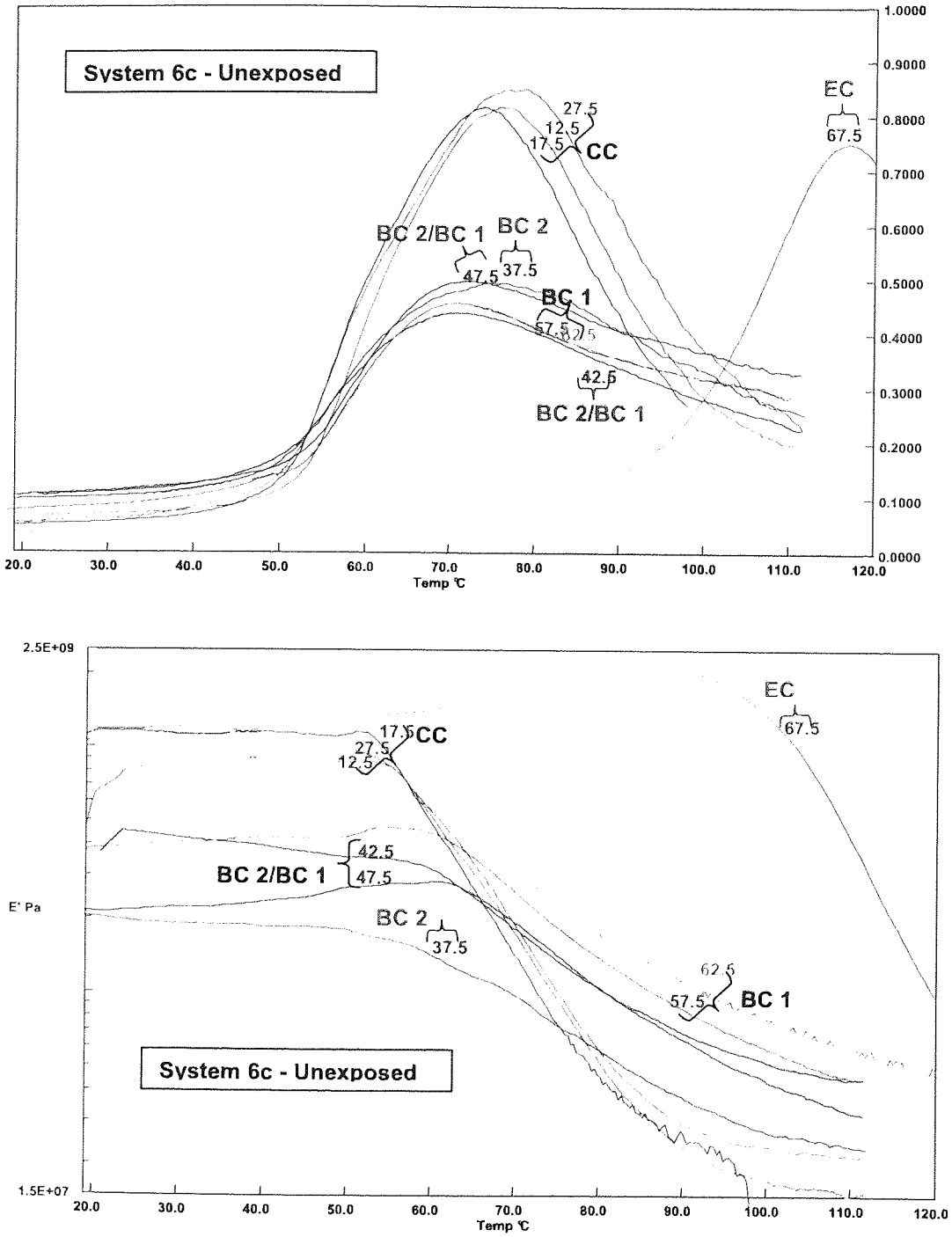

Appendix 4.1.6 Depth profiling of tan δ (Tg) and elastic modulus (E') for unexposed System 6c (WB). Numbers on curves are the nominal layer depths in μm.

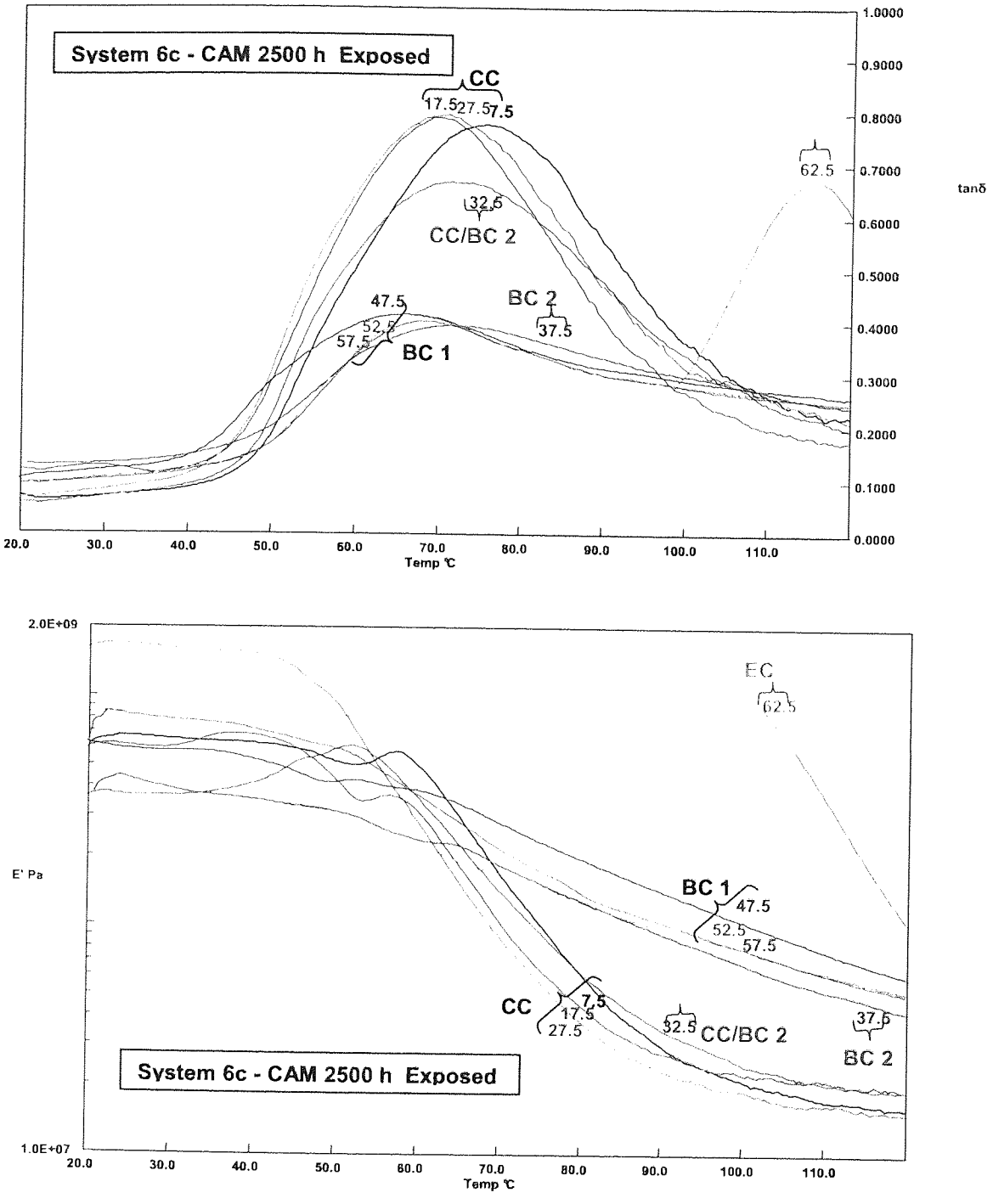

Appendix 4.1.7 Depth profiling of tan δ (Tg) and elastic modulus (E') for exposed (accelerated weathering – CAM 2500 h) of System 6c (WB). Numbers on curves are the nominal layer depths in μm.

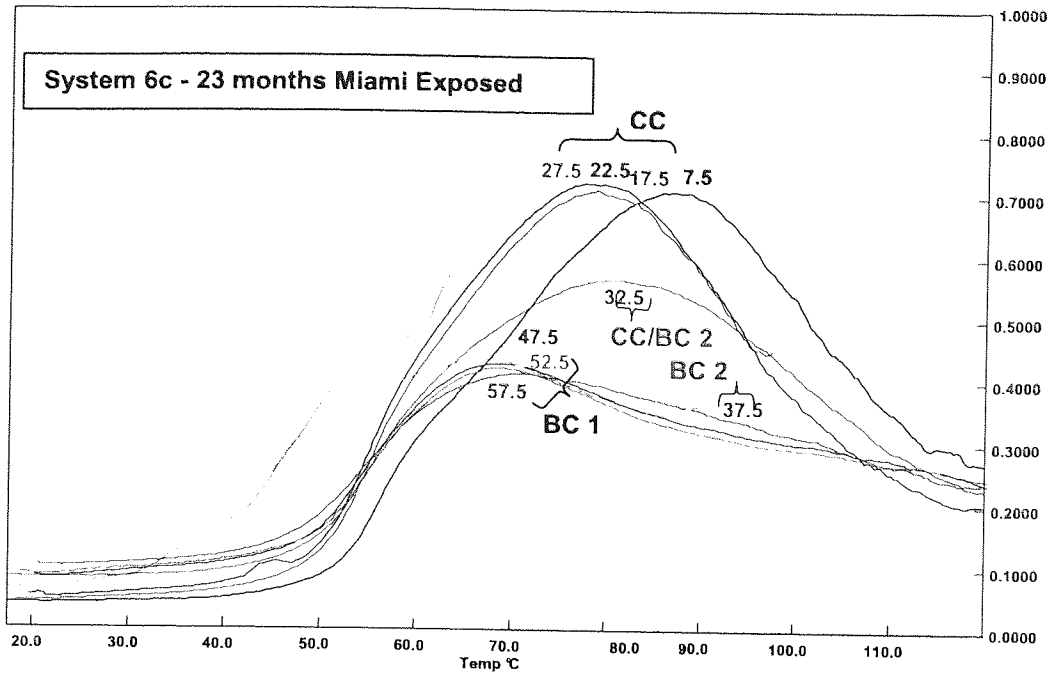

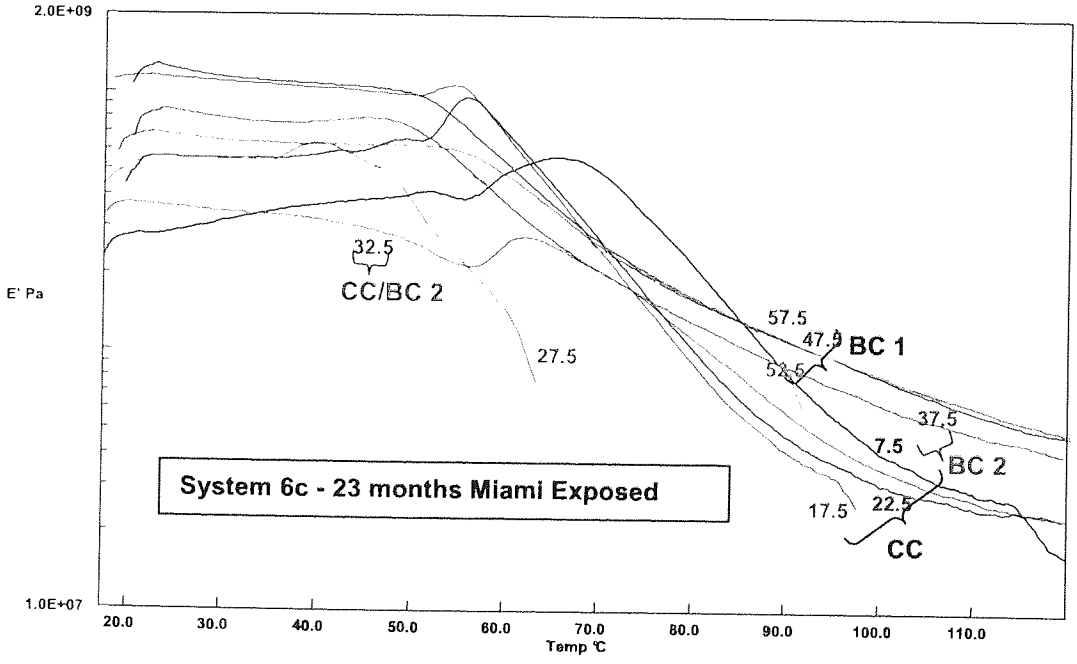

Appendix 4.1.8 Depth profiling of tan δ (Tg) and elastic modulus (E') for exposed (natural weathering –23 months Miami) of System 6c (WB). Numbers on curves are the nominal layer depths in μm.

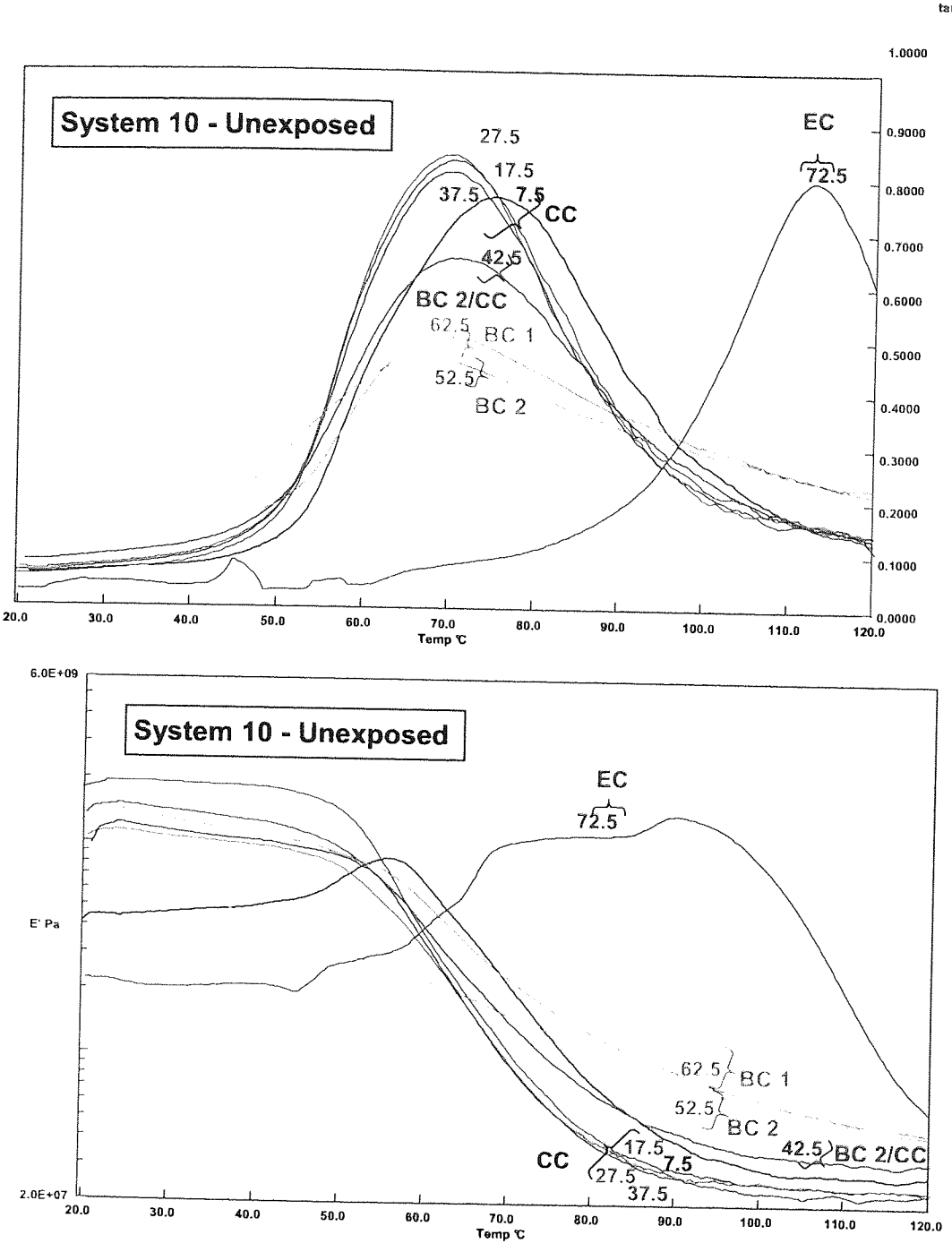

Appendix 4.1.9 Depth Profiling of tan δ (Tg) and elastic modulus for unexposed System 10 (WB). Numbers on the curves are the nominal layer depths in μm.

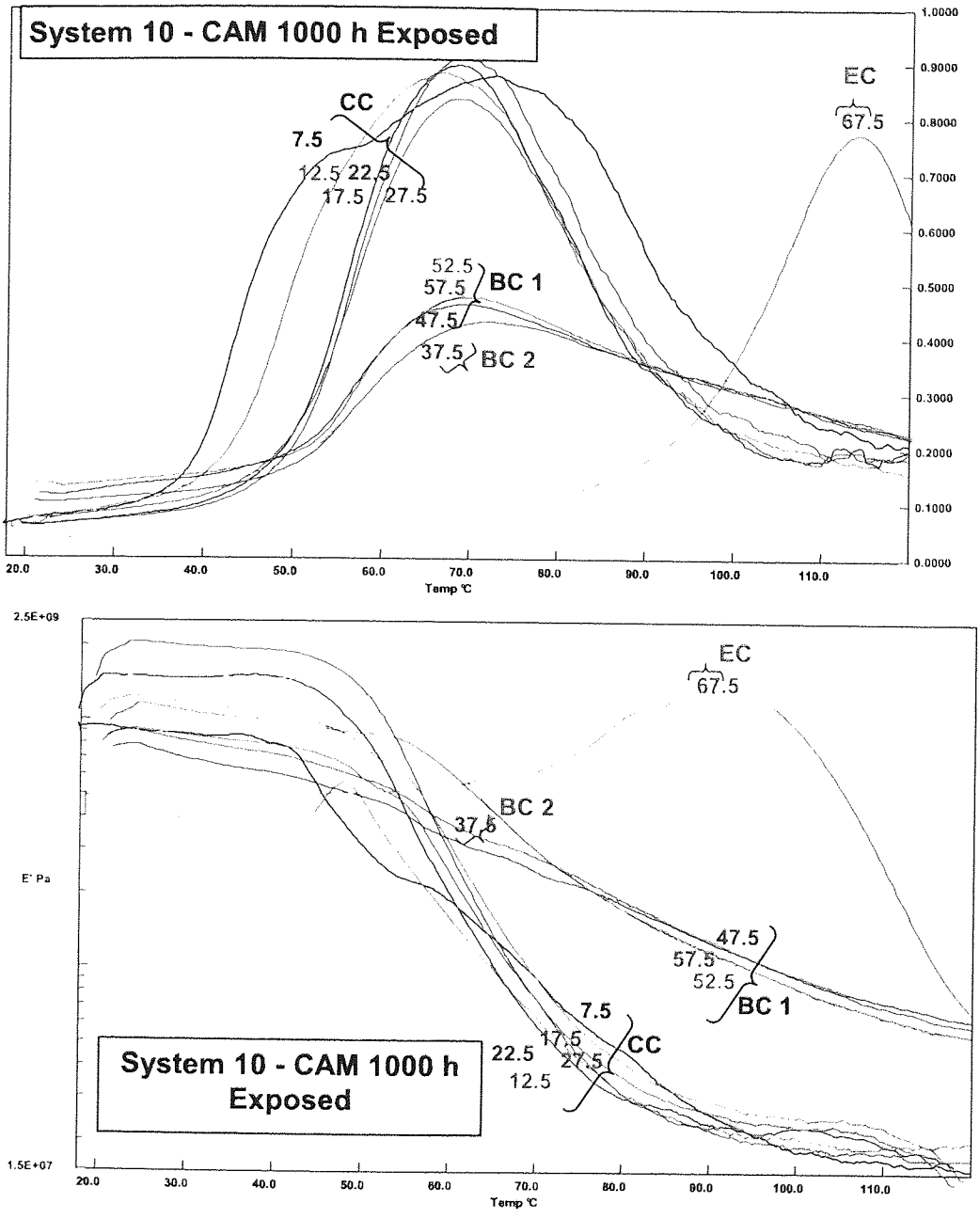

Appendix 4.1.10 Depth Profiling of tan δ (Tg) and elastic modulus for exposed (accelerated weathering – CAM 1000 h) of System 10 (WB). Numbers on the curves are the nominal layer depths in μm.

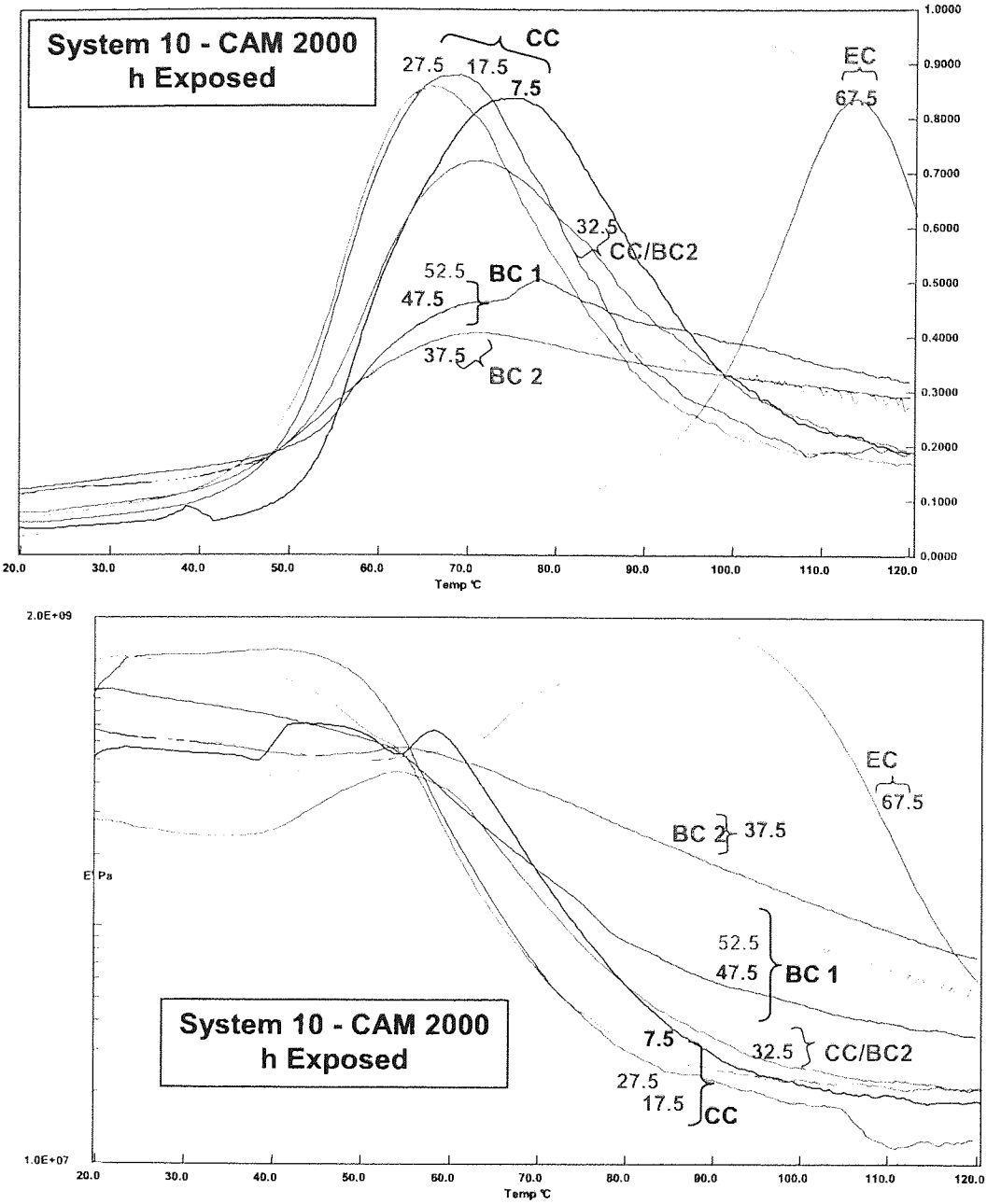

Appendix 4.1.11 Depth Profiling of tan δ (Tg) and elastic modulus for exposed (accelerated weathering – CAM 2000 h) of System 10 (WB). Numbers on the curves are the nominal layer depths in μm.

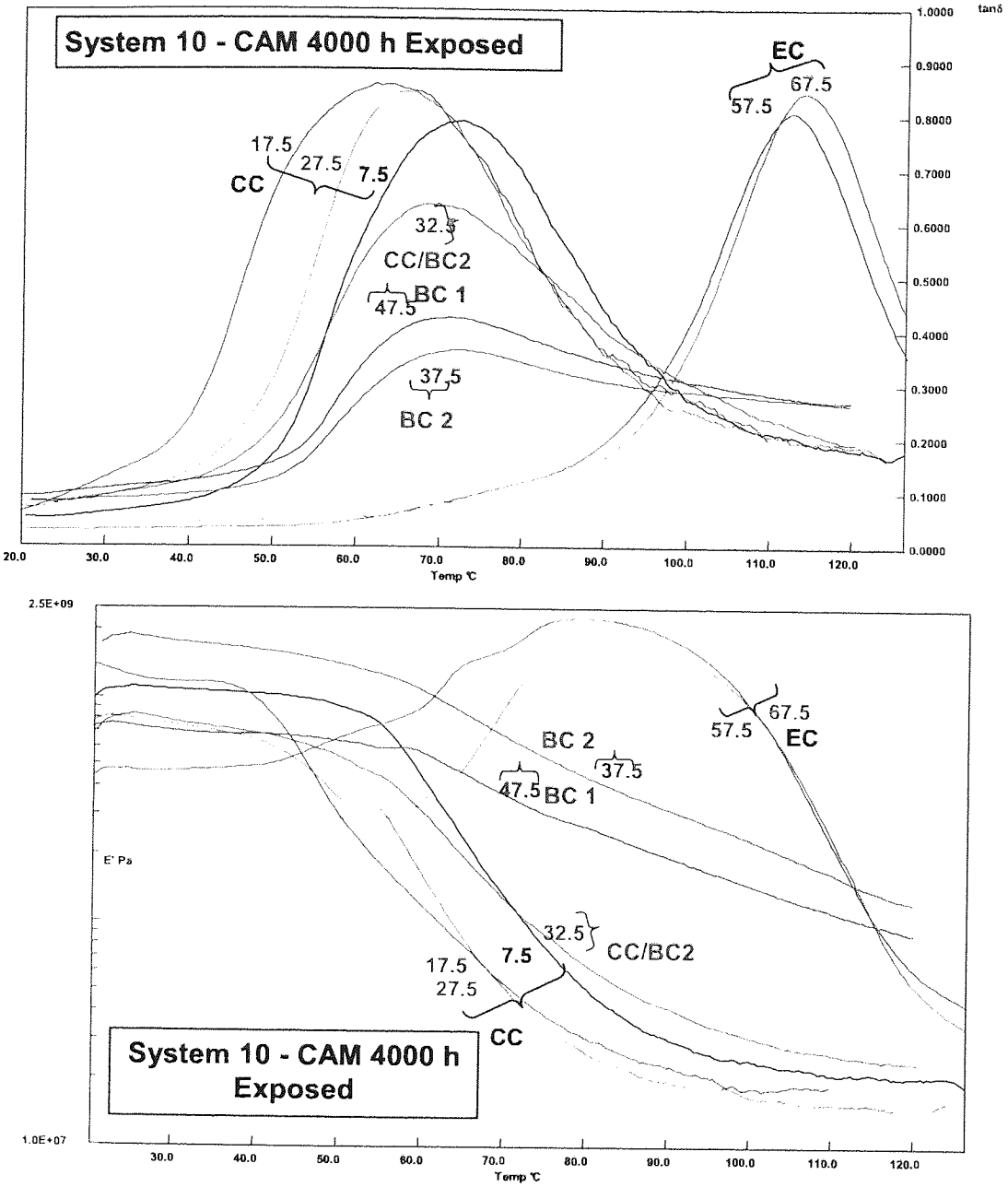

Appendix 4.1.12 Depth Profiling of tan δ (Tg) and elastic modulus for exposed (accelerated weathering – CAM 4000 h) of System 10 (WB). Numbers on the curves are the nominal layer depths in μm.

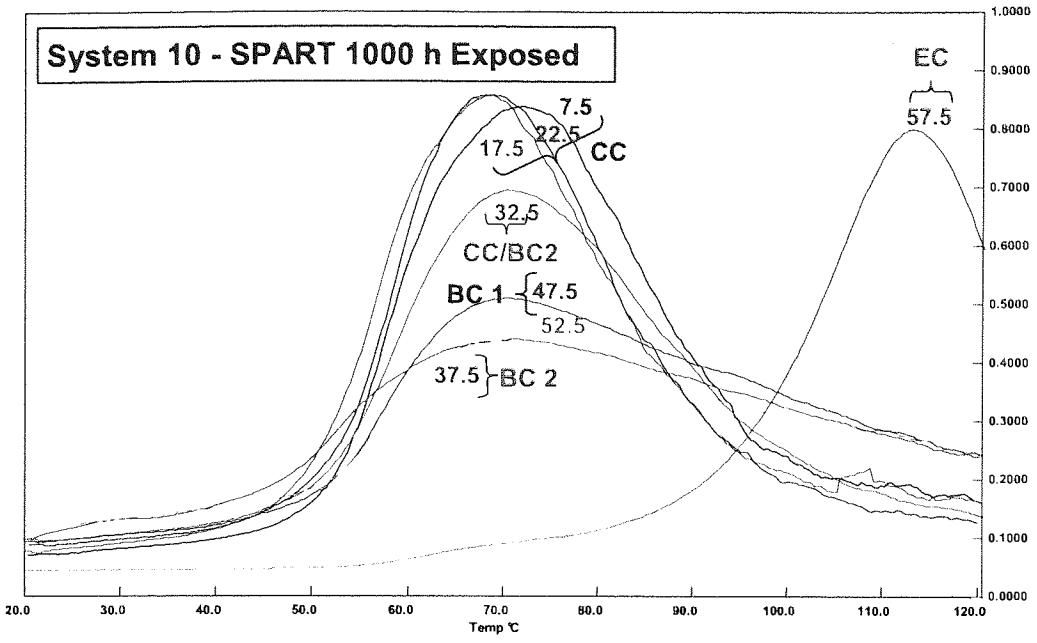

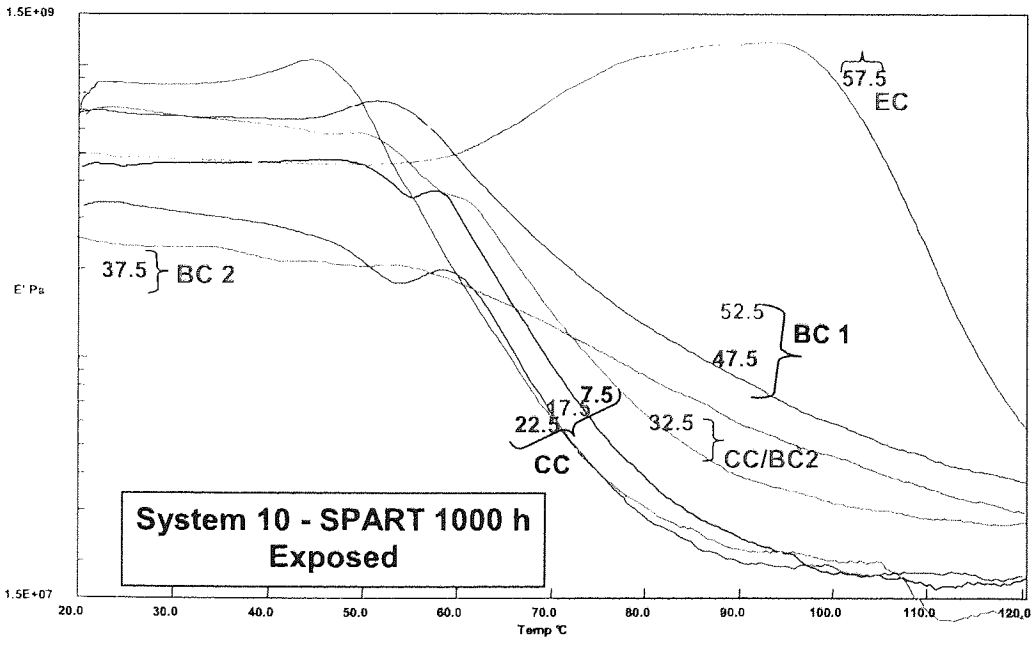

Appendix 4.1.13 Depth Profiling of tan δ (Tg) and elastic modulus for exposed (accelerated weathering – SPART 1000 h) of System 10 (WB). Numbers on the curves are the nominal layer depths in µm.

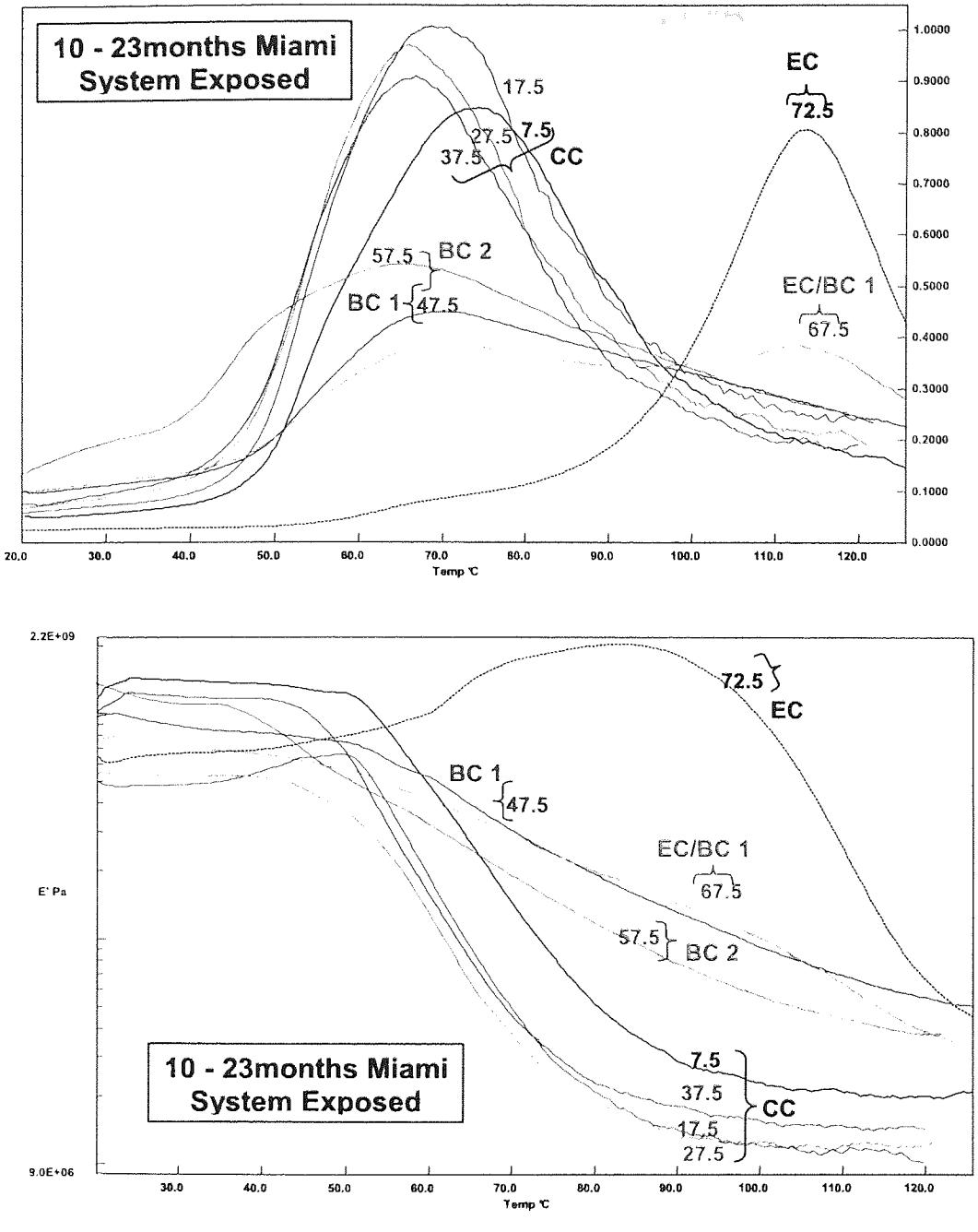

Appendix 4.1.14 Depth Profiling of tan δ (Tg) and elastic modulus for exposed (natural weathering – 23 months in Miami) of System 10 (WB). Numbers on the curves are the nominal layer depths in μm.

A4.2 DMA Tg and E'min data at different weathering times

Appendix 4.2.1 Depth Profiling data of tan δ (Tg) and elastic modulus for unexposed and weathered (both artificial and natural) of System 3 (SB). The depths are the nominal layer depths in μm.

System 3										
Depth/μm	CAM Exposure Time/hours								Miami Exposure Time/months	
	0		1000		2000		4000		23	
	E'min/E+7 Pa	Tg/°C	E'min/E+7 Pa	Tg/°C	E'min/E+7 Pa	Tg/°C	E'min/E+7 Pa	Tg/°C	E'min/E+7 Pa	Tg/°C
2.5										
7.5	2.6	145.5	2.9	149.7	3.9	147.8			2.5	149.1
12.5										
17.5	2.9	141.1	2.2	142.7	3.8	142.4	2.8	144	3	145.3
22.5							3	138		
27.5	1.2	141.1	2.2	130.4	2.4	138	2.1	135	3.4	138.4
32.5	3.6	117								
37.5			3	88.6	3.2	101.9	2.5	90	2.3	129.2
42.5										
47.5	3.5	107.7	3.1	105.7		95.5	3.5	101	2.3	96.2
52.5					2.9	102.3				
57.5	3	107.6	2.7	102.4	1.7	102.3	3.7	98	2.7	103.4
62.5										
67.5	3	105.9			2.3	99	2.3	96.9	1.1	101.9
72.5										
77.5	4.6	103.9			3.3	100.9	2.7	92.8	2.5	99.9
82.5							2.7	112		
87.5	2.5	114.9							2.8	99.8
92.5										
97.5	3.2	115.9							2.5	119.6

Appendix 4.2.2 Δ Depth Profiling data of tan δ (Tg) and elastic modulus for unexposed and weathered slices (both artificial and natural) of System 3 (SB). The depths are the nominal layer depths in μm.
ΔChange = $value_{time=t}$ – $value_{average\ across\ the\ clearcoat\ at\ t=0}$

System 3

	CAM Exposure Time/hours																Miami Exposure Time/months			
	0				1000				2000				4000				23			
Depth/μm	E'min/E+7 Pa	3rd layer	Tg/°C	3rd layer	E'min/E+7 Pa	Δ E'min/E+7 Pa	Tg/°C	Δ Tg/°C	E'min/E+7 Pa	Δ E'min/E+7 Pa	Tg/°C	Δ Tg/°C	E'min/E+7 Pa	Δ E'min/E+7 Pa	Tg/°C	Δ Tg/°C	E'min/E+7 Pa	Δ E'min/E+7 Pa	Tg/°C	Δ Tg/°C
2.5																				
7.5	2.6		145.5		2.9	0.0	150	8.6	3.9	1.0	148	6.7					2.5	-0.4	149	8.0
12.5																				
17.5	2.9	2.9	141.1	141.1	2.2	-0.7	143	1.6	3.8	0.9	142	1.3	2.8	-0.1	144	2.8	3	0.1	145	4.2
22.5													3	0.1	138	-3.4				
27.5	1.2		141.1		2.2	-0.7	130	-10.7	2.4	-0.5	138	-3.1	2.1	-0.8	135	-5.9	3.4	0.5	138	-2.7
32.5																				
37.5																	2.3	-0.6	129	-11.9

Appendix 4.2.3 Depth Profiling data of tan δ (Tg) and elastic modulus for unexposed and weathered slices (both artificial and natural) of System 6c (WB). The depths are the nominal layer depths in μm.

System 6c						
	CAM Exposure Time/hours				Miami Exposure Time/months	
	0		2500		23	
Depth/μm	E'min/E+7 Pa	Tg/^{0}C	E'min/E+7 Pa	Tg/^{0}C	E'min/E+7 Pa	Tg/^{0}C
2.5						
7.5			1.6	75.3	2.8	87.4
12.5	2.2	76.4				
17.5	2.5	74	2	70.6		78.9
22.5					2.3	78.9
27.5	1.5	77.8	1.5	70.6		
32.5			1.9	72.6	2.4	80.8
37.5	2.3	76.1	3.9	70.6	4.1	69.2
42.5	4.5	71.6				
47.5	3.2	72	6.1	66.2	4.4	69.7
52.5			5.1	68.4		67.7
57.5	4.5	72.4	5	68.9	4	68.8
62.5	4.2	72.7	5.1	115.3		
67.5	3.6	117.3				

Appendix 4.2.4 Δ Depth Profiling data of tan δ (Tg) and elastic modulus for unexposed and weathered slices (both artificial and natural) of System 6c (WB). The depths are the nominal layer depths in μm.
ΔChange = $value_{time=t} - value_{average\ across\ the\ clearcoat\ at\ t=0}$

System 6c												
	CAM Exposure Time/hours								Miami Exposure Time/months			
	0				2500				23			
Depth/μm	E'min/E+7 Pa	3rd layer	Tg/^{0}C	3rd layer	E'min/E+7 Pa	Δ E'min/E+7 Pa	Tg/^{0}C	Δ Tg/^{0}C	E'min/E+7 Pa	Δ E'min/E+7 Pa	Tg/^{0}C	Δ Tg/^{0}C
2.5												
7.5					1.6	-0.6	75	-1.1	2.8	0.6	87	11.0
12.5	2.2	2.2	76.4	76								
17.5	2.5		74		2	-0.2	71	-5.8			79	2.5
22.5									2.3	0.1	79	2.5
27.5	1.5		77.8		1.5	-0.7	71	-5.8				
32.5					1.9	-0.3	73	-3.8	2.4	0.2	81	4.4
37.5	2.3		76.1		3.9	1.7	71	-5.8				

Appendix 4.2.5 Depth Profiling data of tan δ (Tg) and elastic modulus for unexposed and weathered slices (both artificial and natural) of System 10 (WB). The depths are the nominal layer depths in μm.

System 10												
Depth	CAM Exposure Time/hours								SPART Exposure Time/hours		Miami Exposure Time/months	
/μm	0		1000		2000		4000			1000	23	
	E'min/ E+7 Pa	Tg/°C	E'min/ E+7 Pa	Tg/°C	E'min/ E+7 Pa	Tg/°C	E'min/ E+7 Pa	Tg/°C	E'min/ E+7 Pa	Tg/°C	E'min/ E+7 Pa	Tg/°C
2.5												
7.5	2.7	75.8	1.6	73	1.8	75.1	2	72.5	1.7	71.4	2	74.5
12.5			2	67								
17.5	2.4	70.6	1.7	69	1.7	68.3	1.8	63.8	1.2	69	1	69
22.5			1.7	69					1.7	68.8		
27.5	2.4	70.4			2	66.4	1.5	66			1.1	66.3
32.5			1.7	69	2.1	71	2.4	69.2	2.7	70.9		
37.5	2.3	70.3	5.6	72	7.5	71	12	72.3	3	70.1	1.4	66.5
42.5	3.1	70.8		61					3	70.3		
47.5			5.9	70	3.5	70.7	8.9	70.7	3.6	69.5	4.6	69.1
52.5	4.3	67.6	5.1	70	5.3	71.2			5	69.5		
57.5			5.3	69			3.3	113	3	113	3.8	65.9
62.5	4.4	69.2									2.9	69.6
67.5			3.7	114	3.1	114	2.6	114			2.9	113
72.5											3.2	114
77.5	3.1	113										

Appendix 4.2.6 Δ Depth Profiling data of tan δ (Tg) and elastic modulus for unexposed and weathered (both artificial and natural) of System 10 (WB). The depths are the nominal layer depths in μm.
ΔChange = $value_{time=t} - value_{average\ across\ the\ clearcoat\ at\ t=0}$

System 10

	CAM Exposure Time/hours																SPART Exposure Time/hours				Miami Exposure Time/months			
	0				1000				2000				4000				1000				23			
Depth/μm	E'min/E+7 Pa	3rd layer	Tg/°C	3rd layer	E'min/E+7 Pa	Δ E'min/E+7 Pa	Tg/°C	Δ Tg/°C	E'min/E+7 Pa	Δ E'min/E+7 Pa	Tg/°C	Δ Tg/°C	E'min/E+7 Pa	Δ E'min/E+7 Pa	Tg/°C	Δ Tg/°C	E'min/E+7 Pa	Δ E'min/E+7 Pa	Tg/°C	Δ Tg/°C	E'min/E+7 Pa	Δ E'min/E+7 Pa	Tg/°C	Δ Tg/°C
2.5																								
7.5	2.7		76		1.6	-0.8	72.7	2.1	1.8	-0.6	75.1	4.5	2	-0.4	72.5	1.9	2	-0.7	71.4	0.8	2	-0.4	74.5	3.9
12.5					2	-0.4	66.9	-3.7																
17.5	2.4	2.4	71	70.6	1.7	-0.7	69.4	-1.2	1.7	-0.7	68.3	##	1.8	-0.6	63.8	-6.8	1	-1.2	69	-1.6	1	-1.4	69	-1.6
22.5					1.7	-0.7	68.6	-2.0									2	-0.7	68.8	-1.8				
27.5	2.4		70						2	-0.4	66.4	##	1.5	-0.9	66	-4.6					1	-1.3	66.3	-4.3
32.5					1.7	-0.7	68.6	-2.0																
37.5	2.3		70																		1	-1.0	66.5	-4.1

A4.3 Confidence limits of DMA Tg and E'min data

Appendix 4.3.1 DMA confidence limit information for sample 6c, unexposed, heated at 5^0C/minute.

	E'min	Average at 5^0/min		SD		RSD		Confidence		Confidence	
Tg/^{0}C	x E 6 Pa	Tg	E'min	Tg	E'min	Tg	E'min	Tg	Tg	E'min	E'min
82.5	9.1	82.6	16.2	0.70	7.48	0.85	#	0.56	82.6 ± 0.6	5.98	16 ± 6
82.1	21										
82.1	13										
83.9	29										
82.1	14										
82.7	11										

APPENDICES: CHAPTER 5

A5.1 Diffusion Results

5.1.1 Traditional Method using the theoretical diffusion curves at 30^{0}C

Table A5.1 Experimental Diffusion Data at 30^{0}C

C(x,t)	C(x,t)/Co	Film Number	x	x/l
2.8	**1.12**	2	0.000044	**0.33**
2.1	**0.84**	3	0.000066	**0.5**
1.7	**0.68**	6	0.000132	**1**
1.8	**0.72**	7	0.000154	**1.2**
2.3	**0.92**	9	0.000198	**1.5**
2.4	**0.96**	10	0.000222	**1.7**
2.8	**1.12**	11	0.000242	**1.8**
2.8	**1.15**	12	0.000264	**2**

Where;

C(x,t) = Experimentally measured concentration of Cyasorb in the polymer film, %w/w

Co = maximum solubility of the additive in the polymer at the specified temperature

= 2.5w/w % at 30^{0}C.

Film Number = Position of the film in the stack, 1 at the top.

x = position co-ordinate of the polymer film in the stack, with respect to x = 0 at the centre of the film.

l = ½ the total thickness of the stack of polymer films

= 0.000132m

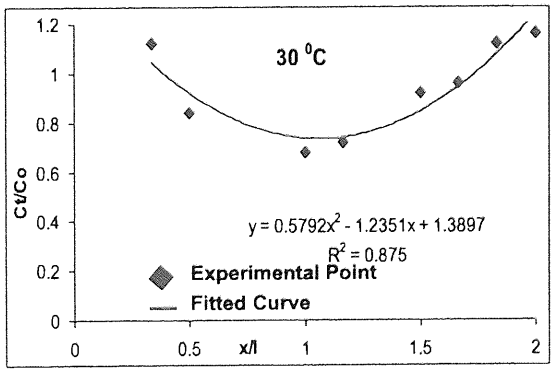

Figure A5.1 Experimental diffusion data for 30^{0}C

The experimental points were fitted to a quadratic curve. Both the actual experimental values and the fitted curve were then compared to the theoretical curves. Starting with the actual values, the experimental data was plotted on the theoretical curves in **Figure A5.2;**

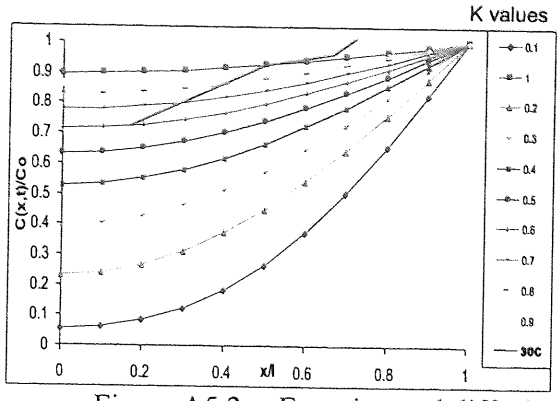

Figure A5.2 Experimental diffusion data for 30^0C, fitted to the theoretical curve

Closest fit, K = 0.7, Using equation (1.12), D was found;

$$D = (K * l^{2})/t \qquad (1.12)$$

Where;

l = ½ the total thickness of the stack of polymer films

= 0.000132m.

$l^2 = 1.75 * 10^{-8}$

t = 66 days on test = 5702400 seconds

D = $2.14 * 10^{-11}$ cm^2/s

A5.1.2 Graphical Method at 30^0C

Using data that was fitted to appropriate lines/curves (curve of plot of C(x,t)/Co vs x/l) (determined using the traditional method), appropriate equation of the curve was obtained. Plot of C(x,t)/Co vs.cos(π x/2l) was then generated **Table A5.2, Figure A5.3**.

Table A5.2 Graphical diffusion method at 30^0C, using fitted data

x/l	C(x,t)/Co	x	π x/2l	cos(π x/2l
0.0	**0.733**	0	0	1
0.1	**0.731**	0.0000132	0.157	0.987
0.2	**0.741**	0.0000264	0.314	0.951
0.3	**0.762**	0.0000396	0.471	0.891
0.4	**0.795**	0.0000528	0.628	0.809
0.5	**0.840**	0.000066	0.785	0.707
0.6	**0.896**	0.0000792	0.942	0.587
0.7	**0.963**	0.0000924	1.10	0.454
0.8	**1.04**	0.000105	1.25	0.309
0.9	**1.13**	0.000118	1.41	0.156
1.0	**1.23**	0.000132	1.57	6.13E-17

Co = maximum solubility of the additive in the polymer at the specified temperature = 2.5w/w %

x = position co-ordinate of the polymer film in the stack, with respect to x = 0 at the centre of the film.

l = ½ the total thickness of the stack of polymer films = 0.000132m.

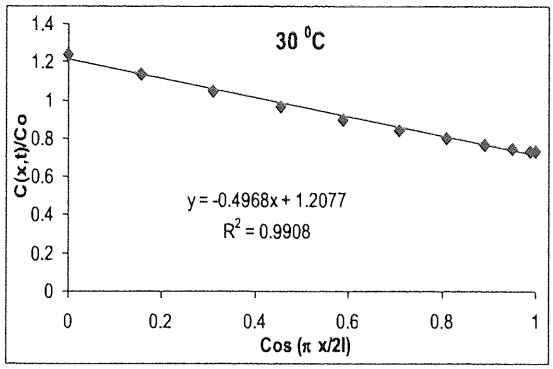

Figure A5.3 Graphical method for calculation of diffusion coefficient using the fitted experimental data.

Slope of chart = -0.4968

l = 0.000132 (from above)

$4l^2$ = $6.97 * 10^{-8}$

t = 66 days on test = 5702400 seconds

$Gradient = 1 - 4/\pi \exp(-D\pi^2 t/4l^2)$

-0.4968 = $1-4/\pi \exp(-D\pi^2t/4l^2)$

-1.4968 = $-4/\pi \exp(-D\pi^2t/4l^2)$

1.9058 = $\exp(-D\pi^2t/4l^2)$

6.7247 = $D\pi^2t/4l^2$

$8.3 * 10^{-11}$ = **cm^2/s**

A5.1.3 Traditional Method using the theoretical diffusion curves at 45^{0}C

Experimental data is given in **Table A5.3**, plotted in **Figure A5.4;**

Table A5.3 Experimental Diffusion Data at 45^{0}C

C(x,t)	C(x,t)/Co	Film Number	x	x/l
5.6	**2.2**	2	0.00044	**0.33**
3.8	**1.5**	4	0.00088	**0.67**
1.7	**0.7**	6	0.00013	**1**
2.5	**1.0**	7	0.00015	**1.17**
4.4	**1.7**	9	0.0002	**1.5**
5.3	**2.0**	10	0.00022	**1.67**
5.7	**2.2**	12	0.00026	**2**

C(x,t) = Experimentally measured concentration of Cyasorb in the polymer film, %w/w

Co = maximum solubility of the additive in the polymer at the specified temperature = 2.6w/w % at 45^{0}C.

Film Number = Position of the film in the stack, 1 at the top.

x = position co-ordinate of the polymer film in the stack, with respect to x = 0 at the centre of the film.

l = ½ the total thickness of the stack of polymer films = 0.000132m.

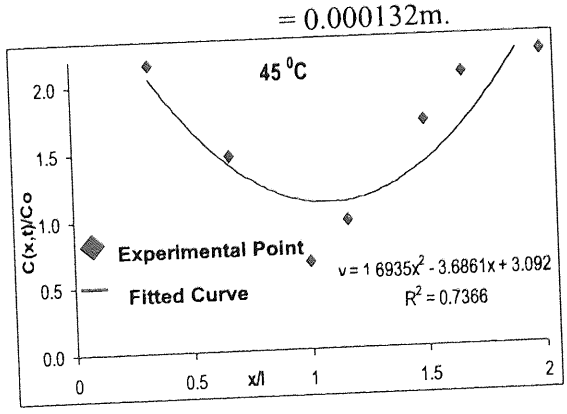

Figure A5.4 Experimental diffusion data for 45^{0}C

The experimental points were fitted to a quadratic curve. Both the actual experimental values and the fitted curve were then compared to the theoretical curves.

Starting with the actual values, the experimental data was plotted on the theoretical curves in **Figure A5.5**.

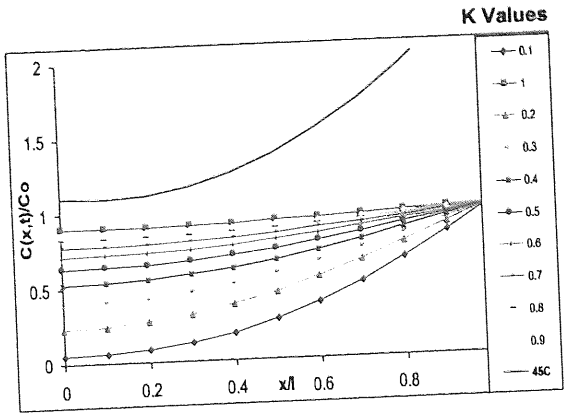

Figure A5.6 Experimental diffusion data for 45^{0}C, fitted to the theoretical curve

A fit could not be found, thus D could not be found.

A5.1.4 Graphical Method at 45^{0}C

Now using data that was fitted to appropriate lines/curves (curve of plot of C(x,t)/Co vs x/l) appropriate equation of the curve was obtained. Plot C(x,t)/Co vs.cos(π x/2l) was then generated **Table A5.4, Figure A5.6.**

Table A5.8, graphical diffusion method at 45^{0}C, using fitted data

x/l	C(x,t)/Co	x	π x/2l	cos(π x/2l
0.0	**-1.26**	0	0	**1**
0.1	**-1.27**	0.0000132	0.157	**0.988**
0.2	**-1.25**	0.0000264	0.314	**0.951**
0.3	**-1.19**	0.0000396	0.471	**0.891**
0.4	**-1.10**	0.0000528	0.628	**0.809**
0.5	**-0.98**	0.000066	0.785	**0.707**
0.6	**-0.83**	0.0000792	0.942	**0.588**
0.7	**-0.64**	0.0000924	1.100	**0.454**
0.8	**-0.41**	0.0001056	1.257	**0.309**
0.9	**-0.15**	0.0001188	1.414	**0.156**
1.0	**0.14**	0.000132	1.571	**0.000**

Co = maximum solubility of the additive in the polymer at the specified temperature = 2.6w/w %

x = position co-ordinate of the polymer film in the stack, with respect to x = 0 at the centre of the film.

l = ½ the total thickness of the stack of polymer films = 0.000132m.

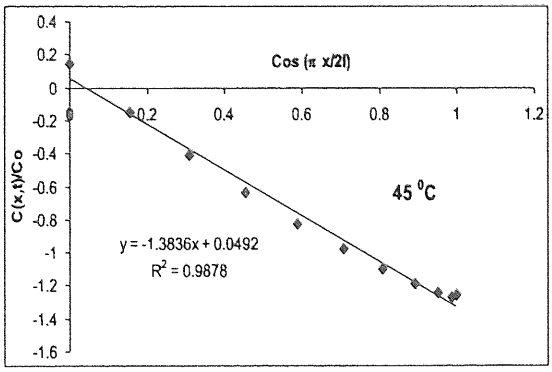

Figure A5.10 Graphical method for calculation of diffusion coefficient using the fitted experimental data.

Slope of chart = -1.3836

l = 0.000132 (from above)

$4l^2$ = $6.97 * 10^{-8}$

t = 66 days on test = 5702400 seconds

$Gradient = 1 - 4/\pi \exp(-D\pi^2 t/4l^2)$

-1.3836 = $1-4/\pi \exp(-D\pi^2 t/4l^2)$

-2.3836 = $-4/\pi \exp(-D\pi^2 t/4l^2)$

3.039 = $\exp(-D\pi^2 t/4l^2)$

20.89 = $D\pi^2 t/4l^2$

0.000001456 = $D\pi^2$

D = $2.6 * 10^{-10} cm^2/s$

A5.1.5 Traditional Method using the theoretical diffusion curves at 60^0C

Experimental data is given in Table A5.5, plotted in Figure A5.7;

Table A5.5, Experimental Diffusion Data at 60^0C

C(x,t)	C(x,t)/Co	Film Number	x	x/l
2.7	1.08	1	2.95E-05	1.67E-01
2.4	0.90	2	5.90E-05	3.33E-01
2.1	0.76	3	8.85E-05	5.00E-01
1.9	0.69	5	1.18E-04	6.67E-01
1.8	0.68	6	1.48E-04	8.33E-01
1.8	0.68	7	0.000177	1
1.9	0.69	8	0.000207	1.166667
2.1	0.77	9	0.000236	1.333333
2.1	0.79	10	0.000266	1.5
2.1	0.80	11	0.000295	1.666667
2.3	0.83	12	0.000325	1.833333
2.7	0.99	13	0.000354	2

C(x,t) = Experimentally measured concentration of Cyasorb in the polymer film, %w/w

Co = maximum solubility of the additive in the polymer at the specified temperature = 2.7w/w % at 60^0C.

Film Number = Position of the film in the stack, 1 at the top.

x = position co-ordinate of the polymer film in the stack, with respect to x = 0 at the centre of the film.

l = ½ the total thickness of the stack of polymer films = 0.000177m.

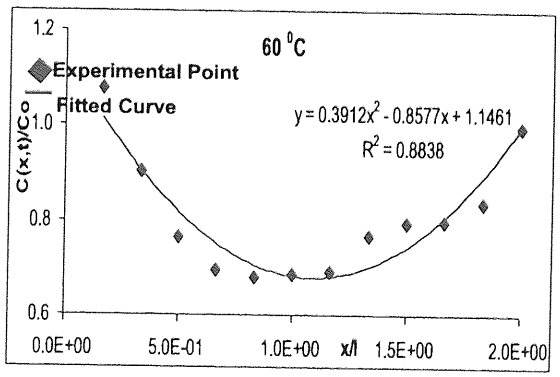

Figure A5.7 Experimental diffusion data for 60^0C

Equation of line fitted to the experimental data;

$y = 0.3912x^2 - 0.8577x + 1.1461$, thus points to plot on the theoretical curve, the curves are shown in Figure A5.8.

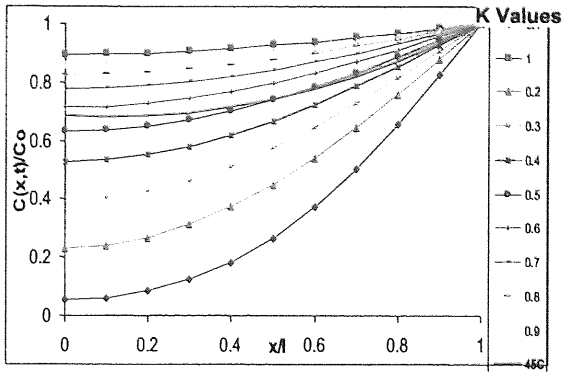

Figure A5.8 Graphical method for calculation of diffusion coefficient using the fitted data.

Closest fit, K = 0.5,

D $= (K * l^{2})/t$ Where;

l = ½ the total thickness of the stack of polymer films

= 0.000177m.

l^2 $= 3.13 * 10^{-8}$

t = 8 days on test = 691200 seconds

D $= \mathbf{2.3 * 10^{-10}\ cm^2/s}$

A5.1.6 Graphical Method at 60^0C

Now using data that was fitted to appropriate lines/curves (curve of plot of C(x,t)/Co vs x/l) (determined using the traditional method, Fig. 15), appropriate equation of the curve was obtained. Plot C(x,t)/Co vs.cos(π x/2l) was then generated Table A5.6, Fig. A5.9,

Table A5.6, graphical diffusion method at 60^0C, using fitted data

x/l	C(x,t)/Co	x	π x/2l	cos(π x/2l
0.0	**0.679**	0	0.000	**1**
0.1	**0.676**	1.77E-05	0.157	**0.988**
0.2	**0.680**	3.54E-05	0.314	**0.951**
0.3	**0.692**	5.31E-05	0.471	**0.891**
0.4	**0.712**	7.08E-05	0.628	**0.809**
0.5	**0.739**	8.85E-05	0.785	**0.707**
0.6	**0.775**	0.000106	0.942	**0.588**
0.7	**0.818**	0.000124	1.100	**0.454**
0.8	**0.869**	0.000142	1.257	**0.309**
0.9	**0.928**	0.000159	1.414	**0.156**
1.0	**0.995**	0.000177	1.571	**0.000**

Co = maximum solubility of the additive in the polymer at the specified temperature = 2.7w/w %

x = position co-ordinate of the polymer film in the stack, with respect to x = 0 at the centre of the film.

l = ½ the total thickness of the stack of polymer films = 0.000177m.

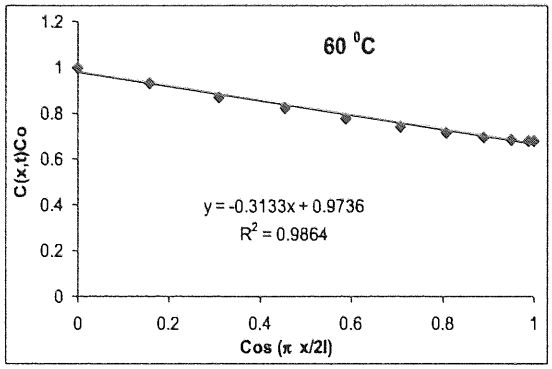

Figure A5.9 Graphical method for calculation of diffusion coefficient using the fitted experimental data

Slope of chart = -0.3133

l = 0.000177 (from above)

$4l^2$ = $1.27 * 10^{-7}$

t = 8 days on test = 691200 seconds

$Gradient = 1 - 4/\pi \exp(-D\pi^2 t/4l^2)$

-0.3133 = $1-4/\pi \exp(-D\pi^2t/4l^2)$

-1.3133 = $-4/\pi \exp(-D\pi^2t/4l^2)$

1.672 = $\exp(-D\pi^2t/4l^2)$

5.323 = $D\pi^2t/4l^2$

D = **$9.8 * 10^{-10} cm^2/s$**